

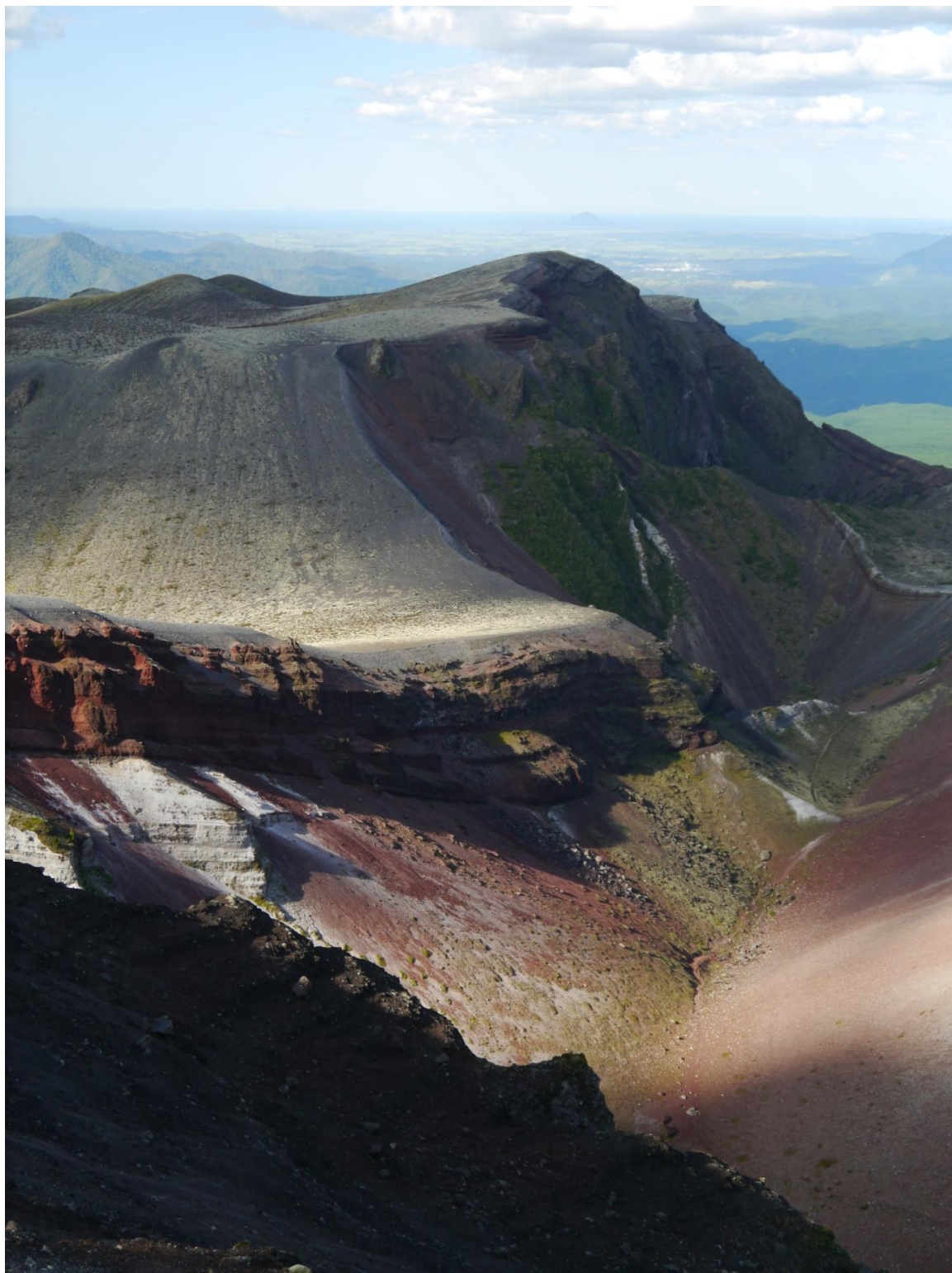
Controls on rhyolite lava dome eruptions in the Taupo Volcanic Zone

Paul Allan Ashwell

*A thesis submitted in partial fulfilment
of the requirements for the degree of
Doctor of Philosophy in Geological Sciences
at the University of Canterbury*

October 2013

Dedicated to Eva Ashwell



View from Ruawahia, across the 1886AD fissure and Wahanga dome towards the Bay of Plenty and White Island (extreme distance, centre left)

Abstract

The evolution of rhyolitic lava from effusion to cessation of activity is poorly understood. Recent lava dome eruptions at Unzen, Colima, Chaiten and Soufrière Hills have vastly increased our knowledge on the changes in behaviour of active domes. However, in ancient domes, little knowledge of the evolution of individual extrusion events exists. Instead, internal structures and facies variations can be used to assess the mechanisms of eruption.

Rhyolitic magma rising in a conduit vesiculates and undergoes shear, such that lava erupting at the surface will be a mix of glass and sheared vesicles that form a permeable network, and with or without phenocryst or microlites. This foam will undergo compression from overburden in the shallow conduit and lava dome, forcing the vesicles to close and affecting the permeable network. High temperature, uniaxial compression experiments on crystal-rich and crystal-poor lavas have quantified the evolution of porosity and permeability in such environments. The deformation mechanisms involved in uniaxial deformation are viscous deformation and cracking. Crack production is controlled by strain rate and crystallinity, as strain is localised in crystals in crystal rich lavas. In crystal poor lavas, high strain rates result in long cracks that drastically increase permeability at low strain. Numerous and small cracks in crystal rich lavas allow the permeable network to remain open (although at a lower permeability than undeformed samples) while the porosity decreases.

Flow bands result from shear movement within the conduit. Upon extrusion, these bands will become modified from movement of lava, and can therefore be used to reconstruct styles of eruption. Both Ngongotaha and Ruawahia domes, from Rotorua caldera and Okataina caldera complex (OCC) respectively, show complex flow banding that can be traced to elongated or aligned vents. The northernmost lobe at Ngongotaha exhibits a fan-like distribution of flow

bands that are interpreted as resulting from an initial lava flow from a N – S trending fissure. This flow then transitioned into intrusion of obsidian sheets directly above the conduit, bound by wide breccia zones which show vertical movement of the sheets. Progressive intrusions then forced the sheets laterally, forming a sequence of sheets and breccia zones. At Ruawahia, the flow bands show two types of eruption; long flow lobes with ramp structures, and smaller spiny lobes which show vertical movement and possible spine extrusion. The difference is likely due to palaeotopography, as a large pyroclastic cone would have confined the small domes, while the flow lobes were unconfined and able to flow down slope. The vents at Ruawahia are aligned in a NE – SW orientation. Both domes are suggested to have formed from the intrusion of a dyke.

The orientations of the alignment or elongation of vents at Ngongotaha and Ruawahia can be attributed to the overall regional structure of the Taupo Volcanic Zone (TVZ). At Ngongotaha, the N – S trending elongated vent is suggested to be controlled by a N – S trending caldera collapse structure at Rotorua caldera. The rest of the lobes at Ngongotaha, as well as other domes at Rotorua caldera, are controlled by the NE – SW trending extensional regional structure or a NW – SE trending basement structure. The collapse of Rotorua caldera, and geometry of the deformation margin, are related to the interplay of these structures. At Ruawahia, the NE – SW trending vent zone is parallel to the regional extension across the OCC, as shown by the orientation of intrusion of the 1886AD dyke through the Tarawera dome complex.

The NE – SW trending regional structures observed at both Rotorua caldera and Okataina caldera complex are very similar to each other, but differ from extension within the Taupo rift to the south. Lava domes, such as Ngongotaha, that are controlled by this structure show that the 'kink' in the extension across Okataina caldera complex was active across Rotorua caldera during the collapse at 240 ka, and possibly earlier.

This study shows the evolution of dyke-fed lava domes during eruption, and the control of regional structures in the location and timing of eruption. These findings improve our knowledge

of the evolution of porosity and permeability in a compacting lava dome, as well as of the structures of Rotorua caldera, the longevity of volcanic activity at dormant calderas and the hazard potential of dyke-fed lava domes.

Acknowledgements

This thesis is the culmination of over 4 years of research, funded by EQC, GNS Science, Mighty River Power, the Department of Geological Sciences at the University of Canterbury, the Mason Trust Fund and the Marsden Fund, all of whom are gratefully thanked for their funding.

The greatest support I received during this time was from my supervisors, Dr. Ben Kennedy and Prof. Jim Cole. The guidance and feedback I received when honing my skills and ideas were crucial in producing this thesis. I am truly grateful that they trusted a fresh-faced, unknown Honours student from the UK with formulating his ideas and theories into this PhD thesis. Both were also central in gaining funding for the majority of the project, without which I would not have been able to continue my studies.

I would like to thank Ken Raureti and the Ruawahia 2B Trust for allowing access to Tarawera, and especially to Ken for his interest and passion for the mountain.

The staff of the Department of Geological Sciences are also thanked, in particular Dr. Travis Horton, Prof. Jarg Pettinga, Dr. Catherine Read, Dr. Darren Gravely, Dave Bell and Dr. Chris Oze for their interest in my project, and for passing on vital research and teaching skills. Thanks also to; Rob Spiers, Sacha Baldwin-Cunningham (thanks for the 'temporary' rock storage!), Cathy Higgins, John Southward, Kerry Swanson, Janet Brehaut, Janet Warburton and Chris Grimshaw. Extra special thanks go to Pat Roberts for solving any and all administrative and financial problems that arose during my research here.

Thanks also to the 'Munich Crew' of Prof. Yan Lavallee, Jackie Kendrick and Fabian Wadsworth for their (ongoing) patience and support with the extremely tricky subject of viscosity and rheology.

My fellow students here at UC made every difficult stage bearable, and I would thank them all. The 'Old Guard' of (now Dr.'s) Rose Turnbull, Tom Wilson, Sam Hampton, Kate Pedley and Chad Deering took me under their collective wing and showed me the ropes, whilst simultaneously terrifying me with their knowledge. My thesis Brothers and Sisters in arms; Sam McColl and Nick Thompson (both office mates), Greg de Pascale (newer office mate), Johnny Wardman and Carolyn Boulton (party fiends), Josh Blackstock (music maestro), Tom Brookman (outdoor enthusiast), James Cowlyn (trusted manservant Bigglesworth) and especially Felix von Aulock and Jackie Dohaney (fellow volcano lovers) made my time here glorious. I am extra thankful for the support from J.D. in these last few weeks. The 'New Kids'; Paul Siratovitch, Johnathon Davidson, Florence Begue, Tim Stahl, Sharon Hornblow, Nick Riordan, Tim Stahl, Hamish Cattel, Sarah Bastin, Louise Vick, Emma Rhodes, and Heather Bickerton – thanks for all the beers. Also, special mentions to Dave and Caitlin Manthei, Goetz and Ike von Aulock, Abby Young, Naomi Thompson, Tamsin Laird, Gregor Lucic, Narges Khajavi, Janelle Irvine, Melissa Rotella and Simon Barker, Eva Hartung, Signe Wiingaard and 'M.C.' Hebert.

I would also like to thank my far off family – my Mum and Dad, Helen and James, Papa and all the rest, for their constant and genuine support and encouragement, and for allowing me to leave them for years at a time to chase volcanoes around the world. Sorry for making you worry, Mum! Also, thanks to my 'adopted' family of Dave, Wendy, George, Kelly and Mac.

And finally, without whom I would have given up years ago, I would like to extend my deepest thanks to my wonderful girlfriend Laura, for compassion and understanding, proof reading and generally keeping me sane and happy.

Contents

Abstract	IV
Acknowledgements	VII
List of figures	XIII
List of tables	XV
List of publications	XVI
1: Introduction	1
1.1 Objectives.....	3
1.2 Geological setting.....	3
1.2.1 History of lava dome eruptions in the TVZ	7
1.2.2 Lava domes and eruptive history at Rotorua caldera.....	9
1.2.3 Lava domes and eruptive history at Okataina caldera complex.....	11
1.4 Growth, coalescence and shrinkage of bubbles in conduits and lava domes.....	15
1.5 Lava dome eruption styles	21
1.5.1 Morphology and types of lava domes and flows.....	21
1.5.2 Facies architecture at lava domes	27
1.5.3 Internal structures of lava domes.....	31
1.6 Structure of the Taupo Volcanic Zone.....	33
1.6.1 Regional structure of the TVZ	33
1.6.2 Links between tectonics and volcanism in the TVZ	34
1.7 Questions to be addressed in this thesis	37
2: Methodology	38
2.1 Uniaxial compression experiments.....	39
2.2 3D Computed tomography and image analysis	40
2.3 Connected porosity	42

2.4 Permeability.....	44
2.5 Geochemistry.....	49
2.6 Field mapping techniques.....	49
Preamble	51
3: Porous network and viscosity evolution in a compacting pumiceous lava	
Dome	52
3.1 Introduction.....	54
3.2 Lava dome architecture.....	57
3.3 Samples and methods.....	58
3.4 Results.....	61
3.4.1 Compaction mechanics.....	61
3.4.2 Evolution of the porous network.....	65
3.4.3 Cracking of samples.....	68
3.4.4 Viscous deformation in samples.....	71
3.4.5 Permeability evolution.....	71
3.5 Interpretation.....	72
3.6 Rheological Analysis.....	74
3.7 Discussion.....	77
3.7.1 Rheology of porous and crystal bearing magma.....	77
3.7.2 Permeability evolution of porous magma.....	79
3.8 Implications for volcanic systems.....	82
3.9 Conclusions.....	87
Preamble	89
4: Dyke fed dome eruptions: comparing and contrasting two dyke-fed rhyolitic domes in the Taupo Volcanic Zone	90
4.1 Introduction.....	93

4.2 Geological setting.....	95
4.3 Results	99
4.3.1 Ngongotaha Dome	99
4.3.2 Ruawahia Dome	107
4.4 Discussion.....	115
4.4.1 Facies interpretation and eruption sequence at Ngongotaha.....	115
4.4.2 Facies interpretation and eruption sequence at Ruawahia.....	122
4.4.3 Comparison of extrusion style at Ngongotaha and Ruawahia, and other domes worldwide.....	127
4.4.4 Block and ash flow production at Ngongotaha and Ruawahia.....	130
4.5 Conclusions	132
Preamble	134
5: Insights into caldera and regional structures and magma body distribution from lava domes at Rotorua Caldera, New Zealand	135
5.1 Introduction	137
5.1.1 Regional setting	142
5.2 Method.....	146
5.3 Results	146
5.3.1 Spatial distribution, age and morphology of lava dome at Rotorua Caldera	146
5.3.2 Geochemistry	151
5.3.3 Internal structures of Ngongotaha Dome.....	156
5.4 Discussion.....	161
5.4.1 Geochemical and petrological links	161
5.4.2 Structural controls in Rotorua Caldera and the TVZ.....	164
5.4.3 Timeline of dome eruption at Rotorua Caldera.....	170
5.5 Conclusions	172

6: Conclusions	173
6.1 Hazards associated with new lava dome growth models	175
6.2 Statements to the findings of this study.....	177
6.2 Future research.....	179
7: References	180
8: Appendices	217
Appendix A: Geochemical data table	217
Appendix B: Digital video files of tomography	229
Appendix C: Copy of Chapter 5 as journal article	230

List of figures

1.1 Geological setting of New Zealand.....	5
1.2 Simplified map of the Taupo Volcanic Zone (TVZ)	6
1.3 Locations of lava domes in the TVZ.....	8
1.4 Shaded D.E.M. of Rotorua caldera	9
1.5 Shaded D.E.M. of Okataina caldera complex.....	13
1.6 Diagram summarising bubble growth and collapse mechanism	19
1.7 Examples of flow lobes.....	25
1.8 Images of dome structures	26
1.9 Examples of spiny lobes	27
1.10 Diagram of hypothetical lava dome	30
1.11 Structural trends across the TVZ.....	36
2.1 Diagram of uniaxial press at LMU, Munich	40
2.2 Graph of porosity loss against axial strain	44
2.3 Diagram of gas permeameter at University of Canterbury and sample	47
2.4 Typical graph of the relationship between modified gas pressure gradient and gas volume flux	48
3.1 Diagram of cores at each axial strain increment.....	60
3.2 Strain rate and AE emission during 50% axial strain deformation.....	63
3.3 Graphs of changes in porosity and barrelling	66
3.4 Porosity and permeability evolution with time	67
3.5 Selected tomography images.....	69
3.6 Bubble shape and size changes in NP	70
3.7 Apparent and relative viscosity measurements.....	76
3.8 Relationship between open porosity and permeability for compression and vesiculation experiments	81
3.9 Model of compression in crystalline and non-crystalline lava domes	85
4.1 Hypothesised flow band orientations	94

4.2 Map of Rotorua caldera and Okataina caldera complex	98
4.3 Images of internal structures of interior facies at Ngongotaha dome	101
4.4 Map of flow bands and facies at Henderson’s Quarry	102
4.5 Breccia zone and spherulitic obsidian sheets of interior sheet facies at Ngongotaha dome	104
4.6 Thin section and photos of pumiceous carapace at Ngongotaha dome	106
4.7 Interior facies of Ruawahia	109
4.8 Photos of breadcrust surface, ‘ropey’ texture, ramp structures and flow banding at Ruawahia dome	110
4.9 Map of flow bands and facies at Ruawahia dome.....	112
4.10 Overview of breccia zone facies within interior facies at Ruawahia dome.....	113
4.11 Eruption model of lobe at Ngongotaha.....	118
4.12 Eruption timeline of Ngongotaha dome.....	121
4.13 Eruption model of Ruawahia dome cross section	125
4.14 Eruption timeline of lobes at Ruawahia dome	126
5.1 Map of the Taupo Volcanic Zone showing calderas and structures.....	139
5.2 Diagram of flow bands of 3 types of conduits.....	141
5.3 Simplified geological map of the Rotorua caldera.....	145
5.4 Regional, caldera collapse and basement related structures at Rotorua Caldera	148
5.5 Whole rock TAS diagram of Rotorua caldera domes.....	152
5.6 Selected geochemical diagrams of Rotorua caldera domes.....	153
5.7 Flow band orientation at Henderson’s Quarry, Ngongotaha	157
5.8 Flow band and fracture rose diagrams and stereonet of Ngongotaha, compared to orientations of structures in other areas of the TVZ	159
5.9 Schematic representations of the evolution of Rotorua caldera (451 - 0 ka)	163
5.10 Oblique shaded D.E.M. of the central TVZ	168

List of Tables

1.1 Questions to be addressed in this thesis	38
3.1 Summary of uniaxial compression experiments	64
5.1 Whole rock XRF analysis of samples from pre- and post- caldera collapse, Rotorua caldera.....	154
5.2 Summary of grouping of lava domes of Rotorua caldera	155
6.1 Statements as to the findings of this study.....	177

List of Publications

Below is a list of peer reviewed, published papers and papers in preparation that have come directly from this research. Where appropriate, a chapter link is included; however, some are not directly relevant to this body of work, and have therefore been omitted as part of this thesis.

In first author publications (Chapter 3, 4 and 5), I performed the fieldwork or experiments and analysis as well as writing the article. In papers in which I am a co-author, I contributed to fieldwork, data collection and editing of the article.

Chapter 5:

P.A. Ashwell, B.K. Kennedy, D.M. Gravley, F.W. von Aulock and J.W. Cole. 2013. Insights into caldera and regional structures and magma body distribution from lava domes at Rotorua Caldera, New Zealand. *Journal of Volcanology and Geothermal Research*. 258, pp 187-202.

Chapter 3:

P.A. Ashwell, J.E. Kendrick, Y. Lavallée, B.M. Kennedy, K-U. Hess, F.W. von Aulock, J.W. Cole and D.B. Dingwell. In prep. Porosity and permeability evolution in a compacting lava dome. Target journal: *Journal of the Geological Society, London*.

Chapter 4:

P.A. Ashwell, B.M. Kennedy and J.W. Cole. In prep. Dyke fed dome eruptions: comparing and contrasting two dyke-fed rhyolitic dome building eruptions in the Taupo Volcanic Zone. Target journal: *Bulletin of Volcanology*.

The following publications have also benefitted from this research, but they are not included within this thesis:

F.W. von Aulock, B.M. Kennedy, C. Oze and **P.A. Ashwell**. In review. Water diffusion during bubble growth in magma. *Earth and Planetary Science Letters*.

Y. Lavallée, M. Heap, T.M. Mitchell, B.M. Kennedy, **P.A. Ashwell**, T. Hirose and D.B. Dingwell. In prep. Lava dome or spine? It's a matter of comminution. Target journal: *Geology*.

Conference presentations:

Playing Vulcan: Re-creating the subterranean conditions that spawn rocks. **P.A. Ashwell**, B. M. Kennedy, F. W. von Aulock, K. Buchanan, D. Drabble & J. Cole. *GeoNZ 2009, Oamaru*.

Volcano in the basement; a new experimental rig for the development of volcanic textures. **P.A. Ashwell**, B.M. Kennedy, K. Buchanan, D. Drabble and F. W. von Aulock. *AGU 2009*.

Eruption style and emplacement processes of Ngongotaha Dome, Rotorua. **P. A. Ashwell**, B. M. Kennedy, F. W. von Aulock & J. W. Cole. *GSNZ 2010, Auckland*.

Linking the internal structures of lava domes to eruption style: An example from Ngongotaha Dome, Taupo Volcanic Zone, New Zealand. **P. A. Ashwell**, B. M. Kennedy, F. W. von Aulock & J. W. Cole. *IUGG 2011, Melbourne*.

Experimental Results on the Compaction of Pumiceous Lava Domes. **P.A. Ashwell**, J.E. Kendrick, Y. Lavallee, B.M. Kennedy, K.U. Hess, F.W. von Aulock, J.W. Cole & D.B. Dingwell. *GSNZ 2011, Nelson*.

Distribution of water related to flow banding and microlites in obsidian. F.W. von Aulock, C. Oze, B.M. Kennedy, T. Cox, F. Begue and **P.A. Ashwell**. *GSNZ 2011, Nelson*.

Permeability development during compaction of pumiceous dome lavas: testing the permeable foam collapse model. **P.A. Ashwell**, J.E. Kendrick, Y. Lavalée, B.M. Kennedy, K.U. Hess, F.W. Von Aulock, J. Cole and D.B. Dingwell. *AGU 2011*.

Experimental Compaction of Pumiceous Dome Lavas. J. Kendrick, **P.A. Ashwell**, Y. Lavalée, B.M. Kennedy, K.U. Hess, J. Cole, and D.B. Dingwell. *EGU 2012*.

Microfracture development and foam collapse during lava dome growth. **P.A. Ashwell**, J.E. Kendrick, Y. Lavalée, B. Kennedy, K.U. Hess, J.W. Cole and D.B. Dingwell. *AGU 2012*.

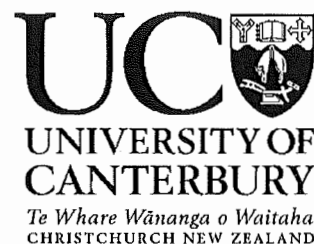
Investigating the inflation of lava domes following block and ash flows. **P.A. Ashwell**, M.E. Edwards, B.M. Kennedy and F.W. von Aulock. *IAVCEI 2013, Kagoshima*.

Linking lava domes to their structural setting. **P.A. Ashwell**, B.M. Kennedy, D.M. Gravley and J.W. Cole. *IAVCEI 2013, Kagoshima*.

The formation and hydration of cracks in cooling volcanic glass. F.W. von Aulock, B.M. Kennedy, C. Oze, Y. Lavalée, A.R. Nichols, K.-U. Hess and **P.A. Ashwell**. *IAVCEI 2013, Kagoshima*.

Isobaric bubble growth and collapse in magma. F.W. von Aulock, B.M. Kennedy, C. Oze and **P.A. Ashwell**. *IAVCEI 2013, Kagoshima*.

Deputy Vice-Chancellor's Office
Postgraduate Office



Co-Authorship Form

This form is to accompany the submission of any PhD thesis that contains research reported in co-authored work that has been published, accepted for publication, or submitted for publication. A copy of this form should be included for each co-authored work that is included in the PhD thesis. Completed forms should be included at the front (after the thesis abstract) of each copy of the thesis submitted for examination and library deposit (including electronic copy).

Please indicate the chapter/section/pages of this thesis that are extracted from co-authored work and provide details of the publication or submission from the extract comes: *Chapter 5: Insights into caldera & regional structures and magma body distribution at Rotoma Caldera.*

Please detail the nature and extent (%) of contribution by the PhD candidate:

Paul has undertaken all the fieldwork, interpretation and structural analysis. The supervisors role has been for discussion and help with editing of the final manuscript, hence have been included as co-authors

Certification by Co-authors:

If there is more than one co-author then a single co-author can sign on behalf of all

The undersigned certifies that:

- The above statement correctly reflects the nature and extent of the PhD candidate's contribution to this co-authored work
- In cases where the PhD candidate was the lead author of the co-authored work he or she wrote the text

Name:

Signature:

Date:

J.W. Cole

A large, stylized handwritten signature in black ink, appearing to be 'J.W. Cole'.

22.10.2013.

Chapter 1

Introduction

Lava domes are extrusions of viscous andesitic to rhyolitic lava. They can be formed in a range of settings, from inside the crater of a stratovolcano (such as Mt. St. Helens and Taranaki volcanoes; Vallance et al. 2008; Platz et al. 2012), as extrusions following caldera collapse (such as at Long Valley caldera, USA; Bailey et al. 1976), or as extrusions with no relation to calderas or stratovolcanoes (such as at Rotorua caldera; this study). The eruption of a lava dome is usually a slow (weeks to months), incremental process of endogenous or exogenous growth that may be accompanied by rockfall and larger dome failure episodes which form a skirt of talus material and block and ash flow deposits (Hale 2008). While eruptions of small andesitic to dacitic lava domes have been well documented (such as those at Mt. St. Helens or Soufrière Hills volcanoes; Watts et al. 2002b; Scott et al. 2008), there have been only 4 recognised rhyolitic lava dome or flow eruptions in the last 100 years (Novarupta in 1912, Tulumán in 1953-57, Chaitén in 2008 – 2010 and Puyehue-Cordón Caulle in 2011; Reynolds et al. 1980; Adams et al. 2006; Pallister et al. 2010; Tuffen et al. 2013). The paucity of rhyolitic lava dome eruptions within historical records means that little is known of their styles of extrusion and growth. The exposed internal structure of old, eroded lava domes can be used as a proxy for modern dome eruptions, and experimental volcanology has advanced sufficiently that laboratory experiments can recreate the temperatures and pressure of rhyolitic lava domes allowing conceptual models to predict how rhyolitic lava domes may erupt and evolve, and how hazardous they may become..

Here I will summarise the field, experimental and location specific volcanological literature pertinent to: (1) The role of rhyolitic lava domes in the history of the Taupo Volcanic Zone, (2)

bubble growth, coalescence, shrinkage and cracking, (3) lava dome morphology and facies architecture and (4) the links between tectonics and lava domes in the Taupo Volcanic Zone.

These sections in the introduction complement chapters 3, 4 and 5.

1.1 Objectives

This thesis aims to use fieldwork and laboratory experiments to investigate the internal structure of Ruawahia lava dome, Okataina caldera complex (OCC), and Ngongotaha lava dome, Rotorua caldera, to constrain the controls on the eruption styles of rhyolitic lava domes. This will be achieved by the following objectives:

- To parameterise the process of porous lava compaction in crystal rich and crystal poor lavas by performing high temperature, uniaxial compression experiments on samples of varying porosity to quantify the evolution of porosity and permeability (Chapter 3).
- To compare and contrast the internal structures, facies variations and eruption styles of Ruawahia and Ngongotaha lava domes (Chapter 4).
- To use the internal structure and regional structure at Ngongotaha to assess the control of tectonics on eruption morphology and style at Ngongotaha (Chapter 5).
- To use geochemistry and age relationships of lava domes of Rotorua caldera to assess the links between tectonics, caldera collapse and lava domes (Chapter 5).
- To re-evaluate the association of block and ash flow hazards with rhyolitic lava domes with reference to new data and models for dome growth (Chapter 6).

The two field areas of this project are Ngongotaha dome, Rotorua caldera, and Ruawahia dome of Tarawera dome complex, OCC, Taupo Volcanic Zone (TVZ), New Zealand.

1.2 Geological Setting

The geological setting of the TVZ is important to understand the structural controls and controls on magmatism at Ngongotaha lava dome, in Rotorua caldera, and Ruawahia lava dome, in the OCC. The TVZ is part of the Taupo – Hikurangi subduction system and has been active for at least 2.0 Ma, and possibly much earlier (Cole & Spinks, 2009; Wilson et al. 2009). The TVZ is a southerly extension of the Tonga – Kermadec system, and was created by the oblique

subduction of the Pacific plate under the Australian plate (Figure 1.1), (Cole & Lewis 1981). To the east of the TVZ is a wide (~150 km) accretionary prism and a frontal ridge, consisting of Mesozoic basement rocks of sandstones and greywackes. The latter consists of the Torlesse and Waipapa Supergroups, which are considered to be the basement rocks of much of the North Island (Mortimer 2004), and have contributed to the caldera collapse styles at Rotorua caldera and the OCC (Milner et al. 2002; Seebeck et al. 2010). Thinning of the crust has allowed mafic magma underplating at a depth of between 16 to 20 km (Harrison & White 2004; Reyners et al. 2006), which is considered to be the source of the basaltic eruptions of the TVZ, and the trigger for some of the rhyolitic eruptions (Leonard et al. 2002; Nairn et al. 2005; Shane et al. 2007).

Volcanism in the currently active TVZ can be separated into three distinct segments – northern and southern andesite-dominated segments, separated by a dominantly rhyolitic segment (Figure 1.2). Crystal fractionation and minor assimilation of basement rock leads to the eruption of andesitic magmas in the southern and northern parts (controlled by lower H₂O content of under-plated basalt) and rhyolitic to dacitic volcanism in the central TVZ (where the basalt has higher H₂O contents of around 2 wt%; Deering et al. 2011). Crystal fractionation in individual magma chambers also leads to higher silica, post-Plinian lava domes at Tarawera (Leonard et al. 2002) and Rotorua (Chapter 5); a decrease in the extent of crystal fractionation may decrease silica during a prolonged dome eruption (Scott et al. 2013). There is little temporal or spatial correlation of crystal content between calderas, ignimbrites and lava domes, although ignimbrites erupted between a particularly active period in the TVZ between 340 – 320 ka are crystal rich (Wilson et al. 2009). Dome extrusions immediately following large caldera eruptions may be petrologically similar to the ignimbrites (Milner et al. 2002); large time gaps between dome extrusions and large explosive eruptions produce chemically and petrologically distinct lava domes (Chapter 5; Brown 1994; Milner et al. 2003) that indicate changes in the magmatic system (Chapter 5). New injections of magma into a system may destabilise the chamber,

leading to eruption (Leonard et al. 2002; Shane et al. 2008; Matthews et al. 2012) or changes in the petrology or geochemistry of lava domes (Chapter 5).

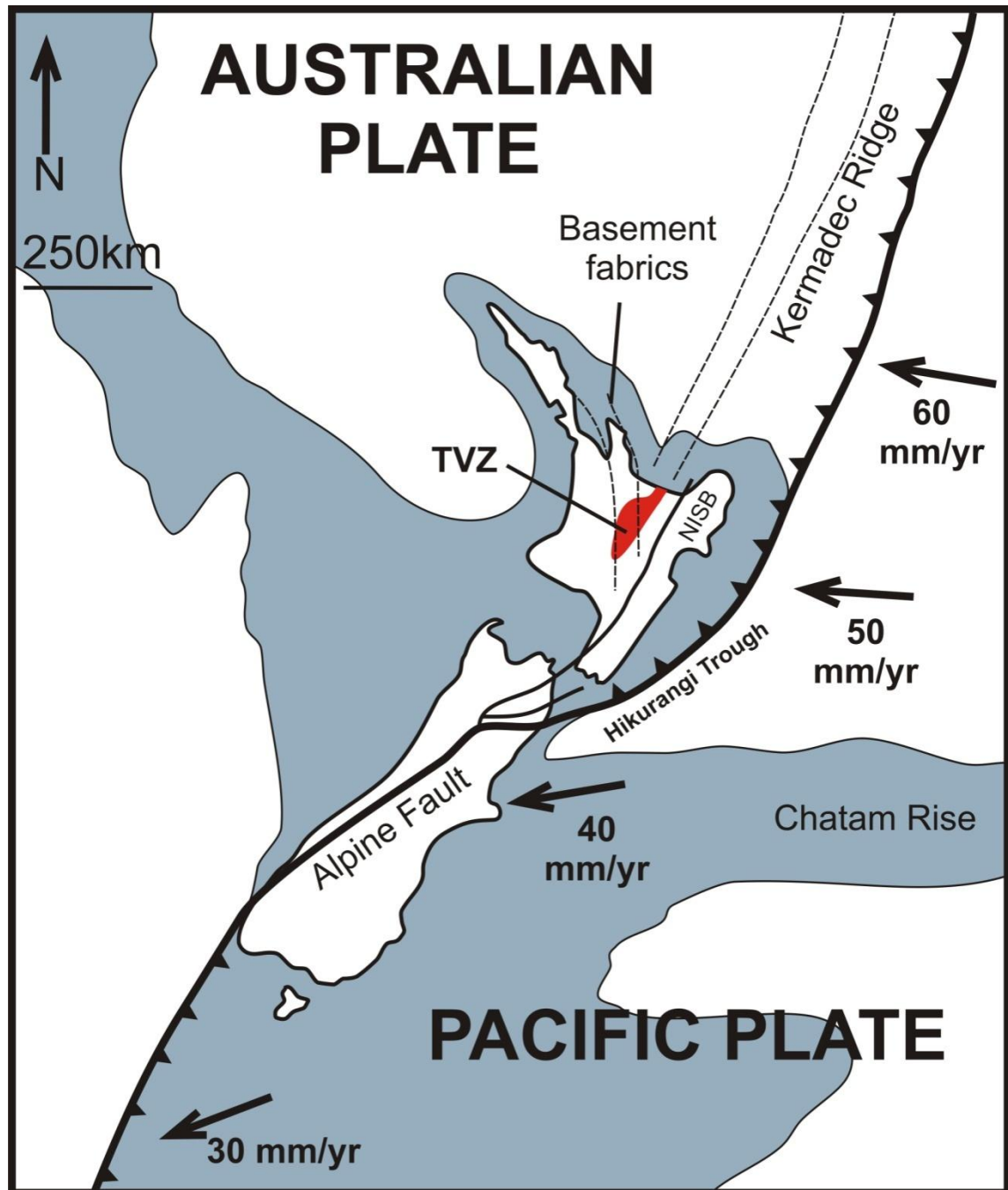


Figure 1.1: Geological setting of New Zealand on the boundary of the Australian and Pacific plates. TVZ is marked as the red area, while the blue area shows the continental shelf around New Zealand. NISB = North Island Shear Belt. Rates from Walcott (1987).

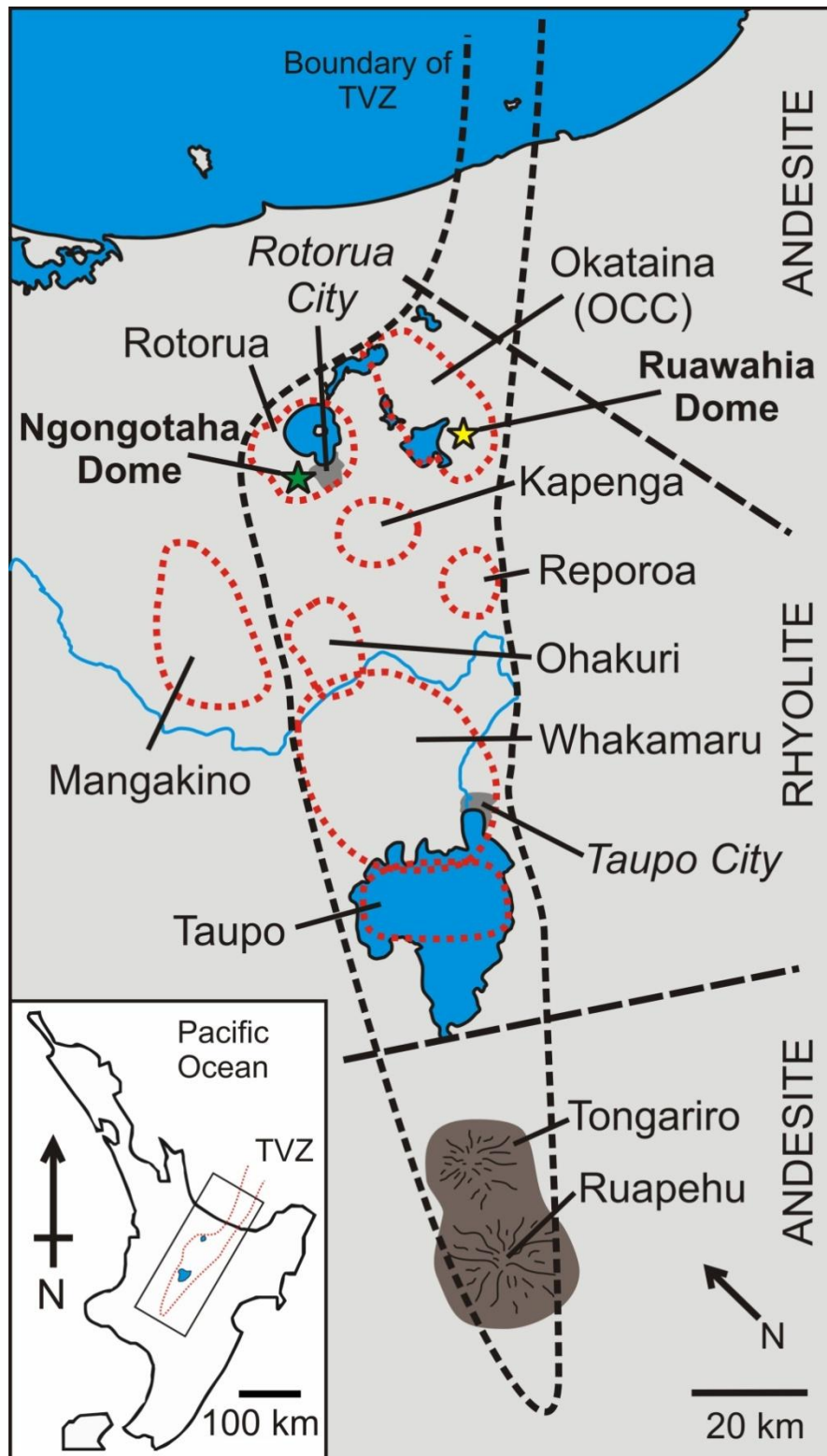


Figure 1.2: Simplified map of the Taupo Volcanic Zone (TVZ), with locations of active calderas, field areas (stars) and populated areas, as well as the transition from andesite dominant areas to rhyolite dominant. Insert: Map of the North Island of New Zealand to show location of TVZ, box dictates the area covered by the larger map.

1.2.1 History of lava dome eruptions in the TVZ

Throughout the geological history of the TVZ rhyolitic lava domes have erupted, and are one of the most common landforms (Figure 1.3). Evidence of older domes is sparse; geothermal drill cores are often the only source of information on buried lava domes (Cole et al. 2010). The oldest known lava dome eruption was at the now inactive Mangakino caldera, to the west of the active TVZ (Figure 1.2; Houghton et al. 1995), and has been dated at 1270 +/- 0.05 ka (Briggs et al. 1993). Domes of the Whakaahu dome belt, on the margin of Whakamaru caldera (close to the Western dome complex; Figure 1.3), extruded at ~1050 ka (Brown 1994), but the exposure of similarly aged domes in the TVZ is poor. Geothermal boreholes at OCC have been able to stratigraphically correlate lava domes with the ~550 ka Opunoke Ignimbrite, which may have represented the first eruptive episode from OCC (Cole et al. 2010; see also section 1.2.3).

In the period between 340 ka and 240 ka, 8 caldera eruptions (Wilson et al. 2009) produced over 3000 km³ of magma (Gravley et al. 2009), and is considered to be an 'ignimbrite flair up' which has produced nearly half of the total amount of erupted material in the TVZ (Gravley et al. 2009). Many of these ignimbrites, such as the ~340 ka Whakamaru (Brown et al. 1998; Wilson et al. 2009; Matthews et al. 2012), the ~240 ka Mamaku (Milner et al. 2003; see also section 1.2.2) and the ~230 ka Kaingaroa (Nairn et al. 1994; Wilson et al. 2009) were followed shortly after by lava dome extrusions (Brown 1994; Beresford & Cole 2000; Milner 2001). For example, the Whakamaru caldera now contains many lava dome extrusions and associated block and ash flows (Figure 1.2 and 1.3) which erupted irregularly between 305 to 80 ka (Leonard 2003). Ages of domes in the Western dome complex cluster around 287 – 313 ka (Houghton et al. 1991), but range over 100,000 years either side of these ages (Brown et al. 1998; Houghton et al. 1991). The two major dome complexes in the Maroa volcanic centre, the Maroa East and Maroa West complexes both erupted over a short time span between ~251 to 222 ka (Leonard 2003) Lava dome eruptions continued in the area encompassing the Whakamaru and Taupo calderas up to

~80 ka (Leonard 2003), including the ~100 ka Ben Lomond lava dome (Figure 1.3; Stevenson et al. 1994). Isolated dome eruptions in the Maroa volcanic centre have also been dated as young as 14 and 62 ka (Wilson et al. 2009).

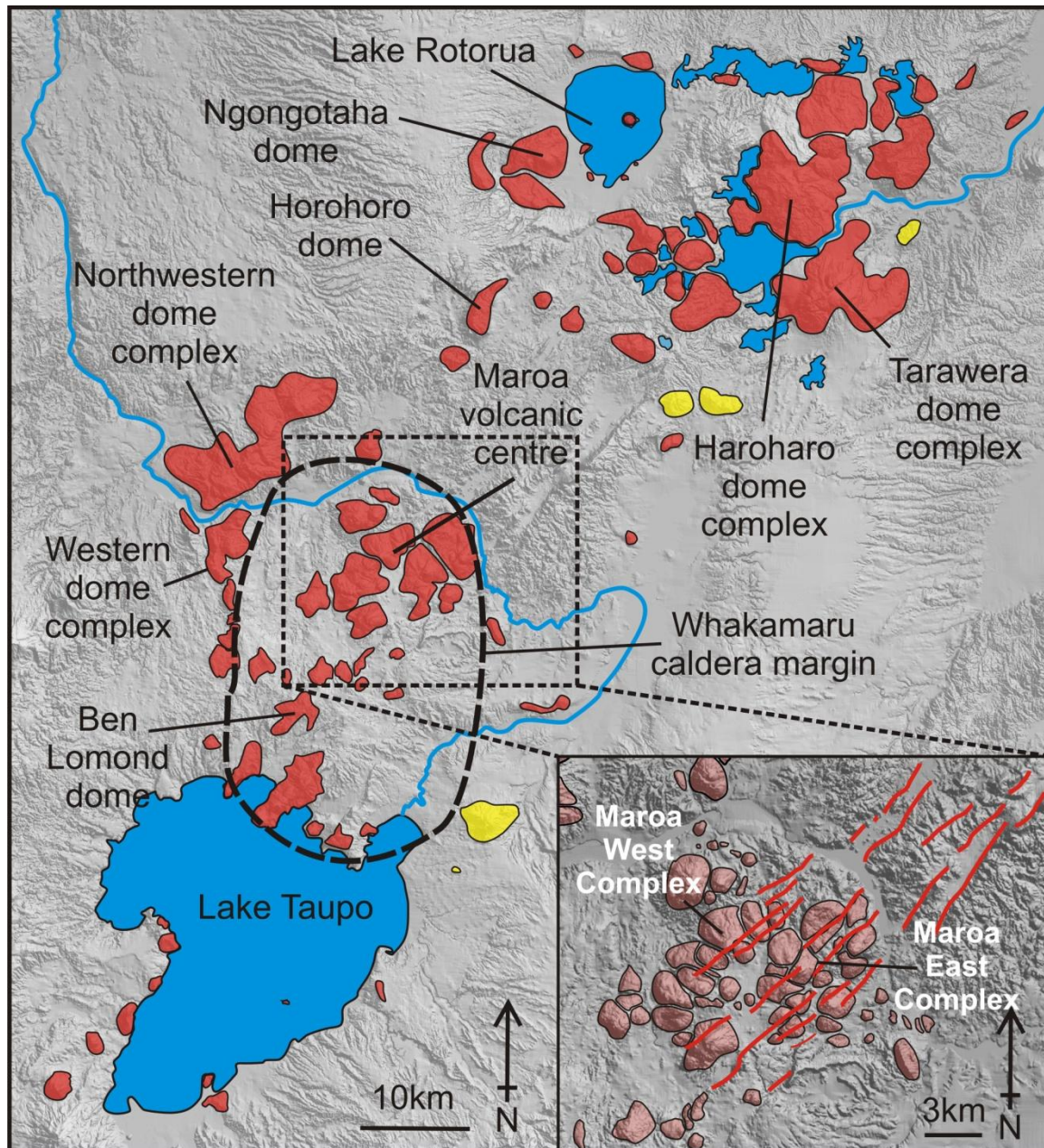


Figure 1.3: Locations of large rhyolitic (red) and dacitic (yellow) lava domes in the TVZ, with particular domes mentioned in text marked on map. Inset: Detail of Maroa volcanic centre with relationship of lava domes (pink) to regional structures (red lines). Locations from Nairn (2002) and Leonard et al. (2010).

A nearly complete record of eruptions from c. 50 ka to present has been preserved due to fewer of large scale, smothering caldera eruptions (Danišik et al. 2012). In this time period, a total of 16 large, lava-extruding eruptions have occurred from the Maroa area, Taupo and Rotorua calderas and OCC which have a total volume of 51 km³ (Wilson et al. 2009) and include the Tarawera and Haroharo dome complexes (see section 1.2.3).

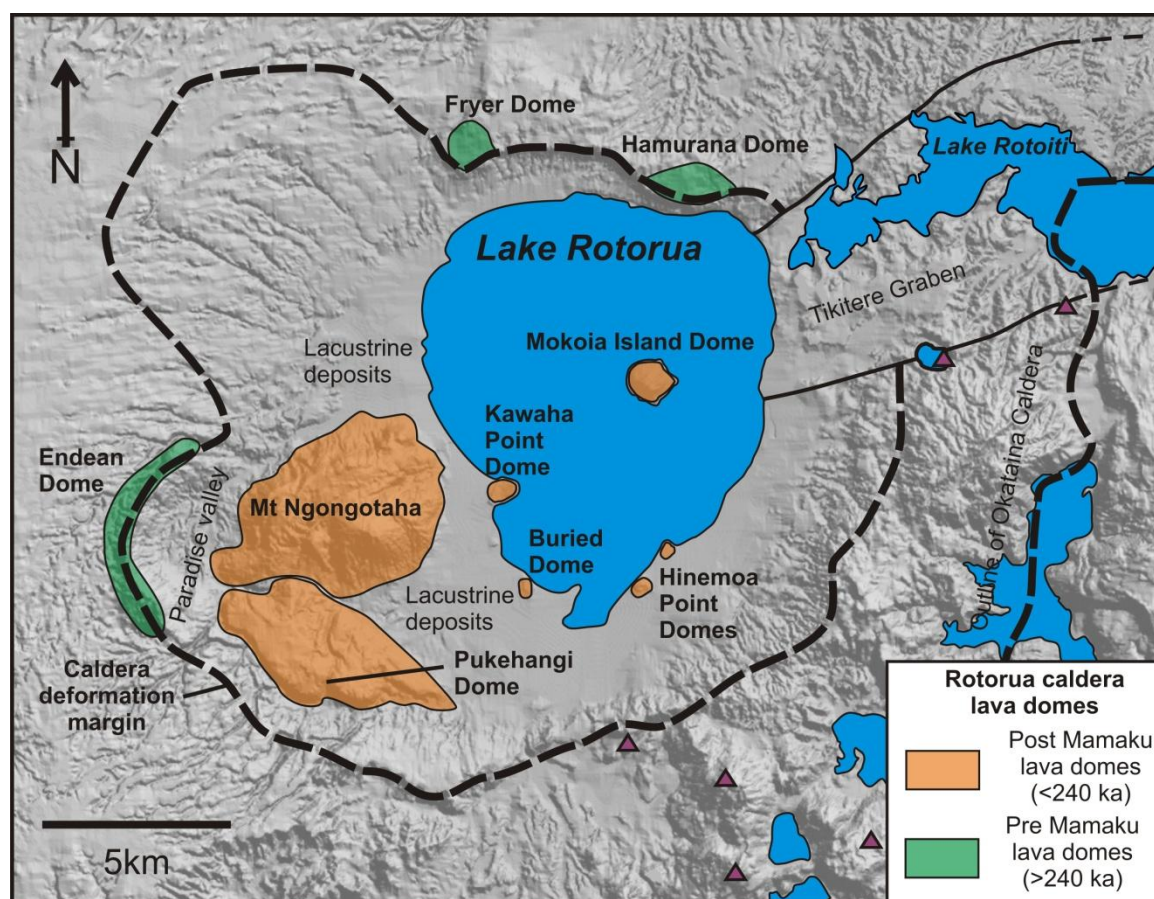


Figure 1.4: Shaded D.E.M. of Rotorua caldera, showing pre-Mamaku lavas in green and post-collapse lavas in orange. Non-Rotorua caldera vents are marked by purple triangles. Dome locations from Milner (2001).

1.2.2 Lava domes and eruptive history at Rotorua caldera

The eruptive history of Rotorua caldera is punctuated by eruptions of rhyolitic lava domes. Rotorua caldera is located to the north-central TVZ (Figure 1.2), offset from the currently active

rifting axis (see section 1.6). The volcanic history of Rotorua caldera is poorly preserved, but it is believed to have been dominated by a single large ignimbrite-forming eruption and collapse event during the 240 +/- 11 ka Mamaku eruption (Milner et al. 2003; Gravley et al. 2007). The deformation margin (outer edge of deformation due to caldera collapse) of the caldera cuts through ~451 ka pre-Mamaku lava domes (Figure 1.4; Milner 2001; Deering et al. 2010); however the relationship of these domes to the caldera is unclear. These domes are discussed further in Chapter 5.

The >96 km³ (DRE) Mamaku eruption began with a phreatomagmatic eruption, with fine grained airfall and accretionary lapilli deposits found at the base of the ignimbrite sequence (Milner et al. 2003). The ignimbrite ranges from dacitic (66 – 69.7 wt% SiO₂) to rhyolitic (70.2 – 76 wt% SiO₂) with blebs of andesitic material (58.4 – 61.8 wt% SiO₂) recorded towards the top of the sequence (Milner et al. 2003). Rare rhyolitic lava lithics within the basal sequence suggests the presence of older lava domes in the vicinity of the Mamaku vents that were destroyed during the eruption (Milner 2001). The basal sequence grades into the main ignimbrite body, in some places up to 280 m thick (Milner et al. 2003), which likely coincides with a drastic increase in energy of the eruption, as well as collapse of the caldera. A near simultaneous eruption of the Ohakuri ignimbrite, from the Ohakuri caldera to the south of Rotorua (Figure 1.2), is shown by the interbedding of both Mamaku and Ohakuri ignimbrite units (Gravley et al. 2007). This dual eruption led to the lateral removal of magma in the area between the Mamaku and Ohakuri vents creating an area of NNE – SSW to NE – SW trending subsidence visible directly south of Rotorua caldera (Gravley et al. 2007) from the Horohoro fault scarp which bisects the Horohoro lava dome (Figure 1.3).

Volcanic activity continued inside Rotorua caldera following the eruption of the Mamaku ignimbrite, with two periods of dome growth following the collapse of Rotorua caldera (Chapter 5). The post-collapse domes show two alignment orientations that correspond to the NE – SW

trending rifting and the NW – SE orientated basement structures which also controlled the asymmetric, piecemeal collapse of the caldera (Milner et al. 2002). The elongated domes of Ngongotaha and Pukehangi (Figure 1.4) have been suggested to have formed from a series of aligned vents along possible fault structures (Cole & Spinks 2009). Chapters 4 and 5 investigate the internal structures of Ngongotaha dome, and the links between regional and caldera structure and lava dome eruptions at Rotorua caldera.

Ngongotaha dome is a prominent hill to the northwest of Rotorua city and consists of 6 lobes which can be distinguished by surface topography (Figure 1.2 & 1.4). The dome is a NE – SW elongated lava dome with prominent lobes elongated N – S to NE – SW, and is bordered to the north and west by Paradise Valley (and beyond that the scarp of Rotorua caldera), to the south by Pukehangi lava dome and to the east by lacustrine plains associated with the Lake Rotorua (Figure 1.4). The summit of the dome is a prominent peak on the southern side, which sits on a small plateau created by other lobe eruptions. The dome erupted following the 240 ka Mamaku eruption, but before the post-240 ka highstand of Lake Rotorua (Marx et al. 2009). Chapter 5 addresses the poor age control of Ngongotaha and other domes at Rotorua caldera.

1.2.3 Lava domes and eruptive history at Okataina caldera complex

The association of caldera volcanism and lava dome eruptions is exemplified by the OCC; a large, active, rhyolitic caldera in the central-northern TVZ, and to the east of Rotorua caldera (Figure 1.2). Known volcanism began at c. 550 ka, with the large (~90 km³) Opunoke ignimbrite (Cole et al. 2010; Nairn 2002). Rhyolitic fragments within the ignimbrite, and other ignimbrites encountered at depth in nearby geothermal boreholes, may indicate earlier explosive and effusive activity was also present at OCC (Cole et al. 2010). Geothermal boring through the Kawerau geothermal region (to the east of the OCC) intersects several rhyolite domes that extruded between the Opunoke ignimbrite and the ~325 ka Matahina ignimbrite (Bailey & Carr 1994; Cole et al. 2010). None of these domes are exposed at the surface.

The oldest exposed lava domes in the OCC are the earliest domes of two intra-caldera dome complexes, the Haroharo and Tarawera dome complexes (Figure 1.5). The Haroharo dome complex consists of 4 main eruptive episodes between ~25 and ~5.5 ka (Leonard et al. 2010), producing overlapping rhyolitic lava domes and lava flows (Figure 1.5; Nairn 2002; Smith et al. 2005; Smith et al. 2006; Cole et al. 2010). The youngest of these episodes, the Whakatane rhyolites, form a NE – SW trending vent zone (Figure 1.5) that is parallel to the regional rifting structure across OCC (Smith et al. 2006).

The Tarawera dome complex, to the south of the Haroharo dome complex, likewise consists of a series of overlying lava domes built up in 5 separate eruptions in the last ~22 ka (Figure 1.5; Leonard et al. 2010). The oldest domes at Tarawera are the 21.8 +/- 0.5 ka Hawea and Ridge lavas on the eastern edge of the dome complex and the 17.6 +/- 0.4 ka Te Puha, Western, Southern and Rotomahana domes of the Rerewhakaaitu eruption, which underlie the youngest domes on the western and south-western flanks (Figure 1.5; Nairn 2002; Shane et al. 2007; Leonard et al. 2010).

Dome eruptions during the 13.6 +/- 0.2 ka Waiohau eruption formed domes on the northern and western areas, extruding onto the older Hawea and Ridge lavas, and onto which the youngest domes have extruded (Figure 1.5; Speed et al. 2002; Leonard et al. 2010). The Waiohau lavas are known to have formed large block and ash flows to the NE and S from dome collapse which contain large, pristine clasts of obsidian (Figure 1.5; Speed et al. 2002).

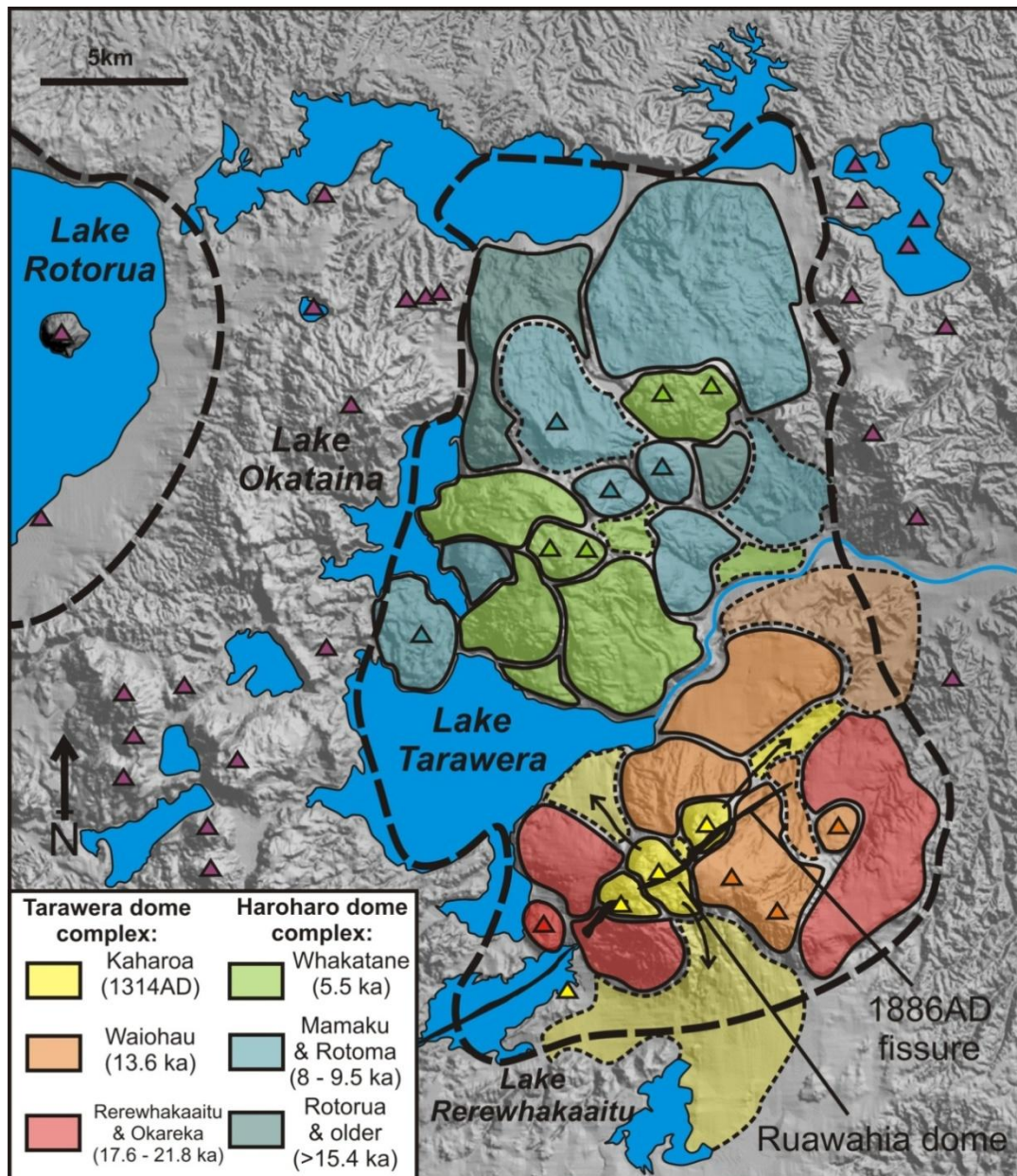


Figure 1.5: Shaded D.E.M. of Okataina caldera complex (OCC). Thick black dashed line indicates the deformation margin of the OCC. Blues/greens indicate the domes and flows Haroharo dome complex, while red/ yellows are Tarawera dome complex, see ages in lower left box. Areas with dashed borders are pyroclastic deposits; arrows from the Kaharoa domes indicate dome collapse directions. The 1886AD rift is shown in black across Tarawera. Triangles indicate vent locations of Haroharo (blue/greens) and Tarawera domes (red/ yellows) and other non-OCC vents (purple) from Nairn (2002), Smith et al. (2006) and Cole et al. (2010), ages of domes from Leonard et al. (2010).

The youngest dome forming eruption of the OCC includes the domes of Wahanga, Tarawera, Crater and Ruawahia, extruded during the later stages of the 1314AD Kaharoa eruption (Chapter 4; Cole 1970a; Cole 1970b; Nairn et al. 2001; Leonard et al. 2002). The Kaharoa eruption also formed a large pyroclastic cone underneath, and to the east of, Ruawahia dome from the initial explosive Plinian phase, as well as large block and ash flow deposits on top of the previously deposited block and ash flows from the Waiohau eruption (Figure 1.5; Nairn et al. 2001; Nairn 2002). The domes extruded towards the end of the eruption (Cole 1970b), and were controlled by the palaeotopography of the underlying lava domes and pyroclastic cone (Chapter 4). As with the Haroharo domes, the Kaharoa domes are aligned NE – SW, reflecting the underlying structural trend across the OCC (Cole 1970b; Nairn et al. 2001; Smith et al. 2006; Rowland & Sibson 2001; see section 1.6). Ruawahia dome, the focus of this thesis, comprises of two large flow lobes in a NW and SE direction. A large pyroclastic apron has been shed from the NW flow lobe, while widespread block and ash flow deposits on the southern margin of the dome complex have been sourced to the SE flow lobe (Figure 1.5; Nairn et al. 2001). Ruawahia is bounded to the west by the contemporaneous Tarawera dome and to the east by the Ruawahia tuff cone, deposited during the initial Plinian eruptive phase.

The last major eruption from the OCC was the 10th June 1886AD Tarawera eruption, a large basaltic Plinian eruption that claimed at least 108 lives (Keam 1988). A basaltic dyke intruded through the dome complex, resulting in a violent eruption due to sealing of the conduit (Kennedy et al. 2010) and interaction with hydrothermal and lake water (Houghton et al. 2004; Sable et al. 2006). This formed a fissure, which has exposed the cores of the Kaharoa domes (Figure 1.5), and destroyed the then world famous Pink and White Terraces. Several Maori villages from the Ngāti Rangitihi iwi on the shores of Lake Tarawera were completely buried by ash, lapilli and mud from the eruption, and still remain buried to this day.

There is strong archaeological evidence to suggest the first human settlers arrived before the 1314AD Kaharoa eruption (Lowe et al. 2000). The Ngāti Rangitahi iwi have the mana whenua (power and authority to use the land to support themselves) of Mt. Tarawera and the catchment of the Tarawera river, and are the kaitiaki (guardians) of the mountain. Oral histories inherited from the early settlers survive to this day. The Ngāti Rangitahi relate that the domes of the Kaharoa eruption were formed when Ngātoroirangi, who arrived on one of the canoes of the Great Migration, was called upon to battle a taniwha (spirit/ guardian), who preyed upon weary travellers on the shores of Lake Tarawera. Ngātoroirangi engaged the taniwha, slowing it with prayers, and was able to overcome come it, and forced the taniwha into the ground on top of Mt. Tarawera. He commanded the mountain to rise up and bury the taniwha, analogous to the eruption of the Kaharoa domes. 'Ruawahia' can be translated into 'pit' (rua-) and 'tearing' (-wahia), and suggests that the pre-1886AD eruption shape of the dome was one with a cleft or rift in the centre. Maori oral traditions also suggest that the 1886AD eruption was a result of the taniwha escaping the mountain to punish those who had abandoned their duties as kaitiaki of the mountain.

The 1886AD fissure, as well as the domes in the Haroharo and Tarawera dome complexes share a NE – SW trend; an orientation which is shared in numerous faults across and to the south-west of the OCC (Rowland & Sibson 2001; Acocella et al. 2003; Seebeck et al. 2010; see section 1.6). Regional and basement structures at Rotorua caldera and the OCC are an important control on the location and morphology of lava domes. This link is investigated further in Chapters 4 and 5.

1.4 Growth, coalescence and shrinkage of bubbles in conduits and lava domes

The growth, coalescence and shrinkage of a bubble network are the primary controlling factors in the ability of a magma to produce explosive or effusive eruptions, and are themselves controlled by the volatile content of the magma. The porosity of lava domes can vary from highly porous pumice (80 % porosity) to dense obsidian (<10 % porosity; Jaupart & Allegre 1991; Klug &

Cashman 1996; Castro & Cashman 1999; Smith et al. 2001; Mueller et al. 2005; Wright et al. 2009; Mueller et al. 2011). The generally low mean porosity (<40 %) of bubble networks (Mueller et al. 2005) frozen into lava domes has been explained from two perspectives; (1) Limited bubble growth from a magma with a low volatile content (Heiken 1978; Eichelberger & Westrich 1981; Fink 1983) and (2) Bubble coalescence and shrinkage/ collapse from an initially bubbly magma following outgassing (Taylor et al. 1983; Eichelberger et al. 1986; Westrich et al. 1988; Swanson et al. 1989; Westrich & Eichelberger 1994).

Until the 1980s it was assumed that the low porosity of lava domes was the result of reduced bubble growth from magmas that contained limited amounts of dissolved volatiles (Taylor 1958; Heiken 1978; Eichelberger & Westrich 1981; Fink 1983). These ideas were driven by the idea that magma chambers were stratified or zoned in volatile content (Eichelberger & Westrich 1981). However, following the coring of the Inyo domes in the 1980s by Eichelberger et al. (1984; 1985) and Goff (1986), a new hypothesis was introduced which stated that lava domes formed as a highly porous, bubbly, 'foam'; bubbles then coalesced, shrunk and were resorbed during ascent and extrusion to produce obsidian (Eichelberger et al. 1986; Westrich et al. 1988; Swanson et al. 1989). Further evidence was presented by Eichelberger (1989) to show that this was possible; experiments showed that the outgassing of a magmatic foam could leave no relic bubble textures (Westrich & Eichelberger 1994). The two theories were combined by Fink et al. (1992) to include textural observations on lava domes and isotopic evidence of in situ vesiculation. Fink's 'Beyond the permeable foam' model (1992) suggested that magma chambers that were stratified or zoned in volatiles sourced some dome eruptions, but that the presence of dense obsidian can only be produced by the collapse of a permeable foam. However, the process of vesiculation of the lava continues during flow, allowing effervescence on the surface of the flow, and continued vesiculation in the core from anhydrous mineral crystallisation (Fink et al. 1992). This combined theory has become widely accepted as the model for the eruption of lava domes, however, this model is constantly being refined to assess the controls on why some domes are

associated with explosive eruptions and catastrophic pyroclastic flows and some are non hazardous.

During the ascent of magma, a reduction in pressure allows volatiles to exsolve and create bubbles (Figure 1.6A; Sparks 1978; Proussevitch & Sahagian 1996). Bubbles growth is initially quick, but slows and becomes diffusion controlled once a critical size is achieved (Figure 1.6A; Proussevitch & Sahagian 1998; Navon et al. 1998). In equilibrium conditions, bubbles will grow until they touch, and merge to become a bubble network (Lovejoy et al. 2004; Castro, Burgisser, et al. 2012; Cashman & Sparks 2013). A bubble network, produced by coalescence, shear or cracking, will allow gases to move freely through the magma, and will prevent a build up of pressure inside the bubble (Figure 1.6B; Klug & Cashman 1996; Cashman et al. 2000; Rust & Cashman 2004; Mueller et al. 2005; Takeuchi et al. 2008; Mongrain et al. 2008; Okumura et al. 2009; Lavallée et al. 2013). In flowing magma, cracking of bubble walls and shear elongation of the bubbles will produce a permeable network at lower porosities, and allowing for effective degassing (Zhang & Sanderson 1998; Okumura et al. 2009; Laumonier et al. 2011; Lavallée et al. 2013). If the bubble network has not been created, the bubbles will often have an overpressure of volatiles (Gardner et al. 1996; Mungall et al. 1996; Gardner et al. 1999; Spieler et al. 2004; Gonnermann & Manga 2007) which may lead to failure of bubble walls, fragmentation and an explosive eruption (Spieler et al. 2004; Mueller et al. 2005; Mueller et al. 2008).

'Beyond the Permeable Foam Model' (Fink et al. 1992) has outlined the idea that bubbles grow and shrink during ascent, with late stage sub-aerial effervescence upon extrusion of the lava. However, the processes that control how and why bubble volumes are reduced during the extrusion of a lava dome still require both experimental and textural constraints. Bubble volumes can decrease as H₂O is either resorbed back into the melt or escapes through a bubble network. H₂O resorption can be driven by decrease in temperature, increase in CO₂ concentration, or an increase in pressure (Yoshimura & Nakamura 2010; Watkins et al. 2012; von

Aulock 2013). Volatiles will be resorbed into the melt, enriching the rim of the bubbles or cracks with a higher H₂O content than the rest of the melt (Figure 1.6F). However, I propose that it is outgassing that is responsible for the majority of reduction in bubble volume in lava domes (Figure 1.6 D & E).

A well connected bubble network will allow H₂O to outgas into surrounding rocks or to the atmosphere (Figure 1.6C & D; Stasiuk et al. 1996; Westrich & Eichelberger 1994; Mongrain et al. 2008), preventing fragmentation and facilitating effusive lava flows (Okumura et al. 2009). A network of bubbles will only prevent fragmentation if it is connected enough to allow sufficient gases to escape; excess gas in a connected, but constricted, system will lead to episodic explosive pulses during lava extrusion (Schipper et al. 2013). Outgassing results from the development of permeability and the escape of volatiles through this permeability (Figure 1.6D), and results in a loss of porosity. This loss happens due to (1) shear, (2) compression and (3) surface tension.

Shearing elongates bubbles and creates anisotropic permeability (Wright et al. 2006), increasing the degassing ability even at low porosities (Okumura et al. 2009; Caricchi et al. 2011; Schipper et al. 2013). Shear also leads to development of areas of layered porosity in lava flows parallel to flow direction (Figure 1.6B; Stevenson et al. 1994; Castro & Cashman 1999).

Compression from overlying material will squash bubbles, squeezing exsolved volatiles along permeable pathways or back into the melt, leading to a reduction of the porosity of a melt (Chapter 3; Figure 1.6E; Quane & Russell 2005; Michaut et al. 2009; Quane et al. 2009; Bercovici & Michaut 2010; Avard & Whittington 2012). In large ignimbrites, welding and overburden can significantly reduce porosity (Quane et al. 2009) and can lead to almost complete destruction of bubble textures (Westrich & Eichelberger 1994). In denser lavas, compression will lead to a reduction in porosity, but may also lead to a decrease in viscosity (Avard & Whittington 2012). It is unclear how dense cores of lava domes are formed, as few studies have concentrated on

dome-level processes, but instead on conduit processes (Lavallée et al. 2013; Kendrick et al. 2013). Chapter 3 investigates compression on dome lavas from Ngongotaha and Ruawahia domes.

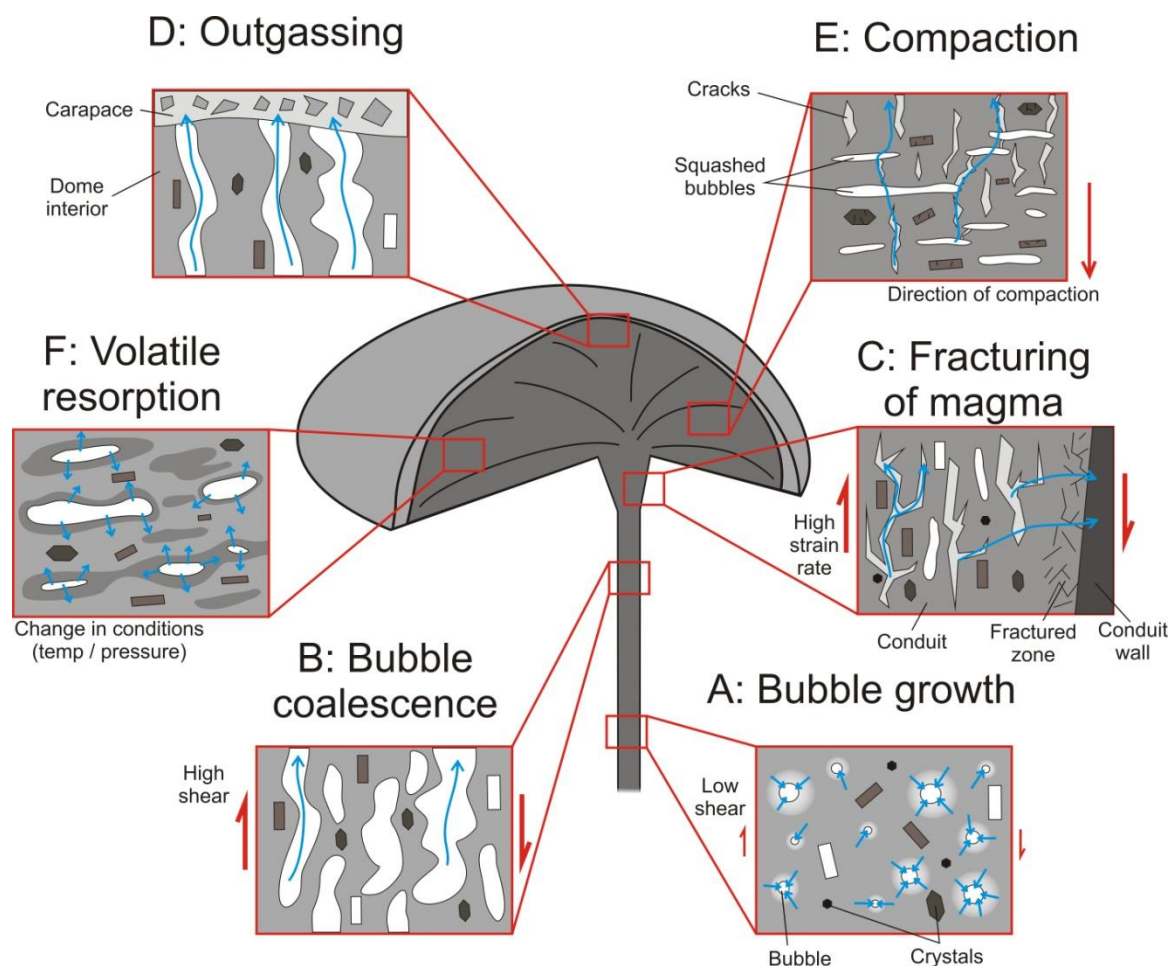


Figure 1.6: Diagram summarising bubble growth (A), coalescence (B), fracturing of magma (C), dome outgassing (D), compaction of bubbles (E) and resorption of volatiles (F). Red arrows show direction and size of shear or compaction forces, blue arrows show pathways of volatile movement in each scenario.

Surface tension resists homogeneous bubble growth in initially small bubbles, requiring large degrees of volatile saturation in order to form bubbles (Mourtada-Bonnefoi & Laporte 1999; Mangan & Sisson 2005; Nguyen et al. 2013). In larger bubbles, surface tension will act to create a rounded bubble, and will smooth out irregular bubble necks during coalescence (Gonnermann & Manga 2005b). The affect of surface tension on the outgassing of bubbles is poorly

researched at present, but the viscosity of rhyolite is likely to limit film drainage and bubble rupture in rhyolite lava domes (Nguyen et al. 2013).

Cracking in lavas can be formed by thermal stresses (Fortin et al. 2011), by brittle failure from high strain rates and accumulated stress exceeding shear strength (Chapter 3; Figure 1.6C; Tuffen et al. 2003; Lavallée et al. 2013). Accumulation of stress in magma occurs during unrelaxed magma deformation (Tuffen & Dingwell 2005), which typically initiates once the product of strain rate and viscosity exceeds 10^7 to 10^8 Pa (Webb & Dingwell 1990; Tuffen et al. 2003; Tuffen & Dingwell 2005) in crystal poor, silica rich magmas. The presence of crystals impacts this accumulation stage by initiating failure at strain rates two to three orders of magnitude lower than for crystal-free magmas (Gottsmann et al. 2009). Cracks will increase permeability (Vinciguerra et al. 2005; Fortin et al. 2011; Collinson & Neuberg 2012), and will align parallel to the direction of maximum stress (Figure 1.6E; Kendrick et al. 2013). Cracking will form permeable pathways (Smith et al. 2006), overcome a reduction in permeability from pore collapse and enable degassing of an otherwise impermeable plug (Lavallée et al. 2013; Kendrick et al. 2013). A well formed porous network, either through a connected bubble network or through multiple cracks, will increase permeability and therefore increase the overpressure needed for fragmentation to occur within the lava (Mueller et al. 2008). Cracking and tuffisite vein formation at the margins of conduits provides degassing pathways for efficient degassing of permeable lava in the centre of the conduit, but cannot account for the amount of degassing required to make the transition to effusive volcanism alone (Castro, Cordonnier, et al. 2012). Abrasion and small fragmentation events form fine grained particles which can fill cracks, where they sinter, reduce permeability and thus reduce their degassing potential (Tuffen & Dingwell 2005); welding of these tuffisite veins, and repeated fracture, has been hypothesised as a method of forming flow bands in crystal poor magmas (Tuffen et al. 2003). This cyclical healing and re-fracturing is suggested to be the cause of microseismicity in ascending magmas (Tuffen et al. 2003; Tuffen & Dingwell 2005; Lavallée et al. 2008; Tuffen et al. 2008).

The extrusion of stable lava domes has been linked to the presence of an efficiently degassing magma in the conduit (e.g. Bull et al. 2012), and so an understanding of the porosity and permeability controls inside of an extruding lava dome is necessary to be able to constrain and predict the behaviour of the eruption. Explosion pits on the surface of obsidian lava flows indicates a build up of pressure in the interior of the flow from continually exsolved gases and a sealed, or poorly connected, permeability (Castro et al. 2002). The overriding control on the porosity and permeability distribution in a lava dome is the outgassing (via cracking or a well connected bubble network) and bubble collapse process, which in turn is controlled by initial porosity, viscosity and crystallinity of the lava. This outgassing process in conduits is well researched; however the literature does not contain many examples of lava dome processes. Chapter 3 aims to investigate the compression and bubble collapse processes of vesicular, non-vesicular, crystal-bearing and crystal-poor lavas.

1.5 Lava dome eruption styles

1.5.1 Morphology and types of lava domes and flows

Lava domes and flows are built up from of a series of lobes, spines, breccias and talus, and can grow exogenously, from extrusion of a spine or breakout flow, or endogenously, through inflation of the core or an individual lobe (Nakada et al. 1995; Stasiuk et al. 1996; Watts et al. 2002a; Maeno & Taniguchi 2006; Hale 2008; Tuffen & Castro 2009; Ramsey et al. 2012; Pallister et al. 2013). Analogue lava extrusion models have suggested a series of differing lava dome morphologies based on differing extrusion rates, cooling rates and yield strength (Fink & Griffiths 1998). The types of lava domes produced (ranging from 'spiny', through 'lobate' and 'platy' to 'axisymmetric') match well to the morphology of natural lava domes of andesitic to dacitic composition (Fink & Griffiths 1998). However, the model does not take pre-eruptive topography or aspects such as crystallinity into account, and does not discuss the production of lava dome structures or textures (such as those produced in analogue experiments by Závada et

al. 2009). In order to incorporate small scale structures and textures observed at Ruawahia and Ngongotaha, I introduce the terms 'flow lobe' and 'spiny lobe'. These terms were defined from structures observed at Ruawahia and Ngongotaha as neither lava dome fitted into the dome classification of Fink and Griffiths (1998). A 'flow lobe' is a lobe that contains features most commonly seen in or within lava flows, while a 'spiny lobe' is a lobe that contains multiple spine-like extrusions. The proportion of flow lobes (lobes with a large (>2) ratio of width to thickness) and spiny lobes (lobes with a lower ratio of width to thickness) will vary according to overall style of extrusion, lava viscosity, palaeotopography and effusion rate (Nakada et al. 1995; Nakada et al. 1999; Watts et al. 2002a; Hale & Wadge 2008; Pallister et al. 2013). A lava dome may contain multiple lobes of either the flow- or spiny- type, or a mixture of the two.

Flow lobes (Figure 1.7) are lobes with lava flow-like characteristics that may be covered in expansion fractures from continued magma intrusion into the lobe, from bubble growth within the lobe or from gravitational spreading (Figure 1.8B; Bull et al. 2012; Watts et al. 2002a). These lobes form through either endogenous or exogenous (such as breakout flows) methods, during lower effusion rate eruptions but may also represent a lower viscosity lava (Nakada et al. 1995; Nakada & Motomura 1999; Sparks et al. 2000; Watts et al. 2002a; Pallister et al. 2013). Pressure ridges (or ogives) and ramp structures can form on the top of flow lobes, and are continuous, arcuate features that form perpendicular to flow direction (Figure 1.7), due to movement of the ductile flow core underneath a solidified exterior (Fink 1980; Cas & Wright 1988; Maeno & Taniguchi 2006). Pressure ridges are observed on the obsidian flows of California (Fink 1980) as well as the Chao dacite flow, Chile (de Silva et al. 1994) (Figure 1.7). Ramp structures form when lava from the core of the flow is forced up along a shear zone and out of the top of the flow, producing a ridge (Cas & Wright 1988). Large ramp structures (several tens of metres across) on Rocche Rosse obsidian flow, Lipari show the extrusion of near solidified lava during flow stagnation, with subvertical flow banding dipping back towards the vent (Cortese et al. 1986; Cas & Wright 1988; Gottsmann & Dingwell 2001). Ramp structures could therefore represent the

transition from endogenous growth through flow and inflation, to exogenous spiny lobe extrusion during the cooling and solidification (and therefore increasing viscosity) of a flow front.

Spiny lobes are lobes that contain structures similar to lava spines but with a more homogenous core with few shear band structures, which retain a traditional dome-like shape, such as Chaitén (Figure 1.9C). Spines are intact, almost solid extrusions of lava forced out along shear zones directly above a conduit (Nakada et al. 1999; Watts et al. 2002a; Watts et al. 2002b; Tanguy 2004; Hale & Wadge 2008; Scott et al. 2008; Vallance et al. 2008; Kendrick et al. 2012) and are associated with high extrusion rates (Watts et al. 2002a) and/ or increases in viscosity (Nakada & Motomura 1999). Shear bands from the conduit propagate into the dome due to an increase in shear stress and the boundary between conduit and dome, which then focuses the intruding lava into a spine. This behaviour suggests that shear zones may explain the transition from endogenous to exogenous dome growth (Hale & Wadge 2008). Spines often have smooth, striated sides and are generally void of any blocks or talus (Figure 1.8A) that is the result of shear along a large fault in the shallow conduit or dome (Watts et al. 2002b). Vertical striations represent slickensides from brittle deformation and friction in the conduit (Cashman et al. 2008; Kendrick et al. 2012), and horizontal striations form at levels of coverage by debris apron and gouge deposits, showing uneven extrusion rates and start-stop slipping of the spine (Figure 1.8B; Vallance et al. 2008). Some lava domes, such as Unzen, produce a petal-like structure of multiple spine-like extrusions in the early stages of dome growth (Nakada et al. 1999). The individual petals were separated by 'peel' structures (deep fissures with curved walls formed by the separation of the lava extrusions), which enabled the individual extrusions to expand radially away from the conduit (Nakada et al. 1999).

In spiny lobes, no large or continuous shear zones connect the spine like extrusions on the surface of the dome to the conduit-dome transition. Instead, the spine-like extrusions are analogous to ramp structures, and are forced out due to continued, but unfocused, lava

extrusion into the lobe. These extrusions must form small shear or breccia zones (such as Sahetapy-Engel & Harris, 2008), but these do not propagate from the conduit, as is suggested to be the case in the extrusion of true spines (Hale & Wadge 2008).

The extrusion of flow lobes vs. spiny lobes is dependent on lava viscosity, extrusion rate or palaeotopography; a change in one of these parameters can shift the style of extrusion and hazard potential of a lava dome (Nakada et al. 1999; Watts et al. 2002a) (Chapter 4). If it is assumed that the source magma volatile content, and therefore melt viscosity, does not drastically change throughout the course of a single dome eruption, then a shift from one lobe type to the other will indicate a change in extrusion rate or viscosity (by increased degassing or from crystallisation). The shift will also change the spatial variations in internal structures and facies, as well as the hazard potential of the growing lava dome. It is therefore imperative to understand the processes behind the formation of these features, and where they may be located in a lobe.

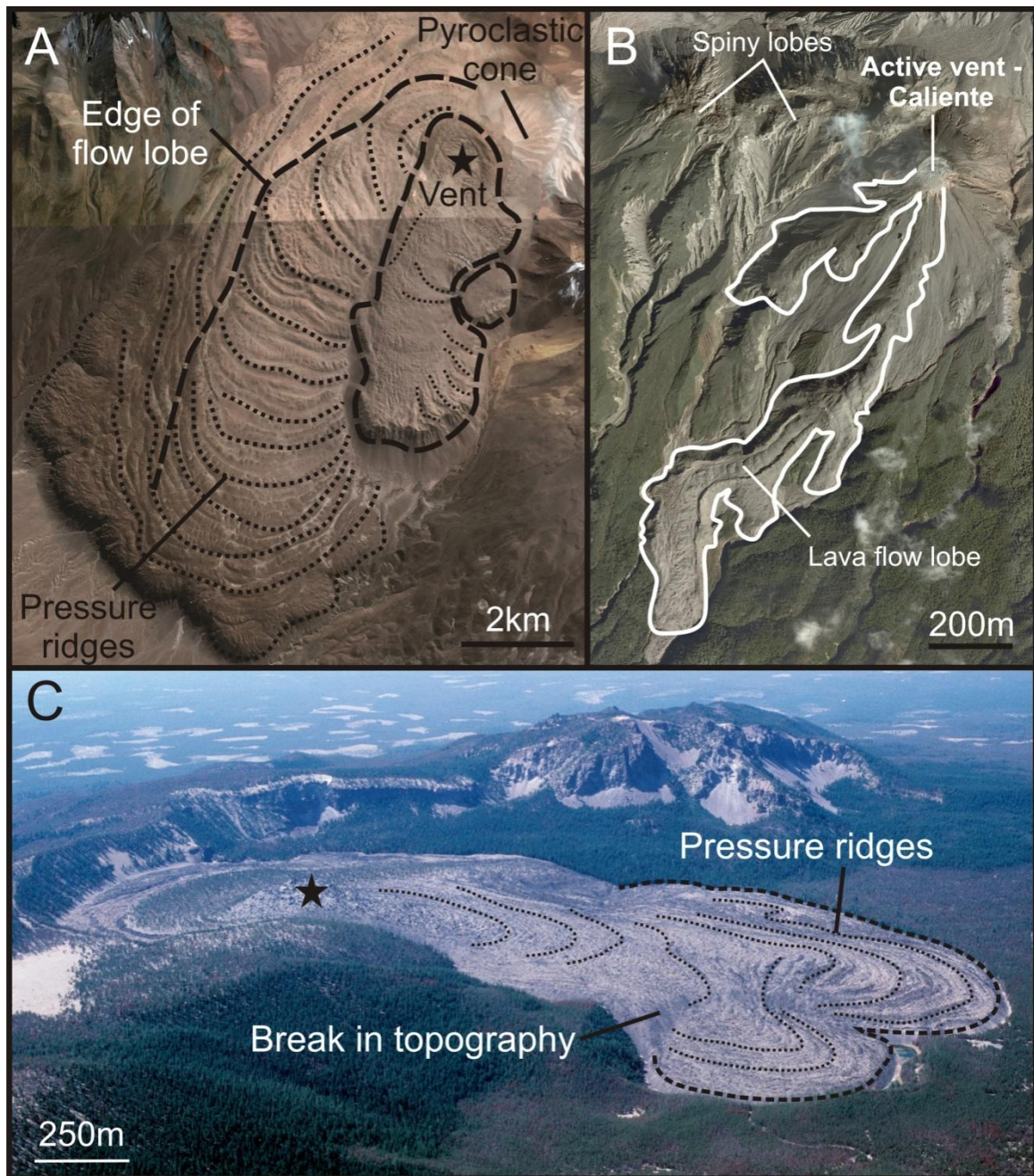


Figure 1.7: Examples of flow lobes. *A: Satellite image of Chao dacite flow, Chile. Flow features from de Silva et al. (1994). B: Viscous lava flow lobes from Santiaguito volcanic complex, Guatemala. C: Large flow lobe of Big Obsidian Flow, Newberry volcano, with flow features similar to Fink et al. (1983). Photo from USGS.*

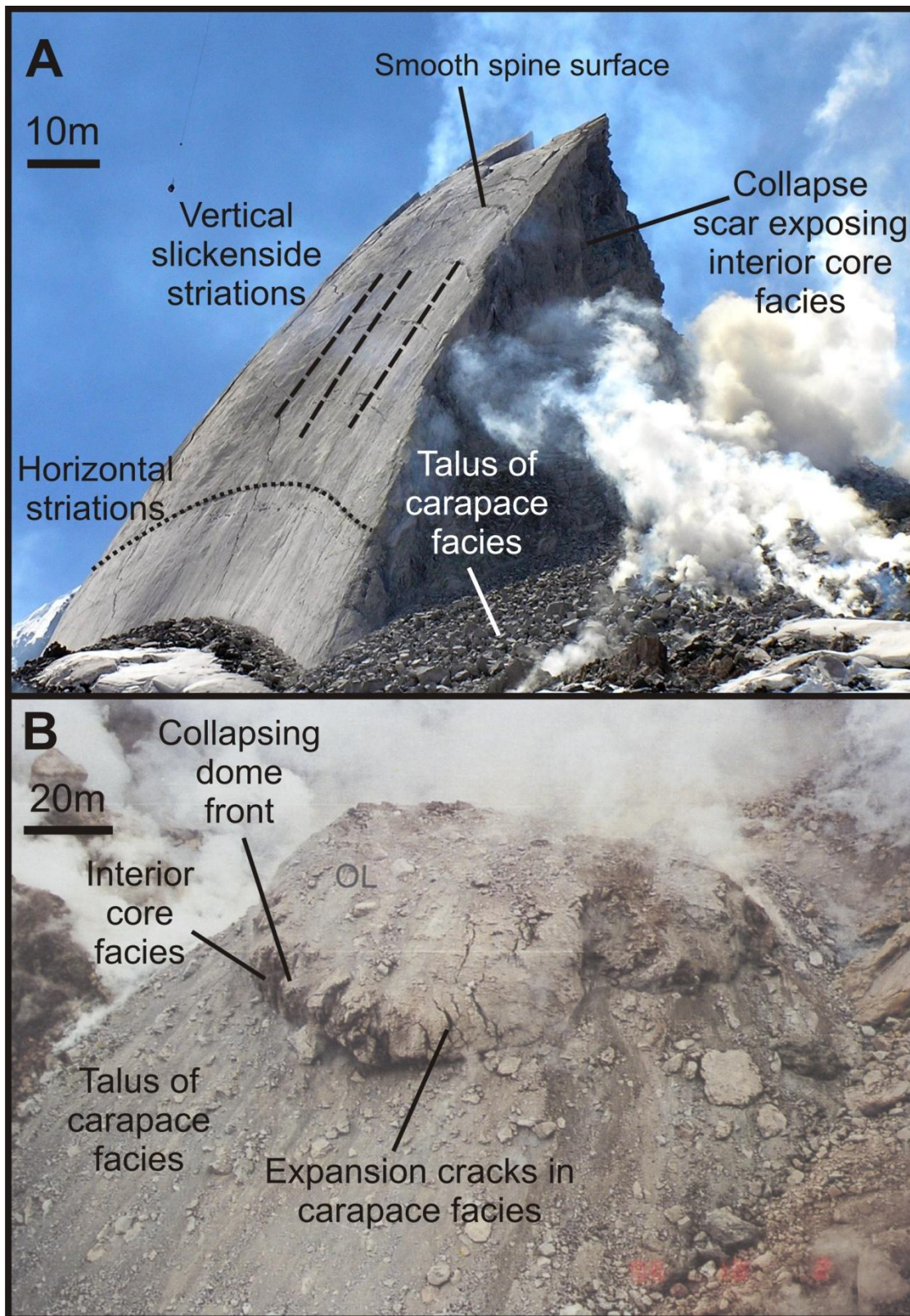


Figure 1.8: Images of dome structures. A) Photo of the Whaleback on the dome of Mt. St. Helens, April 2006. Photo by Dan Dzurisin of USGS. B) Photo of lava lobe extruded at Soufrière Hills volcano, October 1996, from Watts et al. (2002b).

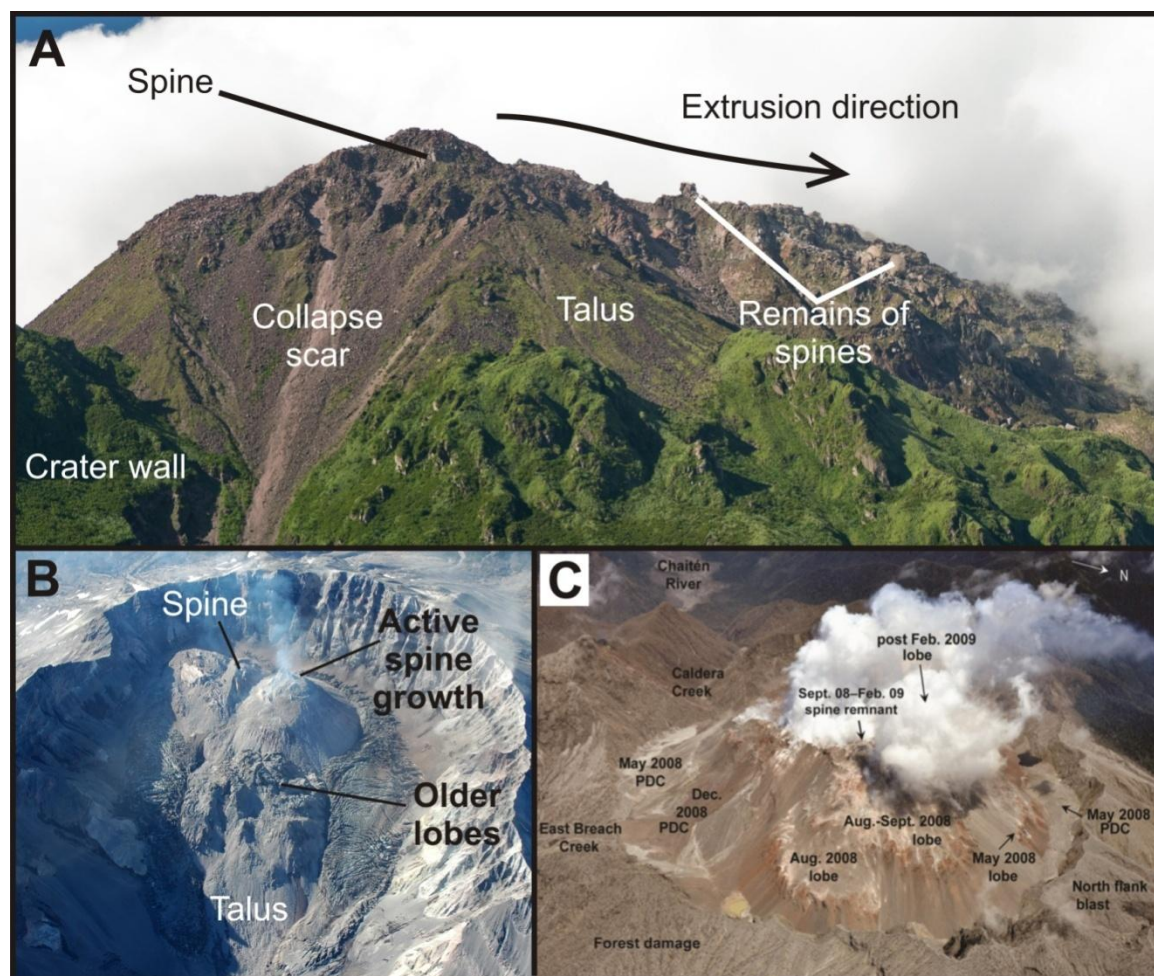


Figure 1.9: Examples of spiny lobes and spiny domes. A: Photo of southern face of Unzen dome, Japan, showing spines and extrusion direction. Photo is author's own. B: Aerial photo of domes of Mt. St. Helens in September 2006 showing active spine growth and older domes. Photo from USGS. C: Oblique aerial photo of Chaitén dome, Chile, showing individual lobes and spines. Taken from Pallister et al. (2013).

1.5.2 Facies architecture at lava domes

A lava dome consists of a series of facies that are related, and can be ascribed to differing extrusion environments in, and on, a lava dome. The facies of a lava dome as proposed by Christiansen & Lipman (1966), were a foliated, dense rhyolite core was surrounded by a 'vitrophyre', which in turn was covered by breccia. The drilling and mapping of rhyolitic lava flows in the western USA (Eichelberger et al. 1984; Eichelberger et al. 1985; Goff et al. 1986;

Manley & Fink 1987), expanded this initial view, and was able to link the facies variations to eruptive processes. In the rhyolitic obsidian flows examined, a basal breccia is overlain by a crystalline rhyolite core (with regions of dense obsidian and coarsely vesicular pumice) which is surrounded by a finely vesicular, partly brecciated carapace (Figure 1.10). These variations are caused by degassing as well as variations in viscosity, devitrification (Manley & Fink 1987) and local variations in flow conditions (Castro & Cashman 1999).

Most lava domes consist of 3 distinct facies: 1) an interior facies, composed of the dense lava core, 2) a basal breccia facies, composed of autobrecciated material that is over-ridden by the core as the dome grows, and 3) a carapace facies of pumiceous material and talus breccia (e.g. Cole 1970b; Sahetapy-Engel & Harris 2008; Hale 2008; Hale et al. 2009; Tuffen & Castro 2009; Pallister et al. 2013; Figure 1.10).

The carapace facies of the flow is often pumiceous, and best represents the vesicularity of the erupting foam (Fink et al. 1992). Surface vesiculation continues to occur during extrusion, so the carapace may end up with a higher vesicularity than when it initially erupted (Fink et al. 1992). However, it will not have undergone as much bubble collapse as the interior of the lava dome, and therefore may be the only near-conduit porosity material left. Rockfall and block and ash flows form a talus apron that often covers structures on the top and sides of the dome (Hale et al. 2009; Pallister et al. 2013). The size, and appearance, of the blocks on the surface of the dome have been used to characterise types of lava domes, and reflect eruption dynamics (Fink & Anderson 2000). Low extrusion rates form larger slabs due to less intense fragmentation than higher rates (Fink & Anderson 2000), a relationship which was repeated in laboratory experiments (Fink & Griffiths 1998). In situ dome surfaces in the carapace facies are often highly vesicular, and can show evidence of rapid failure-induced vesiculation and expansion in the form of highly spheroidal and large vesicles (Wright et al. 2007; Scheu et al. 2008). The existence of dense lava in the carapace can be evidence of extrusion of interior core facies through the

carapace (i.e. a spine), but can be considered as part of the carapace facies if features such as crease structures are present (Anderson & Fink 1992). These fissures are the result of multiple fracturing and expansion of a lava dome, forming a widening fracture that is lined with parallel, near horizontal striations (Anderson & Fink 1992).

The interior facies of lava domes consists of a dense core. The dense core may be formed from the collapse and densification of a pumiceous foam (see Chapter 3); during extrusion, the lava flow sheds blocks of carapace facies, and as it grows, it will over-ride these blocks, which form the basal breccia facies (Kilburn 2000). The core is not often homogenous; the extrusion of spines along shear zones may also produce spine or breccia facies within the core, consisting of cross cutting, deformed and shattered zones (Chapter 4) (Watts et al. 2002a; Kendrick et al. 2012; Lavallée et al. 2013) (Figure 1.10). Breccia facies within the core facies can also form from the propagation of fractures into the dome core from the carapace during ramp structure extrusion (Maeno & Taniguchi 2006) or from selective devitrification during fluid flow (Dadd 1992).

Facies variations are most commonly described as differences in vesicularity between a dense, collapsed core and vesicular carapace (eg. Cole 1970a). The extrusion of less vesicular, more viscous lavas may stem from a decrease in extrusion rate, allowing more time for collapse of the bubble network due to a longer residence period, effective degassing and limited cooling in the conduit (Westrich & Eichelberger 1994; Burgisser & Gardner 2004; Mongrain et al. 2008; Nakamura et al. 2008; Suzuki & Fujii 2010). However, highly vesicular lithologies found within the core of a dome can be attributed to the intrusion of foamy magma towards the end of the dome eruption (Williamson et al. 2010) or to multiple extrusion episodes where the vesicular lava represents carapace facies of earlier, buried extrusions (Chapter 4). Continued extrusion of vesicular magma at Novarupta was capped by older dense, degassed lavas from earlier dome growth, forming a dense carapace and a vesicular interior (Adams et al. 2006). Following the

formation of a dense (33 – 45 % porosity) blocky dome at Redoubt, highly vesicular (55 – 66 % porosity) lava (albeit with a lower Si content than previous extrusions) was observed to extrude on top of the previous dome, towards the end of the eruption (Bull et al. 2012). In both cases highlighted above, highly vesicular material continued to erupt, but the internal structure of the lava dome controlled where continued extrusion occurred.

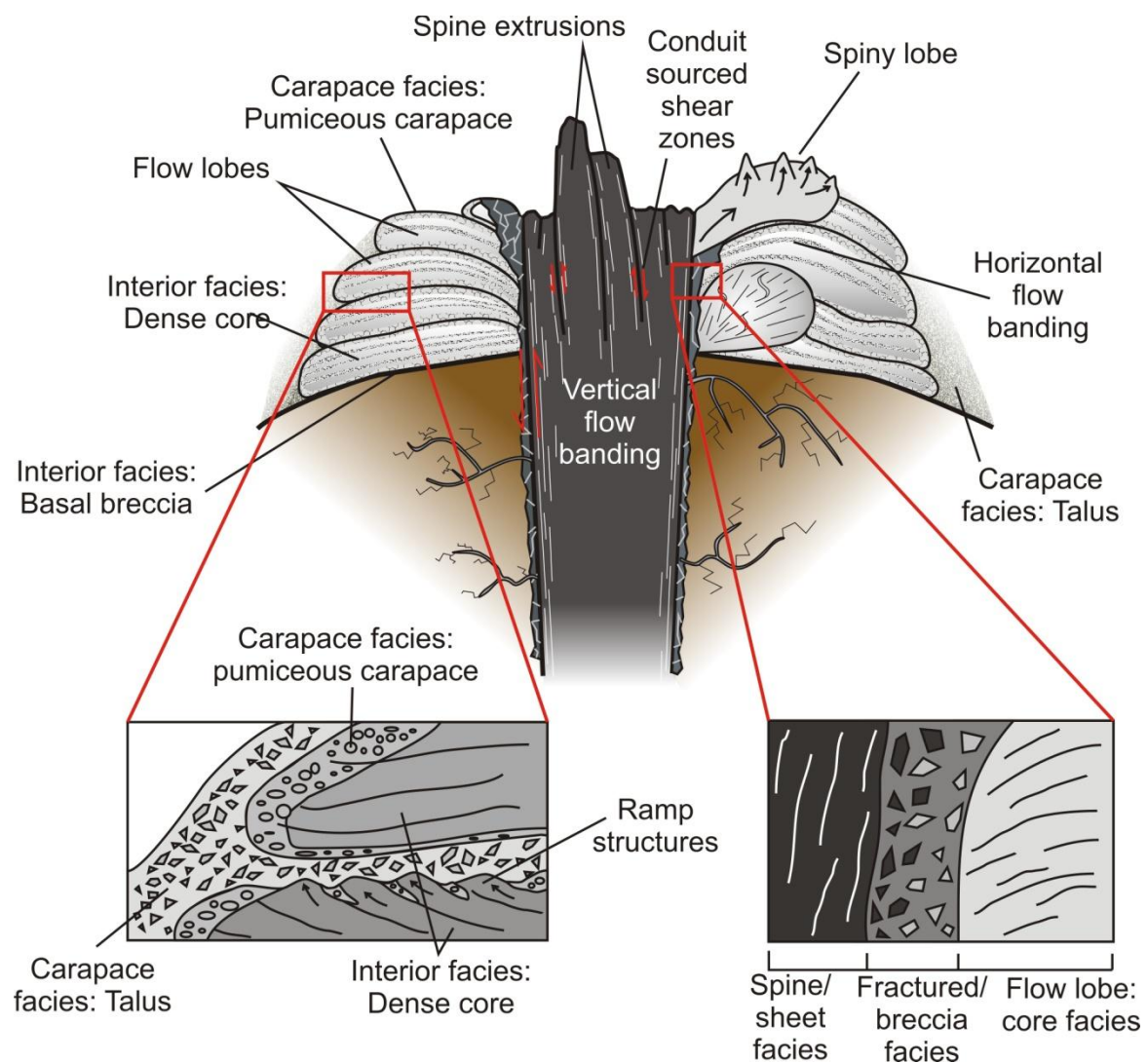


Figure 1.10: Diagram of a hypothetical lava dome consisting of spines, spiny lobes and flow lobes, containing internal structures and facies described in text.

1.5.3 Internal structures of lava domes

The internal structures of lava domes such as flow bands, fractures and breccia zones form during brittle and ductile deformation processes in the conduit and in the dome during extrusion; the formation of which are greatly dependant on total strain, strain rate and viscosity (Dingwell 1996). Here, I summarise how total strain, strain rate and viscosity effects lava domes in relation to the formation of internal structures.

Flow banding is produced by ductile strain forming flattened or stretched bubbles, variations in porosity, aligned crystals or water content, or can be identified from differences in devitrification or chemistry (Manley & Fink 1987; Seaman et al. 1995; Castro & Cashman 1999; Gonnermann & Manga 2005a; Seaman et al. 2009; von Aulock 2013). Flow banding that is produced inside of a conduit or lava dome, forms in response to localised differences in strain rate within a conduit or flow (Figure 1.10; Fink & Anderson 2000; Tian & Shan 2011) and can often show extreme localised orientation variations due to intricate folding (Castro & Cashman 1999). This viscous flow also aligns phenocrysts and can separate microlites in bands of high and low microlite concentration (Allen & McPhie 2003), as well as leading to variations in porosity and vesicle geometry across flow bands (Okumura et al. 2009). The variation in vesicularity in flow bands can lead to differences in H₂O content (Castro et al. 2005), which will further affect the evolution of the flow bands, and may lead to secondary boiling and explosive decompression (Castro et al. 2002; Castro et al. 2005). High strain rates may also lead to fracturing in high viscosity magma and formation of tuffisite veins (Tuffen et al. 2003; Maeno & Taniguchi 2006), and repeated fracturing, brecciation and healing of magma can form flow banding (Tuffen et al. 2003; Gonnermann & Manga 2005a).

The viscosity of the lava is determines whether the strain rate results in brittle or ductile behaviour (Dingwell 1996). Viscosity is controlled by melt viscosity (i.e. temperature, geochemistry and volatile content), crystallinity and vesicularity (Lavallée et al. 2007; Giordano

et al. 2008; Quane et al. 2009; Cordonnier et al. 2009; Avard & Whittington 2012; Kendrick et al. 2013). Due to different cooling and degassing histories within a dome, viscosity may vary, and as a result explain the variation in internal structures, such as porosity and breccia formation, within lava domes. The temperature and cooling profile of a lava dome affects crystal growth and crack development (Seaman 2013; von Aulock et al. 2013), which may lead to redistribution of water into the fractures and cavities, and weakening of the dome (Fink & Manley 1987; Smith et al. 2001; von Aulock et al. 2013). Crystalline domes, such as Soufrière Hills and Unzen, often form well defined shear zones that facilitate spine extrusion and degassing (Nakada et al. 1999; Watts et al. 2002a; Sahetapy-Engel & Harris 2008; Lavallée et al. 2013).

Shearing in crystal-poor lavas causes shattering, and forms brecciated zones instead of spine extrusion, as the comminution of crystals helps form discrete shear zones, and enables the extrusion of spines (Chapter 4; Lavallée et al. in prep.). Vesicularity has a much lower affect on viscosity than crystallinity (Chapter 3; Manga et al. 1998; Rust & Manga 2002; Quane et al. 2009; Avard & Whittington 2012; Mader et al. 2013), but allows effective degassing and prevents fragmentation (see section 1.4). In lavas close to the brittle-ductile transition, shearing caused by flow can create brittle fractures known as cavitation, especially when close to rigid structures such as crystals or lithic fragments (Smith et al. 2001). This process forms pores in low vesicularity lavas which can extract volatiles from the surrounding lava and provides degassing pathways. It will, however, create areas of weak lava that may contribute to failure of the flow or dome edge (Smith et al. 2001).

While the formation of internal structures is controlled by total strain, strain rate and viscosity, the orientation and distribution of internal structures will be controlled initially by conduit geometry and size, and by flow and spreading if the dome is able to do so. At Caliente Dome, Santiaguito, heat loss at the summit is primarily focussed around a ring structure (Sahetapy-Engel & Harris 2008) that is suggested to be the surface expression of a permeable fractured

region that derives from shear zones in the conduit (Figure 1.10; Sahetapy-Engel et al. 2008). Similar ring structures are seen in the Ohaaki geothermal field in the TVZ, suggesting that the permeable fractured region is used as a pathway for geothermal fluids (Rissmann et al. 2011). This ring structure may be analogous to shear bands which emanating from the conduit through the lava dome. Similar structures have been observed at Soufrière Hills have been linked to the transition from endogenous to exogenous dome growth, where large mega-spines extrude out of the dome after deforming the surface of the dome (Hale & Wadge 2008).

In order to predict the flow behaviour of a lava dome, the links between conduit shape and size, flow structures and topography must be investigated. The flow and internal structures of lava domes are formed during extrusion, and are initially controlled by the shape and size of the conduit and modified during flow and spreading. Therefore, with detailed mapping of internal structures at exposed lava domes, these links can be investigated. Ruawahia and Ngongotaha domes are excellently exposed, and represent differing styles of eruption, from crystal-poor, post-caldera collapse volcanism (Ngongotaha) to crystal-bearing non-caldera collapse related volcanism (Ruawahia). Chapter 4 examines these domes, and produces eruption models that link the structures and facies to extrusion processes, and examines the similarities and differences between the domes.

1.6 Structure of the Taupo Volcanic Zone

1.6.1 Regional structure of the TVZ

The regional structure of the TVZ is a NE – SW orientated active rift that is concentrated in a band that runs from the Whakatane Graben, through the OCC and the Taupo Rift and ceases at the southern margin of the TVZ, at Mt. Ruapehu (Rowland & Sibson 2001; Figure 1.11). This structure has a primary control on many of the calderas (Davy & Caldwell 1998; Milner et al. 2002; Spinks et al. 2005; Gravley et al. 2007; Seebeck et al. 2010) and stratovolcanoes (Cole

1990; Nairn et al. 1998) in the TVZ. The rifting zone of the TVZ represents a basin superimposed on top of a volcanic arc (Wilson et al. 1995). In the central TVZ, normal faults with a general NE – SW trend (Figure 1.11), and a moderate to high dip (60 – 90°; Acocella et al. 2003) have produced a wide series of grabens that have accumulated hundreds of metres of ignimbrite deposition. This orientation is also reflected in numerous aligned vents, lava domes and in caldera collapse styles and geometry.

1.6.2 Links between tectonics and volcanism in the TVZ

The Taupo, Rotorua and the OCC all show a tectonic control on collapse through caldera margins partly aligned with the NE-SW trending structure, as well as gravity anomalies (Davy & Caldwell 1998; Milner et al. 2002; Seebeck et al. 2010). The twinned Mamaku and Ohakuri ignimbrite eruptions (from the Rotorua and Ohakuri calderas respectively) at ~240 ka were partially sourced from magma stored laterally in the area between the Rotorua and Ohakuri calderas (Kapenga caldera; Figure 1.2; Gravley 2004; Gravley et al. 2007). This withdrawal of magma created a graben of approximately 40 km² aligned with the rift; the downthrow associated with this graben cut through the large Horohoro dome, forming a prominent fault scarp known as the Horohoro Fault, reflecting a change in the rift orientation across Rotorua and OCC (Chapter 5; Figure 1.11; Gravley et al. 2007). Alignment of vents associated with rifting and dyke intrusion is observed intra-caldera (Cole & Hunt 1968; Nairn & Cole 1981; Seebeck & Nicol 2009) as well as inter-caldera (Cole 1990; Rowland et al. 2010; Leonard et al. 2010). At the OCC, extension in the last 25 kyrs has been achieved through intrusions of dykes with complementary faulting, while faulting outside of the caldera to the SE is suggested to be purely tectonic in origin and older, apparently extinct (Seebeck & Nicol 2009).

Lava domes in the TVZ also reflect the overall structural trend (Figure 1.3 & 1.11). Domes in the Maroa volcanic centre (Leonard 2003) and the OCC (Cole 1970b; Leonard et al. 2002; Smith et al. 2006; Cole et al. 2010) are aligned with the regional structure, and may have erupted as a series

of aligned vents sourced from a shallow dyke (Leonard 2003; Figure 1.3). Other lava domes with a possible regional tectonic structural control include the domes of Rotorua (Chapter 5; Milner 2001) and Taupo (Cole et al. 1998; Liu et al. 2005; Wilson et al. 2005; Figure 1.3).

While the structural trends of lava domes are obvious, the links between the domes themselves and the underlying tectonic structure have not been convincingly made. In Chapter 4, I link the internal structures of lava domes to the location and orientation of the conduit. The location and shape of this conduit will be controlled by the local and regional structures. In Chapter 5, I explore the possible tectonic controls on Ngongotaha dome and Rotorua caldera, and produce structural maps that explain the morphology and location of other lava domes at Rotorua caldera.

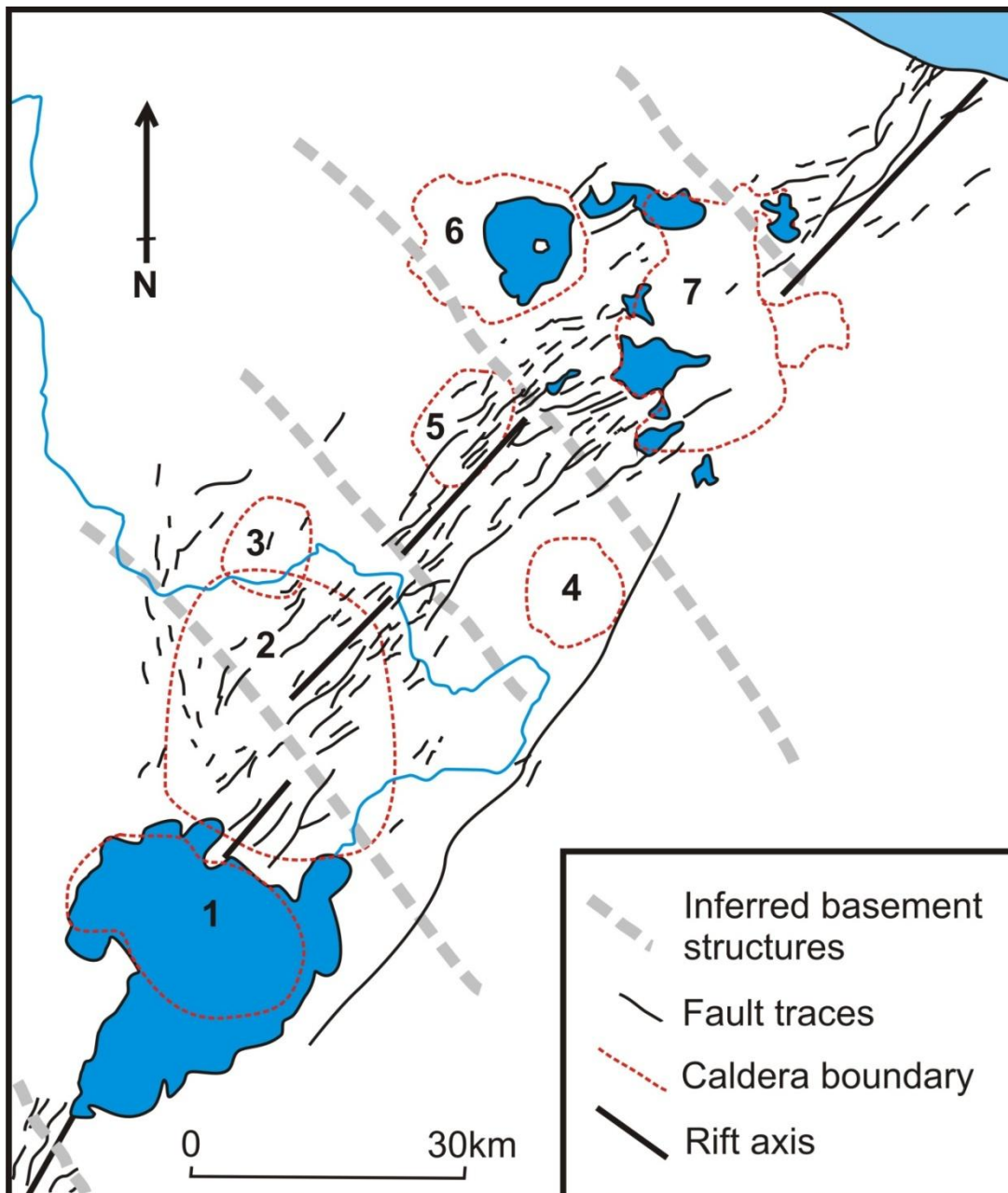


Figure 1.11: Structural trends across the TVZ, based upon Rowland et al. (2001). Each segment of rift axis is separated by accommodation zones that are inferred to be relic basement structures. Calderas are numbered as such; 1) Taupo, 2) Whakamaru, 3) Ohakuri, 4) Reporoa, 5) Kapenga, 6) Rotorua and 7) OCC.

1.7 Questions to be addressed in this thesis

This thesis aims to investigate the controls on lava dome processes, in order to reconstruct the eruptions of Ngongotaha and Ruawahia domes, and link these to the host calderas. Chapter 2 summarises the methodology of the experiments, data collection and analysis, and explains why these techniques were used. Chapter 3 will examine porosity and crystallinity controls on compaction within the erupting Ngongotaha and Ruawahia domes, and will explain the differences in vesicularity of the interior facies of each. Chapter 4 uses mapping of internal structures at Ngongotaha and Ruawahia to reconstruct the timeline of dome extrusion, and intends to focus on differences in eruption style and hazards associated with each. Chapter 4 also suggests possible vent shapes and locations, and links this with the extrusion style. Chapter 5 investigates the structure of Rotorua caldera, and how this has controlled lava dome growth at Ngongotaha. It also seeks to explain how the other lava domes of Rotorua caldera were controlled by the regional structure, and what this means to the tectonics of the area.

A series of objectives for this thesis were set out at the start of this chapter; individual questions which aim to investigate these objectives are detailed below.

Question	How this will be addressed	Chapter reference
<i>What happens to the porosity and permeability of a foam during extrusion of a lava dome?</i>	The porosity and permeability of dome lavas of varying porosities is recorded after the application of uniaxial stress.	Chapter 3
<i>How do properties of lava such as crystallinity or vesicularity affect how a lava dome compacts?</i>	Strain rate, viscosity and tomography of dome lavas of differing crystallinity and porosity after compression are studied to analyse the effects of crystals and bubbles.	Chapter 3
<i>How can the internal structures of lava domes be attributed to eruption styles?</i>	Internal structures, such as flow bands and breccia zones, in Ngongotaha and Ruawahia are mapped, and are used to infer eruption styles and timing.	Chapters 4
<i>What links can be drawn between the internal structures of lava domes and their structural setting?</i>	Analyses of internal structures at Ngongotaha and Ruawahia are compared to local structures across Rotorua caldera and the OCC, respectively, as well as to the wider regional tectonics.	Chapter 4 and 5
<i>What can lava domes tell us about the structure and history of calderas?</i>	Geochemistry, structures and age constraints of lava domes at Rotorua caldera are used to infer distribution of faults and caldera collapse structures, and a timeline of lava dome eruptions at Rotorua caldera is presented.	Chapter 5
<i>What implications to volcanic hazards does this research show?</i>	Utilising the answers to questions above, I suggest what the implications of this research are.	Chapter 6

Table 1.1: Summary of questions to be answered in this thesis.

Chapter 2:

Methodology

In the previous chapter, I summarised the evolution of lava dome facies by bubble growth and collapse, lava extrusion and cooling, and production of internal structures. The links between lava dome morphology, structure and textures, both local and regional, were explored and the aims and questions for this project were set out. In this chapter, I will summarise the experimental methods, data collection, analytical methods and field mapping techniques that were utilised throughout the study in order to fulfil the questions raised in Chapter 1. As the thesis is written in paper format, methodology sections in the individual chapters are kept to a minimum length and in this section I provide some supplementary methodologies, detailed sample preparation methods and analysis guidelines in order to provide the reader with means to repeat the experiments and fieldwork utilised by this study.

2.1 Uniaxial compression experiments

In order to investigate the compression of lava dome material, a high temperature uniaxial press (Hess et al. 2007) at Ludwig Maximilians Universität (LMU), Munich was employed to simulate the conditions inside a lava dome and volcanic conduit (Chapter 3). The press is able to heat samples up to 1050°C while exposing them to a constant uniaxial force of up to 300 kN or a constant strain rate of between 10^{-7} to 10^0 s⁻¹. Our experiments were performed at a sample temperature of 900°C with the piston in freefall (equivalent to a force of 2.5 kN), in order to simulate pressures of 3 MPa within a lava dome (such as at the base of a large, ~200 – 300m thick dome). Uniaxial compression was chosen to represent the compression of a dome, as an unconfined dome will be able to move laterally and produce textures that uniaxial compression would be most suited for. The load and temperature were limitations of the apparatus, but will still be relevant to the production of textures in a lava dome. The samples were deformed at strain increments of 10 % between 10 and 60 % (see Chapter 3). A diagram of the press is shown in Figure 2.1.

Cores of samples were cut perpendicular to bubble elongation in order to correspond to the compression of near horizontal flow bands in a lava dome (see Chapter 3), with a diameter of ~25 mm and a length of ~50 mm. The ends of the core were cut parallel and the length and porosity measured (see section 2.3) before and after experimentation. One core from each sample was heated (unloaded) to 900°C at 2°C per min, and cooled to record porosity changes due to thermal effects. Another core was then placed in the press, and heated at a rate of 2°C/min to 900°C (+/- 5°C) and left to thermally equilibrate. Once temperature was steady for several hours, the press was lowered until touching the sample then raised slightly and left for 1 hour for the temperature to re-equilibrate to 900°C to account for the slight decrease in temperature from lowering of the piston. The press was lowered until touching the sample once more, and then allowed to compress the sample by freefall. The target total strain was

calculated from initial height of the sample, and the press stopped when the target strain increment was achieved. The press was raised; the furnace switched off and allowed to cool to room temperature. During the experiment, acoustic emissions were measured (see Chapter 3). Porosity, permeability and X-ray computed tomography were then performed on the core.

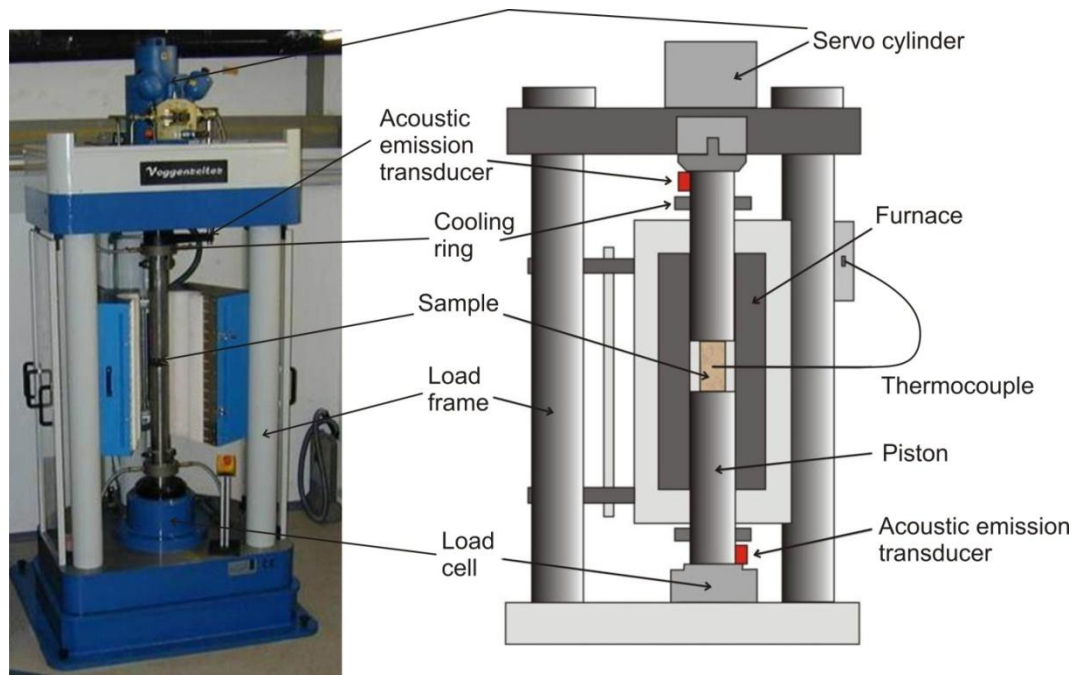


Figure 2.1: Diagram of uniaxial press at LMU, Munich.

2.2 3D Computed tomography and image analysis

3D Computed Tomography (CT) is an extremely effective tool for imaging bubbles and structures in lavas. CT scans have been shown to be an effective method for permeability (Polacci et al. 2008; Okumura et al. 2009; Degruyter et al. 2010a; Degruyter et al. 2010b; Schipper et al. 2013) and porosity studies (Song et al. 2001; Polacci et al. 2006; Polacci et al. 2009) in lavas. However, bubble walls that are thinner than 1 – 5 μm are usually below the level of resolution (Song et al. 2001; Bai et al. 2008) unless a very small sample size is used. Following compression experiments, 3D CT was performed to image textural changes in the samples. Two scales of image were produced – large scale on cores between 25 and 50 mm diameter and of varying

lengths, in order to record macro structures such as cracks, and small scale on fragments of less than 1 mm size in order to gauge changes in bubble shape and image bubble walls of 1 – 5 μm . While permeability can be calculated using CT images, it requires sufficiently high resolution and small sample size (less than 5mm; Degruyter et al. 2010a); these small samples will likely miss large scale cracks which will greatly affect permeability (Vinciguerra et al. 2005; Fortin et al. 2011; Collinson & Neuberg 2012; Kendrick et al. 2013). Instead, we rely on gas permeability measurements recorded in two perpendicular orientations (see section 2.4). The tomography was acquired via a v/tome/x s 240 micro-CT scanner from General Electric using a high power X-ray tube and a drx-250 rt detector system at LMU, Munich, and 'Ruby' detector (25 μm Gadolinium Oxysiphide phosphor detector with a PCD.edge scientific CMOS sensor) at the Australian Synchrotron, Melbourne. The scans were acquired at a voltage of 120 kV and a current of 167 nA for an exposure time of 1 s, cumulating 2000 images which provided a Pixel/Voxel size resolution of 14.78 μm at LMU, and 6.1 μm at the Australian Synchrotron. The raw tomography images are then converted using X-tract software into orthogonal slices, which were imported into ImageJ software to analyse 3D crack size and bubble shape. The edges of the image slices are removed due to edge effects, then brightness, contrast and threshold levels of the images are adjusted (and kept the same between samples) to pick out cracks, crystals or glass. Crack width (X) and length (Y) (i.e. perpendicular measurements on a plane parallel to the image slices) were calculated by measuring pixel width and multiplying by the resolution while crack height (Z) (i.e. distance of crack over long axis of core) was calculated by counting the number of image slices the crack appeared in. The height of the core is known, and can be divided by the number of slices to give an absolute value. However, due to the reduction in height of cores during compression, a reduction in sample length due to compression may also reduce the crack height (Z), even though the crack propagates through more of the sample. I therefore use crack width (X) and length (Y) as quantifying features of crack size. Bubble shapes

are qualitatively measured between undeformed and deformed samples, and range from elongated tubes to oblate spheroids.

2.3 Connected Porosity

The porosity of volcanic rock is a measurement of the percentage volume of pore spaces in the rock. Large changes in porosity of a volcanic rock can indicate drastic changes in vesiculation conditions (Rotella et al. 2013). The shapes and sizes of bubbles are indicative of conditions in the conduit or during flow, as rounded bubbles will become progressively elongated or flattened with shear or compression (Rust et al. 2003; Okumura et al. 2009; Caricchi et al. 2011). Analysis of shapes and sizes of bubbles will indicate conditions in the conduit or during flow, as rounded bubbles will become progressively elongated or flattened with shear or compression (Rust et al. 2003). Both natural and experimental fragmentation studies have used porosity to gain insights into conduit processes (Spieler et al. 2004; Kennedy et al. 2005). In a compacting, vesicular lava, porosity will show rock density changes as pore spaces are squeezed out or cracks open.

In the compression experiments (Chapter 3), porosity measurements were taken before and after deformation in order to quantify the porosity changes over the course of the uniaxial compression experiments. Porosity was calculated in Chapter 3 using an accupyc 1330 from micrometrics at LMU with helium gas (as used by Spieler et al. 2004; Kennedy et al. 2005; Kueppers et al. 2005; Mueller et al. 2005; Scheu et al. 2006; Scheu et al. 2008; Mueller et al. 2011). Porosity measurements were also used to differentiate between lava facies and types at Ngongotaha and Ruawahia (Chapter 4). These measurements used nitrogen gas in a ultrapycnometer 1000 at Massey University, Palmerston North (as used by Platz 2007; Pardo 2012). Gas pycnometry is used over water as a gas will give a more accurate porosity reading due to the lower molecule size and will therefore detect smaller pore sizes, and increase the accuracy of the final reading (Platz 2007).

To measure the density, and therefore connected porosity, the sample is cored at 25 mm diameter, and the ends cut parallel at approximately 50 mm in length. The cores were dried thoroughly in an oven, and kept dry during pycnometry measurements (Platz 2007). The exact volume of the cores was calculated by averaging multiple diameter and length measurements with accurate callipers. This ensures that any irregularities in the sides of the core created during coring are taken into account, and is also used to calculate barrel volume in heavily deformed samples (Chapter 3). A minimum of 5 length and width values were averaged for each core. The cores were then weighed on a set of scales accurate to +/- 0.001 g.

Gas pycnometers work on a principle of detecting a pressure change due to the addition of a solid medium (the sample – of volume V_0) into the sample chamber. The chamber (of volume V_1) is sealed and is pressurised to a user defined pressure (P_1). A second, isolated chamber with a known volume (V_2) is then pressurised to a higher pressure than in the sample chamber (P_2). A valve is then opened between the two chambers, and the system is allowed to equilibrate to an intermediate pressure (P_3). The skeletal volume of the core is then calculated according to:

$$V_0 = \frac{(P_3V_1 + P_3V_2 - P_1V_1 - P_2V_2)}{(P_3 - P_1)}$$

(Equation 1)

Connected porosity is calculated by subtracting the skeletal volume of the sample (volume calculated by the pycnometer) from the measured volume of the core. The difference between these values will be the volume of pore spaces which, when expressed as a percentage of the total volume, will give connected porosity. A minimum of 5 runs per sample were performed to determine standard deviation. The largest difference recorded from the pycnometer was approximately +/- 1%, but the errors from analogue measurements (such as width and length of core) are likely to be higher but hard to quantify.

The samples exhibit a range in natural connected porosity of several % (see Chapter 3). In order to compare final porosities, a method of calculating porosity loss was required. The amount of porosity lost (i.e. initial porosity minus final porosity) fitted very well when plotted against axial strain (see Figure 2.2). These best fit lines can then be used to calculate the amount of porosity lost at any strain increment, regardless of initial porosity. The equations on Figure 2.2 were used to calculate maximum (using highest initial porosity value per sample), minimum (using lowest initial porosity value per sample) and average porosity loss (using average initial porosity value) curves shown in Chapter 3.

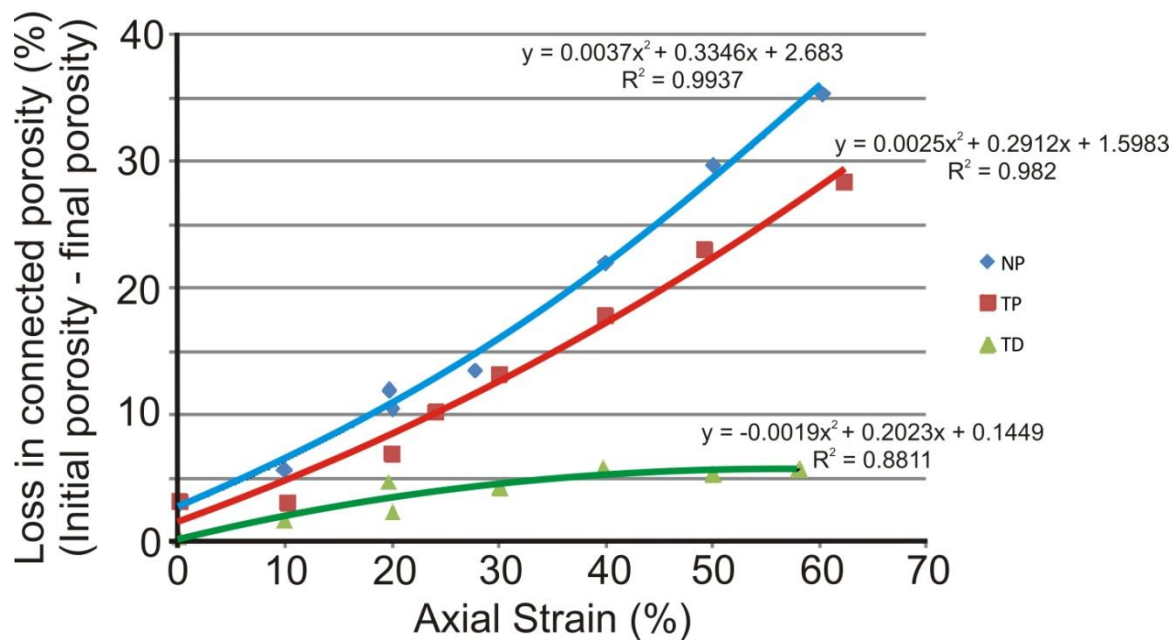


Figure 2.2: Graph of porosity loss against axial strain.

2.4 Permeability

Permeability is a measure of how easily a fluid or gas can move through a material. In volcanic systems, the permeability of a lava or magma will control the ability to effectively degas, which

will in turn partly affect the explosivity of an eruption (Klug & Cashman 1996; Mueller et al. 2005; Nakamura et al. 2008; Mueller et al. 2008; Rust & Cashman 2011).

Permeability is weakly linked to the porosity of a lava (Saar & Manga 1999; Takeuchi et al. 2009; Yokoyama & Takeuchi 2009; Rust & Cashman 2011), but strongly linked to the shape of the vesicles and the amount of connectivity between them, as the permeability of a single pathway will be controlled by the width of the smallest gap between vesicles (Saar & Manga 1999; Rust & Cashman 2004; Mueller et al. 2005; Wright et al. 2006; Yokoyama & Takeuchi 2009). Many studies have investigated the permeability of pumices of experimentally created foams (such as Nakamura et al. 2008; Takeuchi et al. 2008; Wright et al. 2009; Rust & Cashman 2011), or permeability changes due to cracking (Vinciguerra et al. 2005; Fortin et al. 2011; Collinson & Neuberg 2012).

While porosity will have one measurement per sample, permeability will differ depending on the direction it is calculated in, especially in highly anisotropic pumices or lavas (Wright et al. 2006). For the compaction experiments of Chapter 3, the cores were cut such that any bubble elongation was perpendicular to the long axis of the core. For permeability measurements, two smaller cores were then drilled; one parallel (against bubble elongation) and one perpendicular (with maximum bubble elongation) to the long axis. This ensures that the maximum ranges of permeability values were collected.

The permeability measurements were conducted at the University of Canterbury, using a gas permeameter that is based upon the designs of Takeuchi et al. (2008). The permeameter setup is shown in Figure 2.3A. The permeameter consists of a standard air compressor, a pressure regulator, a sample holder and a manometer (recording pressure differences across the sample) and a flow rate meter (Figure 2.3A and B). Compressed air is used as a medium to reduce cost. The method of Wright et al. (2006) and Takeuchi et al. (2008) was employed to measure gas permeability of cores of rhyolite from Ruawahia and Ngongotaha domes. As for porosity,

permeability was measured on deformed and undeformed samples in order to quantify the changes in permeability during the compression experiments. Using gas as a medium, instead of a non-compressible fluid, necessitates that the compressibility of the gas must be considered. To this end, the Forcheimer Equation has been introduced (Innocentini et al. 1999) that splits standard Darcian permeability (as gained through liquid permeability) into Inertial (k_2 – known as non-Darcian permeability) and Viscous (k_1 - analogous to Darcian) permeability. These two permeabilities take into account the turbulent nature of gas flow through bubbles, and the effect of eddies on the overall permeability. The Forcheimer equation is:

$$\frac{P_2^2 - P_1^2}{2P_0L} = \frac{\mu_{gas}}{k_1} v + \frac{\rho_{gas}}{k_2} v^2 \quad (\text{Equation 2})$$

Where P represents pressure (P_2 at the sample at which gas is entering, P_1 at the sample at which gas is leaving and P_0 at the place where the flow rate is recorded) and L is length of sample. Together, the left side of the equation is known as the modified pressure gradient. μ_{gas} and ρ_{gas} are the viscosity and density of the gas medium at the temperature at which the experiment is conducted (assumed to be constant in this case). The values used are $\mu = 0.00018$ Pa-s and $\rho = 1.2$ kg/m³. V is known as the gas volume flux, and is calculated by dividing the flow rate by the cross sectional area of the sample.

A dried core of 10 mm diameter is measured and then placed in a length of heat-shrink rubber tubing (containing heat activated glue to adhere to the sample on the inside) with a small wooden stopper on either end. Several small washers were then placed on one end to act as ballast. The sealed core is then placed in 'K1' resin in a circular mould (Figure 2.3C). The washers help to keep the sample in an upright position in the resin. The sample needs to be as parallel to the sides of the mould as possible. Once set, the sample is cut through the wooden stoppers, which are removed to expose the core (Figure 2.3C). The cut surfaces of the resin cylinder are then ground flat, and the sample is then dried at a low temperature (less than 40°C).

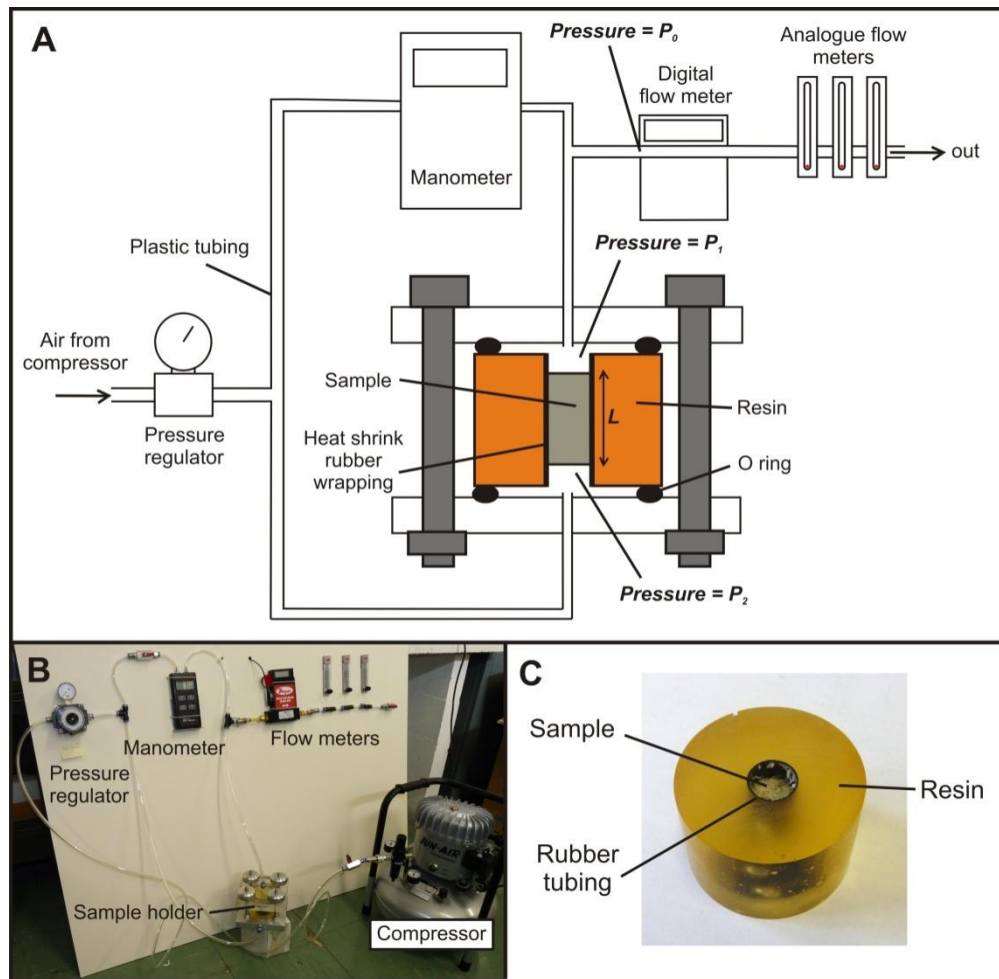


Figure 2.3: A: Diagram of gas permeameter. B: Picture of gas permeameter at the University of Canterbury. C: Picture of sample encased in resin.

The sample is then placed in the sample holder, and clamped down against a rubber O-ring (Figure 2.3A). This seals the sample so that gas can only flow through the sample itself. A series of permeability experiments are then conducted using a range of initial pressures and flow rates. A pressure regulator is used to create an even flow rate with a set pressure from the air compressor. The gas is then allowed to flow through the sample for 1 to 2 minutes to allow the flow to equilibrate before the pressure difference across the sample and the flow rate is measured. The modified gas pressure gradient is plotted against the gas volume flux (Figure 2.4), and k_1 and k_2 values are calculated from the equation of the best fit line (which follows the

equation $y = ax^2 + bx$ (where y = modified gas pressure gradient and x = gas volume flux)). This is then combined with Equation 2. k_1 and k_2 then become:

$$k_1 = \frac{\mu}{b}$$

(Equation 3)

$$k_2 = \frac{\rho}{a}$$

(Equation 4)

Errors from the permeability measurements are difficult to quantify due to the human component of measuring widths and lengths of core, and analogue methods of measuring gas flow. Instead, repeated measurements of cores were performed, and the difference of the highest and lowest permeability measurements was used to give a conservative error margin.

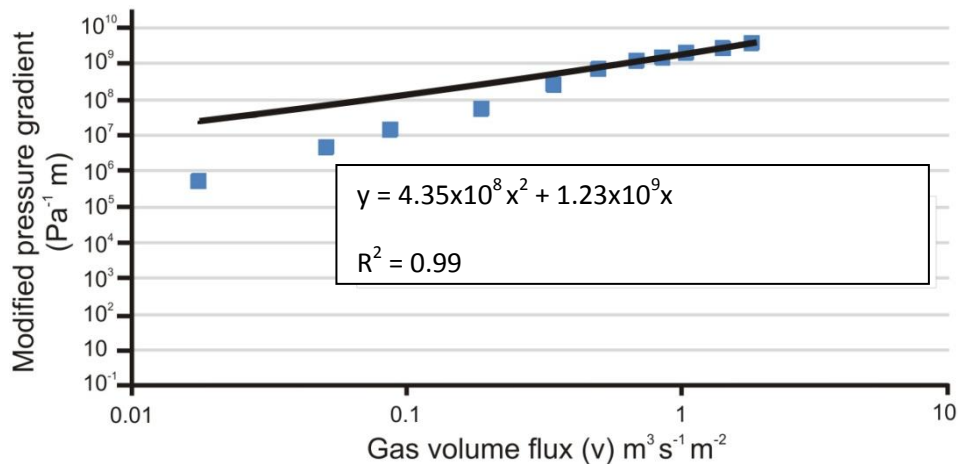


Figure 2.4: Typical graph of the relationship between modified gas pressure gradient and gas volume flux (see Equation 2) after 11 measurements, with 'a', 'b' and R^2 values for this particular sample.

2.5 Geochemistry

In Chapter 5, I use X-Ray Fluorescence (XRF) to group rhyolite domes at Rotorua caldera to study the relationship between lava domes and caldera structure. These geochemical analyses were presented in PhD theses but never published in journal articles. Analysis performed by Richnow (1999), Milner (2001) and Deering (2009) used lithium tetraborate fusion beads and pressed powder pellets. XRF analysis on major and trace elements was performed on a Phillips PW 1400 X-ray spectrometer (by Richnow, 1999) and a Phillips PW-2400 X-ray spectrometer (by Milner, 2001) at the University of Canterbury following the techniques of Norrish and Hutton (1969). Only major element analyses with totals of 99.5 +/- 1.0 wt% were accepted (Richnow, 1999).

2.6 Field mapping techniques

47 field days over 3 field seasons were spent mapping Ngongotaha and Ruawahia domes in detail using GPS and aerial photos, concentrating on mapping key structures linked to eruptive and post eruptive processes. These included flow banding and bubble elongation, fracturing, density, brecciated and shear zones and facies variations.

Facies variations were distinguished by differences in porosity, colour and texture in the field and based on facies first suggested by Richnow (1999). Thin sections of typical samples were analysed and characteristic petrological features incorporated into field description and facies classification.

At Henderson's Quarry, Ngongotaha, the dome was split into levels based on quarrying activity, and each level into faces. These individual faces were photographed and flow bands and fractures were measured and located on a sketch of the face. Samples were collected every ~20 m (measured with paces) to give a comprehensive and unbiased collection for later analysis. Fractures relating to dome cooling or later faulting were distinguished from quarrying fractures by appearance; quarrying fractures were feathery and discontinuous, whereas fractures related

to faulting were planar, continuous and were often covered in a thin layer of mineralisation. Flow band measurements (width, orientation, lateral extent) were collected every 2 m at the base of the quarry face and, where possible, at the top. Measurements of both limbs of folds in flow bands ensured that measurements in folded areas were representative. A degree of 'field confidence' was also assigned during fieldwork to the measurements of true dip and strike of flow bands, and only 'high field confidence' flow bands were included in maps in Chapter 4. This resulted in over 300 flow band measurements at Ngongotaha.

At Ruawahia, the faces exposed inside the 1886AD fissure are extremely steep, and so only measurements could be made at the base of the fissure. To counter this, mapping of Ruawahia included outcrops along the top and edge of the NW flow lobe resulting in mapping of a large area of the dome surface. Here, aerial photos were used to scout areas of outcrops, which were then mapped using GPS, and flow bands were recorded every 2m (where outcrop was accessible). Orientated samples were collected from areas of weak flow banding; a flow band orientation could then be gained through thin section analysis based on orientations of flattened vesicles. Additional samples were collected from Ruawahia-sourced block and ash flow deposits to the south (Nairn et al. 2001). These block and ash flows contain a large variety of fresh, glassy clasts with a range in density that represents the core to carapace facies. Blocks that are most similar to core facies density and textures were used in Chapter 3, as in situ dome core lavas were often devitrified and affected by the 1886AD Tarawera eruption.

Preamble

In Chapter 1, I explore the literature on bubble growth, coalescence and outgassing. Upon ascent, volatiles in magma exsolve and bubbles grow, coalescing into a network that controls degassing pathways, and ultimately whether a magma will fragment, forming an explosive eruption, or extrude as a bubbly lava. The literature has concentrated on bubble growth processes and there are few studies concerning the nature of bubble collapse inside lava domes. Here, I present the results and discussion of compaction experiments on cores of lava dome material. The experiments model the effect of the overburden of a lava dome, and how this compacts the porous network; leading to a dense lava dome core and/or shutting off gas escape pathways and leading to explosive fragmentation of the dome. All porosity measurements given in this chapter are connected porosity, unless otherwise stated, while all crystallinity measurements are dense rock equivalent (DRE) of phenocryst stages only.

I aim to submit this chapter to Earth and Planetary Science Letters for publication.

Chapter 3:

Porous network evolution in a compacting pumiceous lava dome

The presence of gas in magma drives volcanic eruptions and the ability for magma to degas controls the likelihood of explosive events. The porous network in a lava dome reflects the evolution of bubble growth and compaction, as well as crack propagation and healing. Lava dome eruptions undergo cycles of degassing, quiescence and explosions that indicate permeability cycling. Part of this cycle is driven by the overburden of the dome and continued magma ascent which compact the porous network and shut off permeable degassing pathways. Here, I investigate the mechanics of this model.

Uniaxial deformation (at 900°C and 3 MPa of constant applied stress) experiments were performed on samples from lava domes in the Taupo Volcanic Zone; A lava sample from Ngongotaha dome near Rotorua which is highly vesicular and crystal-poor (~58 % connected porosity) and two lava samples from Ruawahia dome, Tarawera dome complex; a one highly vesicular and crystal-rich (~50 % connected porosity), and a second moderately vesicular and crystal-rich (~24 % connected porosity). The evolution of the porous network was systematically quantified via X-ray computed tomography, He-pycnometry and gas permeability. Porosity measurements every 10 % strain increments evidence the progressive densification of the foam, whilst permeability fluctuations reveal interplays between an increased isolation of compacting pores and crack propagation. Our results show that constant stress deformation is characterised

by a non-linear decrease in strain rate. The rate of compaction is controlled by the viscosity of the melt and our experiments define the relative importance of crystals and bubbles. Crystal-poor, high vesicularity lavas compacted at relatively high rates, with limited lateral barrelling and the formation of long cracks during the initial, high strain rate portion of compaction. Crystal-rich lavas compact slower; fractures favourably nucleate in the crystal phase and only propagate macroscopically in the later stage of compaction, alongside visible barrelling of the sample. Such contrasting crack development helps explain the contrasting permeability pathways, though similar overall permeability, of the compacted crystal-poor and crystal-rich samples.

The findings show that in absence of confining pressure, compression of a pumiceous lava dome may not form a dense, impermeable plug. Instead, crack development works against porous network closure, allowing compacting lava to degas. Crystals also drastically increase viscosity and negate any influence of porosity shown after only low strain. This interplay between porosity closure and crack propagation is an important consideration to make when assessing the vulnerability of a lava dome to undergo a catastrophic explosive failure.

3.1 Introduction

The eruption of lava domes involves a complex interplay between deformation (Okumura et al. 2009; Avaré & Whittington 2012) crystallisation (Sparks et al. 2000; Caricchi et al. 2007; Lavallée et al. 2007; Cordonnier et al. 2009), bubble nucleation, growth, coalescence and outgassing (von Aulock et al. in review), and crack propagation and healing (Tuffen et al. 2003; Castro et al. 2012b). These processes create and destroy permeable degassing pathways that ultimately control the explosivity and stability of the dome (Klug & Cashman 1996; Rust & Cashman 2004; Mueller et al. 2005; Takeuchi et al. 2005; Mueller et al. 2008; Nakamura et al. 2008; Takeuchi et al. 2008; Wright et al. 2009). Lava domes are generally the result of the extrusion of high-viscosity permeable magmas (Fink et al. 1992; Matthews et al. 1997; Yoshimura & Nakamura 2008), which range from crystal-poor to crystal-rich and of rhyolitic to andesitic composition. The growth of a lava dome can be endogenous, occurring through inflation of the dome carapace, or exogenous, occurring through a series of extrusions of individual lava lobes and spines (Nakada et al. 1999). Structural analysis of endogenous lava domes have revealed that they commonly have a vesicular carapace surrounding a denser, stratified interior (Fink et al. 1992; see Chapter 4). It has been postulated that stratification of the volatiles in the magma chamber and subsequent vesiculation contributes to the resultant dome stratifications (Fink 1983). An alternative hypothesis is that porosity stratification in lava domes results from progressive foam collapse in the shallow conduit and in the dome itself (Eichelberger et al. 1986; Fink et al. 1992). In exogenous lava domes, this stratification is generally not observed (Nakada et al. 1999; Watts et al. 2002a; Vallance et al. 2008; see Chapter 4). Instead, internal variation in porosity appears associated with strain localisation induced by the emplacement of individual lobes and spines (Wright & Weinberg 2009; Holland et al. 2011; Lavallée et al. 2012; Kendrick et al. 2013; Lavallée et al. 2013).

The nature of the permeable network inside a dome controls the efficiency of degassing, and thus the amount of remaining gas that charges the internal bubble pressure. If the gas pressure exceeds the relaxation of the surrounding magma, failure will ensue (Mueller et al. 2008). But importantly to this scenario, the amount and distribution of the gas overpressure inside the dome will dictate the severity of fragmentation and whether the dome rock will simply fracture and form a network to allow gas escape or whether it will be completely consumed by an explosive eruption (Matthews et al. 1997; Herd et al. 2005; Mueller et al. 2005; Loughlin et al. 2010). Thus it is crucial to consider the permeability of dome structures on microscopic and macroscopic scales.

Microscopically, permeability in lava domes is controlled by the evolution of bubbles (size, anisotropy, connectivity) and microcracks (Mueller et al. 2005; Wright et al. 2006; Bouvet de Maisonneuve et al. 2009; Yokoyama & Takeuchi 2009; Nara et al. 2011; von Aulock et al. 2013) and the ability of bubbles and cracks to nucleate (Sparks 1978; Proussevitch & Sahagian 1996), grow and propagate (Lovejoy et al. 2004; Castro et al. 2012a; Cashman & Sparks 2013), coalesce (Klug & Cashman 1996; Takeuchi et al. 2008; Okumura et al. 2009; Laumonier et al. 2011) or heal (Tuffen et al. 2003; Cabrera et al. 2011; Castro et al. 2012b). Shear zones, flow bands, rupturing and fragmentation events may locally accentuate the connectivity of the bubbles and cracks, thus favouring an anisotropic permeable network (Smith et al. 2001; Okumura et al. 2009; Laumonier et al. 2011; Avard & Whittington 2012; Castro et al. 2012b; Lavallée et al. 2013). Macroscopically, large fracture zones (caused by recurring gas and ash explosions or sustained shear) or facies boundaries (e.g. fault, breccia or shear zones) form extensive pathways that feed gas and ash explosions and bleed large regions of the dome by inducing relatively deep, high-pressure gradients (Johnson et al. 2008; Sahetapy-Engel & Harris 2008; Schipper et al. 2013).

Although crucial to the understanding of dome eruptions, the permeability relationships between the micro- and macroscopic scale bubbles and cracks remains elusive.

Crack propagation and coalescence are efficient mechanisms to increase permeability. In crystal-poor liquids, cracking takes place across the glass transition if the strain rate exceeds the relaxation rate of the liquid structure (Tuffen et al. 2003), which gets more sluggish during cooling (Dingwell 1996). Such phenomena commonly occur in high strain rate regions of feeding conduits (Tuffen et al. 2003; Cabrera et al. 2011). In crystal-rich dome lavas, cracks nucleate in crystals (Lavallée et al. 2007; Cordonnier et al. 2009; Kendrick et al. 2013) as they accumulate high stresses (Deubelbeiss et al. 2011). Fracture propagation between the crystals is controlled by the applied strain rate and becomes increasingly localised (and aligns with the principal stress vector) with an increased applied stress (Lavallée et al. 2013).

Bubble outgassing, compaction and healing are efficient mechanisms to reduce permeability. Internal bubble pressure reduction and contact between fracture surfaces may induce healing via structural relaxation (Tuffen et al. 2003; Cabrera et al. 2011; Castro et al. 2012b). The efficiency of healing may be affected by the presence of fragments in cracks (e.g., tuffisites), which depends on the bubble and crystal content, the diffusion timescale and applied stress (Tuffen et al. 2003; Quane & Russell 2005; Kolzenburg et al. 2012). Quane and co-authors (2005; 2009) demonstrated that during compaction, densification of a porous foam shares a non-linear relationship with its rheological response. Capitalising on this observation, I seek to evaluate the compactional response of foams with different bubble and crystal fractions on the evolution of the permeable porous network.

3.2 Lava dome architecture

The internal structures at Ngongotaha dome, Rotorua caldera, and Ruawahia dome, Tarawera dome complex, in the TVZ were examined and mapped. Both lava domes exhibit intricate, but mechanically informative internal structures (Chapter 4).

Ngongotaha dome (Figure 1.4) is a c. 4 km diameter rhyolitic lava dome consisting of 6 individual flow lobes erupted ca. 200 ka, following the Mamaku eruptions that produced Rotorua caldera (Chapter 5). The outer carapace of Ngongotaha dome consists of a brecciated talus covering a finely vesicular pumiceous lithology. The pumiceous carapace of Ngongotaha has low crystallinity (3 – 5 %), elongate bubbles (maximum 58 %) and minor amounts of spherulitic crystallisation and devitrification (thought to be post eruptive) compared to the rest of the dome. The core of Ngongotaha, exposed by quarrying, in contrast shows a low porosity (~10 %) and complexly flow-banded, devitrified obsidian (Chapter 4) with pristine and near vertical, dense structures that I propose to be “squeeze up” dykes. Generally flow bands are steep in the core of the dome and shallow near the flanks of the dome. The orientation of flow bands suggests that the dome extruded from a linear fissure in a fan-like style to produce a lobe elongate parallel to the fissure orientation (Chapter 4 and 5).

Ruawahia dome is a c. 1.5 km diameter rhyolitic lava dome formed during the 1314AD Kaharoa eruption at Tarawera dome complex, OCC (Cole 1970b; Nairn et al. 2001; Nairn et al. 2004). The lava dome rocks have a high phenocryst content (~65 % DRE) and overall restricted variation in porosity from carapace to core. The core of Ruawahia has a moderate connected porosity (22 – 26 %) and is partially devitrified (containing post eruptive spherulites) with stretched bubbles indicating steeply dipping flow units (Chapter 4). Generally, the carapace has a slightly higher porosity (25 – 35 %) compared to the core, and is weakly flow banded with little to no glass

devitrification. However, locally, the carapace of Ruawahia is more porous (~55 %) containing well rounded bubbles, indicative of bubble growth with little post-vesiculation strain. The blocks in block-and-ash flows generated during dome extrusion (Nairn et al. 2001) show a larger variation in vesicularity, ranging from dense obsidian (5 – 10 % porosity) to inflated breadcrust bombs (64 %) and generally contain fewer spherulites and devitrified glass when compared to the dome core.

3.3 Samples and methods

Three natural samples were selected to assess the evolution in permeability of dome lavas when subjected to compression (Figure 3.1): 1) NP; a finely vesicular (50 – 58 %), crystal-poor (~3 % DRE) pumice from the breccia of the dome carapace at Ngongotaha (assumed to have quenched rapidly to preserve the bubble textures at extrusion), with dominantly highly elongated small bubbles (less than 75 μm to 500 μm) and less common areas of coarse irregular shaped bubbles (from 0.5mm to 5mm). 2) TP; a vesicular (44 – 52%), crystal-rich (~65% DRE) rock with a range of bubble sizes (<60 μm – 2 mm), from a block-and-ash flow generated from Ruawahia dome (assumed to represent eruptive porosity without foam collapse or in situ vesiculation overprint). 3) TD; a moderately vesicular (23 – 26 %), crystal-rich (~65 % DRE) dome rock with few small bubbles (<5 mm) in a dense glass with highly elongated bubbles (~150 μm), from the same block-and-ash flow generated from Ruawahia dome as TP. These samples were chosen because they have similar melt viscosities; NP of 2.63×10^9 Pa·s and TP and TD of 3.09×10^8 Pa·s, using geochemistry from Richnow (1999) and Nairn et al. (2004), and pre-experiment water contents from Kennedy et al. (2010) and von Aulock et al. (2013) according to input into the GRD viscosity model of Giordano et al. (2008). Therefore, the behaviour of NP can be contrasted with TP to compare a low crystallinity sample with a high crystallinity sample and the behaviour of TP can

be contrasted with TD to evaluate the impact of a higher vesicularity. Samples from the vesicular carapace at both domes were used as they are the closest representation of the vesicularity of the initial extrusions at both domes. Post-extrusion vesiculation may have occurred alongside some bubble collapse, but not to the same degree as that in the centre of the dome.

The rocks were cored into several cylindrical samples (25 mm in diameter and 50 mm in length) perpendicular to bubble elongation. The cores were heated to 900°C; once thermally equilibrated, the cores were subjected to a constant applied, compressive stress of ~3 MPa using a uniaxial deformation press at Ludwig-Maximilians University (LMU) (see Hess et al. 2007).

Syn-deformation acoustic emissions (AE) were monitored (at 5 MHz) via two wideband AE sensors (optimised between 100 and 1000 kHz). The samples were deformed to comparable strain increments (i.e., 10, 20, 30, 40, 50 or 60 %) to systematically evaluate the consequence of strain on the permeable porous network (Figure 3.1). Porosity measurements (using He-pycnometry in an Accupyc 1330 from Micrometrics) were performed on each sample both before and after deformation (see Chapter 2 for details). For samples with selected strain increments (0, 20 and 60 %), X-ray computed tomographic imaging (using high power X-ray tube and a drx-250rt detector system with a pixel/voxel size resolution of 14.78 μm at LMU; see Chapter 2) of the porous network was utilised. Following these non-destructive, post-deformation analyses, the samples were re-cored into two smaller cores of 10 mm diameter, 8 to 25 mm in length, axial and radial to the initial sample geometry to assess the anisotropy development of the permeable network. Permeability measurements were performed with compressed air in a gas permeameter assembled at the University of Canterbury using the designs developed by Takeuchi et al., (2008) using pressure gradients of between 7×10^{-3} to $3 \times$

10^{-1} MPa (see Chapter 2). Additional tomography was then performed on the Australian synchrotron using the 'Ruby' detector (see Chapter 2) at a pixel/voxel size resolution of $6.1 \mu\text{m}$, on 10 % and 60 % strain samples to assess bubble shape change and crack initiation.

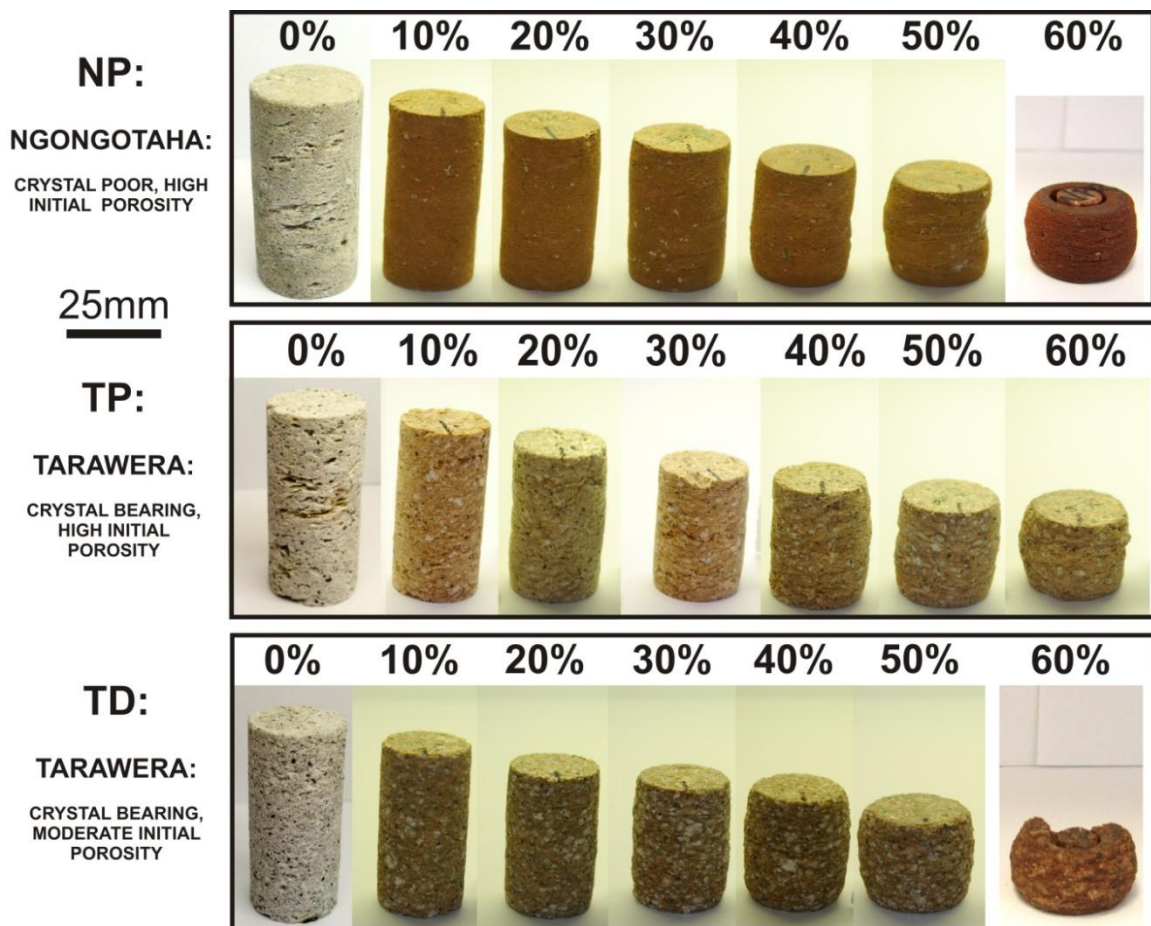


Figure 3.1: Diagram of cores at each axial strain increment. 60 % axial strain on samples NP and TD have been re-cored before photograph.

Our natural samples show a range in initial porosity (NP = 50 - 58 %; TP = 44 - 52 %; TD = 23 - 26 %) which complicates direct comparison of final connected porosities. I use the relationship between the change in porosity to the strain achieved in each experiment in order to calculate the expected amount of porosity loss at any strain, regardless of initial porosity (see Chapter 2). To take into account the variability in porosity, I use this relationship to calculate porosity using the maximum and minimum porosity values for each sample, as well as the average porosity value, and compare these empirical relationships to measured porosity values.

3.4 Results

3.4.1 Compaction mechanics

Uniaxial compression induced a distinct mechanical response for all three samples dependent on strain rate, porosity and crystallinity (Figures 3.2 and 3.3). Constant loading produced an initially, relatively high strain rate of $\sim 10^{-4} \text{ s}^{-1}$, which non-linearly decreased down to 10^{-6} s^{-1} at 60 % axial strain. The denser sample TD compacted at a slower rate compared to similarly crystalline but higher porosity TP. In contrast, TP compacted more slowly than the less crystalline but similarly porous NP (despite a higher melt viscosity). Deformation was accompanied by a minor amount of AE generated by cracking events (Figure 3.2). The energy released by acoustic events appears to dominate the initial portion of deformation (from 0 to 20 % strain), when the strain rate is highest. The AE count is highest in TP (Figure 3.2B) compared to TD (Figure 3.2C) or NP (Figure 3.2A) indicating that both high strain rates and high crystallinity contributes to high AE counts.

Barrelling (increase in radial strain) of the samples is strongly dependant on porosity and, to a lesser degree, crystal content (Figure 3.1 and 3.3B). I define the onset of barrelling as when the

ratio of width change to length change after compression increases past 0.05 (see Figure 3.3B). For NP and TP the onset of barrelling occurs at porosities of 40 – 43 % between 10 and 20 % strain, the denser sample TD is significantly barrelled at 10% strain due to the lower initial porosity of ~24 % (Figure 3.3B).

In summary, our experiments at constant stress show strain rate is a product of viscosity and hence affected by both the porosity and crystallinity of the magma. Barrelling occurs when strain can no longer be accommodated through porosity loss; in crystal-rich samples this starts at ~40 % porosity, and accommodates all strain at ~20 % porosity. A summary of strain, time, porosity and permeability of all samples is shown in Table 3.1.

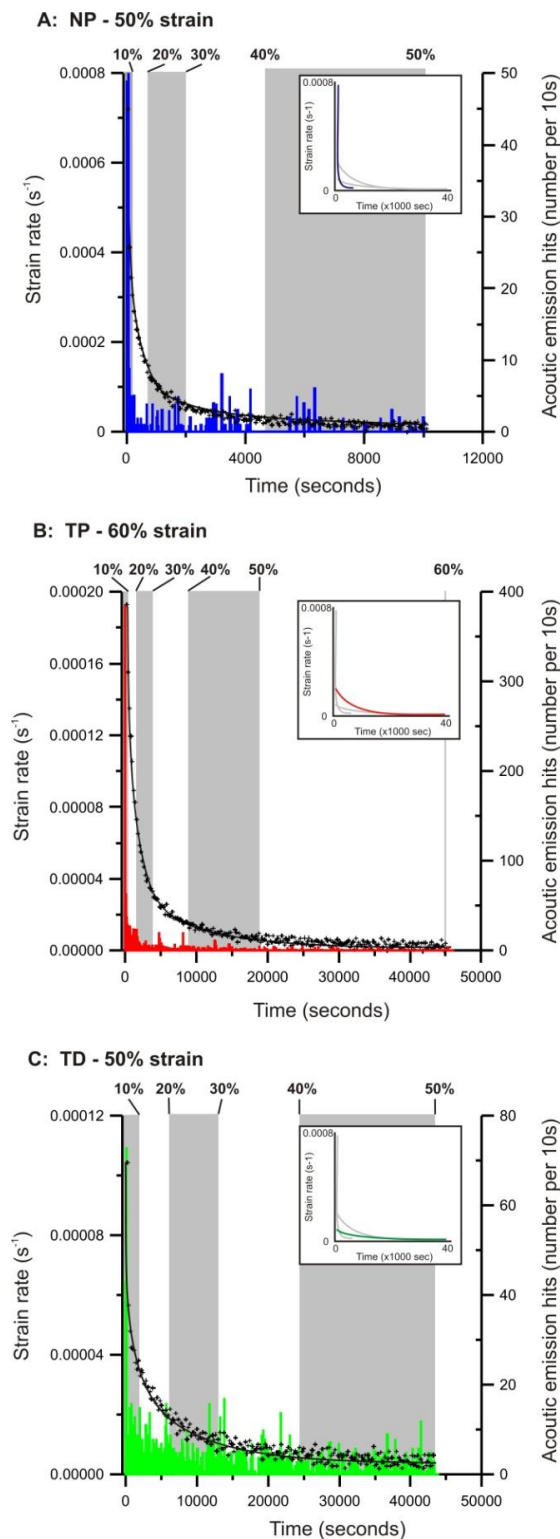


Figure 3.2: Strain rate (black dots and line – best fit trendline) and AE emission (coloured bars) during 50 % (NP and TD) or 60 % (TP) axial strain deformation. Grey boxes indicate when each strain increment (at top of graph) is reached. Inset graph shows comparison of strain rates with that of other samples.

Sample ID	Strain	Starting Porosity (%)	Ending Porosity (%)	Change in porosity (%)	Permeability k1 A (log m2)	Permeability k2 A (log m2)	Permeability k1 B (log m2)	Permeability k2 B (log m2)	Time
NP									
3	0.0	57.95	54.90	-3.05	-12.72	n/a	-13.32	n/a	N/A
1	9.8	56.18	50.53	-5.65	-14.87	n/a	-14.66	-9.73	275
2	19.7	49.97	38.03	-11.94	NO CORE	NO CORE	NO CORE	NO CORE	1724
10*	20.0	53.85	43.37	-10.48	-9.24	-13.38	-13.80	-9.19	N/A
4	27.7	52.78	39.29	-13.49	-9.48	-13.33	-13.46	-7.75	1815
11	39.9	52.13	30.13	-22.00	-11.56	-17.51	NO CORE	NO CORE	8353
12	50.0	57.58	27.88	-29.70	-11.21	-17.56	NO CORE	NO CORE	10140
2'	60.2	49.97	14.62	-35.35	NONE	NONE	NO CORE	NO CORE	23818
TP									
7	0.0	50.64	4.52	-3.12	-13.90	-9.16	-13.23	-8.68	N/A
12	10.2	44.14	41.10	-3.04	-16.44	-13.40	-15.10	-11.02	1030
2	20.0	45.37	38.42	-6.95	NO CORE	NO CORE	NO CORE	NO CORE	2741
5	24.1	49.05	38.88	-10.17	-13.01	-10.00	NO CORE	n/a	2217
14	29.9	44.45	31.22	-13.23	-17.62	-14.00	-16.42	-13.18	8762
10	39.8	45.74	27.97	-17.00	-15.89	-13.15	-16.08	n/a	12446
9	49.1	45.26	22.27	-22.99	-17.62	-14.00	NO CORE	NO CORE	29055
2'	62.3	52.27	23.96	-28.31	-15.59	-13.10	NO CORE	NO CORE	45300
TD									
4	0.0	24.46	24.17	-0.29	-15.54	-11.74	-14.02	-9.53	N/A
1	9.9	24.39	22.75	-1.64	-15.17	-11.20	-13.67	-9.88	2384
3	19.6	25.58	20.88	-4.70	-14.68	-11.35	-15.42	-10.46	5493
2	20.0	22.69	20.37	-2.32	NO CORE	NO CORE	NO CORE	NO CORE	6017
5	30.0	25.37	21.10	-4.27	-15.87	-13.24	-14.70	-10.26	14806
7	39.7	23.54	17.78	-5.76	-16.61	-12.89	-15.57	n/a	22795
9	49.9	23.44	18.16	-0.53	NO CORE	NO CORE	NO CORE	NO CORE	43301
11	58.0	24.51	18.83	-5.68	-16.38	-13.14	-14.70	-11.49	174095

Table 3.1: Summary table of strain, porosity, permeability and time of all experiments. 'NO CORE' means that no core was left over or was lost, and 'n/a' means that permeability value could not be gained.

3.4.2. Evolution of the porous network

Sample examination through tomography and pycnometry provides us with a physical basis for the mechanical response monitored. Our empirically calculated porosity values (dashed and solid coloured lines in Figure 3.4) match well to measured porosity (darker solid circles in Figure 3.4), suggesting that initial variations in porosity of undeformed samples do not greatly affect the degree of bubble collapse as the amount of porosity reduction at each strain increment is not related to the initial starting porosity (see Chapter 2). Porosity analysis shows that compression resulted in an porosity reduction which began immediately (i.e. at 10 % strain, Figure 3.4). Samples NP and TP both had an increasing rate of porosity reduction with strain, such that the largest reduction of porosity occurs between 50 and 60 % strain (Figure 3.3A) or at the lowest connected porosity (Figure 3.3C). Conversely, low porosity (and crystal bearing - TD) showed a decrease in the amount of porosity reduction to zero (i.e. a maximum porosity reduction threshold had been reached) between 50 and 60 % strain (Figure 3.3A). All porosity loss in TD occurred up to this point and subsequent compression lead to a slight increase in porosity (Figure 3.3A). The connected porosity value of TP at 60 % strain is similar to undeformed TD porosity (Figure 3.4); the rate of porosity reduction in TP may have reached a peak and further compression may lead to a transition to TD behaviour, as suggested by the near continuous trend in barrelling behaviour between TP and TD in Figure 3.3B. However, further compression of TP past 60% strain would be needed to confirm this. In crystal-rich samples, porosity did not decrease below ~20 % (Figure 3.3C), while crystal-poor samples at 60 % strain had a low porosity of ~14 % (Figure 3.3C). This low value may have been due to a lower initial porosity in this sample of 50% (compared to average of ~54%); our empirically calculated porosity values indicate that average porosity will reduce to at least ~17% (Figure 3.4A). This

calculated value of ~17% is used in Figure 3.3 to represent the calculated connected porosity of NP at 60% strain.

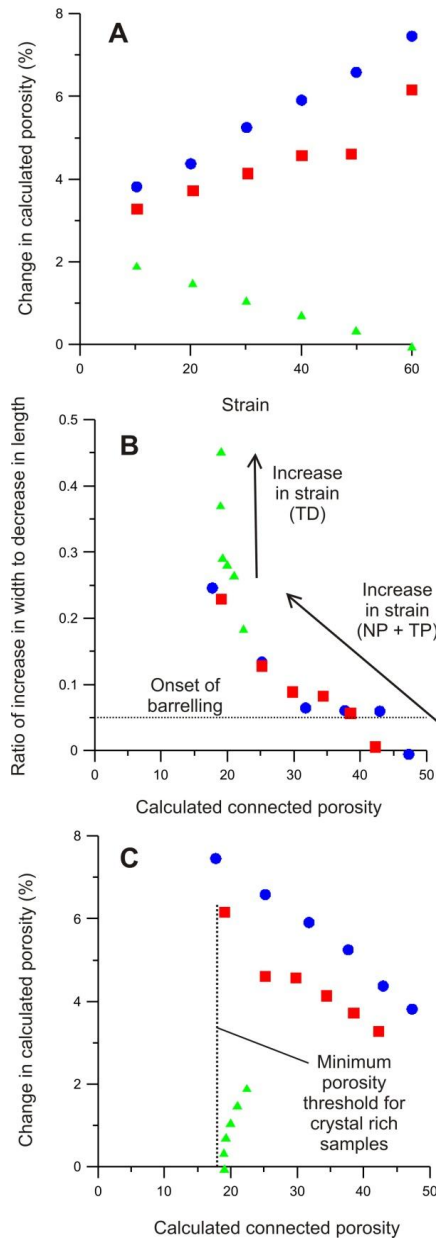


Figure 3.3: Graphs of changes in porosity and barrelling. A: Graph showing rate of porosity change against strain. B: Graph showing onset of barrelling at a ratio of width increase to length decrease of 0.05. C: Graph showing change in porosity against final calculated porosity, showing minimum porosity threshold for crystal bearing samples of ~20%. Blue circles = NP, Red squares = TP and Green triangles = TD.

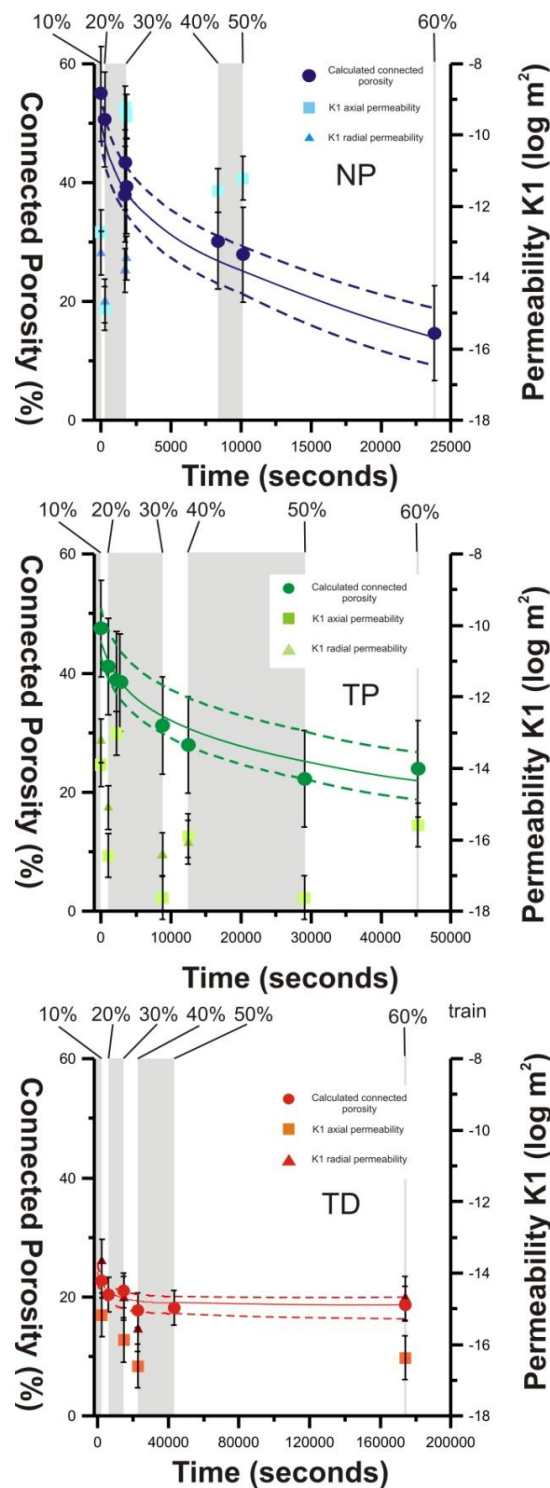


Figure 3.4: Porosity and permeability evolution with time with samples NP (blue), TP (red) and TD (green). Solid and dashed lines represent average and maximum/minimum calculated porosity curves respectively. Circles indicate porosity measurements, squares are axial permeability k_1 , triangles are radial (along flow elongation) permeability k_1 measurements.

3.4.3 Cracking of samples

Microscopic analysis shows that brittle and viscous components to strain are accommodated differently in each sample due to the relative proportion of liquid, crystals and bubble phases and initial compaction strain rate (Figure 3.5). In absence of crystals (NP), cracks propagate between bubbles, primarily parallel to the main compressive stress. Large cracks develop (~0.06 mm wide; Figure 3.5) across half the length of the NP sample at 20 % strain. These cracks propagated further and widened (~0.12 mm) with increased strain (60 %; Figure 3.5). The response of the porous network to compression differed when the samples were crystal rich.

In crystal bearing melts, cracking began in the crystals (Figure 3.5) and was limited by crystal size and number density, with cracks of 0.05 mm wide appearing at 20 % strain (Figure 3.5), and propagating to 0.1 mm wide at 60 % strain (Figure 3.5). Large, jagged cracks (0.5mm wide) in the glass were also observed at 60 % strain in sample TD (Figure 3.5), opening parallel to radial strain and related to the large degree of barrelling in TD (Figure 3.3B). Hairline cracks are observed in crystals in TP and TD pre-deformation; these cracks widen parallel to radial strain and propagate parallel to axial strain, and are therefore most obvious in 'XY' orientation tomography scans in all samples (Figure 3.5 and 3.6).

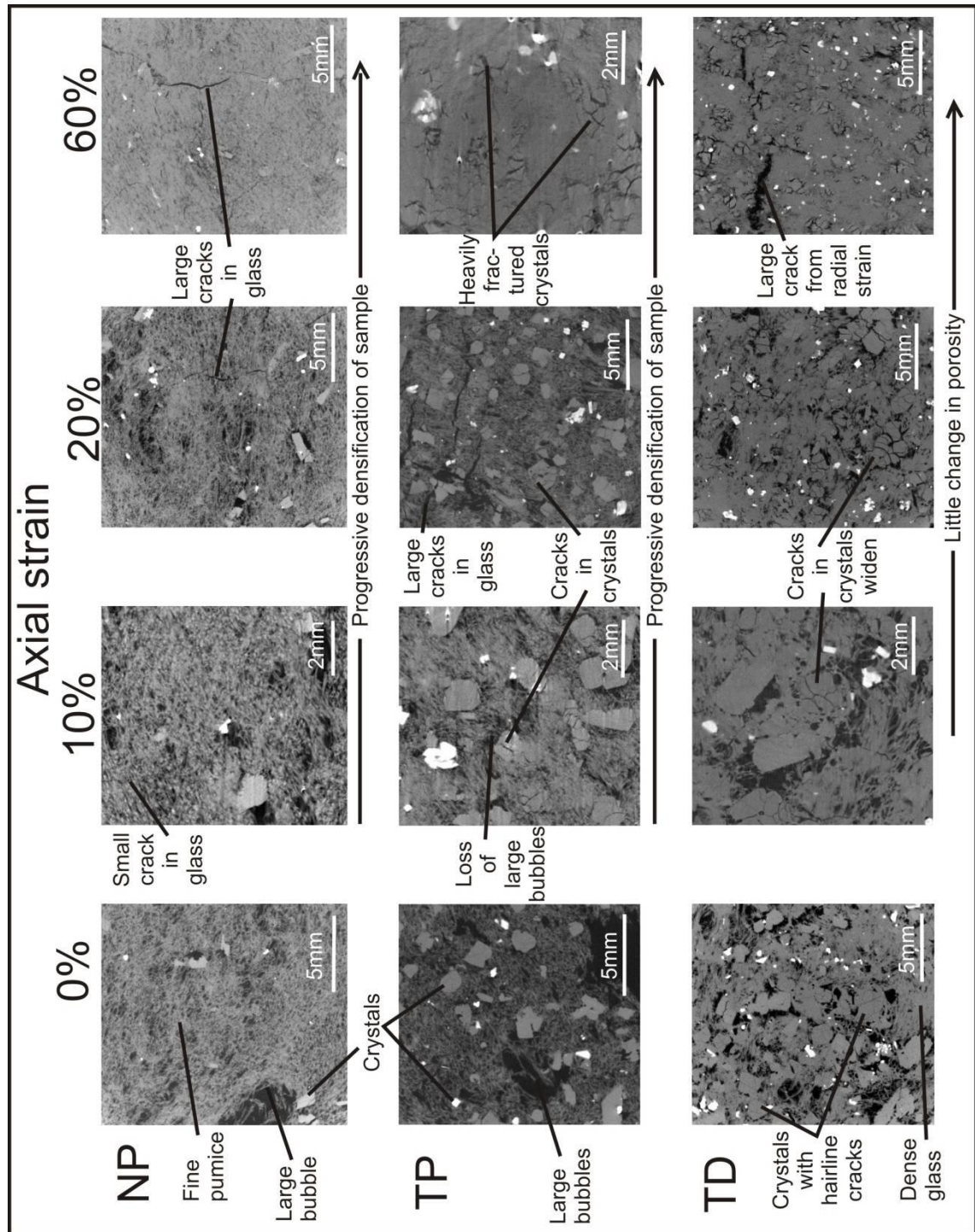


Figure 3.5: Tomography images (in X-Y dimensions) from undeformed (0%), 10%, 20% and 60% strain samples from NP, TP and TD. Features described in text are labelled. Primary stress direction is into the page (i.e. Z dimension).

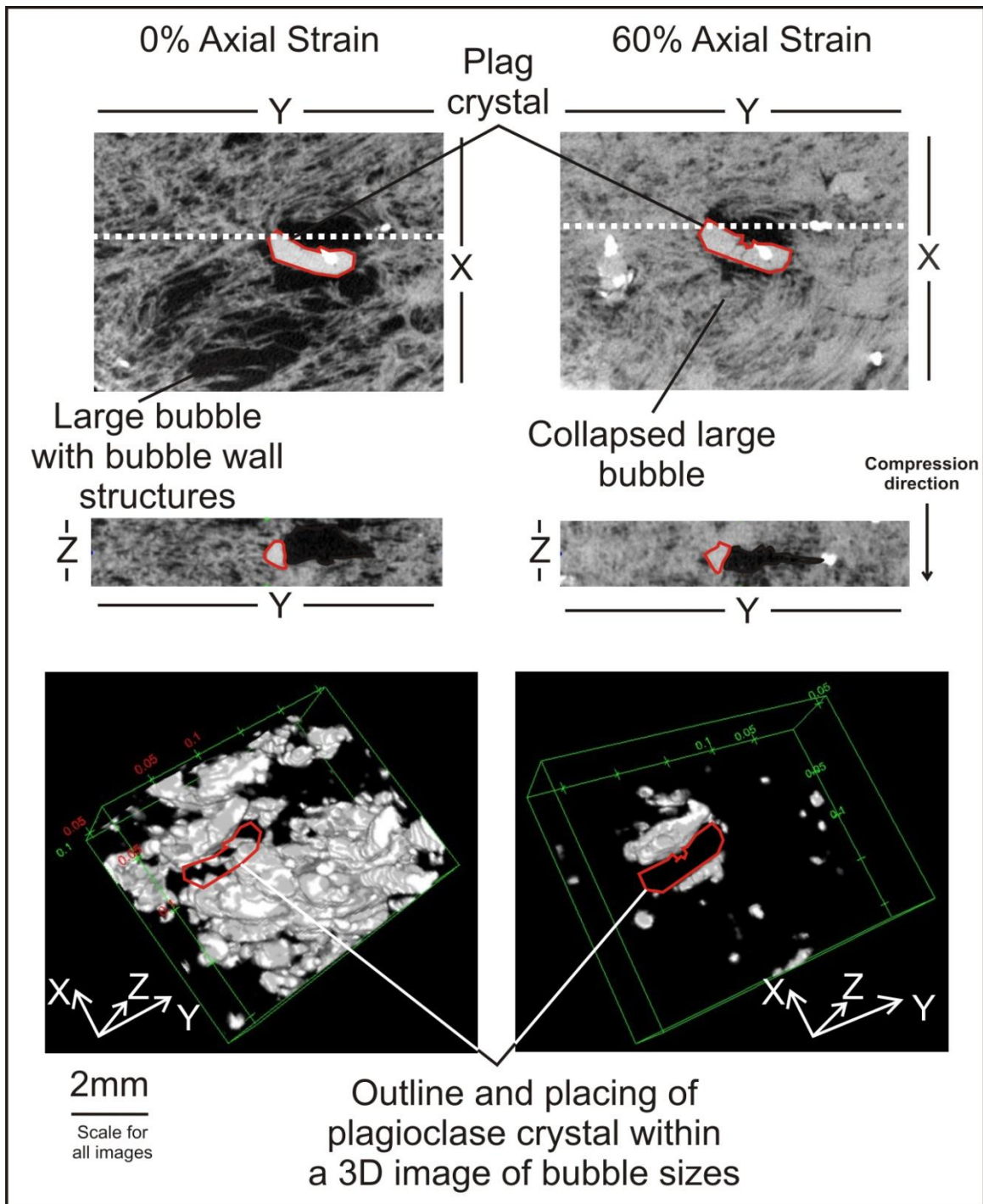


Figure 3.6: Bubble shape and size changes in NP between 0 % and 60 % axial strain. XY (perpendicular to compression direction) and YZ (parallel to compression direction slices shown (YZ slices correspond to dashed white line)). Bottom: 3D image of bubbles above 30 μm with position of plagioclase crystal shown for reference.

3.4.4 Viscous deformation in samples

In all samples bubbles changed shape, with large bubbles collapsing quickly in NP and TP between 20 and 60 % axial strain (Figure 3.5). Small bubbles remained after high (60%) strain in all samples. Analysis of a coalesced bubble cluster in NP between 0 and 60 % strain shows a drastic reduction in number of <30 μm bubbles and bubble size (Figure 3.6). Large vesicles are quickly compacted and are infilled with bubble wall shards and smaller bubbles, reducing their size and overall porosity of the sample (Figure 3.4 and 3.5). In the vicinity of crystals, a pressure shadow forms which protects bubbles from total compression (Figure 3.6). Bubbles, even those protected by crystals, are squashed in a direction parallel to the principle stress direction, while elongation in perpendicular dimensions can increase due to barrelling; however this is only observed when there are large amounts of barrelling.

3.4.5. Permeability evolution

The permeability values measured orthogonally for each sample (k_1 radial permeability and axial permeability) constrain the permeable network anisotropy associated with bubble compaction and crack formation. Permeability measurements from all pre-deformation samples show a similar value for both axial and radial permeability (within ~ 1 log unit). In NP, axial permeability decreased slightly before drastically increasing at 20 % and 30 % strain (Figure 3.4). At 60 % strain, measurable axial permeability of NP is zero. Analysis of the tomography from the NP 60 % strain sample used for gas permeability shows no large cracks, unlike in the low strain samples. Large cracks remain in the larger sample, however (Figure 3.5). Radial permeability remained relatively constant between 0 and 20 % strain.

In crystal-rich samples, both radial and axial permeability showed an overall decrease from 0 – 60 % strain. This decrease was not steady, however, with fluctuations in the axial permeability. Both TD and TP appeared to reach a plateau in permeability at around 30 to 40 % strain (Figure 3.4), decreasing to around 10^{-17} m²; a drop of 2 log units for (TD) and 4 log units for (TP) from the permeability of undeformed samples.

In summary, crystal-poor pumiceous NP showed large increases in permeability during compaction at medium to low strains and a large reduction in permeability at high strains. Crystal-rich pumiceous TP showed a large but variable decrease in permeability during compaction, and crystal-rich dense TD showed a smaller, steady decrease in permeability during compaction.

3.5 Interpretation

The contrasting physical behaviour of the samples can be attributed to characteristic styles of deformation associated with the changing strain rate of the experiments, crack formation and bubble collapse.

The tomography (Figure 3.5) shows that crack formation was greatest during maximum strain rates between 0 and 20 % strain. In NP, cracks formed that were axial parallel and long (half of the length of the sample), and as a result induced large changes in axial permeability but small changes in radial permeability or open porosity (Figure 3.4). The lack of cracks in the core of NP at 60 % strain led to zero measurable gas permeability, as the connected bubble content was too low (~14 %) to form a network. This zero measurable permeability was due to the small core size used in the permeability measurements, however; large cracks were still noted in tomography from the large core size and therefore a larger core size would likely have a

measurable permeability. In crystal-rich samples, cracks focussed in the crystals and were too short (maximum of 1 mm) to induce large changes in axial or radial permeability or porosity. The presence of these cracks in the tomographic images of low strain samples is supported by the highest acoustic emissions also occurring between 0 – 10 % strain, suggesting the fractures were formed very quickly, then widened and propagated in order to have an effect on permeability (Figure 3.2).

Porosity measurements show that bubble compaction occurs throughout the experiments and controls connected porosity reduction (Figure 3.4). At low strain, bubble compaction and porosity reduction is accommodated by axial strain with little radial strain (Figures 3.3B and 3.4) and bubbles reduce in axial dimensions but radial dimensions stay relatively constant (Figure 3.5 and 3.6). Porosity is reduced proportionally to strain down to 30 % porosity. Below 30 % porosity in all samples, barrelling becomes significant. Cracks widen and propagate, and bubbles begin to be stretched, parallel to radial strain (Figure 3.5). The amount of barrelling is greater in crystal-rich samples (Figures 3.1 and 3.3B). This transition to barrelling is also coincident with a decrease in strain rate (Figure 3.2). At the low experimental stresses, the average calculated porosity of our samples does not reduce below ~20 % as strain is increased. Measured porosity in the crystal-poor (NP) sample decreases to 14 % at 60 % strain, due to a low initial porosity and the lack of crystals. At high strain NP shows no evidence of a decrease in rate of porosity reduction (Figure 3.3A and C).

In summary, cracks form in the glass at high porosity associated with high strain rates and in the absence of crystals these drastically increase the permeability. Bubble walls viscously deform and reduce porosity and permeability; below 30 % porosity, increasing strain drives barrelling and porosity reduction was limited. In crystal bearing samples, strain was localised within

crystals at high strain rates, but were not long or wide enough to increase permeability. Bubble compaction lead to permeability of 2 to 4 log units lower than undeformed samples.

3.6 Rheological analysis

As the experiments were done under constant stress, the resultant strain change with time recorded as mechanical data can be used to calculate the apparent viscosity. The apparent viscosity of the porous magma was calculated via a modification of the Gent (1960) equation developed for a parallel plate viscometer:

$$\eta = \frac{2\pi Fh^5}{3V\delta h/\delta t(2\pi h^3 + V)} \quad (1)$$

where h is the height (m), F is force applied, and V is the volume of melt (m^3) (see Hess et al. 2007). The volume of the sample during compaction (including the affect of barrelling) is calculated based upon the relationship of measurements of volume with strain, allowing for the Gent equation to be used even at high strain.

All samples show a non-linear increase in the apparent viscosity as a function of strain. The apparent viscosities of all samples increased by approximately 1 order of magnitude up to 25 % strain (Figure 3.7A). In sample TD, the apparent viscosity reaches a strain invariant value at moderate (>10 %) strains, while in TP and NP a gradual increase to a metastable (but differing) value at high strains (>25 %) suggest that the role of both crystals (TD and TP) and bubbles (TP and NP) is important in assessing the rheological evolution in our experiments. To understand the effect of crystals or bubbles, I calculate the relative viscosity (η_r) according to:

$$\eta_r = \eta_a / \eta_o \quad (2)$$

Where η_a is the apparent viscosity and η_o is the melt viscosity as calculated by the GRD model (Giordano et al. 2008) for the sample temperature of the experiment and using previously measured water contents from the same volcanoes (von Aulock et al. in review). At 900°C the melt viscosity η_o of the Ngongotaha interstitial melt is 2.63×10^9 Pa·s, and of the Tarawera interstitial melt is 3.09×10^8 Pa·s (Kennedy et al. 2010). I assume no loss of water during the experiments and little to no viscous heating of the sample in the experiments. However, this is unlikely to be the case, and so it is probable that the viscosity calculations are underestimated.

The results show that the relative viscosity (η_r) of TP and TD are higher than NP, despite a lower melt viscosity (Figure 3.7B). This difference is attributable to the higher crystallinity of TP and TD relative to NP where the presence of more than ~40 % phenocrysts increases the apparent viscosity (Lavallée et al. 2007; Mader et al. 2013). The relative viscosity of NP <5 % strain is below 1 Pa·s, showing that the lack of crystals and high porosity lowers apparent viscosity below the melt viscosity (Figure 3.7B). The relative viscosity sharply increases to 1 at ~5 % strain. TP exhibits a lower relative viscosity to TD and increases to the same as TD past 30% strain, showing that porosity lowers the apparent viscosity within this porosity window (Figure 3.7B). At higher strain, the apparent viscosity of TP overtakes that of TD, suggesting that once barrelling has been initiated, it may lower apparent viscosity by aligning crystals (Lavallée et al. 2007). By comparing the relative viscosity of NP (<1) to TP (>10), I observe the increase in viscosity caused by an increase in crystallinity by ~60 %. By comparing TP to TD I observe the increase in relative viscosity of ~10 – 40 (at low strain) caused by the decrease in porosity of 25 %.

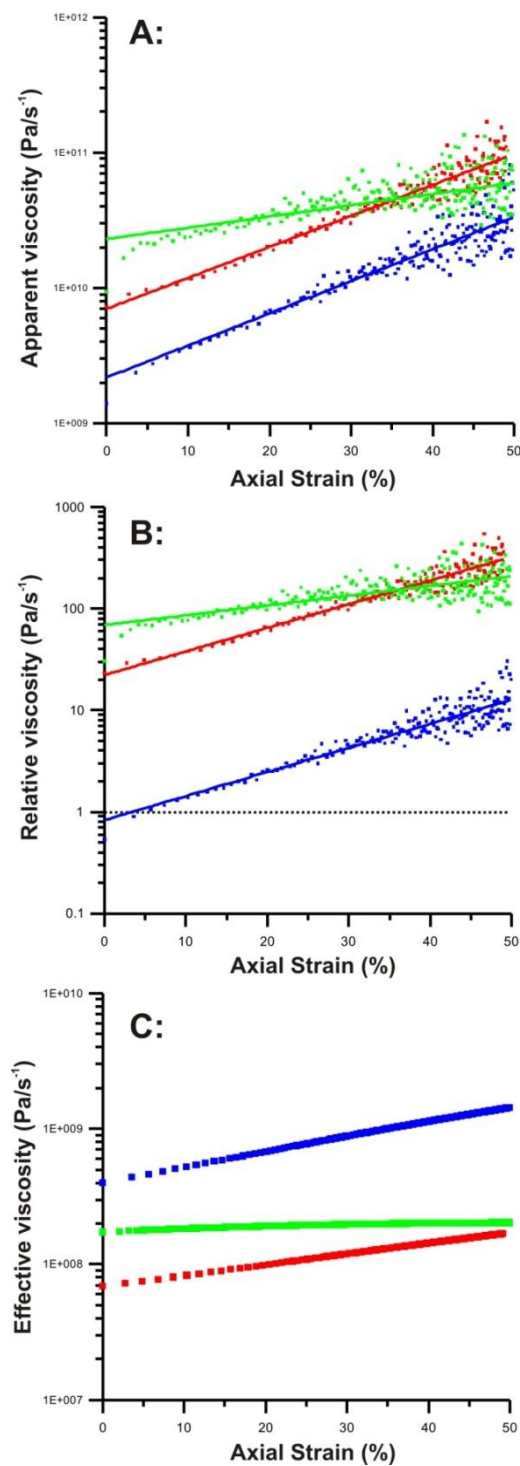


Figure 3.7: Apparent, relative and effective viscosity measurements. In all graphs, NP is blue, TP is red and TD is green. A: Apparent viscosity using equation 1 (Gent 1960). B: Relative viscosity curves. Dashed line at 1 Pa·s relative viscosity represents where apparent viscosity is equal to melt viscosity. C: Effective viscosity using average calculated porosity and melt viscosity, from Quane et al. (2009).

A similar behaviour has been described by Quane and Russell (2005) who attributed the transient effective viscosity (η_ε) to changes in the porosity (Φ) of the foam, according to:

$$\log \eta_\varepsilon = \log \eta_o - \frac{\alpha \Phi}{1 - \Phi} \quad (3)$$

Where α is an empirical adjustable parameter. Equation 3 describes how a decrease in porosity will accompany an increase in effective viscosity, which is similarly observed in our experiments. Our results, using a similar α value to Quane et al. (2009) of 0.78 and using calculated average porosity values, underestimate viscosity by over 1 order of magnitude in TD and TP and less than 1 order of magnitude in NP (Figure 3.7C). The effective viscosity trends of NP and TP are similar (Figure 3.7C), reflecting the similar rate of porosity reduction (Figure 3.3A and 3.4). The effective viscosity of NP is higher than both TP and TD, due to higher melt viscosity of NP and lack of a term for crystallinity in equation 3, but it is closest to the apparent viscosity of NP, calculated with equation 1. In its current form equation 3, therefore, is unsuitable for use for analysing the effective porosity from compression of crystal bearing rocks.

3.7 Discussion

3.7.1 Rheology of porous and crystal bearing magma

The effect of total crystallinity, crystal size, crystal shape, porosity and bubble shape on the rheology of porous or crystal bearing magma is well studied in magma with isolated bubbles or unfractured crystals. However, real magmas frequently contain connected bubbles as well as fractured crystals.

Isolated bubbles that deform and elongate with flow are defined by a high capillary number (ratio of shear strain and bubble size to surface tension of the bubble) and cause a decrease in effective viscosity (Manga et al. 1998; Rust & Manga 2002). Bubbles with a low capillary number will act as rigid bodies, stay spherical and increase the effective viscosity of the melt (Rust & Manga 2002). Under compaction, Quane et al. (2009) showed that sintered ash (melt plus bubbles) deformed at a high strain rate which decreases over the first 10 to 30 % strain. As porosity reduced, the effective viscosity (as calculated by equation 3) increased. Our experiments are similar to those of Quane et al. (2009), showing an initially high strain rate and increase in viscosity as porosity is removed by compaction. However, our viscosity increases more rapidly with strain than predicted using equation 3. Manga and Loewenberg (2001) suggested that porosity up to 50 % volume fraction will decrease the relative viscosity by a factor of less than 3; our results show a increase in relative viscosity of similar magnitudes after 30 % strain (or a reduction in connected porosity of ~15 %), suggesting that even a small number of crystals, and the continually evolving bubble network, have a large effect on the viscosity (as shown by the comparison of relative viscosity in NP to TP).

Few studies include both crystals and bubbles, as the combined effect of both on the rheology is complex. Bagdassarov and Pinkerton (2004) showed that the apparent shear thinning behaviour of foams is dependent on the previous shearing history. Pistone et al. (2012) subjected crystal bearing material (55 to 65 % volume) to shear stress, which caused a shear thinning effect from crystal size reduction and localised shear strain. Crystal-poor magmas (24 %), on the other hand, exhibited shear thickening due to bubble coalescence and effective outgassing. A relative increase in crystallinity, and decrease in porosity, leads to an increase in lava strength which produces localised areas of deformation and resists changes in pressure from the source magma (Smith et al. 2011). Kendrick et al. (2013) showed that, in crystalline, low porosity lavas, strain

hardening dominated at low axial stress (~3 MPa), whereas crack coalescence drives shear thinning at higher stress (12 – 24 MPa) in the same magma. This resulted in no loss, or even a slight increase, in porosity at 30 % strain.

Our crystal-rich samples (TD and TP) show a large increase in viscosity compared to NP (Figure 3.7), while fractures form in crystals at high strain rates (Figure 3.5). However these fractures do not continue to form or coalesce to produce strain weakening behaviour. Instead, bubbles outgas, enabling compaction of bubble walls and leading to melt squeezed laterally, which locally increases the crystal content and develops a crystal/ glass framework. Individual crystals form a pressure shadow that protects nearby bubbles (Figure 3.6) which, combined with fracturing of the crystals, may explain why permeability is not closed completely (Figure 3.4). This framework increases the viscosity, produces lower strain rates and prevents porosity reduction past ~20 %.

3.7.2 Permeability evolution of porous magma

The permeability of a porous magma can control the transition from explosive to effusive eruptions, or vice versa (Mueller et al. 2005). Many authors have experimentally shown that stress, strain rate, strain, melt viscosity, crystallinity and vesicularity affect how bubbles connect or fractures form, as well as the evolution of porosity and permeability.

Here, I compare the effect on porosity and permeability evolution from the compaction experiments. Low stress and moderate strain rate decompression experiments (decompression rates of between 0.05 to 0.002 MPa/s over time spans of between 200 and 6000 seconds) on crystal-poor rhyolite cores of $6.47 \log \text{ Pa}\cdot\text{s}$ (melt viscosity at 900°C) viscosity samples by Takeuchi et al. (2009) produced porous magma with >80 % porosity that showed an increase of nearly 4

log units in k_1 permeability (Figure 3.8). However, this study did not include shear stress alongside bubble growth. High stress and low strain rate (0.01 to 0.029 s⁻¹) rotational shear experiments by Okumura et al. (2009) on crystal-poor rhyolitic melt (77 wt% SiO₂ and 0.5 wt% H₂O at 975°C) showed that permeability increases of nearly 2 orders of magnitude occurred at moderate (33 %) shear strain and a relative small change in porosity, as bubbles connect through shearing (Figure 3.8). Lavallée et al. (2013) showed that crystalline (50 – 60% DRE), low porosity (10 to 30 %) andesitic samples cracked and radial expanded under high uniaxial stress (28.5 to 76 MPa) to produce large increases in porosity (<30 %) and increases in permeability of up to 1 log unit (Figure 3.8). Similar, but lower stress, experiments (2.8 to 24 MPa) by Kendrick et al. (2013) showed cracks forming in similar magmas with small increases in porosity and permeability (Figure 3.8).

Our samples show a complex history of porosity and permeability changes. These can be described by, A) compacting bubbles (reducing porosity and permeability), B) opening cracks (increasing connected porosity and permeability), and C) closing bubbles (reducing connected porosity and permeability) as shown in Figure 3.8. Generally, the crystal-rich rocks (TP and TD) show a decrease in porosity as well as permeability, while the crystal-poor samples show an increase in permeability and a decrease in porosity. The high porosity samples reduced porosity and permeability significantly as bubble networks collapsed, the low porosity samples showed smaller changes.

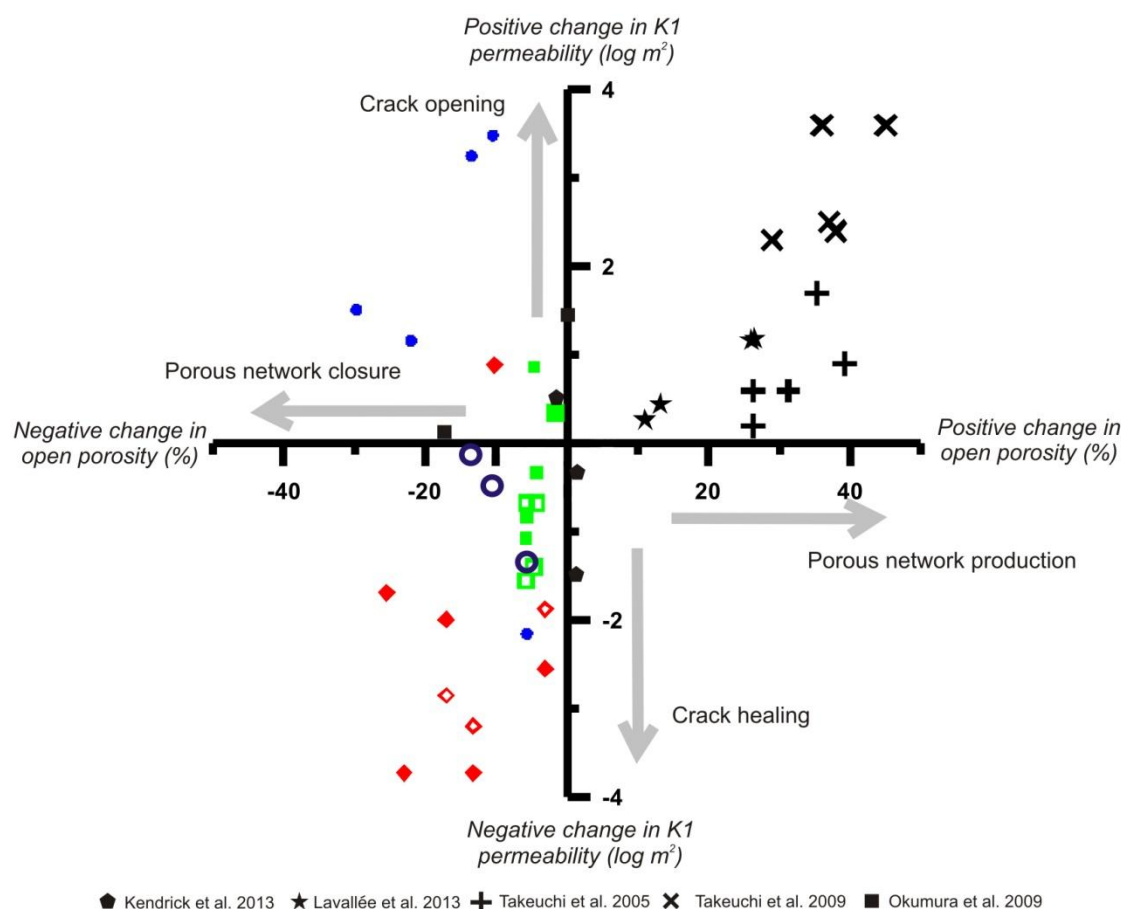


Figure 3.8: Relationship between open porosity and permeability for compression and vesiculation experiments. Colours are from this study; NP = blue, TP = red and TD = green, open shapes are radial permeability, solid shapes are axial permeability. Black shapes denote previously published work by Takeuchi et al. (2005; 2009) Okumura et al. (2009), Kendrick (2013) and Lavallée et al. (2013). Permeability of data from Lavallée et al. (2013) calculated by the relationship to porosity of $k = 10^{-17} \Phi^{3.4}$ as used by Lavallée et al. (2013).

The crystal-rich samples show an overall decrease in both porosity and permeability with strain, alongside an increase in apparent viscosity (Figures 3.4, 3.7 and 3.8). This behaviour suggests that the short, crystal-confined cracks forming in crystal-rich lavas during compaction will not overcome the reduction in permeability from closure of the bubble network and loss of porosity (Figure 3.8). In crystal-poor samples, large increase in permeability (>3 log units) occurred with

small (~10 %) losses in porosity due to the formation of long cracks. These cracks selectively improve the permeability of some areas, as shown by the lack of axial permeability of NP at 60 % strain, due to the lack of large cracks while the bubble network was closed sufficiently (down to ~14 % connected porosity).

When our results are examined in conjunction with previous experiments it is apparent that total stress, strain rate, vesicularity, crystallinity, and cumulative strain all contribute to the relative importance of cracks versus bubble networks for the evolution of permeability. The low stress, high viscosity, high porosity samples allow high strain rates and crack formation; while low crystallinities promote long cracks and large increases in permeability. Higher crystallinities promote short cracks and have little effect of sample permeability. Generally low porosity samples produce lower strain rates, less cracking, and less bubble network closure and permeability reduction.

3.8 Implications for volcanic systems

The range in stress, strain rate, melt viscosity and vesicularity investigated in the experiments are relative to different parts of the shallow conduit and dome, while magmas can be crystal-rich or crystal-poor (Figure 3.9). Uniaxial compression was used to represent compression within a lava dome that is able to spread laterally. These conditions were chosen to be as close to expected conditions within a dome as could be matched with experimental apparatus (i.e. high temperature, low compactional stress, relatively low strain rates and little confining pressure). The stress and temperature used in the experiments were due to limitations of the apparatus and time; the structures produced were similar when experiments were repeated at lower temperatures. The textures and structures produced (such as cracks) in the experiments

changed the distribution of permeability in an isotropically permeable lava; a process which is important for the assessment of outgassing and explosivity of an erupting lava dome.

The stress in this scenario is represented by weight of overburden (depth within dome or conduit), and in a static scenario with a given temperature and load, the strain rate of compaction is controlled by porosity, as a higher porosity will enable higher strain rates. Hence, the shallow conduit or lower dome produces relatively higher stress at lower strain rates (assuming lower porosity), while the upper part of the dome will show high strain rates at lower stresses (assuming higher porosity; Figure 3.9), but only for a finite amount of strain, until compaction has reduced porosity.

The compression of samples NP and TP show the collapse of a crystal-poor and crystal-rich bubbly foam from eruption to burial, while sample TD shows the behaviour of mostly collapsed foam with high crystal content in the upper conduit or lower dome. The near continuous trend of TP into TD in Figure 3.3B, as well as similarity in porosity and textures between TP at high strain, and TD at 0 % strain, suggests that at Ruawahia, the dense core of the lava dome was produced, at least partly, by compaction of a magma similar to TP. Stretched vesicles and localised shear zones indicate that shear strain may have also been important locally in the dome core at Tarawera and Ngongotaha. The stratified flow banding in the core of Ngongotaha dome shares a similar porosity to NP at high strain (see Chapter 4); however the flow banding and convolute folding are dissimilar, as NP did not create flow bands under compaction. This suggests that shear strain played an additional important role, alongside compaction, in formation of the stratification of the dome core at Ngongotaha.

Our experiments have shown that under low stress, both crystal-poor and crystal-rich rocks will produce cracks at the specific load and temperature used, and as a result both rock types remain

locally permeable even after experiencing large amounts of strain. In volcanic systems, cracking may lead to increased permeability and open degassing but only if the cracks are long enough to allow effective gas escape. Large cracks can reduce overpressure but will form zones of weakness that may lead to failure of the dome core.

Studies by Tuffen et al. (2003), Tuffen and Dingwell (2005), Yoshimura and Nakamura (2010) and Kennedy (2010) have shown that these cracks can heal. Although little data exists on this, crack healing would decrease permeability, accompany a minor decrease in porosity (Kennedy et al. 2010) and an increase in strength. Cracking of magma in a natural setting may be responsible for hybrid earthquakes which are concurrent with the extrusion of lava domes, and may be used to predict the behaviour of such volcanic systems (Tuffen et al. 2003; Tuffen & Dingwell 2005; Neuberg et al. 2006; Lavallée et al. 2008; Tuffen et al. 2008).

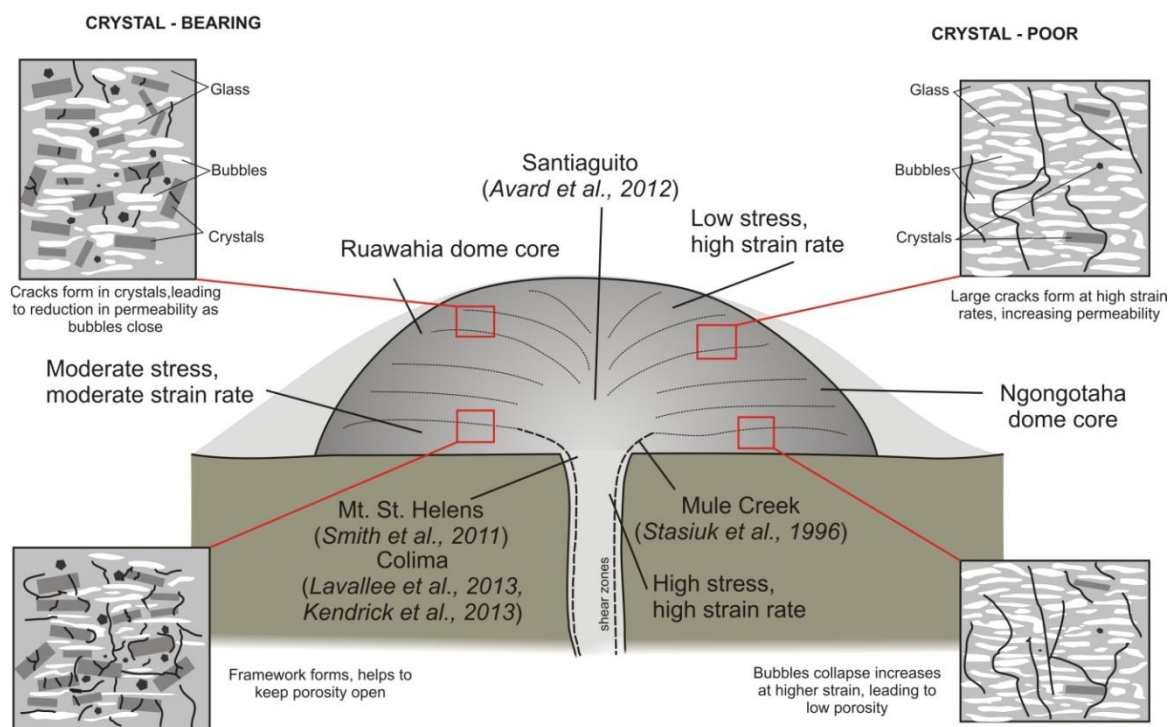


Figure 3.9: Model of compression in crystal-rich (left) and crystal-poor (right) lava domes. Our high strain experiments correspond to large amounts of overburden found in the core and base of lava domes.

High strain rates produced large cracks at low strain in crystal-poor lavas. Fractures in crystal bearing, moderate porosity lavas (TD) are generally focussed within crystals until high strain. This suggests that crystal-poor lavas may therefore be more susceptible to producing larger fractures, as there are no crystal-glass interfaces to stop the advancement of a crack. Crystal-poor lavas will therefore form ineffective plugs which are more susceptible to failure. However, permeability may be highly variable dependent on localisation of fractures.

During the 2008 to 2009 eruption of Chaitén lava dome, a general change from exogenous growth to endogenous growth was observed following the collapse of a large spine (Pallister et al. 2013). Bombs of the crystal free obsidian show well formed tuffisite veins, formed by shear

induced magma cracking and fragmentation (Castro et al. 2012b). H₂O concentrations at the margin of these fractures suggests that this style of cracking may not have been large, long-lived enough, or did not have the diffusion length required to effectively degas the magma, and the sufficient level of brecciation needed for this may only be found at the conduit margin where shear strain is highest, and the cracks intersect highly permeable, porous magma (Tuffen & Dingwell 2005; Castro et al. 2012b). This process of fracturing assumes the fragmentation of material and transport of material into a crack by fluid flow; the individual particles may sinter, reduce permeability, then heal and re-fracture (Tuffen et al. 2003), and reduce permeability. Whilst these cracks allow partial degassing of conduit lava (Schipper et al. 2013; Castro et al. 2012b), in the dome fracturing may occur readily from compression and in enough numbers to allow significant degassing of the dome.

The porosity of crystal bearing samples was also prevented from closing past ~20 % connected porosity by the production of a crystal/ glass framework that resisted compaction. Most permeability models suggest that a percolation threshold of 30 % total porosity is enough to effectively close all permeability (Mueller et al. 2005). However, the combined effect of cracked crystals and imperfect bubble compaction and pressure shadows (Figure 3.6) leaves remnant permeable pathways in our crystal-rich samples. Hence, compaction of crystal-rich lava domes does not completely close permeability and maintains the ability to degas and lower the risk of explosive fragmentation.

An example of compression reducing porosity at a lava dome is Unzen dome, Japan, which produced micro-vesicular pumice prior to dome growth in 1991. The growth of the lava dome in the following 4 years showed a much lower porosity, indicating that collapse of the foam had occurred (Nakada & Motomura 1999). Radial expansion and sagging of Unzen lava dome at a

rate of subsidence of 20 to 40 cm with coincident lateral movement of 50 to 130 cm over 1.5 years was observed in early 1995 (Nakada et al. 1999), suggesting that compression had some part in the compaction of the magmatic foam at Unzen. The dome at Unzen was crystal-bearing (22 to 28 % phenocrysts; Nakada & Motomura 1999), and produced numerous block and ash flows. The compression at Unzen would have produced numerous fractures in crystals, a feature that is common at Unzen (Cordonnier et al. 2009), which may have weakened the dome and facilitated the production of block and ash flows.

3.9 Conclusions

Our compression experiments aimed to investigate the ability of porous and crystal bearing lavas to compact. Our high strain experiments recreate the conditions at the base of a large lava dome, and have recorded the evolution of the porosity and permeability from pumiceous lava to dense, compressed lava (Figure 3.9). The experiments show:

- At constant stress, the rate of compaction is controlled by the viscosity of the melt and our experiments define the relative importance of crystals and bubbles.
- Barrelling of samples increases rapidly when around 20 % porosity is achieved through compression; this coincides with a drop in the rate of porosity reduction, and occurs more readily in crystal-rich samples.
- High initial vesicularity magmas deform at high strain rates which forms large cracks which control permeability.
- In crystal bearing rocks, cracking focuses in crystals, producing many small cracks. In these samples, permeability was controlled by porosity loss through bubble wall compaction.

The similarity of the TP at high strain to undeformed TD supports that our experiments of increasing strain represent progressive burial within a lava pile. The production of a crystal/ glass framework, as well as crystal-dependant production of cracks in lavas is an important consideration when predicting the evolution of porosity and permeability within a compacting lava dome. The production of large cracks in initially vesicular lavas should also be accounted for when assessing the ability for an actively growing lava dome to fail.

Preamble

In the previous chapter, I discuss the porosity and permeability evolution on bubbly magma during compression. Compression occurs during extrusion of a lava dome, and is one of the main processes that controls bubble collapse, creating the dense core facies within the lava dome. Traditional views of lava domes (such as Manley and Fink (1987)) suggest that a stratified porosity will be the result of degassing and recrystallisation processes during extrusion. The internal structures of Ruawahia and Ngongotaha do not share this simple model; this chapter aims to investigate the internal structures and proposes new eruption models and timelines for the growth of each dome. I also suggest what controls the shape and orientation of the vent, as well as why Ruawahia has produced large block and ash flow deposits, whereas Ngongotaha has very few.

This chapter will be submitted to Bulletin of Volcanology, to be considered for publication.

Chapter 4

Dyke fed dome eruptions: comparing and contrasting two dyke-fed rhyolitic domes in the Taupo Volcanic Zone

Lava domes can exogenously erupt as lobes, flows or spines, or endogenously inflate. Transitions in extrusion morphology occur sequentially as a result of a change in eruptive conditions. The morphology of individual lava extrusions will dictate the dome stability and ability to produce devastating block and ash flows. Here I present mapping of two well exposed lava domes – Ngongotaha dome and Ruawahia dome. Both domes have their cores exposed, allowing detailed mapping of the extrusion morphologies and the internal structures including flow banding, shear zones, breccia zones and fractures. I compare and contrast the structures and deposits associated with the two lava domes, and link the structures to dyke-fed eruptions with vent zones parallel to local faults.

The overall morphology of Ngongotaha dome is parallel to regional extensional structures, while the morphology of the northernmost dome lobe is parallel to local caldera collapse faults. The dome lobe exposed in Henderson's Quarry contains; (1) a carapace facies of high porosity (50 – 58 %) crystal poor rhyolite and mixed dense and vesicular talus; (2) a strongly flow-banded recrystallised interior facies with convolute flow folding consistently striking parallel with the dome elongation axis; and (3) sub vertical spherulitised obsidian sheets with similar strikes, each separated by breccia at the

dome axis. There is no evidence of widespread block and ash flow deposits around Ngongotaha. I interpret that the exposed lobe of Ngongotaha erupted from a single, dyke-shaped vent, flowing and endogenously inflating until viscosity and strain rates allowed brittle failure and intrusion of sub vertical sheets interleaved with breccia zones. Other lobes at Ngongotaha erupted in a similar manner from dykes parallel to regional structure.

The domes of the Tarawera dome complex form a chain parallel to regional structure, whereas the morphology of Ruawahia dome is elongate perpendicular to regional structure. Ruawahia dome consists of: (1) a high porosity (44 – 52 %), crystalline (65 % DRE) carapace facies with local bread-crusting and ‘ropey’ flow textures; and (2) an interior facies of dominantly low to moderate porosity (20 – 25 %) with elongate vesicles that mark weak flow bands, and (3) rare interior breccias. The flow bands dip towards individual vents aligned parallel to regional structure. Ruawahia has large block and ash flow deposits sourced from the leading flow fronts to the NW and SE. I interpret that Ruawahia erupted from multiple, aligned vents as a sequence of bulldozing, thickening flow lobes with dominantly ductile interiors and brittle exteriors. Spiny lobes were confined to within the crater of a pyroclastic cone, forming steep internal breccia zones during extrusion.

The parallel trend of flow band strikes and local faults leads us to interpret both domes as being fed by dykes. However, I interpret the different morphologies to be controlled by palaeotopography, extrusion rates, viscosity and crystallinity. Multiple vents, crystal-rich lavas and varied palaeotopography lead to a less stable edifice and increased risk of flow front failure and formation of block and ash flows, as at Ruawahia, while elongate vents, crystal-poor lavas and flat palaeotopography at Ngongotaha lead to confined eruptions and reduced risk of block and ash

flows. Therefore, I conclude that the eruption morphology of the lava domes controls the spatial distribution of potential hazards.

4.1 Introduction

Large dome failure events that create block and ash flows can be caused by the eruptive morphology, and may lead to a transition to an explosive eruption phase (Nakada et al. 1999; Watts et al. 2002a; Carn et al. 2004; Platz et al. 2007; Williamson et al. 2010). The extrusion style of lava domes can be summarised as a continuum between two endmember styles – endogenous (inflation of a lava dome) and exogenous (extrusion of a series of lava spines or flows; Fink & Anderson 2000). Many domes show a transition from one style to another due to a change in eruption parameters such as effusion rate (Nakada et al. 1995; Calder et al. 2002; Kaneko et al. 2002), vesicularity (Platz et al. 2007; Bull et al. 2012), viscosity (Platz et al. 2007) or the production of shear zones inside the dome (Hale & Wadge 2008). Exogenous growth is associated with high viscosity, confined domes with a low effusion rate, such as Mt. St. Helens (Vallance et al. 2008), while endogenous growth accompanies unconfined domes of lower viscosity (Nakada et al. 1995) or higher effusion rates (Hale & Wadge 2008), although endogenous growth can also occur at low effusion rates (Nakada et al. 1999).

The style of extrusion of a lava dome will dictate the arrangement of internal structures such as flow bands, shear zones, fractures/faults, and breccia zones as well as porosity, and vice versa. The textures that define different lava dome extrusions develop from both ductile and brittle deformation.

Viscous deformation of the magma allows densification and the development of flow bands. Porosity reduction in magma occurs when bubbles compact due to overburden pressure (Quane et al. 2009; Chapter 3). Flow bands originate from velocity differences during ascent in the conduit, resulting in shear elongated bubbles and aligned crystals (Stasiuk et al. 1996; Fink & Anderson 2000).

Generally, flow banding will be parallel to the edges of the conduit during ascent or emplacement (Figure 4.1; Stasiuk et al. 1996; Tian & Shan 2011), but the orientations will continue to evolve as the lava erupts. Endogenous or exogenous flow will define the orientation of flow banding (Figure 4.1).

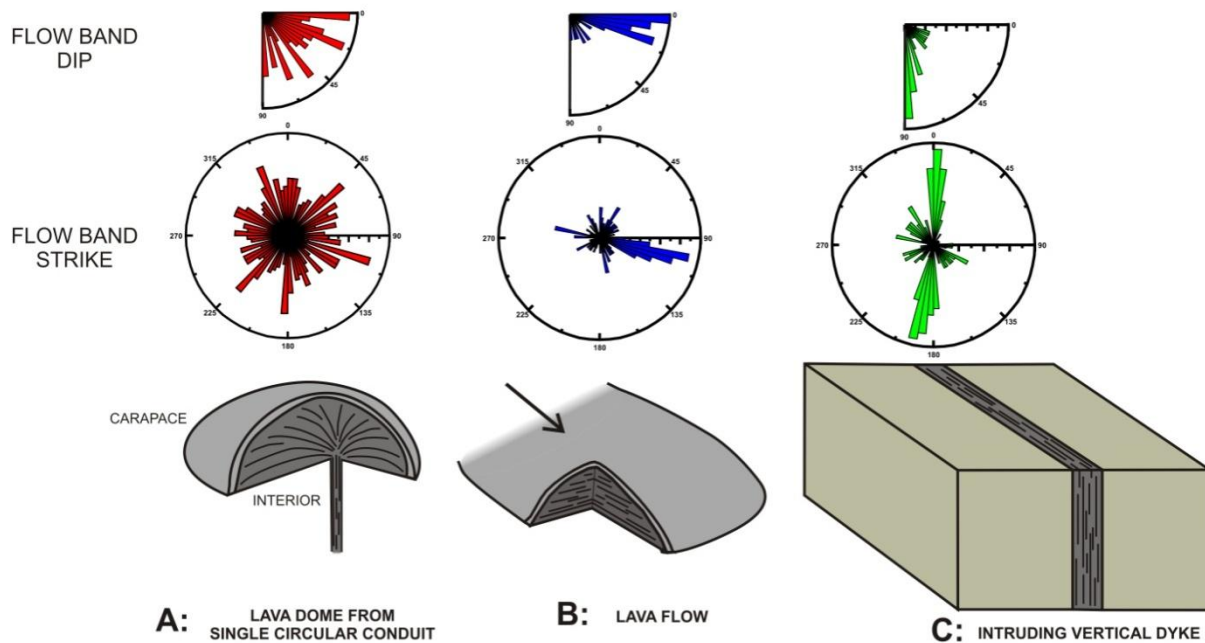


Figure 4.1: Hypothesised flow band orientations from a single, circular conduit sourced lava dome (A), lava flow (B) and dyke (C).

Brittle deformation is also common in lava domes, and important to transitions between endogenous and exogenous growth. The extrusion of spines or plugs can lead to the development of wide breccia or narrow fault zones that allow changes in extrusion rate, degassing and eruptive style (Sparks et al. 2000; Cashman et al. 2008; Sahetapy-Engel & Harris 2008; Lavallée et al. 2013; Kendrick et al. 2012). Fracturing of the magma can lead to the generation of micro-earthquakes

(Lavallée et al. 2008; Tuffen et al. 2008; Smith et al. 2009), formation of tuffisite veins (Tuffen et al. 2003) and the development of permeable fractures that may produce planes of weakness that lead to dome failure (Kendrick et al. 2013). These processes of flow and fracture are controlled by the temporal and spatial distribution of viscosity and strain rate variations and hence control the spatial and temporal development of lava dome facies. Hence, the complex arrangement of structures, facies and textures in a lava dome are directly linked to the style of extrusion of the dome.

Shallow dyke-fed dome eruptions, where a lava dome is fed directly by the dyke structure rather than a circular conduit, have been suggested previously (Fink & Pollard 1983; Walker 1999; Aguirre-Díaz & Labarthe-Hernandez 2003; Leonard 2003), but based on little evidence other than morphology and vent locations. The style of eruption from dyke-fed vents varies from multiple aligned vents erupting multiple lobes and flows, such as Medicine Lake Highland (Fink & Pollard 1983), Inyo domes (Vogel et al. 1989) or Cordón Caulle (Lara et al. 2004) to the vertical extrusion of a viscous dyke from an elongated vent, such as Hrafninnuhryggur at Krafla (Tuffen & Castro 2009). Here, I present results of detailed field mapping of two large rhyolitic lava domes, Ngongotaha dome and Ruawahia dome, and compare and contrast internal structures, facies, textures, morphology and structural settings. From this, I aim to define distinct eruption models, discuss conduit processes and provide implications for hazard assessment.

4.2 Geological Setting

Ngongotaha and Ruawahia domes are located within the TVZ (Figure 4.2). The TVZ is an intra-arc, silicic- and andesitic-dominated rift system created by crustal thinning from the oblique subduction of the Pacific plate beneath the Australian plate (Cole & Lewis 1981; Cole 1990; Bibby et al. 1995;

Wilson et al. 1995; Spinks et al. 2005). The main structural trend in the TVZ is NE – SW (Figure 4.2), with an offset of the rift axis along relict basement structures observed across Rotorua caldera and Okataina caldera complex (OCC) (Rowland & Sibson 2001; Acocella et al. 2003). This trend is observed in normal faulting (Rowland & Sibson 2001; Villamor et al. 2011), dyke intrusion (Nairn & Cole 1981; Nairn et al. 1998; Seebeck & Nicol 2009) and lava dome alignment (Leonard et al. 2010; Chapter 5). Basement structure is also seen to partially control caldera morphology at Rotorua caldera (Milner et al. 2002) and the OCC (Seebeck et al. 2010), as well as having some control on the placement and morphology of lava domes within Rotorua caldera (Chapter 5).

Field mapping of internal structures of Ngongotaha dome was conducted at Henderson's Quarry, an operational quarry on the eastern edge of the northernmost lobe of Ngongotaha dome (Figure 4.2). Ngongotaha dome is located within Rotorua caldera (Figure 4.2), and is a c. 4 km diameter, ~200 ka, rhyolitic (>73% SiO₂) lava dome that erupted following the collapse of Rotorua caldera during the 240 ka Mamaku ignimbrite eruption (Milner et al. 2003; Chapter 5). Chapter 5 concludes that the northernmost lobe mapped in this study may have been sourced from a N – S trending dyke (Chapter 5), likely related to the edge of a gravity low associated with a caldera subsidence fault, which also trends N – S (Hunt 1992).

Field mapping of internal structures at Ruawahia was conducted within the fissure formed during the 1886AD Tarawera eruption (Nairn & Cole 1981), as well as outcrops along the summit and edges of the NW dome lobe. Ruawahia is located with the OCC, and is a c. 1.5 km diameter, high silica (~76 %, Leonard et al. 2002), high crystallinity (40 – 60 % DRE) lava dome (Cole, 1970b) (Figure 4.2) erupted during the 1314AD Kaharoa eruption (Cole 1970b; Nairn et al. 2001; Leonard et al. 2002; Nairn et al. 2004). The Kaharoa eruption produced 3 other lava domes following a Plinian eruption

that built a pyroclastic cone beneath Ruawahia dome (Cole 1970a) termed Ruawahia Tuff Cone (Nairn et al. 2001). Crater dome, to the SW of Ruawahia, was the first dome extruded, coincident with the Plinian phase, and was buried by pyroclastic material. Tarawera dome, to the SW of Crater dome, erupted following the end of explosive activity, with Ruawahia erupting alongside. Wahanga dome, to the NE of Ruawahia also erupted after the end of explosive activity, but the exact timing of the eruption compared to Ruawahia is unclear.

Significant block and ash flow deposits occur on the NW, NE and SE slopes of Tarawera (Nairn et al. 2001), and contain blocks of varying densities; all sourced from dome collapse episodes of Ruawahia and Wahanga domes. The interior of the lava domes were exposed after the 1886AD Tarawera eruption, where a basaltic dyke, orientated with the overall structural trend across the OCC (Figure 4.2), intruded through and erupted violently out of the domes, and interacted with the hydrothermal system and Lake Rotomahana to produce devastating phreatomagmatic surges (Nairn 1979; Nairn & Cole 1981; Houghton et al. 2004; Sable et al. 2006; Carey et al. 2007). The dyke remelted the dome lava immediately adjacent to it, sealed the margins of the dyke (Kennedy et al. 2010) and explosively excavated a series of large fissures through the cores of the lava domes.

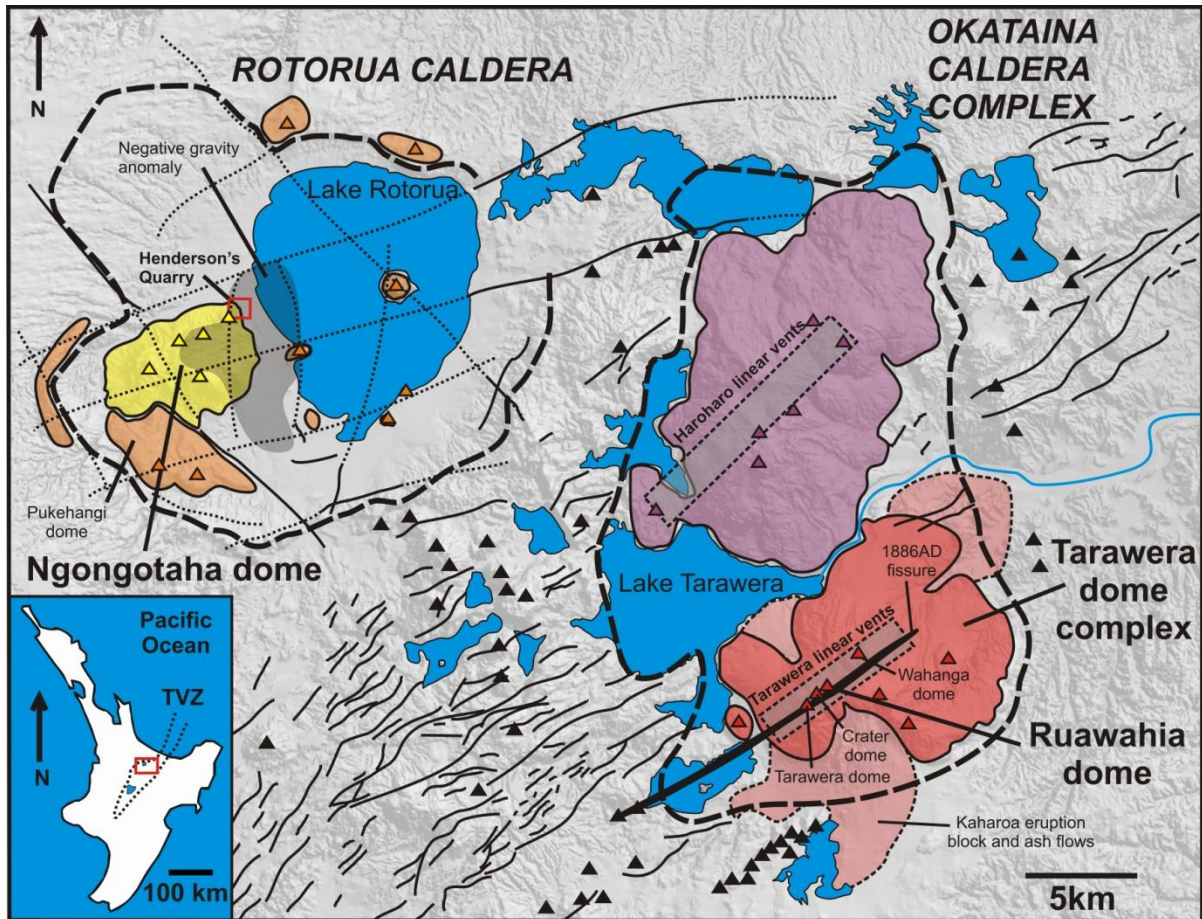


Figure 4.2: Map of Rotorua caldera and the OCC. Black lines indicate fault locations, black triangles are locations of vents (from Villamor et al. 2011), dotted lines indicate inferred structures at Rotorua caldera (from Chapter 5) and dashed lines show caldera topographic margins. Orange domes are other rhyolitic domes of Rotorua caldera (Ngongotaha dome is yellow, with location of study in red square) and purple domes indicate location of Haroharo dome complex. Inset: Map of North Island and TVZ, red box indicates location of Rotorua and the OCC.

4.3 Results

4.3.1 Ngongotaha dome

Ngongotaha dome consists of 6 lobes that make up the NE – SW trending Ngongotaha dome (Figure 4.2). Lava dome facies at the northern dome lobe include (1) an interior flow facies consisting of a flow banded core, 2) an underlying basal breccia facies, (3) an interior sheet facies of spherulitic obsidian sheets interleaved with breccia zones and (3) an exterior carapace facies of finely vesicular pumice and carapace breccia subfacies.

The basal breccia facies at Ngongotaha consists of a spherulitic obsidian breccia exposed in the lowest levels of the quarry, grading over 10 m into the flow banded core (Figure 4.3A and C). The matrix of the basal breccia subfacies is dark grey devitrified glass containing clasts of light pink and grey altered glass, up to 4 cm across, spherulites and patches of perlitised, black to dark red obsidian (Figure 4.3D). The basal breccia shows little to no flow banding and poorly defined fractures (Figure 4.3C and D) and becomes progressively more coherent towards the flow banded core subfacies. The core subfacies is strongly flow banded, with alternating dark and light grey, non-continuous flow bands overprinted by spherulites (Figure 4.3A and B). The flow bands are prominent and generally thin (dark grey bands between 0.2 to 2 cm thick; light grey bands between 1 and 10 cm thick; Figure 4.3B) and in places are convolutedly folded. The colour difference of flow bands is due to differences in amount and colour of microlites and spherulites within each flow band. The flow bands can be traced laterally by up to a meter, but often pinch and merge with other bands. The flow banding dips by $\sim 25 - 35^\circ$ to the W – SW (i.e. towards the axis of the dome; Figure 4.4). Folding of the flow bands results in a bimodal dip distribution in the centre of the dome (Figure 4.4, Level 2 Rose diagram); however, strike values are consistent across the folds and parallel to the elongation

axis of the dome. Numerous spherulites (up to 10 mm), opening structures (up to 50 mm across) and lithophysae (up to 300 mm across) overprint any original textures related to vesicularity (Figure 4.3B). Fractures in the flow banded core subfacies are near vertical, well defined with similar strike and cross cut flow banding. They are open fractures with smooth sides, and have a maximum width of 3 cm and frequently contain evidence of hydrothermal alteration and precipitation as a thin, dark red precipitate coating on the sides of the fractures. An intermediate zone between the interior flow facies and the interior sheet facies is poorly flow banded, and contains angular uncommon clasts of spherulitised obsidian (up to 20 cm) in a white spherulite-rich matrix. Spherulites are common in this zone, but lithophysae and lip structures are not present.

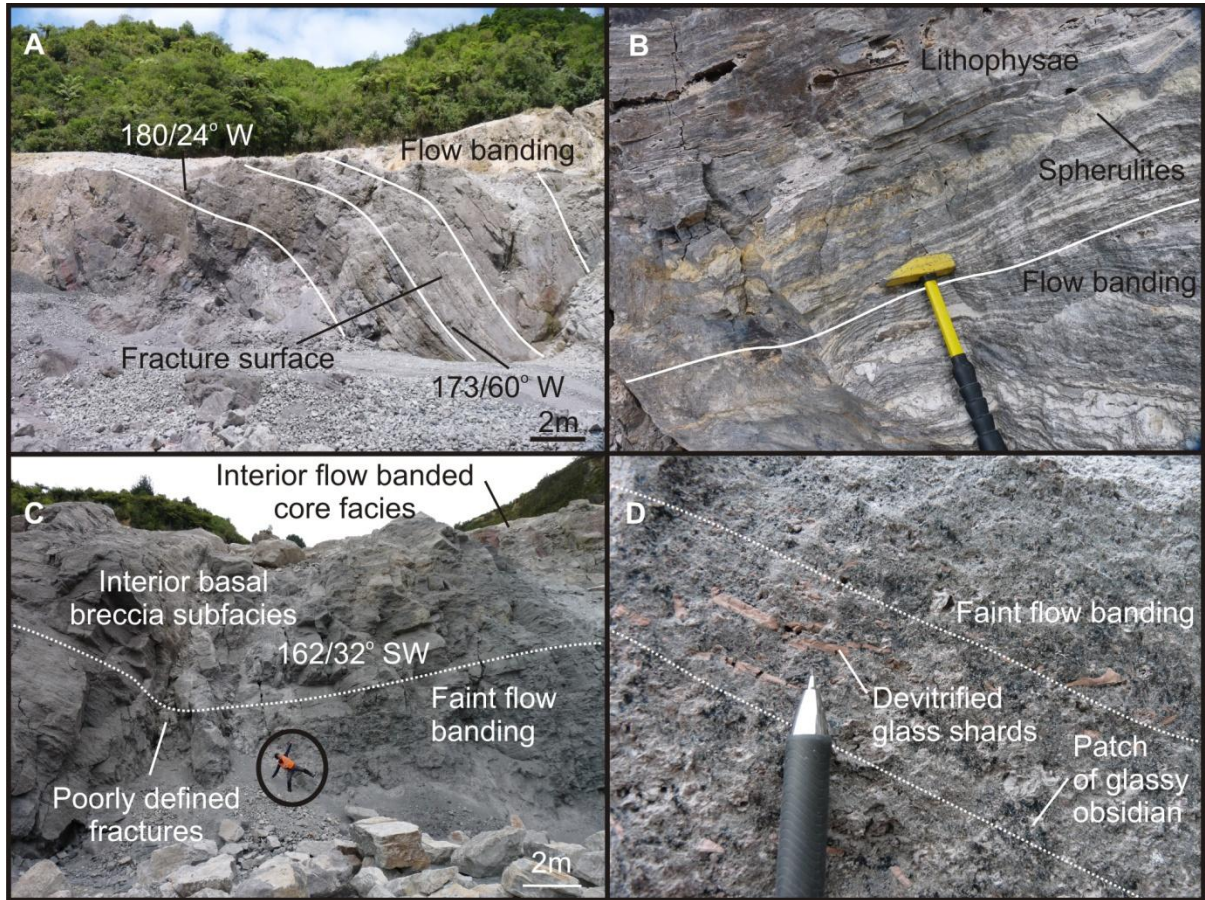


Figure 4.3: Images of internal structures of interior flow facies at Ngongotaha dome. A: Flow banding in the flow banded core facies. B: Close up of flow banding showing dark and light grey layers. Hammer is 30 cm long C: Basal breccia facies beneath flow banded core facies. Figure (circled) for scale D: Close up of basal breccia facies showing faint flow banding and devitrified glass shards.

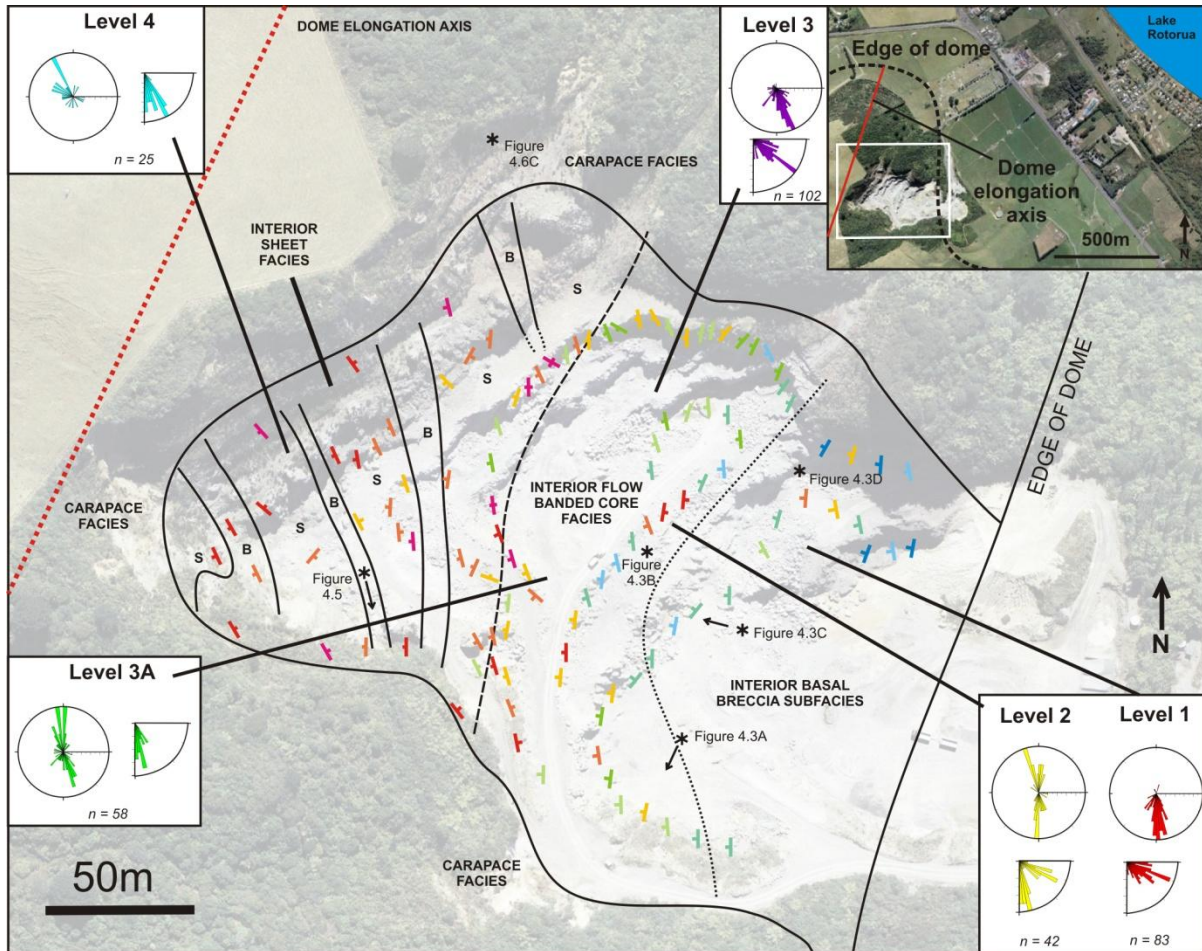


Figure 4.4: Map of flow bands and facies at Henderson's Quarry. Inset: Location of Henderson's Quarry and map area (white square; see Figure 4.2 for position inside Rotorua caldera). Individual level flow band measurements (strike in circle, dip in quarter circle) are shown in rose diagrams. Black stars and arrows indicate positions of pictures in Figures 4.3, 4.5 and 4.6. Cool colours of strike bars indicate low dip, warm colours indicate high dip. B = Breccia zone, S = Spherulitic obsidian sheet.

Towards the centre of the dome, and cross cutting the flow banded core, is the interior sheet facies. This facies includes near vertical sheets of spherulitised obsidian interleaved with breccia zones (Figure 4.5A). The breccia zones range from 0.3 m to over 5 m wide, with clasts of spherulitic obsidian in a silicified white matrix (Figure 4.5C), and can be traced from one side of the quarry to the other (at least 170 m), orientated near N – S along the elongation axis of the dome (Figure 4.4). Small scale breccias within the flow banded core described by Dadd (1992) are generally ~30 cm across, and distinct from the breccias described here. Analysis of the breccia zones in the interior sheet facies shows a slight decrease in overall size of clasts to the centre of the zone (from 30 – 40 cm to 15 – 25 cm), often with a gradational change from angular equant clasts at the margins to sub-angular elongated clasts in the centre (aligned with flow banding in bounding obsidian sheets). This reduction in size and change in shape is also accompanied by a reduction in the clast to matrix ratio from 1 : 0.75 - 0.8 at the margins to 1 : 0.5 to 0.6 in the centre. The boundaries between the breccia and sheets are sharp and aligned with flow banding. Flow directionality in the obsidian sheet subfacies is shown by aligned clasts in the breccias, as well as weak flow banding and relict bubble elongation structures in the sheets (Figure 4.5B and C). Flow orientations in this facies dip near vertically ($>80^\circ$), towards the elongation axis of the dome. Relict flow banding in clasts within the breccias zones is visible, and in most places is close to parallel with flow banding in the sheets and varies up to 40° in clast rich areas. The strike orientations of flow banding in the interior flow banded core facies and sheet facies are consistent at $163 - 179^\circ$ (near N – S) (Figure 4.4). There is an increase in the flow band dip between the interior flow banded core facies and the interior sheet facies (Figure 4.4).

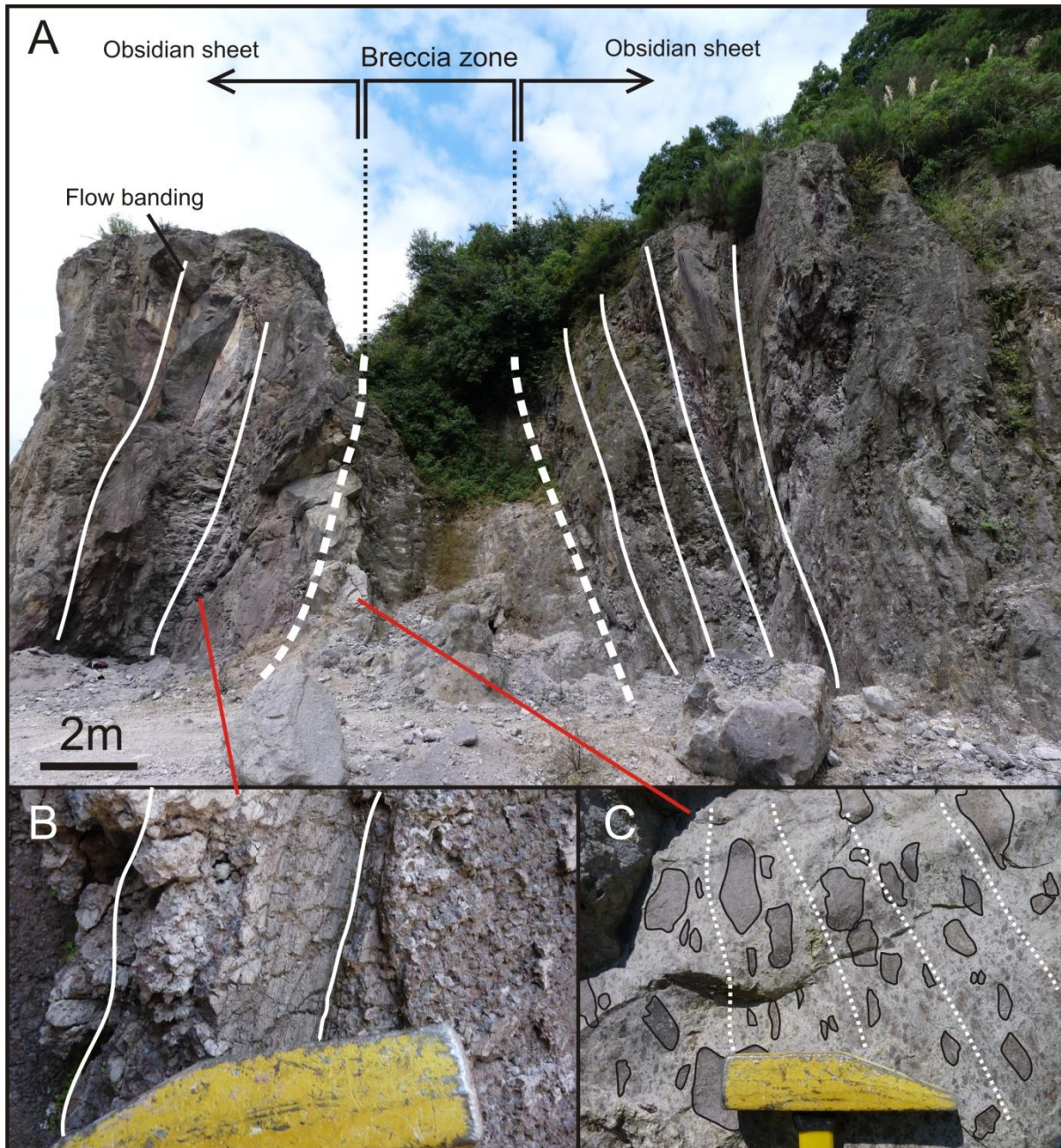


Figure 4.5: A: Breccia zone and spherulitic obsidian sheet of interior sheet facies; white lines indicate flow banding in sheets, dashed white line is boundary between sheets and breccia. B: Close up of spherulitic obsidian sheet. C: Close up of breccia zone with clast alignment (white dashed line) and selected large clasts outlined. Location of photos shown in Figure 4.4.

The carapace facies at the top of the dome consists of finely vesicular pumice and a carapace breccia subfacies (Figure 4.6). The pumice is a light grey, phenocryst poor (<5 %) finely vesicular pumice (50 to 60 % connected porosity of <0.5 mm long elongate bubbles; see Chapter 3) with localised areas of coarser vesicularity (up to 5 mm long; Chapter 3; Figure 4.6A and B). The vesicles within the pumice have been heavily elongated and deformed, forming long tube shaped bubbles with evidence of shear in the glass (Figure 4.6B). The carapace breccia consists dominantly of clasts (up to 0.8 m across) of vesicular pumice with less common clasts of denser pumice and spherulitic obsidian. Also observed in the carapace are fresh, slightly perlitised thin obsidian intrusions that have localised spherulite growth along flow planes (Figure 4.6C; von Aulock et al. 2013) surrounded by thin (<5 cm) 'baked zones' within the breccia.

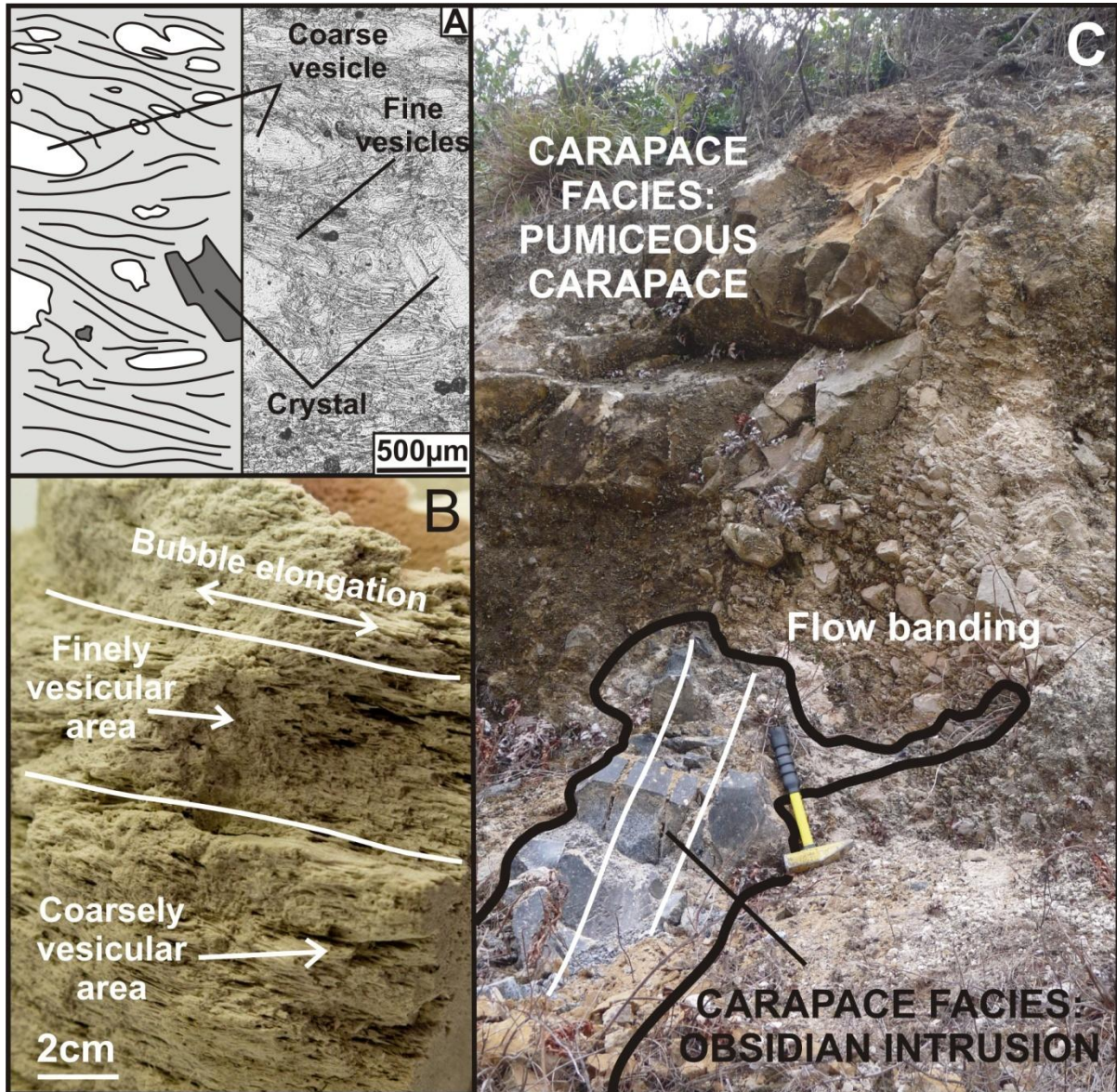


Figure 4.6: A: Thin section photomicrograph (right) and drawing (left) of pumiceous carapace facies B: Photo of pumiceous carapace facies showing coarse and fine pumice areas and flow elongation. C: Carapace facies consisting of pumiceous carapace facies and glassy obsidian intrusion subfacies. White lines show flow banding. Location of photos shown in Figure 4.4.

4.3.2 Ruawahia dome

Ruawahia dome consists of at least 7 lava lobes that comprise the NW – SE trending lava dome. Textural differences at Ruawahia are far less pronounced than those at Ngongotaha, but 3 equivalent facies are observed: (1) an interior core facies of dense, glassy to rarely devitrified lava within the 1886AD fissure and on ridges on the NW lobe, (2) a basal breccia facies of angular blocks of core lava within an ash-like matrix, located beneath the core facies, (3) an exterior carapace facies of vesicular, mostly glassy pumiceous crystalline dome rock with spherical to elongated vesicles is observed on the top and sides of the dome, and as isolated outcrops within the fissure, alongside a talus subfacies of unconsolidated blocks of lava at the edge of the dome and (4) interior breccia zone facies that separate parts of the core facies, and represent a similar breccia facies to Ngongotaha. Distinctive spherulite and porosity variations in the facies and flow band orientations are used to differentiate the individual lobes. The lobes of Ruawahia can be grouped into two distinct types: (A) flow lobes with ramp structures and (B) spiny lobes with breccia zones and spine extrusions. Both types contain the facies described above.

The dense core facies of flow lobes and spiny lobes (see Chapter 1) consist of dense (9 to 33 % porosity) rhyolite with varying amounts of devitrification from grey to red-brown glass with numerous spherulites to pristine glass. The most vesicular areas preserve elongated bubble textures, while in the most devitrified areas, all glass has been replaced with brown to grey spherulites, crystallising preferentially along flow planes, and leaving a weak trace of the flow banding. In less dense samples, areas of microlite-rich dense glass with flat, elongated bubbles and isolated spherulites are inter-layered with less dense, partly microlitic glass with elongated, tubular bubble structures. The dense core subfacies is primarily found within the 1886AD fissure in spiny

lobes, where the centre of the dome is exposed (Figure 4.7A). Ramp structures are observed on the NW flow lobe as a series of parallel ridges trending perpendicular to the flow direction, where dense core subfacies extrudes out of the carapace facies (Figure 4.8C). Flow banding in the ramp structures trends approximately parallel to the ridges, and dips moderately towards the dome summit (Figure 4.9). The dense core facies grades into the basal breccia facies at the very base of the dome. The basal breccia consists of large angular blocks of dense core facies within an ash-like matrix. The basal breccia facies also grades over several metres into the underlying pyroclastic material (Figure 4.7B).

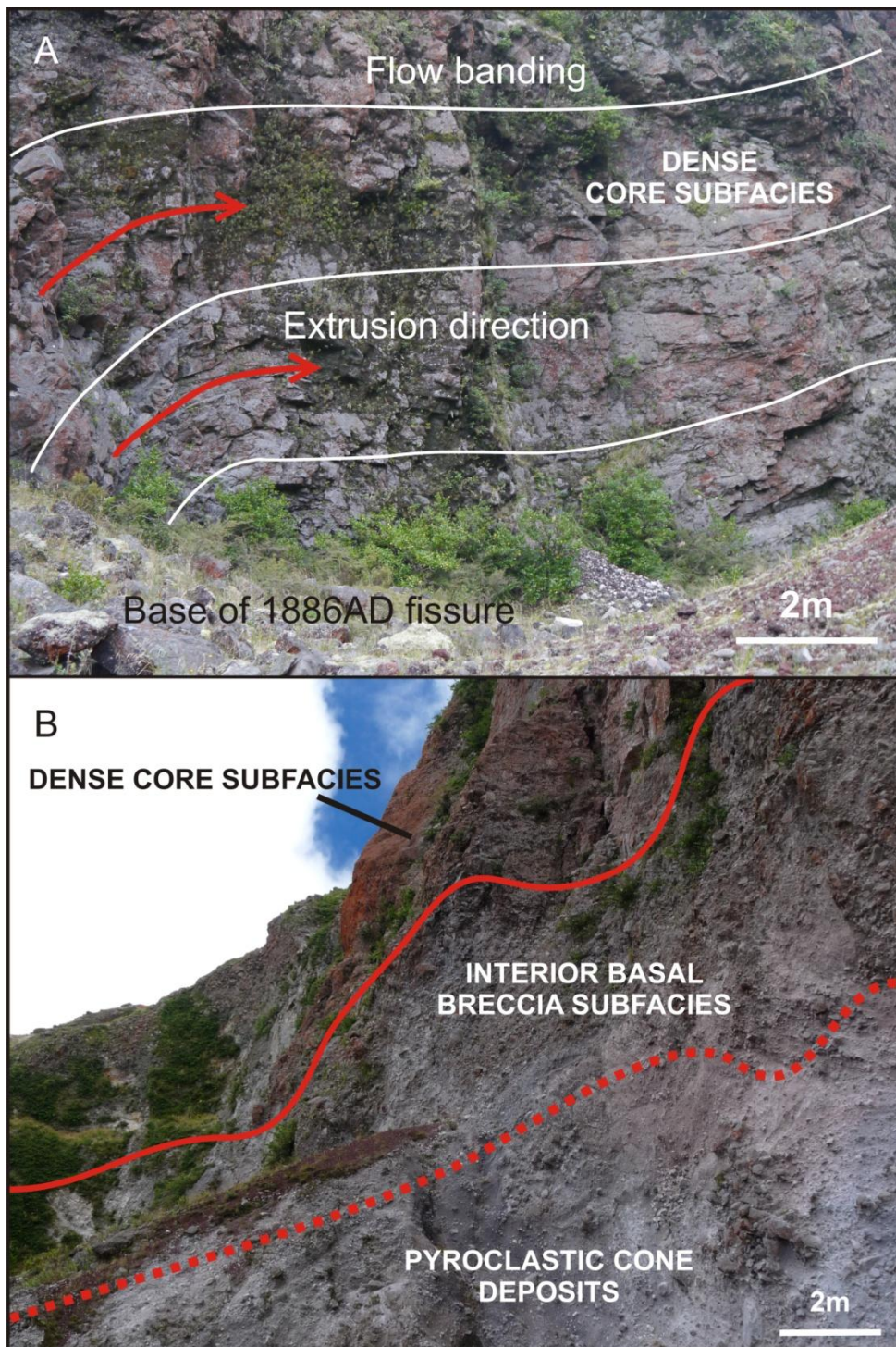


Figure 4.7: Interior facies of Ruawahia. A: Faint flow banding in core facies, at base of 1886AD fissure. B: Pyroclastic cone deposits (bottom) grading into basal breccia subfacies, and interior core facies at top. Location of photos shown in Figure 4.9.

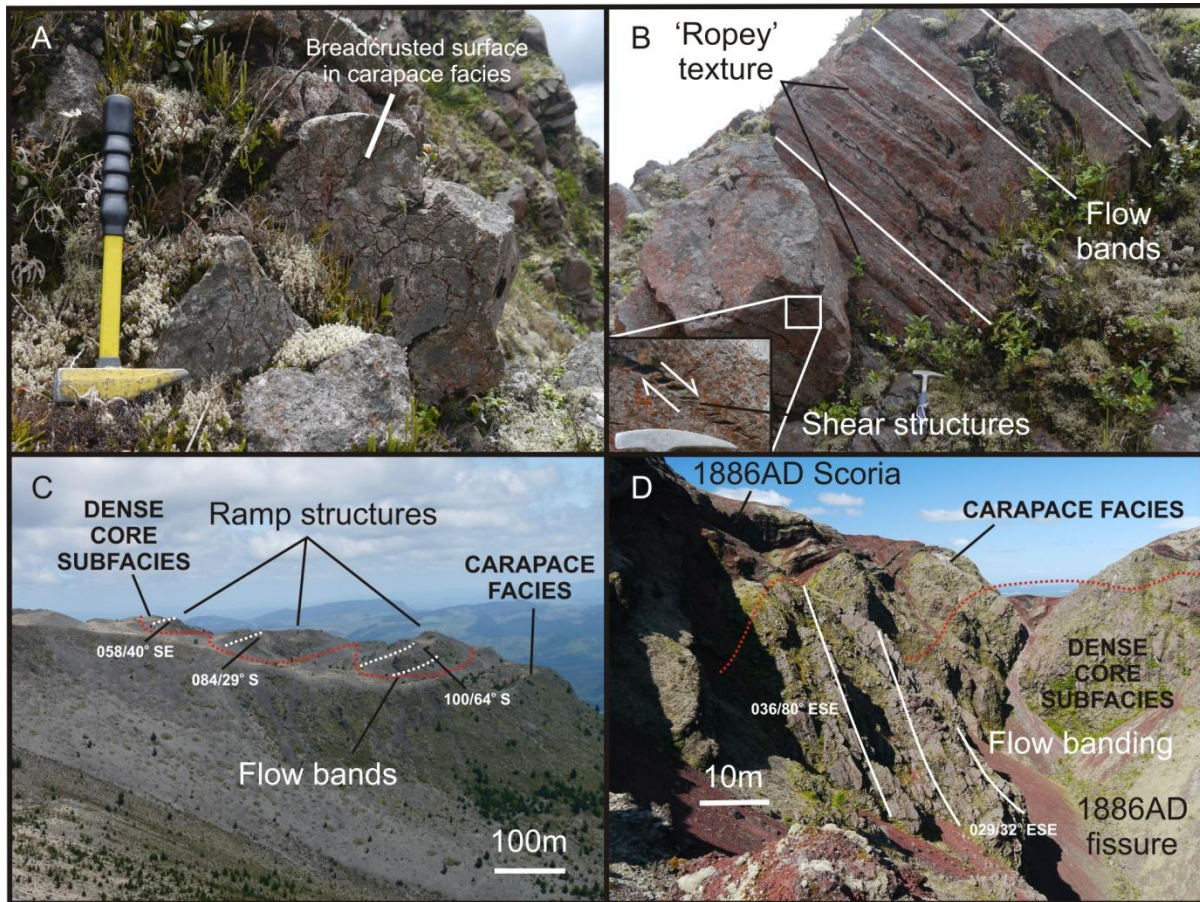


Figure 4.8: A: Breadcrust surface in pumiceous carapace of carapace facies at Ruawahia, at edge of dome. Length of hammer is 30 cm. B: Ropey skin texture and shear structures (inset) in carapace facies from outcrop within 1886AD fissure (hammer for scale). C: View across Ruawahia dome from flank of Wahanga dome, showing ramp structures of interior core facies, surrounded by carapace facies. D: Flow banding of interior core facies in 1886AD fissure. Location of photos shown in Figure 4.9.

The carapace facies of both flow and spiny lobes has moderate to high porosity (35 to 56 %), with common elongated bubbles and a pumiceous appearance. This facies is found along the top surface (including at the top of the 1886AD fissure in spiny lobes) and around the edge of Ruawahia where solid outcrops are not buried by 1886AD scoria (Figure 4.9). Extremely coarse vesicular (54 to 56 % porosity) pumice, with rounded vesicles and a glassy appearance, is observed alongside bread-

crusting and 'ropey' textures (Figure 4.8A and B). 'Ropey' texture is a rounded 'skin' surface that enhances the appearance of flow banding by accenting the vesicularity differences in the bands. They are likely similar to pahoehoe-like structures described by Fink et al. (1992). It occurs commonly on the outer edges of the flow lobes above block and ash flow deposits, but is also observed on internal dome surfaces in spiny lobes exposed in the 1886AD fissure. The carapace facies also contains unconsolidated talus breccia observed at the very edge of the dome, but most of it has been buried by 1886AD scoria (Figure 4.9).

Internal breccia facies are uncommon at Ruawahia, but they are observed between lavas of differing flow band orientations on the sides of the 1886AD fissure (Figure 4.10). A 2 to 5 m wide breccia zone of unconsolidated, angular rhyolite blocks (Figure 4.10B) occurs between southeast dipping and east to northeast dipping bands (Figure 4.10C). The breccia matrix is friable and is not silicified as at Ngongotaha. Differential movement within the breccia zone is difficult to establish as the lithology surrounding the breccia zone is highly devitrified rhyolite with poor flow banding. Matrix supported basal breccias, consisting of large (up to 1.5 m), dense clasts of core facies lavas in an ash matrix are uncovered below interior core facies within the 1886AD fissure. At the southwestern end of the 1886AD fissure, interior core facies lava is observed over-riding basal breccia subfacies (Figure 4.9) which represents the boundary between Ruawahia and Crater domes. Talus breccia in the carapace facies is observed on the northwestern edge of the dome, and consists of clasts (up to 0.75 m) of vesicular lavas with little intra-clast matrix. The talus breccia is assumed to compose the large apron of material that surrounds the dome.

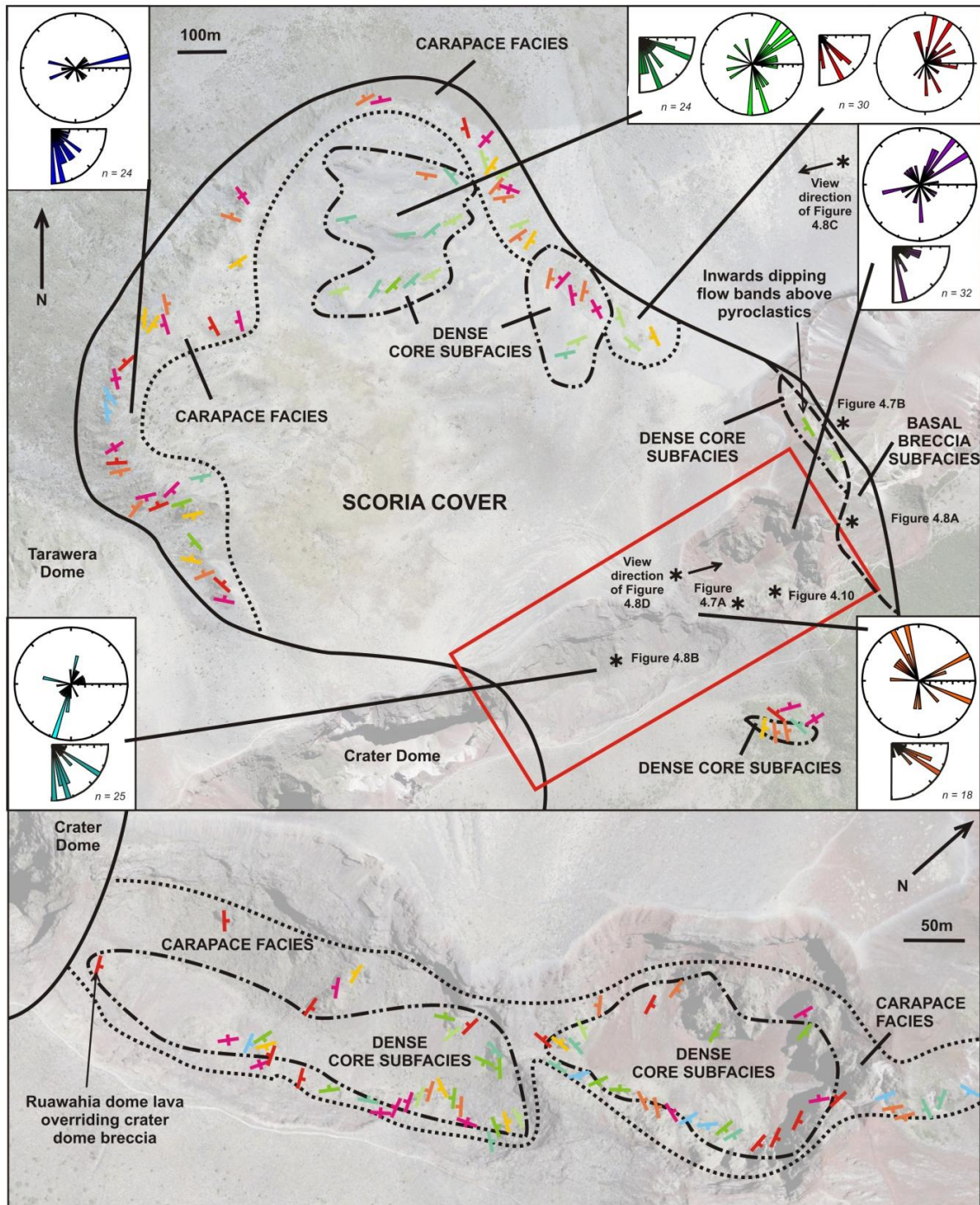


Figure 4.9: Map of flow bands and facies at Ruawahia dome; red box indicates location of bottom map. Warm colours indicate high dip, cool colours indicate low dip. Facies distribution is marked; rose diagrams show strike (circle) and dip (quarter circle) orientations of flow bands at particular areas or in craters. Black stars indicate locations of images in Figures 4.7, 4.8 and 4.10.

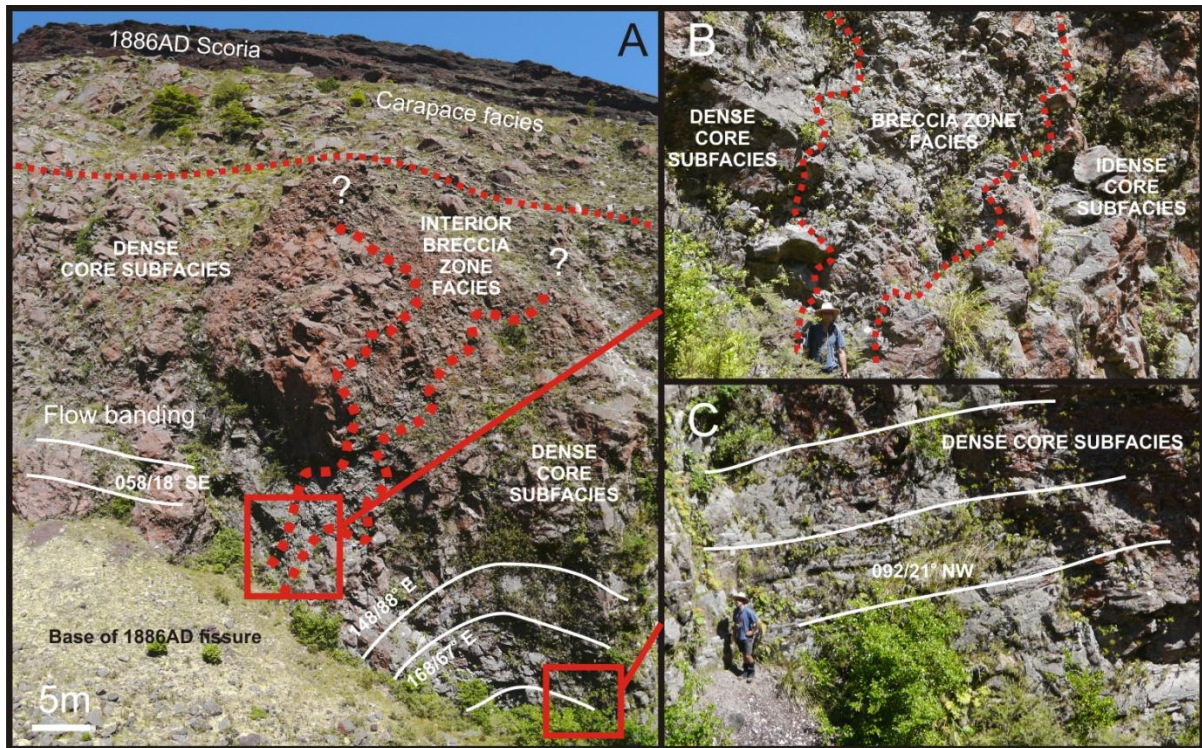


Figure 4.10: A: Overview of breccia zone facies within interior core facies at Ruawahia, with differing flow band orientations on either side. B: Close up of base of breccia zone, showing unconsolidated clasts next to interior core facies rhyolite. C: Interior core facies on right of breccia zone. Figure for scale in B and C.

Flow banding in Ruawahia is generally weak, and exhibits a more complex overall pattern than at Ngongotaha (Figure 4.9). There is no consistent trend in dip or strike, but grouping of dip directions can be used to identify possible vent areas. Ramp structures on the north-western flow lobe all dip towards a vent close to 1886AD fissure with low to moderate dip angles (Figure 4.8C). However, flow banding at outcrops on the edge of Ruawahia are often near vertical, with strike ranging from NE – SW to N – S (Figure 4.9). In 1886AD fissure (within the interior core facies), several groupings of flow bands can be distinguished; in the north-eastern crater, a larger proportion of the flow bands dip to the southeast (Figure 4.9), coinciding with the locations of dense, devitrified rhyolite of

the core facies. At the boundary between Crater dome and Ruawahia domes, flow bands dip back into Ruawahia dome and intact lava is observed over-riding basal breccia facies. Flow banding on the north-western edge of Ruawahia above the pyroclastic deposits dips moderately back into the dome (Figure 4.9).

In summary, the crystal-poor Ngongotaha and crystal-rich Ruawahia domes both show similar exterior and interior facies but each has distinct sheet and breccia facies. The exterior carapace facies is observed at both domes, and consists of a generally elongated pumiceous texture with local ropey skin surfaces, and both domes contain a subfacies of matrix-poor breccias of both dense and pumiceous clasts. A distinct exterior subfacies at Ruawahia is local areas of large rounded vesicles and bread-crusting with little associated preserved flow banding. Both domes are dominated by an interior core facies, that contains strong (Ngongotaha) or weak (Ruawahia) flow banding, which occurs above facies of matrix poor basal breccias (of predominantly dense clasts). At Ngongotaha internal breccias contain more rounded elongate clasts in a coherent matrix interleaved with more obsidian sheets. In addition, the dense interior facies at Ngongotaha is more recrystallised and has stronger flow banding that is convolutedly folded.

Structurally and morphologically these two domes are distinct. Flow bands at Ngongotaha all strike near parallel to the dome axis, whereas at Ruawahia flow bands do not strike parallel to each other. In addition, the lobes studied at Ngongotaha are generally smooth topped and elongate parallel to the dominant flow band strike, whereas at Ruawahia the lobes are elongate perpendicular to the flow direction and contain a more uneven upper surface.

4.4 Discussion

The internal structures of Ngongotaha and Ruawahia domes can be used to reconstruct events during the eruptions. Both domes show a similar transition from pumiceous carapace facies to denser internal facies. The difference in vesicularity of the facies are produced by variations in bubble growth and outgassing, which are in turn controlled by effusion rate, melt viscosity, volatile content and crystallinity (Chapter 3). Flow bands provide evidence to the shape and location of the vent as well as the palaeotopography below the dome. Previous studies at Ngongotaha and Ruawahia (Cole 1970a; Richnow 1999) concluded that the domes were emplaced by a series of viscous flows endogenously inflated from a point source as suggested by onion-skin structures; however, this conclusion does not adequately account for the flow band discrepancies and facies distribution and overall morphology observed at Ngongotaha and Ruawahia.

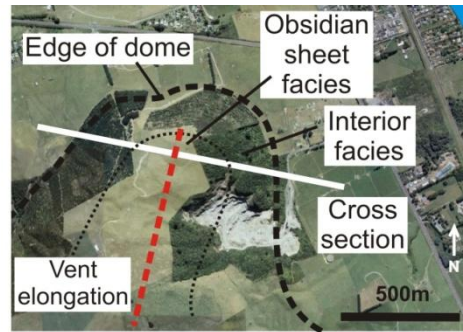
4.4.1 Facies interpretation and eruption sequence at Ngongotaha

Ngongotaha dome erupted onto the relatively flat caldera filling Mamaku ignimbrite. The pumiceous carapace facies of Ngongotaha is the closest representation of the first lava extruded and is the closest approximation of the vesicularity and crystallinity of the lava as it erupted (Eichelberger et al. 1986; Westrich & Eichelberger 1994), although some flow vesiculation may have continued during extrusion (Fink et al. 1992). Shear of near spherical bubbles during extrusion created elongated bubbles (Okumura et al. 2009; Caricchi et al. 2011) and may have lead to formation of flow bands from crystal alignment and outgassing of the bubble network (Manley & Fink 1987).

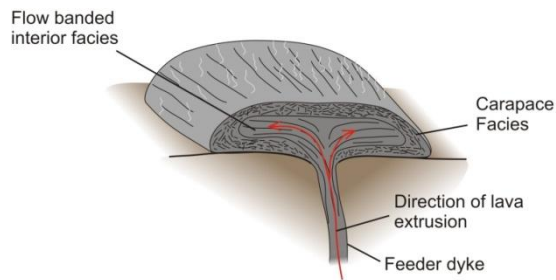
Within the dome interior, compression and shear of the same pumiceous lava formed the dense core facies. The colour differences in the flow banding of the core facies may represent different degrees of bubble collapse (such as that seen by Castro & Cashman, 1999) that then lead to differing devitrification histories that produced the differences in spherulite and microlite growth along the flow bands. Dense, dark flow bands may represent initially collapsed obsidian bands, while the lighter layers represent more vesicular, layers. This difference in vesicularity changed the ability of water to access the obsidian layers, leading to differing devitrification histories. This stratification in vesicularity is also seen in other obsidian flows such as Ben Lomond (Stevenson et al. 1994, von Aulock et al. in review) and in obsidian flows of California (Fink 1983; Fink & Manley 1987; Manley & Fink 1987; Castro & Cashman 1999). The distribution of flow bands in the core facies of the dome have a generally low dip, orientated back towards the axis of the dome, indicating it formed as a lava flow heading away from the dome axis (Figure 4.1B and 4.11, Stage I; Cas & Wright 1988). As the lava moved away from the conduit, a conveyor mechanism transported brecciated pumiceous material from the top and edge to the underneath of the dome (Harris et al. 2004). This slowly cooled and devitrified (von Aulock et al. 2013), forming the devitrified basal breccia subfacies. As the dome grew, the flow front began to stall, causing interior lava to fold (Castro & Cashman 1999), compress and thicken via endogenous growth and convolute folding (Figure 4.11, Stage II; Tuffen et al. 2013). At Ngongotaha, the lack of crystals and relatively high extrusion rate allowed almost complete bubble compression of the interior flow banded facies (Chapter 3), as differing stages of compaction of the pumiceous carapace is observed from blocks within the carapace breccia.

The change from interior flow banded to sheet facies signifies a change in the extrusion style and degassing ability of the dome. In experimental studies by Lavallée et al. (in prep), obsidian is shown to shatter when sheared against obsidian rather than melt to form a discrete pseudotachylyte. The

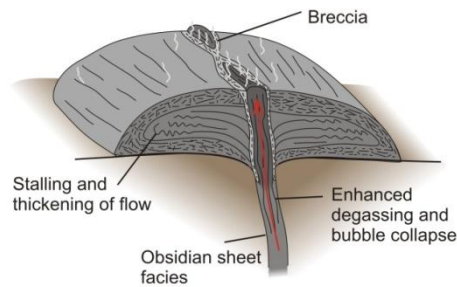
breccia zones at Ngongotaha therefore represent the product of the accumulation of shear strain and subsequent shattering during intrusion of the sheet facies into the interior flow banded facies, similar to fracturing due to shear stress accumulation of unrelaxed magma in conduits (Tuffen & Dingwell 2005). Shapes and sizes of the clasts in the breccias suggest that the damage zone propagated outwards from an initial fracture, creating angular clasts that became progressively rounded and elongated with progressive ductile shear (Storti et al. 2003) or through abrasion. Between the core and sheet facies, a poorly preserved breccia was formed when the first obsidian sheet intruded through the flow banded core facies. Successive obsidian sheets intruded, pushing away previous sheets from the vent and forming the repeated 'obsidian sheet – breccia zone – obsidian sheet' pattern observed in the sheet facies (Figure 4.4, 4.5 & 4.11, Stage III).



Stage I: Extrusion of flow banded interior facies



Stage II: Slowing extrusion rate, intrusion of obsidian sheet facies



Stage III: Multiple obsidian sheet intrusions; end of eruption

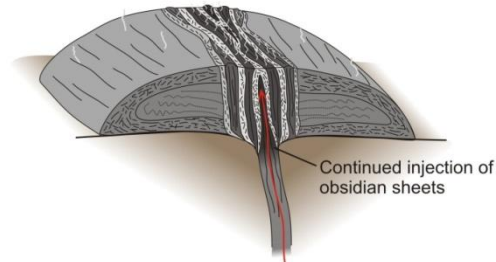


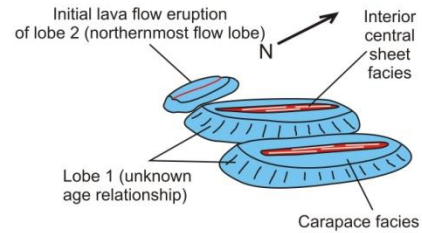
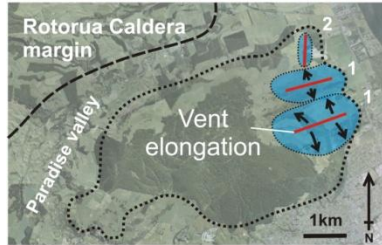
Figure 4.11: Eruption model of lobe at Ngongotaha.

The continuity of the strike of breccia zones and the spherulitic obsidian sheets near parallel to the dome axis suggests that a linear vent fed by a dyke aligned with the dome axis (similar to Tuffen & Castro (2009)). Near vertical flow banding (Figure 4.5) within the spherulitic obsidian and breccia zone subfacies shows near vertical intrusion (Figure 4.11, Stage III) in a process akin to the emplacement of the root of a spine (Cashman et al. 2008). This suggests that the sheet facies was too viscous to flow away from the vent, or was confined and prevented from flowing by previously erupted material (i.e. the initial lava flow of the core facies) in a manner similar to spine emplacement. A lack of morphological evidence of spine extrusion on the top of Ngongotaha dome suggests that the sheets were too thin and unstable to maintain spines above the surface of the dome; the process of comminution of crystal poor lavas is thought to inhibit the extrusion of spines through the lack of a well defined shear zone (Hale & Wadge 2008; Lavallée et al. in prep). Possible relic bubble textures in the sheet facies shows that the spherulitic obsidian may have once been pumice that underwent almost total bubble compaction and outgassing in the conduit to form the dense spherulitic obsidian observed at the top of the dome. The compaction and outgassing of the bubbles in the obsidian sheets may have been due to a longer repose time in the shallow conduit than the core facies, allowing effective vertical degassing, resorption and near total porosity reduction (Westrich & Eichelberger 1994; Mongrain et al. 2008; von Aulock et al. in review). This further suggests that the eruption of the sheet facies coincided with a slowing of eruption rate and, ultimately, end of the eruption.

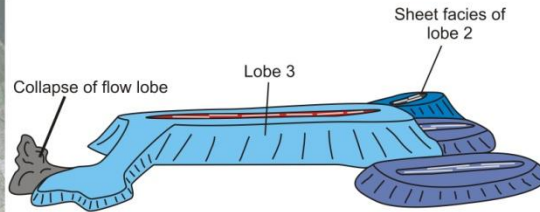
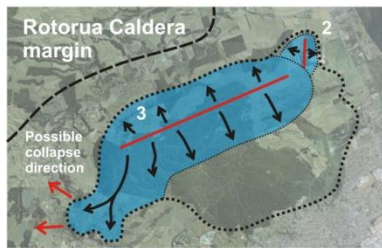
The sequence of eruption lobes at lava domes can be inferred from the morphology of the dome (such as de Silva et al. 1994; Fink & Griffiths 1998). We interpret the elongate nature of other, individual dome lobe eruptions at Ngongotaha to have formed in a similar manner to the northernmost dome lobe as shown in Figure 4.11 and described above. The eruption of Ngongotaha

dome initiated with lobe eruptions at the north-eastern edge of the dome, forming two lobes that have been mostly buried by subsequent extrusions, as well as the northern-most lobe studied here (Figure 4.12, Stage I). This northernmost lobe overlaps the two eastern lobes, suggesting it was extruded afterwards (Figure 4.12, Stage I and II). Following this, a large NE – SW trending dyke extruded a flow lobe on the northern side of the dome. Part of this flow lobe flowed to the south into the modern Paradise Valley (Figure 4.12, Stage II). A second NE – SW trending dyke on the southern side of Ngongotaha, partly confined to the flow lobe into Paradise Valley and to the earlier erupted Pukehangi dome (Chapter 5) (Figure 4.12, Stage III). The final phase of the eruption was a series of extrusions on the southern side of the dome that built the summit area of Ngongotaha (Figure 4.12, Stage IV). The vent to this eruption was not as elongate as other vents, and may represent a transition from a dyke shaped vent to a more central conduit as the summit area is a well defined peak.

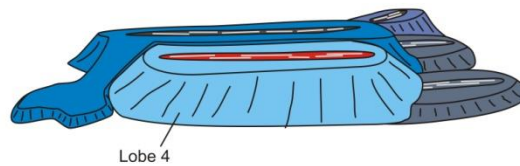
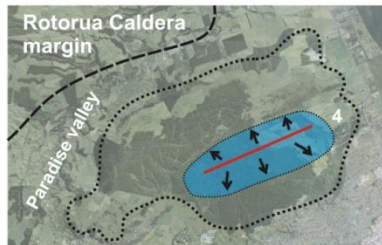
Stage I: Eruption of small lobes on eastern edge of dome, and start of northeastern lobe



Stage II: Northeastern lobe eruption ceases, eruption of large lobe on northern side, producing flow to south



Stage III: Large southern lobe erupts, partially burying eastern lobes



Stage IV: Eruption of summit lobe - confined to small area, resulting in a large lobe than previous eruptions

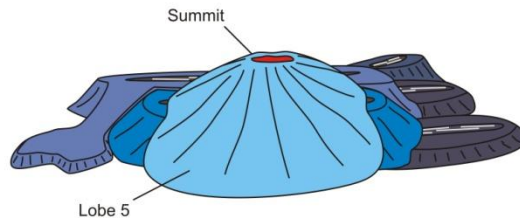
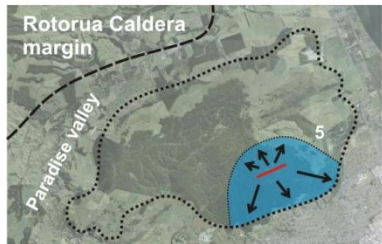


Figure 4.12: Eruption timeline of Ngongotaha dome. The active dome in each stage is highlighted in blue and previously erupted domes in progressively darker shades of blue. The location of the feeder dyke is in red, and black arrows show movement direction of lava away from vent. The lobe in figure 4.11 is the northernmost lobe (2) erupting during stages I and II.

4.4.2 Facies interpretation and eruption sequence at Ruawahia

Ruawahia dome erupted within, and on top of, the Ruawahia tuff cone, and next to the buried Crater dome and the coeval Tarawera dome (Cole 1970b; Nairn et al. 2001). The first eruption of Ruawahia formed the exterior carapace facies of the most devitrified lobes exposed in the 1886AD fissure. Like Ngongotaha, the carapace facies represents the first eruptive phase, and the core facies is the compressed and outgassed equivalent (Chapter 3). 'Ropey' and breadcrust surfaces exposed in the fissure indicate that part of a lobe surface was buried by subsequent lobes (Fink et al. 1992). Ruawahia dome therefore formed by multiple extrusion episodes, rather than a single, thick flow. Small dome-flank failure events during extrusion exposed inner surfaces to atmospheric pressure and temperatures, allowing a small amounts of vesiculation along flow bands (Fink et al. 1992; Scheu et al. 2006) inflating and forming the 'ropey skin' surfaces. These were then buried by subsequent extrusions.

Sequential lobes were forced to over-ride and intrude through each other in a similar manner to the sheet facies at Ngongotaha, creating breccia zones between composite spiny lobes. However, unlike the sheet facies at Ngongotaha, the extrusions have differing flow band orientations (Figure 4.8), suggesting that there were multiple vents along the same dyke-like conduit (Figure 4.9). Flow bands exposed in the northern-most 1886AD crater (within spiny lobes) have moderate to high dips to the south east (~30 to ~80°; Figure 4.8D and 4.9) that suggest that they were pushed out against previously erupted lava, which confined the lobe (Figure 4.13, Stage II and 4.14, Stage II), similar to late stage flow banding in Little Glass Mountain (Fink 1983). The spiny lobes exposed in the 1886AD fissure show generally higher dips than in flow lobes, and have a more uneven top surface. As these domes extruded, they were confined from flowing by either the crater walls of the Ruawahia tuff

cone or from previously erupted lobes. Continued lava extrusion was forced out of the lobes as small spines or ramp structures (Figure 4.13, Stage III), similar to the extrusion of spines following the stalling of previously erupted spines and lobes at Soufrière Hills (Watts et al. 2002a). As the confined spiny lobes grew, they overcame the pressure from ascending magma and shut off the extrusion (Bull et al. 2012), meaning that no spiny lobe was able to overcome the pyroclastic cone crater before the extrusion finished. Extrusion then shifted to another vent (Figure 4.14).

On the top of the northwestern lobe, ridges with interior core facies have extruded through the carapace facies. Flow bands dip at 30 to 40° towards the summit of Ruawahia (Figure 4.9), suggesting that the ridges represent ramp structures up-thrust in a lava flow from a vent close to the 1886AD fissure or pressure ridges from continued extrusion of material once the flow front has stopped (Figure 4.13, Stage IV; Cas & Wright 1988). The flow banding observed on the ridges all follows a similar orientation that dips back towards the 1886AD fissure. Pressure ridges would form anticline-like flow band patterns; this is not observed, and so ramp structures are suggested to be the cause of these ridges. Steep flow bands at the very edge of the NW dome lobe suggest that the leading edge of the dome stalled, causing material behind to bulldoze it, creating ramp structures and thickening the flow (Figure 4.13, Stage IV), similar to that at Rauðufossafjöll, Torfajökull, Iceland (Tuffen et al. 2013). The mechanism for ramp structure extrusion from the flow lobes is similar to that in the spiny lobes. The multiple vents at Ruawahia describe a NE – SW orientated vent zone that encompasses the area of the 1886AD fissure and summit of Ruawahia (Figure 4.14). This vent zone strikes 057° (ENE – WSW; Figure 4.2; Nairn & Cole 1981), and through which dykes associated with previous eruptions, such as the 1886AD basaltic dyke, have intruded. It is most likely related to the rifting across the OCC which also trends ENE – WSW (Rowland & Sibson 2001; Seebeck et al. 2010).

Timing of the vents of Ruawahia can be inferred from flow band directions, and to a lesser extent, the degree of devitrification of each lobe (Figure 4.14). The first flow lobe (lobe 1) erupted from underneath the summit, was able to flow for approximately 0.75 km to the northwest (Figure 4.14, Stage I). Two lobes were then erupted within the crater of the Ruawahia tuff cone (lobes 2 and 3), which, along with lobe 1, limited their lateral extent. These formed small spiny lobes, creating breccia zones as they intruded through other lavas (Figure 4.10). Flow banding suggests that spiny lobe 2 extruded to the southeast inside the Ruawahia tuff cone crater, and spiny lobe 3 to the northwest against lobe 1 or the crater wall (Figure 4.14, Stage II). Another small spiny lobe (lobe 4) was erupted from a vent to the west of lobes 2 and 3, and erupted lava to the southeast, also constrained by the Ruawahia tuff cone (Figure 4.14, Stage II). Flow lobes 5 and 6 erupted from similar vents as flow lobes 1 and spiny lobe 4, and were able to flow to the northwest for over 1 km. These flows were unconstrained by the Ruawahia tuff cone crater, but were restricted on either side by flow lobe 1 to the NE and Tarawera dome to the SW (Figure 4.14, Stage III). The southern flow lobe (lobe 7) was also erupted during this time and flowed to the south-southwest, against the breccia of Crater dome in the southwestern part of the 1886AD fissure. It is likely sourced from a similar vent to spiny lobe 2, although outcrop is limited on this lobe. All spiny lobes were extruded in the first two stages of the eruption (Figure 4.14), suggesting a progressive migration of vents away from the initial dyke intrusion in the location of the 1886AD fissure.

Ruawahia can be translated directly into English from Māori as 'pit' (rua-) and 'tearing' (-wahia), suggesting that the morphology on the summit of the dome had a cleft or fissure in it. This could be the slight gap between the spiny lobes, constrained by the Ruawahia tuff cone crater, and flow lobes on the flanks of the cone (Figure 4.13). However, this feature, if present, has since been buried by scoria from the 1886AD eruption, which is up to 75 m thick near vent (Carey et al. 2007).

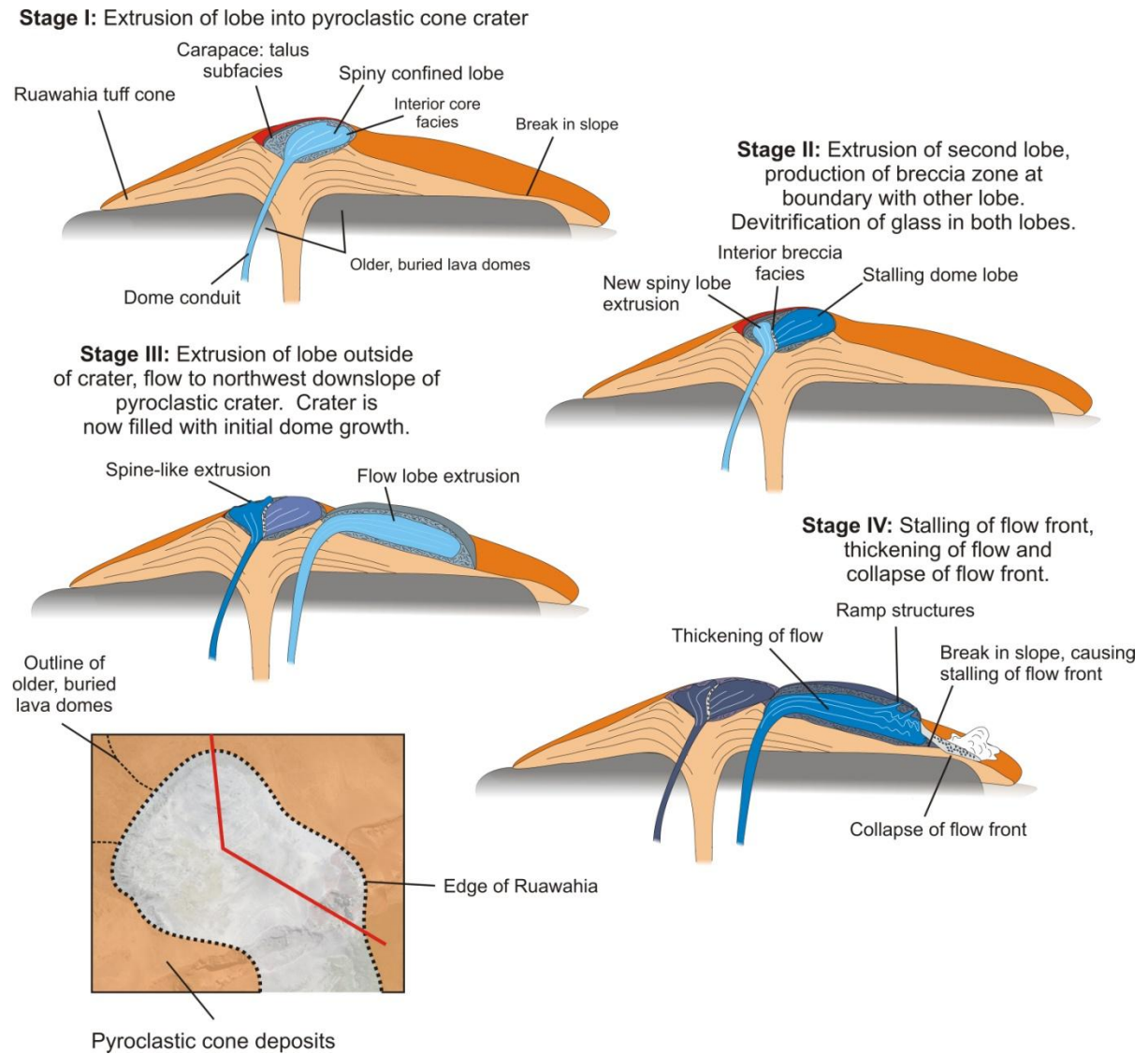


Figure 4.13: Eruption model of Ruawahia dome through cross section along red line on map (bottom left). Pyroclastic deposits are shown in orange, while domes are shades of blue; darker blues indicates older domes.

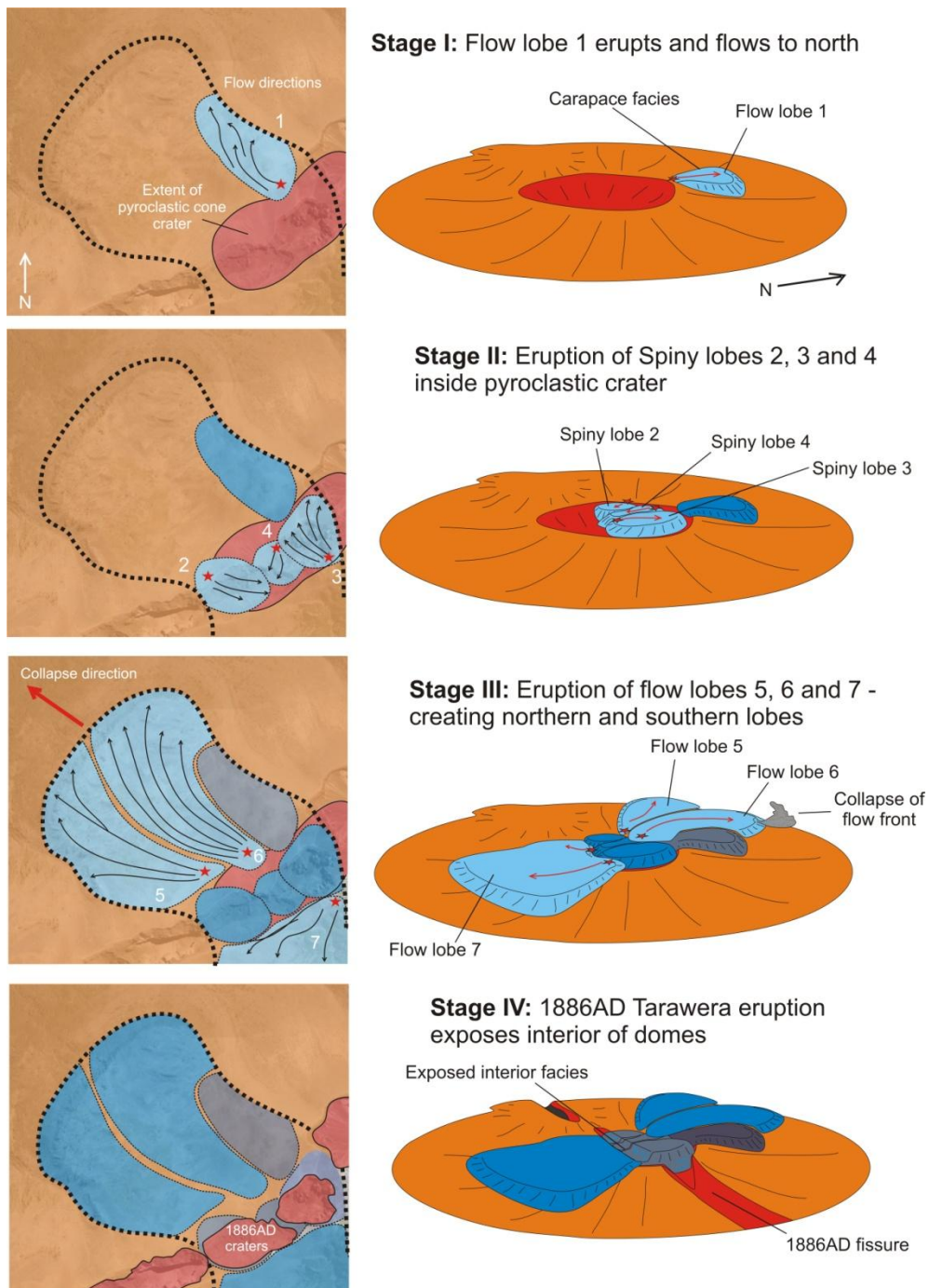


Figure 4.14: Eruption timeline of lobes at Ruawahia dome. Pyroclastic deposits are shown in orange, craters are red and lava domes are shades of blue; darker blues indicate older lobes. Black arrows show movement of lava away from vent (red stars).

4.4.3 Comparison of extrusion styles between Ngongotaha, Ruawahia and other domes worldwide

The variation of dome eruption style at Ngongotaha and Ruawahia can be attributed to properties of the vent/conduit, lava and palaeotopography. I suggest that both Ngongotaha and Ruawahia erupted from elongated or aligned vents which are dyke controlled.

At Ngongotaha, flow band orientations suggest a N – S orientated dyke-controlled conduit. The initial extrusion of pumiceous material produced a short lava flow with a pumiceous upper carapace, basal breccia and flow banded facies; facies which are similar to the small volume lava domes overlying an obsidian dyke at Krafla, Iceland (Tuffen & Castro 2009). This extrusive dyke shows near vertical flow bands directly above the vent, which strike parallel the elongation of the dyke (Tuffen & Castro 2009), similar to Ngongotaha. At Ngongotaha, a change from compacting pumiceous, endogenous flow lobes to dense, confined obsidian sheets suggests a change in vesicularity and viscosity in the conduit. No change in primary crystallinity or in geochemistry occurs between facies, so the viscosity increase was likely caused by a reduction in volatile content due to bubble growth (von Aulock et al. 2013) and bubble collapse from effective degassing and densification (Chapter 3). I propose that a decrease in effusion rate allowed complete degassing of the sheet facies by increasing the time spent degassing in the conduit during ascent. Coupled with an increase in confining pressure from previously erupted material, this forced the denser, more viscous rhyolitic lava through the interior core facies, creating the breccia zone and obsidian sheet subfacies (Figure 4.11). The decrease in effusion rate may have also directly preceded the end of the eruption. During the 1990 – 1995 eruption of Unzen, Japan, a change from exogenous to endogenous growth phase was marked by a reduction in effusion rate (Nakada et al. 1999). It is suggested that the effusion rate controlled the effusive porosity of the lava (Nakada & Motomura 1999), leading to an

increase in bubble compaction, an increase in viscosity and creating a plug. In contrast, the Soufrière Hills lava dome exhibited cyclical behavior of megaspine growth with low effusion rate, and shear lobe extrusion during high extrusion. Little published data exists of changes in vesicularity of the dome at Soufrière Hills, but explosive products show a large variance in vesicularity (Burgisser et al. 2010). A change in extrusion style was noted at Redoubt Volcano during the 2009 eruption by Bull et al. (2012), when vesicular lava covered the dome surface, extruding from cracks on the dome surface. Progressive degassing of magma formed a plug over the conduit and shut off the eruption (Bull et al. 2012). Evolution of the 2011 Cordón Caulle eruption is also thought to have occurred from transitions between foamy and dense magma, resulting in the simultaneous eruption of an obsidian flow with jetting of pumiceous material (Castro et al. 2013; Schipper et al. 2013). I suggest that changes in extrusion rate and vesicularity will induce shifts in extrusion style, and drastically alter the hazard potential of a lava dome.

At Ruawahia, individual flow lobes and spiny lobes were extruded from a series of aligned vents that together define NE – SW trending dyke. The flow lobes flow perpendicular to the vent alignment, similar to flows at Medicine Lake Highland volcano (California) (Fink & Pollard 1983) and Cordón Caulle (Lara et al. 2004). The Cordón Caulle lavas flow away from the aligned vent system, producing compound lava flows (Tuffen et al. 2013), also similar in morphology to long lava flows sourced from Santiaguito dome (Harris et al. 2003) and Chao dacite flow (de Silva et al. 1994). At Ruawahia, the change from the carapace facies to interior facies is also attributed to viscosity controlled compaction in the conduit and dome (Chapter 3). However, the transition between spiny lobes and flow lobes was also affected by pre-eruption topography. The Ruawahia tuff cone formed prior to the extrusion of Ruawahia dome (Cole 1970a; Nairn et al. 2001) and provided a catchment for lobes erupted within the crater. These lobes formed steeply dipping flow bands as lava was

squeezed up and out of the conduit in a confined area, and may have extruded breccia-bounded spines in a similar manner to breccia formation at Ngongotaha (Figure 4.13, Stage II). Simultaneous spiny and flow lobe extrusion was observed during the 2008 to 2009 Chaitén eruption inside the caldera crater left by the initial explosive eruption (Lara 2009). These lobes erupted both endogenously and exogenously, and were forming spines, extruding shear lobes and inflating simultaneously (Bernstein et al. 2013). This behavior is attributed to changing effusion rates, viscosity, intrusion pathways and multiple vents (Bernstein et al. 2013) which are suggested to be dyke fed (Wicks et al. 2011). At Ruawahia, flow lobes that were either erupted outside of the crater, or were able to overcome the crater wall due to larger effusion volumes, were able to flow freely down the slope of the cone in a NW and SE direction (Figure 4.13, Stage III and Figure 4.14). Crater and Tarawera domes prevented any flow to the SW and inward dipping flow bands to the NE of the fissure suggest no flows were able to overcome the crater wall there (Figure 4.9 and 4.14). Flows then reached a break in slope between the pyroclastic cone, earlier buried domes (Cole 1970b) and surrounding plains, and collapsed to form block and ash flows. Confined dome growth during the 1984 to 1996 Lascar Volcano eruption (Matthews et al. 1997) and 2011 Shinmoe-dake, Japan (Kozono et al. 2013) formed flat topped domes whose morphology was controlled by drain-back or compaction processes (Matthews et al. 1997). At Shinmoe-dake plugging of the main conduit forced magma to erupt at the edges of the growing dome (Miyabuchi et al. 2013), suggesting that a dome of sufficient size will be able to shut off extrusion, and force magma laterally. This is similar to new spiny lobe growth within the pyroclastic crater at Ruawahia intruding past previous extrusions from different vents.

4.4.4 Block and ash flow production at Ngongotaha and Ruawahia

The eruption of Ngongotaha is not associated with widespread explosive block and ash flow deposits (Dravitzki 1999) while the eruption of Ruawahia and associated domes produced large block and ash flows to the NW, NE and SW of Tarawera dome complex (Nairn et al. 2001). At both domes, some small dome collapse which form talus aprons occurred during all extrusion episodes; however, large explosive block and ash flows are only recorded at Ruawahia, suggesting that the palaeotopography or differences in crystal or volatile content between the domes may have been an important factor in the production of explosions following dome collapse. At Ngongotaha, all but the final dome lobe eruptions (Figure 4.12, Stage IV) were onto near flat topography created by caldera infill, while at Ruawahia palaeotopography was created by the pyroclastic cone and underlying dome complex (Nairn et al. 2001). Gravitational failure of a lava dome will occur due to over-steepening of a flow front leading to weakening of the dome, a process which readily occurs on slopes (Nakada et al. 1999; Voight et al. 2000; Sparks et al. 2000; Platz et al. 2012) and may be associated with periods of high effusion rate (Calder et al. 2002). Physical characteristics such as melt viscosity, crystallinity and vesicularity will also affect whether the lava forms microfractures and weakens (Chapter 3; Lavallée et al. 2013; Kendrick et al. 2013). Ngongotaha and Ruawahia share a similar melt viscosity and the initial eruptive products have similar vesicularities (Chapter 3), but Ruawahia has a much higher crystallinity (~60 % DRE) than Ngongotaha (<10 % DRE). Under sufficient load, a crystalline lava will produce multiple cracks (Chapter 3) which weaken the overall strength of the rock so that collapse becomes more likely (Kendrick et al. 2013).

Porous lavas require a lower fragmentation threshold before failure. Above 20 % porosity, the fragmentation threshold is lower than 5 MPa (Spieler et al. 2004). Conversely, lower porosities (and

associated lower permeability) require a higher threshold energy for fragmentation (Mueller et al. 2008). Ruawahia samples collapse to ~20 % vesicularity, and form multiple cracks in crystals (Chapter 3); however, these cracks do not increase the permeability drastically (Chapter 3). The combination of these properties suggests that Ruawahia lava requires a high internal pressure within bubbles in order to spontaneously fragment during collapse of a flow front, forming a widespread block and ash flow deposit..

Crystalline lavas are more viscous than non-crystalline lavas at similar temperatures and compositions (Lavallée et al. 2007; Cordonnier et al. 2009; Mader et al. 2013), leading to thickening and over-steepening of the flow front. The collapse of Ruawahia flows was caused by over-steepening due to increasing viscosity of the lava (from cooling and crystallisation) and reaching a break in slope (between pyroclastic beds and older, buried lava domes). Once gravitational collapse started, weakening of the lava due to microfractures, lead to the explosive decompression of the interior of the dome. The hot, pressurized interior then vesiculated, forming the 'ropey' skin texture and highly vesicular collapse scars. Extensive fragmentation did not occur at Ruawahia during dome failure due to the high internal bubble pressure required to fragment the lava. Instead, the hot, pressurized interior vesiculated rapidly when exposed to atmospheric pressure following dome failure. I suggest that the collapse of unconfined flow lobes 1, 5, 6 and 7 were the source for the extensive block and ash flows around Tarawera (Nairn et al. 2001; Hanenkamp 2011).

At Ngongotaha, high permeability from fracturing of the lava on micro- and macro- scales reduced the risk of explosive decompression but may have also weakened the dome. The transition to confined sheet extrusions and this increased permeability may explain the lack of significant block and ash flows at Ngongotaha. Small dome collapse events are likely to have occurred to form a talus

apron around the dome. The final stage of lava dome growth at Ngongotaha may have formed the prominent peak (Figure 4.12, Stage IV), which shows a significant topography was formed at this stage. Small block and ash flows from gravitational collapse (and possible small scale explosivity) at Ngongotaha may have also been buried by the subsequent post-caldera lake; several pyroclastic flows have been described to the northwest of Ngongotaha, but only one was geochemically linked to Ngongotaha (Dravitzki 1999). A small, unconfined lava flow on the southwest side of Ngongotaha (Figure 4.12, Stage II) may have been the source of this block and ash flow (Dravitzki 1999). However, no large, explosively driven block and ash flow, comparable to those at Ruawahia, have been described around Ngongotaha.

4.5 Conclusions

Here, I have presented internal structural and facies changes within the domes of Ruawahia and Ngongotaha that strongly supports that these eruptions were fed from dyke-controlled vents. The near constant N – S orientated flow bands and orientations of obsidian sheet facies at Ngongotaha suggest an eruption from a N – S trending, dyke-sourced vent. In contrast, the flow bands at Ruawahia indicate that a series of lobes and flows erupted from several separate vents aligned in a NE – SW vent zone beneath the summit crater and 1886AD fissure, which I interpret as being fed by a dyke. The dykes were controlled by local caldera collapse or regional extensional structures. Changes from exogenous, spiny lobes or obsidian sheet-forming to flow lobe-forming (or vice versa) can be attributed to a change in effusion rate or in effective degassing and viscosity, or from interactions with the pre-eruption topography. The dense, crystal-free nature of the obsidian at Ngongotaha indicated it was better able to heal and less likely to fail and form block and ash flows. At Ruawahia, porous, crystalline and fractured interiors of unconfined flows, which overlie pre-

existing topography, indicate a propensity to fail catastrophically. Stalling of a flow front at a break in slope caused thickening and bulldozing of the flow leading to block and ash flow production, suggesting that eruption style, morphology and palaeotopography have a strong control on block and ash flow production.

Preamble

In the previous chapter I discussed the eruption models of Ngongotaha and Ruawahia domes. I concluded that both domes were the result of dyke-fed eruptions that controlled the locations of vents as well as the distribution of internal structures within the domes. I postulated that the NE – SW alignment of the vents of Ruawahia was controlled by a similarly-trending dyke, itself controlled by extensional regional structures in a similar orientation. However, the dyke that fed the northernmost Ngongotaha dome lobe trends in a N – S orientation, which is harder to attribute to the regional or basement structures, as structures in Rotorua are not well mapped. In this chapter I explore the structure of Rotorua caldera, and attempt to link the dyke-fed dome eruption to the collapse of the caldera or the ongoing extension within the TVZ.

This chapter was published in Journal of Volcanology and Geothermal Research as:

P.A. Ashwell, B.K. Kennedy, D.M. Gravley, F.W. von Aulock and J.W. Cole. 2013. Insights into caldera and regional structures and magma body distribution from lava domes at Rotorua Caldera, New Zealand. Journal of Volcanology and Geothermal Research. 258, pp 187-202.

It therefore includes some overlap in the description and interpretation of internal structures of Ngongotaha dome with Chapter 4, and where appropriate I have included references to previous chapters in these cases. A copy of the journal article is included in Appendix C.

Chapter 5

Insights into caldera and regional structures and magma body distribution from lava domes at Rotorua caldera, New Zealand

Lava domes emplaced after caldera-forming eruptions are often the only clue to the structure of the caldera and to the regional structure at the time of caldera formation. This is because the deposits from the subsequent eruptions commonly bury subsidence-controlling caldera faults and regional cross faults within calderas. Other calderas and lava domes in the TVZ have been previously reported to show strong regional control. At Rotorua caldera there is a general lack of surface expression of faults, but rhyolite lava domes are well exposed and aligned with regional structures that have been mapped outside of the caldera. The summary of published data and new observations allow these lava domes to be subdivided into three groups based upon their petrology, geochemistry, relative age and spatial distribution: (1) the Kaikaitāhuna group of pre-collapse (451 ka), crystal-rich domes at the caldera boundary, (2) the Utuhina group of crystal-poor, high alkali, post-collapse domes (c. 200 ka) surrounding the locus of collapse and directly related to the earlier (240 ka) Mamaku ignimbrite eruption, and (3) the Ruamata group of crystal-rich, more calcic, less devitrified post-collapse (60 – 36 ka) domes further out from the collapse locus. Mapping of the morphology and internal structures of the Utuhina group domes shows an ENE – WSW elongation direction and vent alignment, which are parallel to and down strike of (A) the extensional rift

orientation independently mapped either side of the caldera, (B) the local caldera morphology and (C) structures mapped at the nearby OCC. A second NW – SE trending orientation in the caldera morphology is parallel to a pre-collapse basement fabric, and has partially controlled the locations of the domes. A third orientation is hinted at through consistent N – S striking flow bands within Ngongotaha dome, which are parallel with a gravity anomaly. I suggest that this orientation is a N – S section of a caldera ring fault that links regional structures and was utilised during caldera collapse. Subsequent dyke intrusion also used this structure, erupting a fissure-style dome that contains radiating flow bands which mimic the orientation of the feeder dyke. However, the structure, morphology and location of post-collapse lava domes generally echo the unburied regional structures outside the caldera indicating that dyke intrusion also occurred along regional structures. I suggest that the regional structures at Rotorua caldera, which are similar to those at the OCC, show that the kink in the orientation of the rift across the TVZ to the SE of Rotorua was active to at least 240 ka, and possibly earlier. This kink is significant due to its proximity and influence on both Rotorua caldera and the OCC and their associated geothermal fields. I conclude that internal structures, such as flow bands and morphology of lava domes are a direct consequence of the shape and location of the feeder dyke, which in turn is controlled by the structure of the caldera and region. I also suggest that the lava dome eruptions at Rotorua were from a series of small, related nested magma bodies. A key outcome of this chapter is the reconstruction of the wider structure of the caldera and surrounding structure based upon the localised internal features, distribution, and morphology of related lava domes.

5.1 Introduction

The structure, location, morphology, and chemistry of lava domes are important in understanding the interplay between caldera-forming eruptions and tectonics. The association of lava domes and large plinian or caldera-forming eruptions has been well documented in the TVZ, and other volcanic systems (Cole 1970b; Irving et al. 1980; Wilson et al. 1984; Nakada et al. 1995; Wilson et al. 1995; Fink & Anderson 2000; Platz et al. 2012).

The calderas of TVZ show a strong regional structural control on their morphologies and eruptive histories (Cole 1990; Wilson et al. 1995; Spinks et al. 2005), and pre-existing fault structures have acted as pathways for eruption of ignimbrites and lava domes (Walker 1984; Cole & Spinks 2009). Caldera collapse structure controls the location of domes at Valles caldera (Smith & Bailey 1968; Heiken et al. 1990; Kennedy et al. 2012) and at the Ubinas-Huaynaputina-Ticsani Volcanic Group, Peru (Lavallée et al. 2009), while the domes of the Inyo Crater Chain and Mono Craters strongly follow the Hartly Springs regional Fault (Vogel et al. 1989; Hildreth 2004), which shares a similar orientation to the faults that control resurgent doming in the Long Valley caldera to the SE (Bailey et al. 1976; Holohan et al. 2008a; Bursik 2009). In extensional regimes dykes intrude parallel to, or within pre-existing faults (Fink & Pollard 1983; Walker 1999; Ziv & Rubin 2000; Seebeck & Nicol 2009). In tectonically controlled areas, such as the TVZ, the locations of lava domes can be directly linked to the regional structure. Domes linearly aligned along major regional faults in the TVZ include the Maroa dome complex (Leonard 2003), as well as the Tarawera and Haroharo dome complexes (Cole et al. 2010). Modern day hydrothermal systems still use these regional pathways (Rowland & Sibson 2004), and it has been shown that buried lava domes can serve as conduits for hydrothermal flow (Rissmann et al. 2011).

Recent work on the OCC (Cole et al. 2010; Figures 5.1B and 5.1C), has shown that reactivation of basement structures and pre-existing rift faults can have a major impact in the geometry and location of caldera collapse structures (Seebeck et al. 2010), leading to an irregularly shaped caldera controlled by the underlying structure. Curved faults at the surface can be produced by subsidence from eruption and/or evacuation of a magma chamber (Martí et al. 1994; Kennedy et al. 2004; Holohan et al. 2005; Acocella 2007), leading to circular-shaped calderas in both natural and experimental settings. Additional subsidence structures may develop as regional tectonics interact with caldera structure (Moore & Kokelaar 1998; Acocella et al. 2002; Holohan et al. 2008b; Petrinovic et al. 2010) such as the Horohoro fault, observed south of Rotorua caldera, which is associated with post-eruptive subsidence related to the Rotorua and Ohakuri caldera-forming eruptions (Gravley et al. 2007). In many calderas, the underlying structure from the collapse or the regional setting has been covered by younger deposits, such as Campi Flegrei (Orsi et al. 1996; Acocella 2010) or Pine Canyon caldera (Drenth & Finn 2007), or by post collapse lakes, such as Taupo (Wilson et al. 1995). In these cases, the post collapse lava domes are often the only remaining volcanic feature not buried. The intra-caldera structure of Rotorua caldera is obscured both by the presence of Lake Rotorua, and its deposits, as well as the presence of significant syn-collapse intra-caldera ignimbrite.

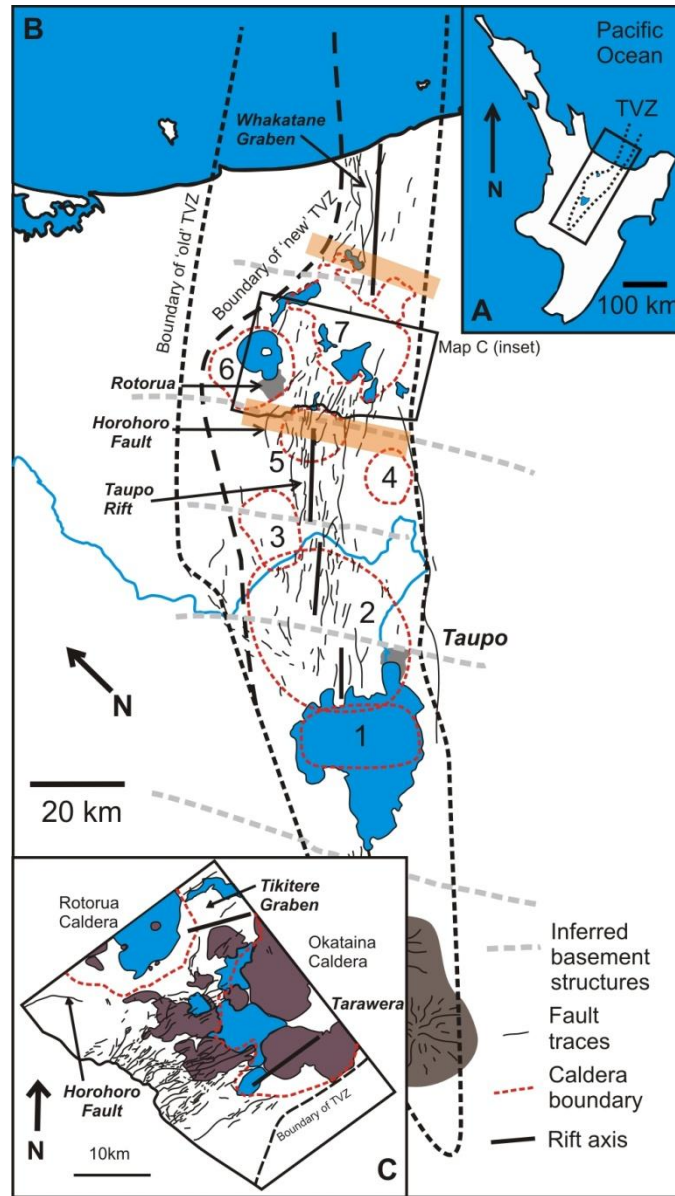


Figure 5.1: Map of the TVZ (See inset A for location in North Island, New Zealand), showing locations of calderas; 1 = Taupo; 2 = Whakamaru; 3 = Ohakuri; 4 = Reporoa; 5 = Kapenga; 6 = Rotorua and 7 = OCC. Superimposed are inferred basement structure orientation (grey dashes lines), major fault traces of the Taupo Rift (small black lines) and rift axes (thick black lines). Orange box is approximate area of pronounced kink in fault orientations across the OCC and Rotorua calderas. Black box denotes location of inset C; a detailed structural map of the OCC, with main areas of extension at Tarawera and the Tikitere Graben. Purple masses are lava domes. The 'young' and 'old' TVZ boundaries show the limits of volcanism and extension of the current ('young') and initial ('old') TVZ location. Data from Cole et al. (2010) and Rowland and Sibson (2001; 2004).

The internal structures of lava domes, such as flow bands and fractures, are directly linked to the method of extrusion, and have been used to reconstruct the morphology of eroded domes (Stasiuk et al. 1996). Flow banding in lava domes can be created during viscous flow during ascent in the conduit, and to a lesser extent, during dome growth. Velocity gradients within the conduit create viscous shear strain along bands (Gonnermann & Manga 2005; Hale & Wadge 2008). This shear elongates and flattens bubbles, and aligns both phenocrysts and microlites (Smith et al. 1994) into banding that can be used to determine the direction of flow. In dykes, the direction of flow bands are parallel to the dyke margin and usually vertical (Tian & Shan 2011; Figure 5.2C), and in lava directly above the conduit, the dip of the flow banding is commonly high (Tuffen & Castro 2009). The flow banding in a dome or lava flow can therefore help distinguish the shape or location of the conduit. A lava dome produced from a point source (i.e. a circular conduit) will have radiating flow banding that varies from near vertical above the conduit, to near horizontal, or even dipping away, at the edges of the dome (Cas & Wright 1988; Fink & Anderson 2000; Figure 5.2A). In this case the first eruptive products can flow or move unimpeded away from the conduit, while later eruptive material intrudes steeply above the conduit. Flow banding in the interior of lava flows is generally more horizontal with a folded upper surface (Fink 1980), and often dips away from the vent if the lava flow is down slope. The older lava in a flow does not impede newer lava from moving away from the vent as much, and so there may be no near vertical flow bands at the conduit (Cas & Wright 1988; Figure 5.2B). Lava flows can also show complex flow folding of the flow bands in the upper part of the flow due to variations in the localised flow conditions (Fink 1980), or by localised viscosity variations (Castro & Cashman 1999). Flow folding causes a large range in dip, although strike should remain similar to that in pre-folded lavas assuming the cause of folding was stalling of the sides of the dome.

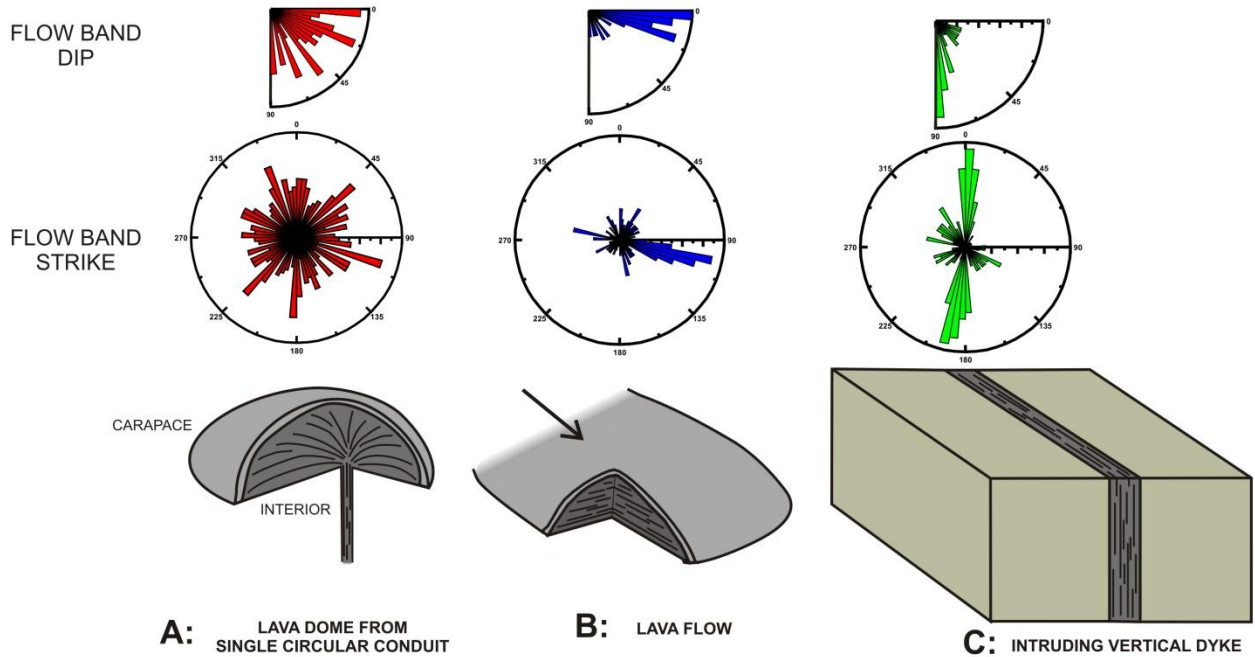


Figure 5.2: Diagram of flow bands from 3 types of conduits, along with rose diagrams illustrating a hypothetical expected distribution of strike orientations and dip variance. A is a single conduit-sourced lava dome eruption, B is a lava flow and C shows flow bands within a dyke.

The chemical composition of lava domes gives insights into the underlying magmatic plumbing system. For example, the chemistry of lava domes at the Valles caldera reveal an intricate magmatic system and magma batch intrusion history (Wolff & Gardner 1995). In addition, the chemistry of lava domes (such as overall silica content) affects their morphology and stability (Fink & Griffiths 1998), which in turn will control the domes ability to shed material and create block and ash flows, which pose a significant threat to human populations (Watts et al. 2002b).

5.1.1 Regional setting

The TVZ is a large volcanic system dominated by silicic and andesitic volcanism. It is located in the central North Island, New Zealand (Figure 5.1A), and was created by the oblique subduction of the Pacific plate underneath the Australian plate (Cole & Lewis 1981; Spinks et al. 2005), producing an area of thinned crust (Bibby et al. 1995) by intra-arc rifting (Cole 1990; Wilson et al. 1995). Volcanism commenced at approximately 2.0 Ma with the onset of andesitic calc-alkaline volcanism. The first ignimbrite eruptions are noted at 1.68 Ma from the Mangakino volcanic centre (Houghton et al. 1995), with 35 recorded ignimbrites from the whole TVZ producing an estimated bulk volume of 15 – 20,000 km³ (Wilson et al. 2009). Rhyolite comprises the vast majority of the material erupted, with minor amounts of andesite, dacite and basalt mainly erupted in the southern and northern parts of the TVZ. Caldera volcanism and associated dome growth is mostly rhyolitic in composition with minor basaltic eruptions. There are 7 active or dormant calderas in the ‘young’ TVZ (Figure 5.1B).

The main extensional fault trend of the TVZ is NE – SW. The rift is split into several offset segments between accommodation zones that show soft-linkage of each segment (Rowland & Sibson 2001). These accommodation zones match with transfer zones suggested by Acocella et al., (2003), which represent a shift from oblique to normal extension of the rift. A pronounced kink in the rift axis trend occurs to the southeast of Rotorua caldera, where it changes from NE – SW to ENE – WSW across the OCC, before returning to NE – SW in the Whakatane graben to the northwest of Rotorua caldera (Figure 5.1B and 5.1C). Rowland and Sibson (2001) suggested that the active extension locations in the accommodation zone across the OCC are at the Tarawera dome complex and at the current Tikitere graben in the NE of Rotorua caldera (Figures 5.1C and 5.3), both of which exhibit differing extension directions to the rift axis in the south. A second structural orientation,

orthogonal to the main rift, is apparent from pronounced offset of each segment across the accommodation, or transfer, zones and is attributed to reactivated basement structures (Rowland and Sibson 2001; Figure 5.1B). These are likely to be relic structures (such as faulting) in the basement greywacke rocks that underlie the TVZ (Mortimer 2004). At the OCC, hard-linkage of the offset rift axes on these reactivated basement structures defines the shape of the caldera (Seebeck et al. 2010). The dominant NE – SW trending regional structure of the TVZ is clearly visible south of Rotorua caldera, where there is a high density of normal fault traces. The NW margin of these structures is bounded by the prominent and arcuate Horohoro fault scarp, which is interpreted to be a post-eruptive subsidence feature related to the paired ignimbrite eruptions of the Mamaku and Ohakuri ignimbrites (Gravley et al. 2007). The shape of the Horohoro fault (Figure 5.1B), and therefore the geometry of the post eruptive subsidence, may reflect the change in extension rift axes orientation that defines the aforementioned ‘kink’.

Rotorua caldera, located in the northern part of the TVZ (Figure 5.1B), is a large caldera that has produced one of the most widespread ignimbrites in the TVZ; the Mamaku ignimbrite, which covers >3200 km² (Wilson et al. 1984; Milner et al. 2002; Milner et al. 2003; Gravley et al. 2007; Cole & Spinks 2009) concurrent with the collapse of the caldera. Although the ignimbrite itself is well documented, the post caldera collapse domes are only mentioned briefly in scientific literature (Dadd 1992; Wood 1992; Milner et al. 2002; Cole & Spinks 2009). At Rotorua caldera, a postulated criss-cross pattern of basement and rift structures defines the margin of the caldera and individual blocks (see Figure 5.4) that Milner et al. (2002) suggested to have formed during eruption of the Mamaku ignimbrite. The age of the Mamaku ignimbrite has recently been confirmed as 240+/- 11 ka (hereafter taken to be 240 ka; Gravley et al. 2007). The main eruption phase of the Mamaku

ignimbrite produced an ignimbrite with a minimum volume of 225 km^3 ($>96 \text{ km}^3$ dense rock equivalent; Milner et al. 2003).

Caldera collapse is believed to have occurred throughout the entire eruption due to the presence of different pumice types throughout the eruption and variations in lithic clast content, but was particularly prevalent during the period when the middle and upper phases of the ignimbrite were emplaced. Previous work has concluded that the Mamaku ignimbrite eruption produced a tectonically controlled, asymmetric, multiple block collapse of the caldera (Milner et al. 2002; Milner et al. 2003), with significant downsag at the caldera margin (Walker 1984; Milner et al. 2002; Acocella 2006). Today, Rotorua caldera lies approximately 10 km NW of the main rift axis (Figure 5.1B); however, the caldera may not have always been on the periphery of the rifting.

In this chapter, I present links between the internal structures of a lava dome, and the interpreted structure of the caldera. I also demonstrate that the location and alignment of the lava domes and the pattern of their extrusion are tectonically controlled, and can help constrain timing of rifting in certain areas. The lack of surface faults at Rotorua caldera precludes the use of fault mapping to investigate the tectonic control. Instead, the internal structures, morphology and timing of lava dome growth can be used as proxies to establish a structural setting of the caldera. This method may be applied to other calderas that also lack surface faults.

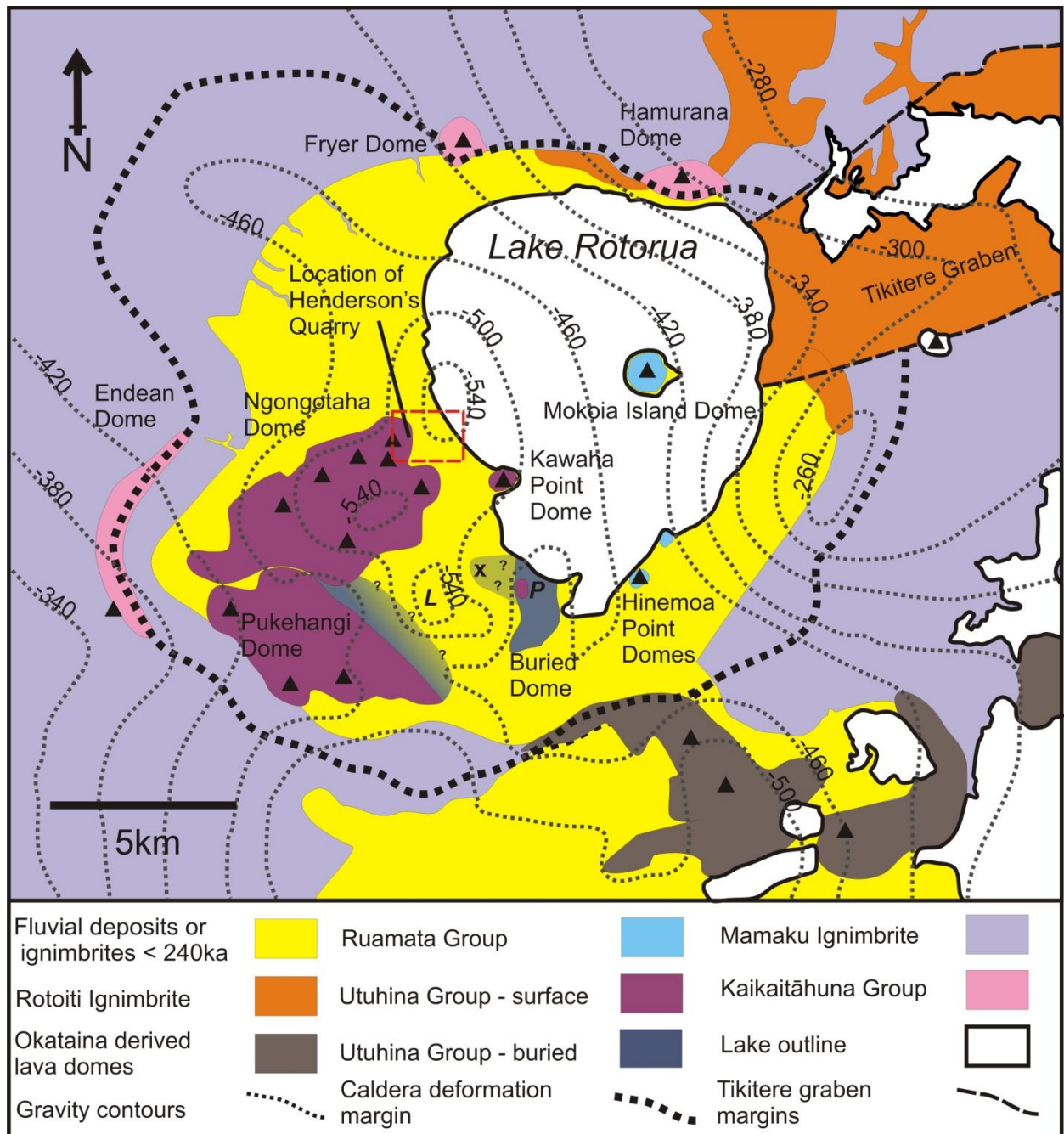


Figure 5.3: Simplified geological map of the Rotorua caldera. Gravity anomaly contours from Rogan (1982) and Hunt (1992). Units are $\mu\text{N}/\text{kg}$. L corresponds to the location of the Linton Park Anomaly, P is the location of the Pukeroa Anomaly, x is the location of borehole RR892 and black triangles show locations of vents from Cole et al. (2005). Geological information based upon data from Milner (2002) and Cole et al. (2005). Red square depicts area shown by aerial photograph in Figure 5.7.

5.2 Method

This chapter brings together field studies and thesis geochemistry and petrography (Richnow 1999; Milner 2001; Deering 2009) of the domes of the Rotorua caldera. These data are combined with better age constraints and maps of regional and caldera-forming structures, to place the domes of Rotorua into three groups – the Kaikaitāhuna, Utuhina and Ruamata groups. Using small scale internal structures within Ngongotaha dome (Figure 5.3), I have gained insights into how dome structures are influenced by the regional and caldera-forming processes of Rotorua. Published gravity data from Rogan (1982) and Hunt (1992), along with sparse surface faults and features from Hunt (1992), Milner (2001) and Cole et al., (2010), provided evidence for an inferred fault map of Rotorua caldera using alignment of domes and internal structures at Ngongotaha dome (this chapter). Previous work on Ngongotaha dome includes theses by Shepherd (1991), Richnow (1999) and Dravitzki (1999) and published work of Dadd (1992).

5.3 Results

5.3.1 Spatial distribution, age and morphology of lava domes at Rotorua caldera

The Kaikaitāhuna group comprises the Endean, Hamurana and Fryer domes, which are found on the south-west and northern boundaries of the caldera (Figure 5.3). Endean dome has been dated to 451 ka (Deering et al. 2010), and this age is inferred for other domes in this group. They have a current volume of 1.5 km³ (Wilson et al. 1984), but the morphology of the domes suggests they were larger prior to the Mamaku ignimbrite eruption, as they have been truncated by the caldera margin. Endean dome outcrops along the caldera margin to the SW of Ngongotaha dome, and is located at the intersection of major regional basement and active rifting faults, which define the caldera margin here (Figures 5.3 and 5.4) (Milner et al. 2002). Fryer and Hamurana domes are

located on the northern edge of the caldera margin, and are likewise associated with non-caldera forming structures (Figure 5.3). Hamurana and Fryer domes have been previously mapped as linked domes at depth (Leonard et al. 2010), but because Mamaku ignimbrite is found outcropping between the two domes (Milner 2001), they have been mapped as two separate entities at the surface.

The post-caldera collapse Ngongotaha, Pukehangi, Kawaha Point and Buried domes are collectively referred to as the Utuhina group. The eruptions forming these domes were focused around in the SW of the caldera, where subsidence was deepest, as shown by a negative gravity anomaly first interpreted by Rogan (1982), and further improved by Hunt (1992) (Figures 5.3 and 5.4). These domes comprise approximately 4.2 km³, the biggest of which is the Ngongotaha dome (Wilson et al. 1984).

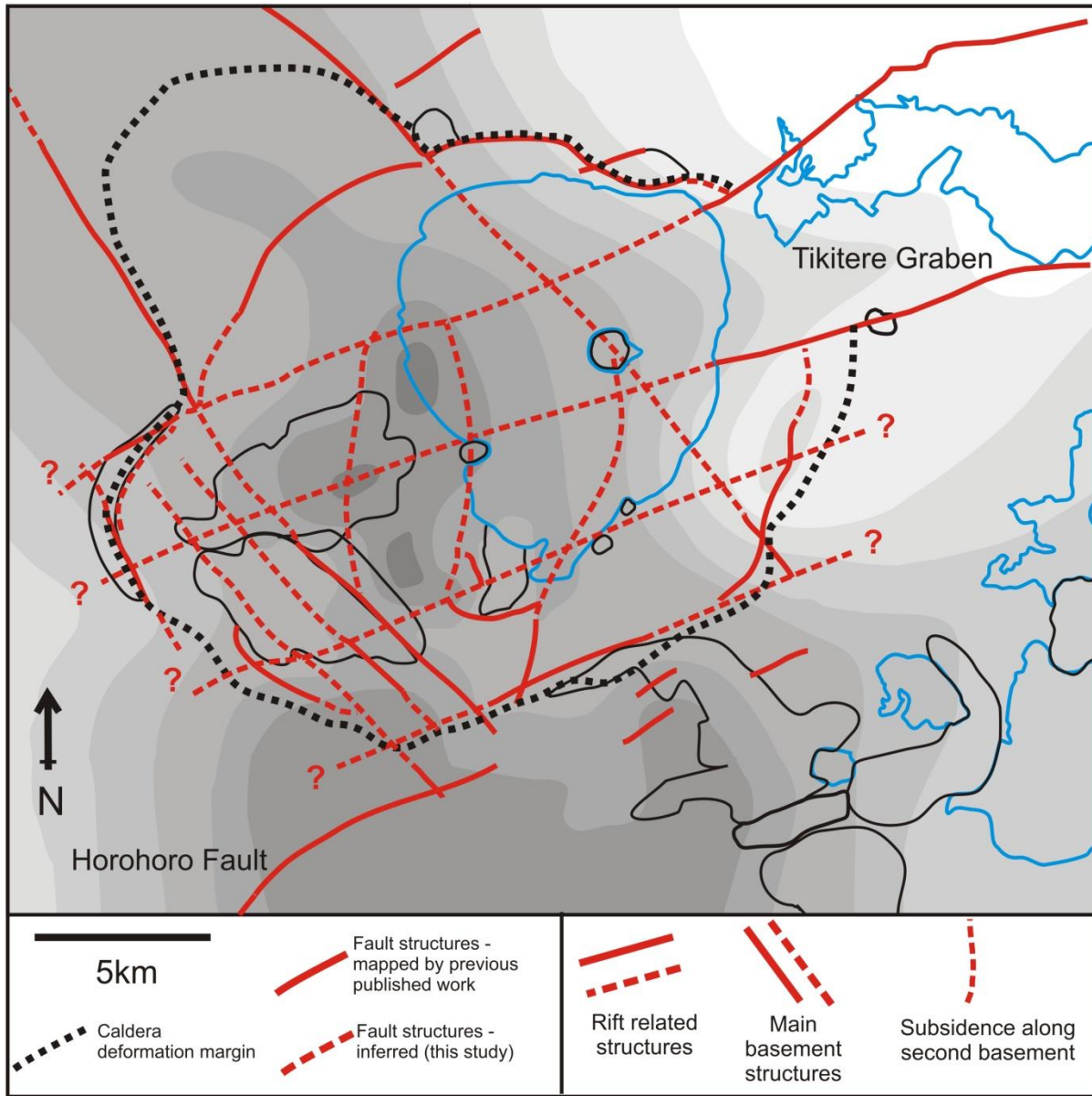


Figure 5.4: Regional (trending NE – SW), caldera collapse (N – S) and basement related (trending NW – SE) structures grouped by strike, and based upon dome elongations and internal structures. Domes are outlined in black (see Figure 5.2 for names) while lakes are outlined in blue. Gravity data are included for comparison to graben and collapse structures, and are taken from Rogan (1982) and Hunt (1992); gradients are $-40 \mu\text{N}/\text{kg}$. Known fault structures are taken from Milner (2001). Inferred fault zones (dashed red lines) are based on gravity gradients, dome locations, continuation of regional scale faults across the caldera, and field measurements of flow bands and fractures sets in lava domes.

Ngongotaha dome has been dated at c. 200 ka (G. Leonard, pers. comm., 2010) (c. 40kyrs younger than the Mamaku eruption) and this age is assumed for the other undated domes of the Utuhina group (due to geochemical similarities described in detail later). Pukehangi dome has been downthrown on the NE side (Milner et al. 2002) and covered by recent fluvial sediments. This has resulted in a NE sloping dome surface and a lack of surface expression of the NE side of the dome. The intersection of the current surface of Pukehangi dome and the sediments is inferred to be the location of a fault across Rotorua caldera, as the orientation of this matches the edge of a large embayment in the caldera margin to the WNW, thought to be caused by a basement structure by Milner et al. (2002) (Figure 5.4). The movement on this fault is not reflected in the morphology of nearby Ngongotaha dome. A single borehole (RR892) drilled to the NNE of Pukehangi encountered a 400m thick rhyolite body, with its top surface starting at a depth of 50m, which may be coincident with the buried section of Pukehangi dome (Hunt 1992) but a gravity anomaly known as the Linton Park Anomaly is located in between the borehole and the rest of Pukehangi dome (Figure 5.3). Differences in the densities of the sediments (1350 to 1780 kg/m^3) and Mamaku ignimbrite (1700 ± 40 kg/m^3) and lava dome material (2110 ± 150 kg/m^3) from the RR892 borehole suggest that this gravity low represents sediments and/or Mamaku ignimbrite rather than a buried lava dome (Hunt 1992). It is therefore most likely that the negative anomaly is subsidence related and close to the centre of the caldera collapse, and that the lava dome encountered at the borehole is not part of the buried section of Pukehangi dome. Ngongotaha dome is the largest dome complex in the Utuhina group, and consists of a total of 6 dome lobes elongated in a NW – SW orientation (Figure 5.3), which was discussed in Chapter 4. One of the three gravity lows associated with the locus of collapse of the caldera floor is situated beneath Ngongotaha dome (Figure 5.4).

A slight positive gravity anomaly (the Pukeroa Anomaly) (Figure 5.4), has been correlated with a buried dome (Hunt 1992), referred to here as Buried dome (Figure 5.2). Only a small part of this dome reaches close to the surface (at Pukeroa Hill), but shallow borehole data has confirmed the presence of a body of rhyolite at depth to the south (Wood 1992; Hunt 1992). Buried dome may be related to the dome encountered at depth by the RR892 borehole drilled to the east. This dome is also closely associated with several geothermal areas around the city of Rotorua, and is bound by two small faults on the west and southern sides, and likely also on the east (based upon extrapolation of a fault to the SE of the dome).

The Ruamata group comprises the other post-collapse domes of Mokoia Island and Hinemoa Point. They contribute to less than 0.2 km^3 of the post-collapse domes (Wilson et al. 1984), and are located in the middle of the modern Lake Rotorua and on its southeastern shore respectively. No absolute dating is available for the Ruamata group, but I have assumed them to have erupted between 60 and 36 ka based upon field relationships with lake terraces from Lake Rotorua. A series of c. <60 to 36 ka terraces are seen on the sides of Ngongotaha dome and Pukehangi dome, but not on Mokoia Island or Hinemoa Point (Kennedy et al. 1978; Marx et al. 2009). At c. 60 ka, the Rotoiti and Earthquake Flat ignimbrites were erupted from the OCC, and to the south of Rotorua caldera respectively (Wilson et al. 1984). The deposition of these ignimbrites would have blocked either drainage routes from Lake Rotorua (northeast through the current Tikitere graben, and south into the Waikato River), and caused the lake to fill to a highstand (Marx et al. 2009). Lacustrine terraces were deposited on the partially submerged domes of the Utuhina group. The exact timing of when this highstand occurred is unclear, as it is uncertain if primary ignimbrite or secondary reworked deposits of these eruptions blocked the lake outflow due to lack of preserved outcrop. A maximum age can be given by the age of the eruptions (c. 60 ka), but the terraces may have formed up to the

42 ka Maketu and 36 ka Hauparu eruptions from the OCC, between which a large lake level drop occurred (Marx et al. 2009). No terrace from this highstand is found on the domes of the Ruamata group, so they are inferred to be younger than these eruptions (Marx et al. 2009). A second lake highstand, produced by a second outlet blocking event caused by the 36 ka Hauparu Eruption, is found on domes of all groups within Rotorua caldera, and can therefore be used as a constraining age (Marx et al. 2009).

While no dome within the Ruamata group shows a preferential elongation, Mokoia Island is close to the intersection of the continuation of the Tikitere graben and a basement structure that has defined part of the NW caldera deformation margin. Hinemoa Point domes do not correspond to any inferred regional structure. They may be related to a collapse-generated feature that has a similar orientation to a fault that is coincident with part of the eastern caldera margin (Figure 5.4).

5.3.2 Geochemistry

The three dome groups can also be distinguished through geochemical affiliations, as summarised in Tables 5.1 and 5.2. All rhyolite domes have a high SiO₂ content (71.14 – 77.13 wt%), and range in total alkalis between 6.84 and 8.57 wt% (Figure 5.5). The Kaikaitāhuna group shows (relative to the other dome groups) a lower Na₂O, as well as total alkali (~7 wt%), but has enhanced V, Ca and Sr (Figure 5.6 and Table 5.1). They also show higher ratios of Sr/Rb and Sr/Y than the other groups (Figure 5.6).

The Utuhina group domes of Ngongotaha, Kawaha Point and Pukehangi are slightly enriched in Na₂O, but relatively depleted in other trace elements (apart from Ti, Y and Zr) and have a higher total alkali content of 7.5 to 8.5 wt% (Figure 5.6 and Table 5.1). Although the Buried dome geochemistry data do not plot consistently within the data cloud of the other dome groups, it does

lies closest to the Utuhina group data. This, alongside its geographic position, indicates it is most likely part to the Utuhina group. The Utuhina group are depleted in V, Ca and Sr (Figure 5.6) when compared to the Kaikaitāhuna group (Table 5.1), and shows a lower ratio of Sr/Rb and Sr/Y (Figure 5.6).

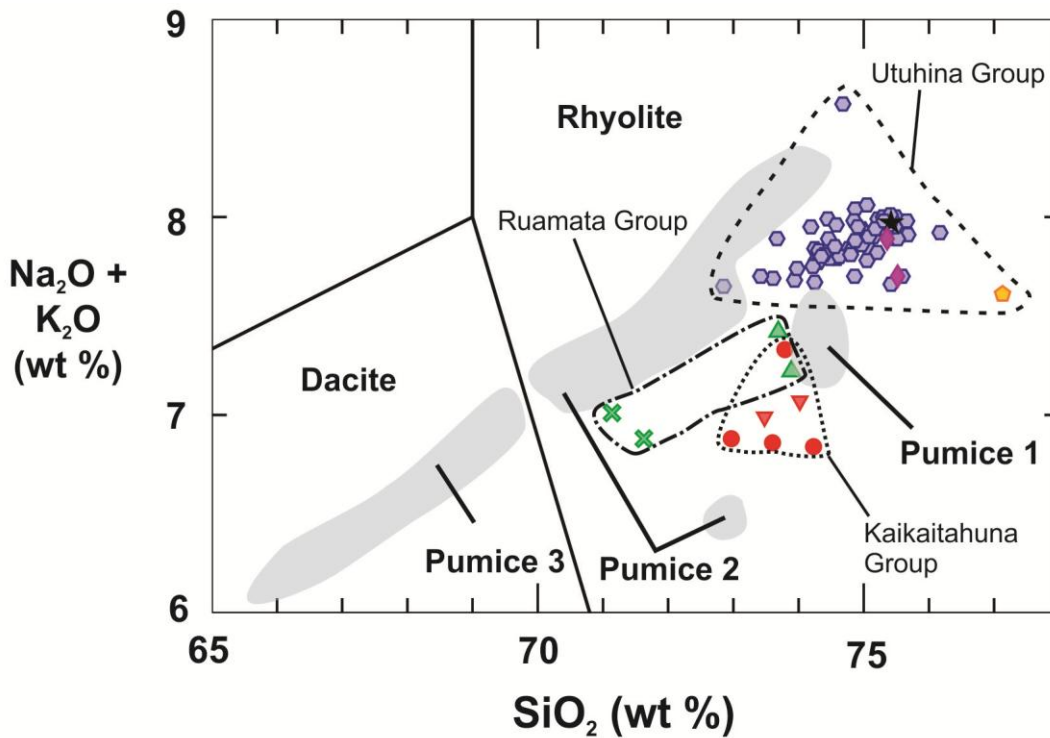


Figure 5.5: Whole rock TAS diagram of Rotorua caldera domes from Milner (2001) with outlines of Mamaku whole pumice XRF analysis from Milner (2003). The three main dome groupings are shown. Key to symbols: Red Circles = Endean dome, Red Triangles = Hamurana dome, Blue Circles = Ngongotaha dome, Black Star = Pukehangi dome, Purple Diamonds = Kawaha Point dome, Yellow Pentagon = Buried dome, Green Triangles = Mokoia Island dome and Green Crosses = Hinemoa Point domes.

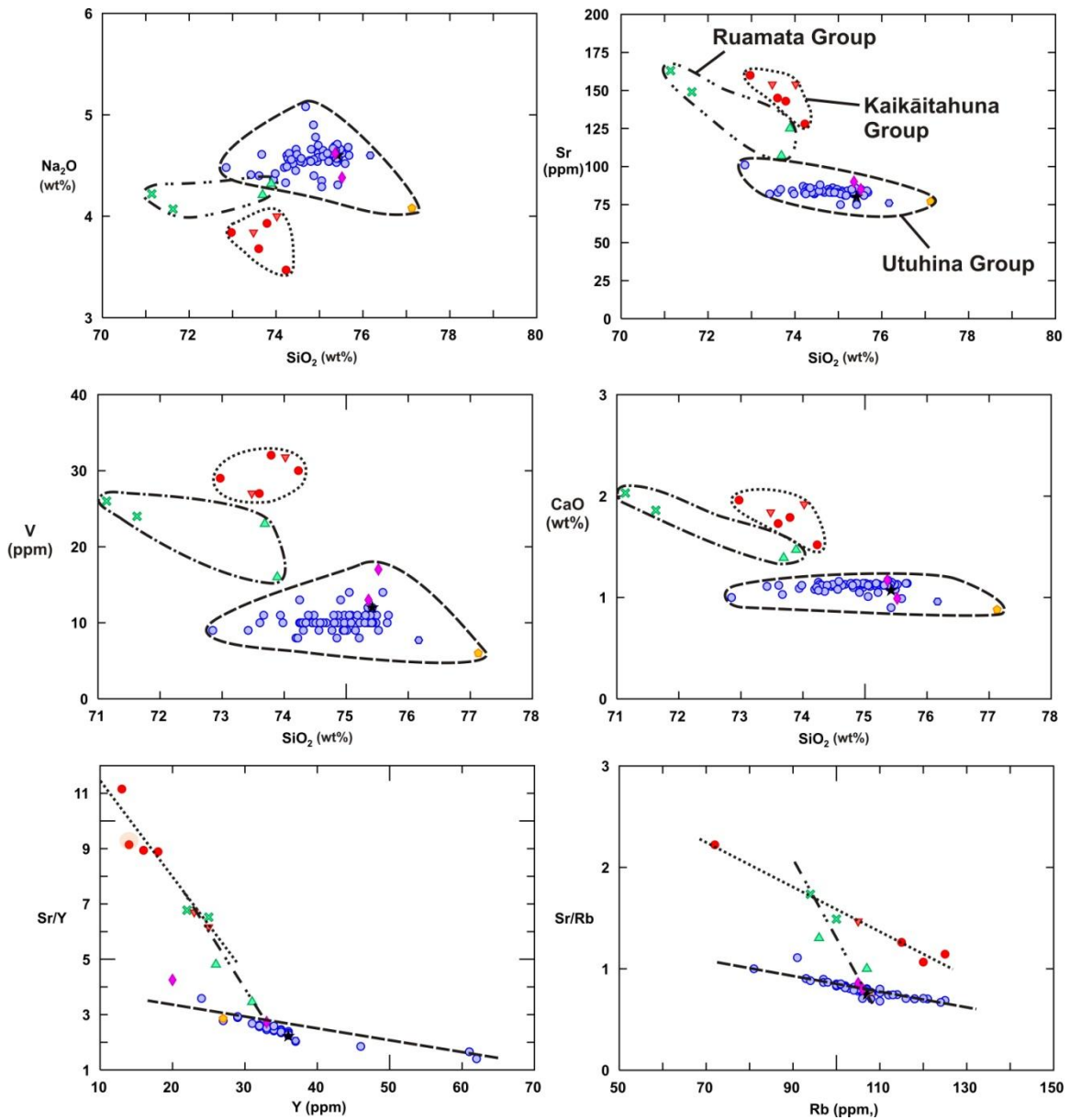


Figure 5.6: Selected geochemical diagrams. Dome groups are circled for clarity. See Figure 5.5 caption for details on individual dome groups.

Sample ID	RR1	RR29	RR28	RR19	NQ-19	NQ-23	NQ-32	NQ-33	NQ-22	RR20	RR32	RR33	RR34	RR21	RR22	RR16	RR17
Source	Endean	Endean	Endean	Hamurana	NG	Obsidian	NG	NG	NG	Pukehangi	Kawaha	Kawaha	Buried Domes	Hinemoa	Hinemoa	Mokoiia Is.	Mokoiia Is.
Lithology	Rhyolite	Rhyolite	Rhyolite	Rhyolite	Pumice	Obsidian	Rhyolite	Rhyolite	Obsidian	Rhyolite	Rhyolite	Rhyolite	Rhyolite	Rhyolite	Rhyolite	Rhyolite	Rhyolite
SiO2	72.97	73.6	74.23	73.48	75.21	74.85	75.31	74.56	74.27	75.42	75.52	75.36	77.13	71.14	71.63	73.89	73.69
TiO2	0.29	0.28	0.31	0.35	0.2	0.18	0.23	0.22	0.22	0.19	0.21	0.2	0.13	0.3	0.29	0.25	0.24
Al2O3	14.55	14.28	13.77	14.39	13.2	13.14	13.35	13.03	13.06	13.19	13.39	13.14	12.95	14.94	14.6	13.91	13.02
Fe2O3t	2.41	2.22	2.4	2.09	1.75	1.78	1.69	1.76	1.74	1.74	1.66	1.73	0.91	2.19	2.23	1.44	2.15
MnO	0.06	0.04	0.03	0.03	0.06	0.05	0.06	0.06	0.06	0.06	0.03	0.06	0.03	0.06	0.06	0.04	0.05
MgO	0.42	0.33	0.26	0.3	0.2	0.21	0.2	0.18	0.21	0.17	0.06	0.2	0.05	0.46	0.44	0.25	0.28
CaO	1.96	1.73	1.52	1.84	1.05	1.14	1.12	1.08	1.13	1.07	0.99	1.17	0.88	2.03	1.86	1.47	1.39
Na2O	3.84	3.68	3.47	3.84	4.54	4.55	4.67	4.54	4.57	4.6	4.38	4.62	4.08	4.22	4.07	4.32	4.21
K2O	3.04	3.18	3.37	3.15	3.28	3.43	3.31	3.31	3.21	3.37	3.32	3.27	3.53	2.79	2.81	2.9	3.21
P2O5	0.06	0.03	0.03	0.03	0.03	0.03	0.02	0.02	0.03	0.03	0.03	0.03	0.02	0.03	0.02	0.06	0.08
LOI	0.67	0.89	0.83	0.72	0.11	0.37	0.33	0.3	1.37	0.47	0.7	0.46	0.55	2.16	2.26	1.7	1.99
Total	100.26	100.25	100.23	100.2	99.64	100.33	100.3	99.07	99.87	100.31	100.27	100.23	100.25	100.31	100.28	100.22	100.32
V	29	27	30	27	8	8	11	9	10	12	17	13	6	26	24	16	23
Cr	7	5	8	3	3	3	3	3	3	3	3	3	5	4	4	5	3
Ni	4	4	3	3	3	3	3	3	3	3	4	5	4	3	3	3	3
Zn	40	32	29	31	36	46	24	39	45	51	32	47	30	39	48	35	43
Zr	154	151	153	219	217	218	208	214	215	220	228	223	143	181	168	186	179
Nb	7	7	6	7	10	9	8	10	10	10	11	10	9	8	8	9	8
Ba	832	759	732	722	820	783	817	773	793	779	767	804	795	770	748	758	716
La	27	16	13	22	32	30	28	31	34	28	23	25	26	15	14	23	23
Ce	54	47	47	69	67	63	47	61	67	83	55	65	62	60	61	60	79
Nd	13	10	10	37	29	32	21	31	38	45	10	27	35	10	10	17	23
Ga	14	13	14	14	15	14	16	15	14	14	15	14	13	15	15	16	14
Pb	11	12	12	13	11	22	12	16	21	18	14	18	18	12	14	17	15
Rb	72	115	120	105	106	106	98	105	107	107	106	105	108	94	100	96	107
Sr	160	145	128	154	84	83	85	84	86	80	85	90	77	163	149	125	107
Th	12	12	11	11	12	14	12	12	13	12	12	10	13	11	9	10	10
Y	18	13	14	23	29	32	29	36	33	36	20	33	27	25	22	26	31

Table 5.1: Whole Rock XRF analysis of rhyolitic samples from both pre- and post-collapse domes. Note – only representative samples from Ngongotaha are presented. See Appendix 1 for full list of samples used for geochemistry.

Dome Name	Age	Location	Petrography	Geochemistry	Structures and textures	Group
Hinemoa Point domes	60 – 36ka (relative)	Eastern edge of Lake Rotorua, SE of caldera	Phenocryst – 20-25%, Plag, Qtz, Biot, Fe/Ti ox	~71% SiO ₂ , ~7% alkalis, large range in most other geochemistry – most likely due to alteration	Glassy, occasional spherulites, perlitised, flow banded	Ruamata
Mokoia Island dome	60 – 36ka (relative)	In centre of Lake Rotorua, centre of caldera	Phenocryst – 20-25%, Plag, Qtz, Orpyx, Hrnbln, Fe/Ti ox	~74% SiO ₂ , 7-7.5% alkalis, moderate V, Sr and NaO, ~1.4% CaO, high Sr/Y, low Y and Zr, moderate to high Sr/Rb	Glassy, occasional spherulites, perlitised, flow banded	Ruamata
Ngongotaha dome	~200ka (dated)	To west of collapse locus, SW of caldera	Phenocryst – 2-5%, Plag, Orpyx, Fe/Ti oxides	73-75% SiO ₂ , 7.5-8% alkalis, Low V and Sr, ~1% CaO, Moderate to high Y, Zr/Y, low Sr/Y and Sr/Rb	Devitrified, flow banded, obsidian sheets bounded by breccia, highly fractured, lithophysae present	Utuhina
Buried dome	~200ka (assumed)	To east of collapse locus, SW of caldera	Phenocryst – 2-5%, Plag, Orpyx, Fe/Ti oxides	77% SiO ₂ , ~6.5% alkalis, low V and Sr, 1% CaO, low Y, Sr/Y, Sr/Rb, Zr and Zr/Y, moderate Rb	Devitrified	Utuhina
Kawaha Point dome	~200ka (assumed)	To east of collapse locus, SW of caldera	Phenocryst – 2-5%, Plag, Orpyx, Fe/Ti oxides	~75% SiO ₂ , 7.5-8% alkalis, low V and Sr, ~1% CaO, moderate Y, Rb, Sr/Y, Sr/Rb, high Zr/Y	Devitrified	Utuhina
Pukehangi dome	≥200ka (assumed from faulted NE edge)	To SW of collapse locus, SW of caldera	Phenocryst – 2-5%, Plag, Orpyx, Fe/Ti oxides	75% SiO ₂ , 8% alkalis, high V and Sr, <1% CaO, moderate Y, Rb, Zr/Y and low Sr/Y and Sr/Rb	Devitrified	Utuhina
Endean dome	451ka (dated) (Deering, 2010)	Outside caldera margin, SW edge	Phenocryst – 20-30%, Plag, Orpyx, Fe/Ti ox, minor Qtz, biot, hrnbln	72-75% SiO ₂ , 6.5-7% alkalis, 1.5-2% CaO, Low Y and Zr, higher Sr/Rb and Sr/Y	Devitrified	Kaikaitāhuna
Hamurana dome	~451ka (assumed)	Outside caldera margin, northern edge	Phenocryst – 15%, Plag, Orpyx, Fe/Ti ox, Clnpyx	74% SiO ₂ , 7% alkalis, 1.75% CaO, Intermediate Y, Zr, Sr/Rb and Sr/Y	Devitrified, flow banded	Kaikaitāhuna
Fryer dome	~451ka (assumed)	Outside caldera margin, northern edge	Phenocryst – 20%, Plag, Orpyx, Fe/Ti ox	No sample for geochemistry	Devitrified, flow banded	Kaikaitāhuna

Table 5.2: Summary of grouping of lava domes of Rotorua. Note that high/ moderate/ low descriptions of geochemistry is relative to the other analyses.

The Ruamata group domes often plot between the other groups, showing relatively low to intermediate SiO_2 , high to intermediate Ca and Sr (Table 5.1 and Figure 5.5), and intermediate ratios of Sr/Y (Figure 5.6) and a low total alkali content of 7 wt% (Figure 5.5). The Hinemoa Point domes plot close to the Kaikaitāhuna group, but the spatial and age differences make them unlikely to be closely linked. This trend is less obvious in the Sr/Rb vs. Rb and Sr vs. SiO_2 plots (Figure 5.6).

In summary, the Kaikaitāhuna and Utuhina groups form distinct geochemical clusters and the Ruamata group shares geochemical affinities with both groups, shown best in Sr/Y vs. Y and Sr/Rb vs. Rb plots (Figure 5.6). In addition, the Utuhina group could be linked to the Mamaku eruption, shown by continuation of a possible crystal fractionation pathway visible in Figure 5.5 (and suggested by Milner (2001)), although further work would be required to confirm this.

5.3.3 Internal Structures of Ngongotaha dome

The internal structure of Ngongotaha dome is exposed in Henderson's Quarry on the north-eastern side of the dome, the only part of any of the Utuhina group domes to be adequately exposed for a detailed study. Flow band orientations (Figure 5.7), fracture orientations (Figure 5.8B) and lithology changes (Figure 5.7) were mapped and compared to the regional structure of both Rotorua caldera and the TVZ (Figures 5.1 and 5.8C).

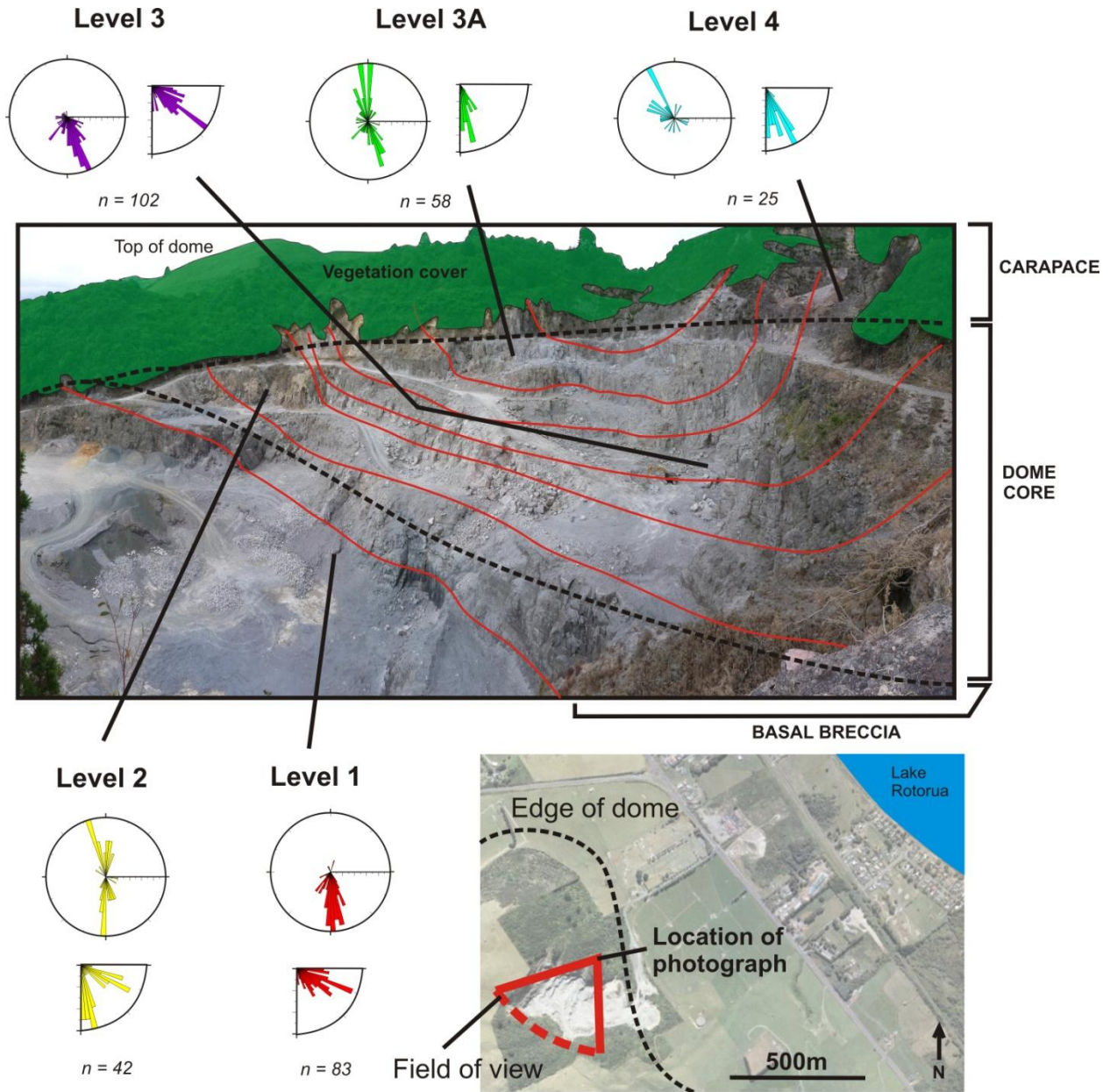


Figure 5.7: Flow band orientation at Henderson's Quarry, Ngongotaha dome. View is to SW in red cone on aerial photograph (see Figure 5.3 for location inside of Rotorua caldera), red lines delineate general flow band orientation, while dashed black lines mark transition from basal breccia to core, and from core to carapace. Rose diagrams show orientation (full circle) and dip (quarter circle) of flow bands from each level in the dome.

Ngongotaha is an ENE – WSW elongated dome formed from a series of vents aligned in this orientation (Cole & Spinks 2009) (Chapter 4). Henderson’s Quarry is located on a N – S trending lobe of one of the vents from Ngongotaha dome (Figure 5.3). Flow bands are visible throughout Henderson’s Quarry, and are most prominent at lower levels of the quarry representing the core of the dome. In general the flow banding shows an increasing dip towards the top of the dome, with flow bands in the lower dome dipping at $\sim 25 - 35^\circ$ to the W – SW (i.e. dipping towards the centre of the Ngongotaha dome lobe), increasing to near vertical ($>80^\circ$) at the very top (Figures 7 and 8) (Chapter 4). The average strike value for the flow bands ranges from 179° (near N – S trending) in the lower part, to 163° (near NNW – SSE) in the upper part (Figures 5.7 and 5.8). In cross section perpendicular to the strike trend and orientation of the lobe, these flow bands produce a fan-like arrangement from the outer edge to the central part of the dome.

The flow bands are deformed by small scale, localised folding in the centre of the dome, leading to a bimodal dip distribution in the core of the dome (Figure 5.7, level 2). Higher dips are caused by m-scale folds running parallel to the excavation face, as well as parallel to the outside of the dome. A stereonet plot of the limbs of these folds show that the axial trend of these folds runs close to N – S, parallel to the strike of the flow bands, as well as the outer edge of the dome lobe (Figure 5.8). Overall, the orientations of flow banding in Ngongotaha indicate flow directionality from a N – S orientated central feeder dyke outwards to the east and west, perpendicular to the N – S strike of the flow bands. The overall elongation of the dome complex is in a NE – SW direction, and combined with the N – S trending flow bands, suggests a complex structural control on this dome eruption (this is discussed in detail in the next section).

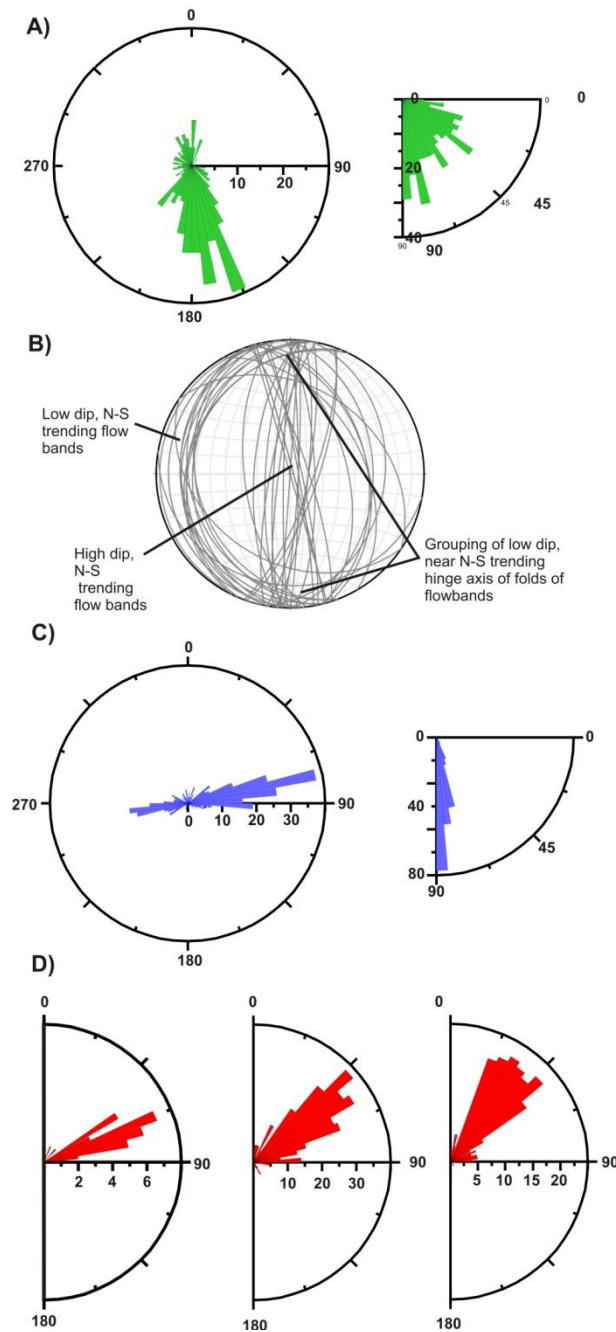


Figure 5.8: A) Flow band strike (left) and dips (right) from Ngongotaha dome ($n=325$), B) Stereonet of flow bands on level 2 (see Figure 7) depicting folds and axial hinge orientation. C) Fracture strike (left) and dip (right) from the inside of Ngongotaha dome ($n=318$) and D) Fault azimuths from surface structures related to the Taupo rift. Left – within the OCC, Centre – Faults to SW of the OCC, Right – Waikato to Okataina domain (from Rowland and Sibson, 2001; Seebeck et al. 2010 and Villamor et al. 2011).

Although rhyolitic, Ngongotaha dome shows different facies based upon vesicularity, presence or absence of flow bands, spherulites or lithophysae, and cohesion of rock. The core facies of Ngongotaha is strongly flow banded with abundant lithophysae, above a basal breccia subfacies of devitrified, finely brecciated and weakly flow banded obsidian (see Chapter 4). At the top of the dome, intact and highly spherulitic obsidian sheets are separated by well annealed obsidian breccias, all showing near vertical flow bands and can be traced across approximately 170 m with little change in orientation of the banding (see Chapter 4). A finely vesicular and partly brecciated carapace facies is found above this (see Chapter 4).

Additionally, Ngongotaha dome exhibits large numbers of fractures that post-date dome growth. These fractures are most evident in the dense core, and cut across the flow bands. They show maximum widths of up to 3cm, and have smooth sides that are covered in a dark red mineralisation. The most common fracture orientation is a general ENE – WSW trend, with strike ranging from 071° to 128° , with most orientations occurring within a bin size of $074 - 078^{\circ}$, and a vertical to near vertical dip ($>75^{\circ}$) (Figure 5.8). No shear displacement has been observed on these fractures; however the discontinuous nature of flow bands within the lithologies makes tracing flow bands across the fractures difficult. Fault azimuth data on the areas of extension to the southwest of the OCC (measured from faults outside of the OCC shown in Figure 5.8C, centre) shows a different orientation to the fractures in Ngongotaha dome. However, faults within the OCC (recorded from faults inside of the OCC, shown in Figure 5.8C, left) shows similar orientation to the strike of fractures.

5.4. Discussion

5.4.1 Geochemical and Petrological Links

The Kaikaitāhuna, Utuhina and Ruamata groups, as differentiated by geochemistry, suggest an evolving magma source beneath and adjacent to Rotorua caldera. Differing trends in both the Sr/Y vs. Y and Sr/Rb vs. Rb of each dome groups suggest that all three groups were sourced from small, isolated magma bodies in the upper crust that underwent fractional crystallisation.

The Kaikaitāhuna group domes can be linked by similar petrography and geochemistry. The Endean and Hamurana domes have slightly different geochemistry (Figures 5.5 and 5.6) and their spatial isolation suggests they are sourced from different magma bodies. There are no geochemical data for Fryer dome, but its similar petrography and close proximity to Hamurana dome suggest that they are related. I postulate that the Kaikaitāhuna Group domes erupted as comparatively small domes from isolated but related magma bodies from a deeper common source (Figure 5.9A).

Milner et al. (2003) suggested a geochemical link between Mamaku ignimbrite pumice and the domes of the Utuhina group, as seen in Figure 5.5. The close spatial relationship also indicates these domes were linked to the eruption of the Mamaku ignimbrite, as they surround the collapse locus (Figure 5.4). The Buried dome does not always plot within the same tight geochemical grouping as the other domes. It also shows the highest SiO₂ value of the Utuhina group (clearly distinct from the rest of the group) (Figure 5.5), suggesting this was sourced from a more evolved but still related magma body. The time gap between eruption of the Mamaku ignimbrite and the domes of the Utuhina group (approximately 40 ka) may have allowed any magma residue left behind from the Mamaku ignimbrite eruption to evolve and produce the slightly higher silica content domes. However, a conspicuous lack of crystals in the dome material of Ngongotaha is less consistent with a crystal-rich, mostly de-gassed residue of the

Mamaku magma and more consistent with a highly evolved fractionate from a similar deeper magma source.

The Ruamata group geochemistry does not fit into either the Kaikaitāhuna or Utuhina groups, but exhibits intermediate values (Figure 5.6). This suggests a separate magma body that may have derived from mixing or contamination of the source of all groups. It is therefore postulated that the magma bodies that sourced Mokoia Island and Hinemoa Point domes were originally the same composition as the domes of the Utuhina group, but underwent some mixing or assimilation of other material before emplacement as small magma bodies in the upper crust (Figure 5.9F). Although the TAS diagram suggests that they are less evolved than the Utuhina group, the relationship between the lake terraces and the domes of Rotorua caldera (described in section 5.3.1) shows that the Ruamata group domes must be younger than the Utuhina group. The lower SiO₂ range of the Ruamata group may be attributed to a small, low silica injection of magma into the source, or assimilation or mixing of low silica material before ascent.

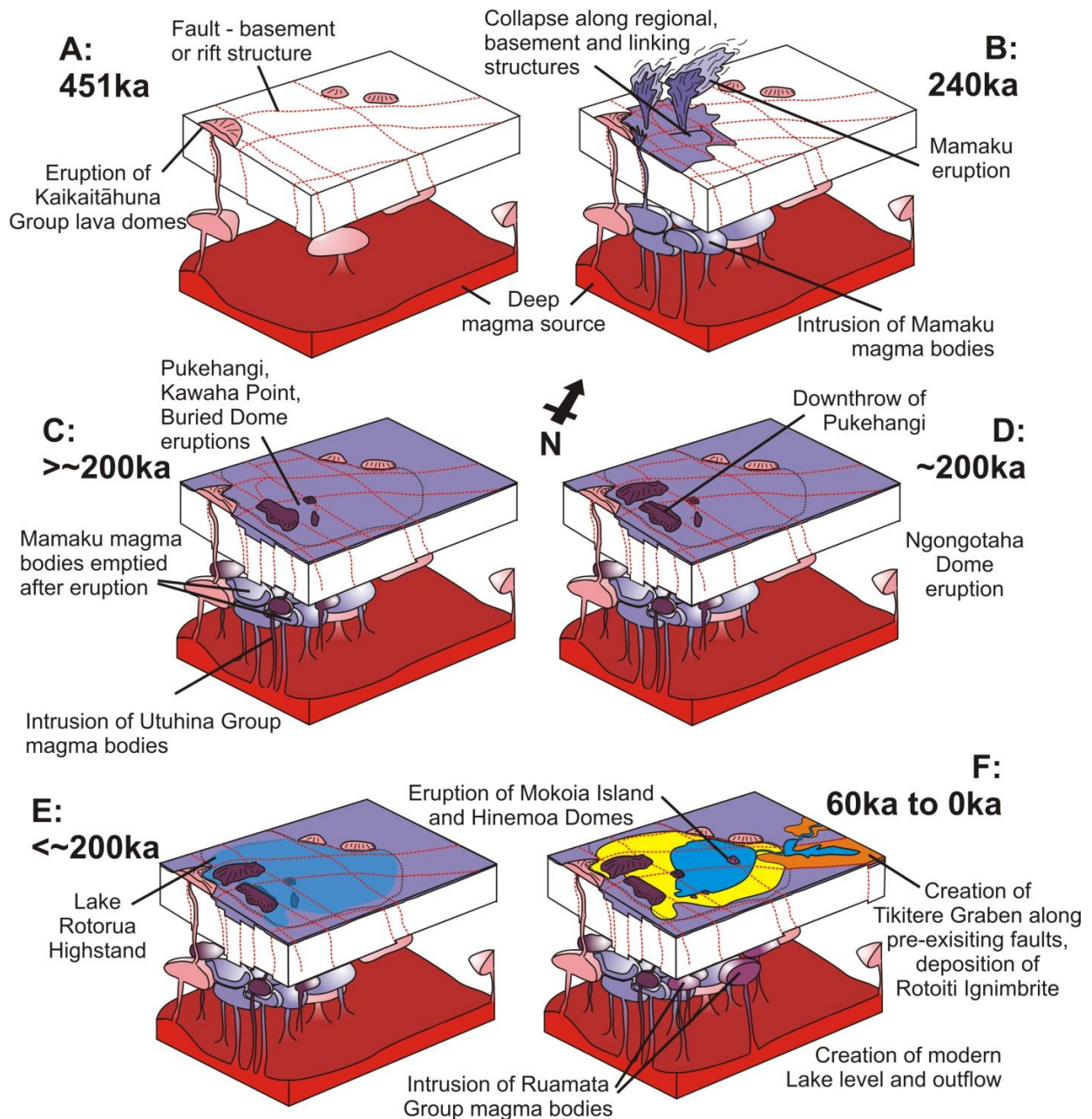


Figure 5.9: Schematic representations of the evolution of Rotorua caldera from eruption of pre-Mamaku lava domes at 451 ka (A), intrusion of Mamaku magma chambers and subsequent eruption of the Mamaku ignimbrite at 240 ka (B), eruption of Pukehangi, Kawaha Point and Buried domes before 200 ka (C), subsidence of NE side of Pukehangi dome, and eruption of Ngongotaha dome at 200ka (D), creation of Lake Rotorua Highstand shortly after the eruption of the Utuhina group domes (E), and intrusion of Ruamata group magma chambers between 200 ka and 60 ka, when Hinemoa Point and Mokoia Island domes erupted and the Tikitere graben enables Lake Rotorua to reduce to the current lake level (F). View is oblique, to the NNW.

5.4.2 Structural controls in Rotorua caldera and the TVZ

The extent of structural control on rhyolitic eruptions is well established in the TVZ (Walker 1984; Beresford & Cole 2000; Milner et al. 2002; Leonard 2003; Spinks et al. 2005; Gravley et al. 2007; Wilson et al. 2009; Cole et al. 2010; Seebeck et al. 2010). Calderas such as the OCC have been the focus of studies linking basement geological structures and rift axes orientations with caldera morphology (Seebeck et al. 2010). The irregular outline of the OCC is due to the reactivation of structures in the basement geology, as well as active rift faults during collapse. Here, basement structures (which may include faults, bedding or cleavage) trend N – S, while extensional faults of the TVZ trend NE – SW (Seebeck et al. 2010). Lava domes within the OCC (e.g. Tarawera dome complex) are aligned with the active rift faulting (Cole et al. 2010). The Maroa dome complex in the Whakamaru caldera also shares a close affinity with faults associated with rifting of the Taupo rift zone (Leonard 2003) (Figure 5.10). Below, I establish that the locations and elongation orientations ($\sim 070^\circ$ and $\sim 140^\circ$) of the Utuhina group vents and domes at Rotorua caldera align with (A) active $060 - 075^\circ$ rifting either side of the domes and (B) $130-140^\circ$ striking basement fabric as defined by the NW caldera margins.

The pre-Rotorua caldera formation lava domes (Kaikaitāhuna group) have been erupted close, or parallel, to the continuation of major independently mapped extensional faults (Milner et al. 2002; Cole & Spinks 2009) and previously mapped linear structures interpreted to represent a basement fabric and later exploited by caldera collapse (Milner et al. 2002) (Figures 5.4 and 5.9A). The full extent, or number, of these domes is unclear due to the destruction and subsequent burial of any dome material after the Mamaku ignimbrite (Rotorua caldera-forming) eruption. I suggest that some structural control may have existed prior to caldera formation. However, the lack of good exposure of both the pre-collapse faults and pre-caldera dome orientations and internal structures makes this interpretation only a suggestion.

The morphology of both the topographic margin and gravity anomaly (Figure 5.4) support the interpretation that the collapse of Rotorua caldera was heavily influenced by regional and local tectonics (Milner et al. 2002; Spinks et al. 2005; Cole et al. 2010). The regional tectonics created large blocks that produced an overall asymmetric, piecemeal collapse, and also contributed to trapdoor style collapse in the large embayment in the northwest part of the caldera (Milner et al. 2002), linked by localised structures formed during collapse. This piecemeal collapse style of Rotorua caldera is also seen at Scafell, Snowdon and Glencoe calderas, UK (Kokelaar 1992; Branney & Kokelaar 1994; Moore & Kokelaar 1998). At these examples, the lower caldera structure is exposed, showing the complex interplay between the collapse and regional faults (such as at Glencoe) and episodic magma emplacement (analogous to a series of nested magma chambers at Rotorua caldera) (Moore & Kokelaar 1998). Caldera collapse dissected the earlier Kaikaitāhuna group domes, by reactivating similar structures that were active during, and were used as pathways for, the earlier eruption of the domes. This is analogous to the eruption of the Horohoro dome and subsequent collateral subsidence and faulting during the eruption of the Ohakuri and Mamaku ignimbrites, reactivating previous structures that may have been used as conduits for eruption (Gravley et al. 2007; Figures 5.9 & 5.10).

The eruption of the later Utuhina group domes were primarily controlled by feeder dykes, producing elongated dome morphologies and vents that are aligned $\sim 070^\circ$ and $\sim 140^\circ$. The 070° trending elongation of Ngongotaha dome is spatially associated with, (A) the margin of the gravity anomaly associated with caldera subsidence, (B) part of the topographic margin in the west of the caldera and (C) the $060 - 075^\circ$ strike of the Tikitere graben independently mapped to the north east of the caldera (Figure 5.4). The 140° trending elongation of Pukehangi dome is (A) downstrike and parallel to independently mapped regional basement structures to the northwest of the caldera, (B) is faulted post

emplacement by a structure with the same orientation which continues to the southeast of the dome, and (C) is parallel to the margin of the gravity anomaly and topographic expression of the caldera.

Ngongotaha dome also shows evidence of influence of a second structure not related to the regional extension. In a N – S trending lobe of Ngongotaha dome (the northernmost lobe), the dome lobe is fully exposed in three dimensions in a large quarry, revealing consistent 163 – 179° (near N – S) striking flow bands with high dips. The continuation of near vertical flow banding at the top of the dome across approximately 170 m, with little change in orientation, suggests that eruption from a singular, near-circular conduit is unlikely (such as Figure 5.2A) and the near vertical dips are not affected by topography (see Chapter 4). This elongated structure can only be explained by the orientation of a feeder dyke (see Chapter 4) (Figure 5.2C). Flow folds have caused large changes in dip and in places reversal of the dip direction; however, the strike has remained relatively consistent. Ngongotaha dome was traditionally thought to be a coulée fed flow from one or two conduits (Richnow 1999). A coulée would produce near horizontal flow bands (or gently dipping in the direction of movement) on the top surface of the flow (Figure 5.2B), with ramp structures or flow folds striking perpendicular to the flow elongation direction (Cas & Wright 1988). The flow banding at Ngongotaha strikes parallel to the N – S elongation direction. Hence, the relationship between dome morphology and flow banding can only be explained by a dyke-fed eruption that accessed a near N – S trending structure (see Chapter 4). However, this near N-S orientation is not shared by any regional or basement structure inferred in Rotorua caldera. I interpret it to be a caldera subsidence structure akin to a small section of a ring fault intruded by a ring dyke (Figure 5.4). This interpretation is also consistent with the roughly N – S striking western margin of the gravity anomaly at Rotorua caldera. At the OCC, N – S faults have been inferred as basement structures that also parallel the general N – S trend of gravity anomalies (Seebeck et al.

2010), and so it is possible that this N – S structure may be linked to a second basement fabric, alongside a NW – SE striking main basement structure at Rotorua caldera.

Fractures in Ngongotaha dome have a mean strike of 074 – 078°, similar to faults mapped inside of the OCC to the east (Figure 5.8B and C, left). The fractures are unlikely to have been caused by cooling, as they are smooth sided and do not show any evidence of high temperature rupture such as striae or cavities. They also all share an overall similar orientation, rather than a radiating pattern from an outer cooling surface that would be expected if the fractures had been caused by the dome cooling and shrinking or settling. The fractures must therefore be younger than the age of the emplacement of the dome and have orientation similar to recent faults in the Tikitere graben and within the OCC.

In extensional tectonic settings, dykes will intrude parallel to the extensional axis orientation (Gudmundsson 1983; Ziv & Rubin 2000; Goldberg 2010). In the TVZ, many of the vents of basaltic and andesitic volcanism are aligned with the axis of extension, most notably the vents of Ruapehu and Tongariro in the south (Nairn et al. 1998; Rowland et al. 2010), and at the OCC (such as the 1886AD Tarawera eruption) (Cole et al. 2010). Extension within the OCC is achieved through intrusion and dykes and subsequent faulting, while extension to the SW, outside of the caldera, is purely tectonically controlled (Seebeck & Nicol 2009). Basaltic dykes originating from the 1886AD Tarawera eruption intruded through a normal ‘master’ fault, which appears to have influenced the location of older rhyolite domes of the Tarawera volcanic complex (Nairn & Cole 1981). Alignments of other rhyolite domes, such as the Haroharo dome complex in the northern part of the OCC (Smith et al. 2006) and the Maroa dome complex (Figure 5.10) (Leonard 2003) in the TVZ, and at Medicine Lake Highland volcano, California (Fink & Pollard 1983), strongly suggest that dyke-fed dome eruptions have occurred, and that the locations and morphologies of lava domes can be used as proxies for dyke locations, and therefore faults.

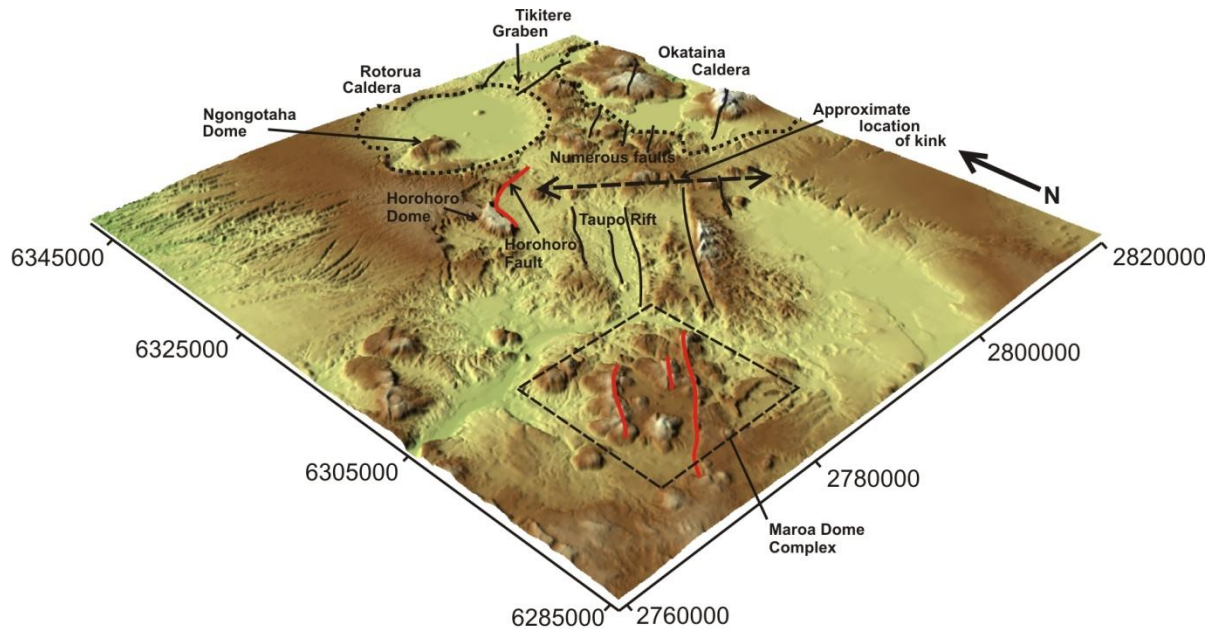


Figure 5.10: Oblique altitude shaded D.E.M. of the central TVZ, showing fault elongated Maroa dome complex and Horohoro dome, with dome eruption related faults highlighted in red. Other major regional faults of the TVZ are highlighted in black. The kink in fault orientation is labelled. Adapted from Leonard (2003).

The morphologies of the Utuhina Group domes can therefore be attributed to the geometry of dykes, which in turn can be used to suggest locations of faulting across Rotorua caldera. The N – S trending alignment at Henderson’s Quarry (Ngongotaha dome) is not shared by the overall morphology of Ngongotaha dome. This could show an en échelon dyke array beneath Ngongotaha dome (such as the 1886AD dyke at Tarawera (Nairn & Cole 1981)), or a difference in the type of controlling structure, from a caldera ring fault (orientated N – S) to a regional extensional fault (orientated ENE – WSW). In both cases, the overall regional structure will trend the same. I infer that these structures associated with the elongation of Ngongotaha dome are down strike and strike parallel with the Tikitere graben suggesting a connection beneath the modern-day Lake Rotorua that has been active at least 240 ka and possibly earlier (Figure 5.4). The elongation, and faulting of Pukehangi dome is also parallel to, and down strike

of, the NW – SE trending sides of a large embayment in the NW caldera margin which has been attributed to a relic basement structure (Milner et al. 2002). The intersection of extensional rift structures and the inferred basement structures will therefore define the piecemeal blocks created during the collapse of Rotorua caldera (Milner et al. 2002) (Figure 5.4).

The kink in the main extension axis of rifting in the northern part of the central TVZ is shown by a change in orientation from NE – SW striking faults in the Taupo rift, to ENE – WSW striking faults across the OCC (Figure 5.1). The fractures and inferred faults at Ngongotaha mostly strike ENE – WSW and suggest that Rotorua caldera lies within the kink, and is intimately linked to the Tikitere graben system. The kink is significant because of its juxtaposition and spatial overlap with Rotorua caldera and the OCC, as well as the location of active geothermal systems at Rotorua and within the Tikitere graben (Figure 5.4 and 5.10). The exact age of onset of rifting at the Tikitere graben is unknown, but the geographical location of the Kaikaitāhuna group domes (such as Endeian dome) along the intersection of Tikitere graben structures with the basement structures suggests that the graben may have been active as far back as 451 ka. The 240 ka collapse of Rotorua caldera appears to have been partially controlled by the extended Tikitere graben structure, the location of Mokoia Island in Lake Rotorua is close to the intersection of both of the inferred basement structures and close to a rift structure that connects the Tikitere graben to Ngongotaha dome (Figure 5.3). A lack of exposure on the dome prevents confirmation from measurable internal structures; however, independent evidence for a younger expression of Tikitere structures exists within the graben itself with a young basaltic eruptive episode at 3.71 +/- 0.1 ka, the location of which is on the southern fault margin (Figure 5.2) (Wilson et al. 1984; Cole et al. 2010; Leonard et al. 2010). In summary, the Tikitere structures share a similar orientation to those within the OCC, showing that for the majority of Rotorua caldera's active history, it shared a

similar extension direction to faults located due east, and may have a closer relationship with the kink in the rift than its modern-day surface expression shows.

5.4.3 Timeline of dome eruption at Rotorua caldera

Based upon published dates and field relationships of lava domes at Rotorua caldera (using Lake Rotorua terraces dating from Marx et al. 2009), I present an updated timeline of dome growth. The Kaikaitāhuna group domes are dated at 451 ka (Deering et al. 2010) for Endeian dome, an age which is applied to other Kaikaitāhuna group domes based upon their geochemical similarities (Figure 5.9A). Although definite evidence of regional structure during this time is lacking, I believe that similarly orientated structures were active during the eruption of the Kaikaitāhuna Group which are located close to intersections between basement derived and regional extensional structures similarly to more recent dome activity. The intersection of these structures may have acted as conduits for magma ascent. At ~240 ka, the Mamaku ignimbrite was erupted, and caldera collapse initiated during the middle and upper phases of ignimbrite deposition (Milner et al., 2003). This morphology of the caldera and resultant gravity anomaly indicate that collapse was strongly affected by the intersections of the ENE – WSW regional extension with the NW – SE basement derived structures (Figure 5.4), creating a piecemeal, asymmetric collapse structure centred around 3 gravity anomalies identified by Rogan (1982). Shortly after the Mamaku ignimbrite was emplaced (a matter of days to weeks; Gravley et al. 2007), the Ohakuri ignimbrite was erupted to the SW of Rotorua caldera. This caused large scale subsidence of the area between the Rotorua and Ohakuri calderas, due to lateral magma withdrawal, creating a NE – SW graben bounded on the west by the Horohoro fault and incorporating the area encompassed by the Kapenga caldera (Gravley et al. 2007; Marx et al. 2009).

~40 kys later, a new more evolved magma, that may have incorporated the residue of the Mamaku magma chamber, erupted as the domes of the Utuhina group (Figures 5.9C and 5.9D). Pukehangi dome is down-thrown on the NE side along a basement fault structure, but this movement does not translate through to Ngongotaha dome. This faulting of Pukehangi dome suggests that it erupted before Ngongotaha, followed by a small amount of tectonically controlled subsidence before Ngongotaha was erupted from dykes through a series of fissures (possibly syn-tectonically) at approximately 200 ka (Figures 5.9C and 5.9D) (see Chapter 4). This movement also shows that the basement structure was affecting the location of eruption of the Utuhina group. Similarly to the Kaikaitāhuna group, the Utuhina group domes used the extensional and basement structures as conduit pathways. Flow banding within Ngongotaha dome suggests a near N – S orientated dyke-fed source (see Chapter 4), using caldera collapse structures that linked extensional and basement structures at depth (see section 5.4.2).

After the Mamaku ignimbrite and Utuhina group domes were erupted, the newly created Rotorua basin (from the collapse of the caldera) began to fill with water and several periods of lake overflow and draining occurred, as volcanic activity from other calderas (primarily the OCC) changed drainage patterns (Kennedy et al. 1978; Marx et al. 2009) (Figure 5.9E). The change in lake levels left several fluvial terraces across the previously erupted domes, with terraces formed from the highest lake stand, occurring at an undetermined time after the Mamaku ignimbrite eruption, found on the flanks of Ngongotaha and Pukehangi (Marx et al. 2009). The temporal relationship between the eruption of the domes and this highstand is unclear. This high lake level was subsequently drained after the eruption of the Utuhina group (due to erosion rather than a volcanic or tectonic cause), and a lower lake level continued to 60 ka when near simultaneous eruptions and deposition of the Rotoiti and Earthquake Flats Breccias altered the drainage pattern from Lake Rotorua. Marx et al. (2009) suggests that the eruption of the Rotoiti Breccia from the OCC initiated and simultaneously infilled the Tikitere graben.

Sometime between the eruption of the Rotoiti and Earthquake Flat ignimbrites and the 36 ka Hauparu eruption from the OCC, Mokoia Island dome was erupted (Figure 5.9F). This is shown from a low lake level terrace, located on the dome of Mokoia Island, that was drowned after pyroclastic deposits from the Hauparu eruption blocked the outflow of Lake Rotorua through the Tikitere Graben (Marx et al. 2009). The exact time of eruption of the Hinemoa Point domes is unclear; the domes are small and so do not show preserved lake level terraces. I suggest that due to similarities in the petrography, geochemistry and geographic location of Hinemoa Point and Mokoia Island domes, they erupted at similar times – i.e. before 36 ka (Table 5.1, 5.2, Figures 5.6 and 5.9F).

5.5 Conclusions

The eruption of the Mamaku ignimbrite, and subsequent caldera collapse of Rotorua caldera, was strongly affected by the regional and basement structures that permeate across the TVZ. The lava domes that erupted following the caldera collapse can give an insight into the location and timing of these regional and local structures. The general vent localities of lava domes, and their overall morphology, were controlled by the geometry of feeder dykes, which are in turn controlled by the regional structure. Caldera structures affected the lava domes on a smaller scale, by allowing part of the dome to erupt along a possible ring fault orientated N – S instead of the vent alignment of ENE – WSW of the rest of the dome. This is shown by flow bands orientated in a fan like arrangement in Ngongotaha dome. I also conclude that:

- A major graben to the NE of Rotorua, Tikitere graben, links with lava dome elongation directions and caldera geometry across Rotorua caldera. This shows that the structures that are presently extending in the Tikitere graben were active during caldera collapse and dyke intrusion (240 ka – ~200 ka) and possibly as far back as 451 ka.

- The 'kink' in the extensional rift axis of the TVZ can be traced to the south of Rotorua caldera. The Tikitere graben shares similar orientations to those seen within the OCC to the east; therefore Rotorua caldera shares an overall similar structure to the OCC. Faults to the south of the OCC show a dissimilar orientation, and to the south of Rotorua, a large fault scarp in the Horohoro dome may trace the approximate location of this kink, as it shows both orientations on either side of the kink.
- Geochemistry of the lava domes into 3 related groups suggests a common source that evolved through fractional crystallisation and/ or assimilation. The final group of domes (the Ruamata group) contains signatures of both other groups, suggesting it was a result of mixing or assimilation of these groups or a commonality in source process, along with a low SiO₂ material.

The lack of surface structure at Rotorua caldera, as shown by Villamor et al. (2011), has been mitigated by studying the internal structure and morphology of preserved lava domes. The same principle can be applied to other calderas to gain an insight into the structural controls of the caldera collapse and dome growth, as well as timing of the eruptions.

Chapter 6

Conclusions

***H**ere, I summarise the findings from Chapters 3, 4 and 5, and provide links between the findings of each chapter. I also provide suggestions to future research considerations in this topic area.*

The collapse of bubbles in a lava dome occurs during ascent in the shallow conduit and during extrusion of the lava. Bubble collapse in the dome due to overburden from the overlying lava can reduce porosity to less than 20% over a time span of hours to days (Chapter 3), and is controlled by viscosity, initial porosity and crystallinity. Bubble collapse is accompanied by crack formation, which generally increases permeability in the orientation of the cracks. In crystal-rich rocks, strain is localised in crystals, resulting in short cracks that only propagate to the glass at high strain. The increase in permeability from these cracks is offset by porosity closure, which decreases permeability of the elongated bubble network. Cracks in crystal-poor rocks are long, selectively increasing permeability and may lead to enhanced degassing during extrusion (Chapter 3). Shear in the conduit and extrusion of dyke-fed flows at Ngongotaha and Ruawahia led to the formation of flow bands (Chapter 4), which record the extrusion directions of the lava and vesicularity differences between the carapace and core.

Flow band orientations in lava flows at both Ruawahia and Ngongotaha radiate away from the proposed vent locations. Stalling of the lava flow front occurs due to viscosity increases (due to cooling or degassing) or topography changes, causing thickening of the flows, deformation of flow bands and leading to collapse of the front of the flow (Chapter 4). At Ngongotaha, this stalling causes a reduction in effusion rate and a transition to exogenous, confined sheets. These sheets are able to degas more efficiently due to heavily brecciated margins (Chapter 3) and more time spent in the conduit, and are erupted as lava which shatters during intrusion into the dome (Chapter 4). Spiny lobes at Ruawahia erupt from vents confined within the crater of a pyroclastic cone, forming vertical flow bands above the vents, compared to gently dipping flow bands in undeformed cores and ramp structures of lava flows (Chapter 4). Collapse of the flow fronts at Ruawahia caused vesiculation of the collapse scar, resulting in breadcrust surfaces, 'ropey' skin textures and spherical vesicles (Chapter 4). I propose that the vents of both Ngongotaha and Ruawahia were controlled by dykes.

These dyke-fed vents correspond to the overall regional and caldera structure across Rotorua caldera and the OCC. Both domes have a similar NE – SW trending regional structural control (Chapter 4), and Ngongotaha shows a modification of a N – S trending caldera collapse structure (Chapter 5). The structural control of Ngongotaha is reflected in the geometry of Rotorua Caldera, which is itself controlled by the intersection of NE – SW trending regional structures and NW – SE trending basement structures (Chapter 5). The intersection of these structures is the basis for the piecemeal style collapse of the caldera, and may explain the locations of other caldera related domes. These domes can be linked by geochemistry which suggests a series of small nested magma chambers beneath Rotorua Caldera post caldera collapse, and show 3 main dome growth phases; pre-caldera development (451 ka), following caldera collapse (~200 ka) domes and later (60 – 36 ka) domes (Chapter 5).

Micro- and macro- structures and textures of lava domes record the extrusion history. Analysis of these structures and the process that create them lead to models of eruptive style that predicts the behaviour and hazard potential of the domes. These models, and the other concepts discussed in this thesis, lead to a better understanding of rhyolitic lava domes of varying lava properties, in a variety of settings and styles.

6.1 Hazards associated with new lava dome growth models

The greatest hazard during a lava dome eruption is the collapse of part, or the entire dome which can lead to the explosive decompression of the interior of the dome. Deposits from gravitational collapse of the domes of Tarawera are observed on the northern, southern and eastern flanks (Nairn et al. 2001), but there is little evidence of explosive fragmentation following these eruptions. Minor pyroclastic deposits are located in Paradise Valley, to the west of Ngongotaha, but only one of these could be geochemically linked to the dome (Dravitzki 1999).

The new eruption models presented in Chapter 4 have shown that eruptions of lava domes in the TVZ are not as straightforward as first assumed, as both lava domes show a shift in extrusion style. This shift will change the hazard potential of the lava dome.

At Ngongotaha, the initial endogenous phase is unlikely to produce large scale collapse, as the dome is assumed to have erupted on a flat, unconfined surface which will not have lead to an over-steepened flow front (Chapter 4). After the switch to exogenous behaviour, the hazard from the extending flow front becomes far less. The extensive breccia zones between sheets of obsidian suggest that degassing of these sheets during emplacement was not hindered. The breccia zones also impede the extrusion of these sheets as spines above the rest of the dome, thereby reducing the hazard from possible spine collapse (Lavallée et al. in prep). Compression experiments on Ngongotaha dome pumice (Chapter 3) suggests that crystal poor rocks are able to compress quickly and efficiently, closing off a large proportion of the bubble network. However, the high strain rates associated with collapse also form large cracks that aid degassing. At high strain, bubble collapse is great enough to close off the bubble network, but degassing can continue as long as the cracks remain open, a process which will occur as long as sufficient stress is present to impede crack closure. The cracks also form a weakness in the rock that may be exploited by increasing overpressure or gravity.

The block and ash flows produced from Ruawahia Dome (Nairn et al. 2001) are most likely formed from the unconfined flow lobes to the north and south. Gravitational failure of the front of the flow is the most likely scenario for dome collapse at Ruawahia, and happened as the front of the flow stalled at a change in palaeotopography from the underlying pyroclastic cone to older buried lava domes (Chapter 4). Numerous cracks focussed in the crystals during compression (Chapter 3) will have weakened the rock, and in situ vesiculation of the leading edge of the flow suggests that the interior of the flow was hot, and pressurised, enough to be

able to vesiculate. Low permeability of compressed lava dome samples (Chapter 3) may have aided this process.

In Chapter 5 I have shown that lava dome eruptions following caldera formation continue after the initial caldera forming eruption. At Rotorua Caldera, a single event caldera, the first dome growth period occurred between the collapse of the caldera at 240 ka and 200 ka, with a second dome growth period occurring between 60 and 36 ka, suggesting that small lava dome eruptions can still be a threat long after caldera forming eruptions have ended. Such a comparatively recent eruption (36 ka) at Rotorua, coupled with active geothermal areas, suggests that magma may still present beneath the caldera, although lateral migration of magma and/or heat transfer from nearby Okataina caldera complex may also be responsible (Heise et al. 2013). The structural map of Rotorua Caldera presented in Chapter 5 may help to predict the locations of future lava dome eruptions, and show that knowledge of the interplay between regional and caldera structures is crucial in understanding post-collapse lava dome formation.

6.2 Statements to the findings of this study

Question	What answer could be provided?	Chapter
1: How do bubbles collapse in a compacting lava dome?	The porosity of a magmatic foam collapses quickly with the application of uniaxial compaction. Bubble shape changes from elongated (due to shear during extrusion) to flattened in the direction of principle stress. Porosity reduces to, less than 15 % in crystal poor samples, and ~20 % in crystal rich samples due to the formation of a rigid crystal framework that resists compaction.	3
2: How do cracks affect the permeability of lava domes?	Cracks form in all samples at low strain, during high strain rate. In crystal rich samples, cracks are localised in crystals until high strain, when cracks propagate to the glass. In crystal-poor rocks, large and long cracks in glass occur during initial high strain rates, and cause large increases in directional permeability, with especially large increases in vertical (parallel to stress) permeability. The crystal-localised cracks in crystal-rich rocks do not overcome the loss of permeability from bubble collapse, but may stop the closure of permeability altogether. Permeability is a	3

	key control on the likelihood of fragmentation within a lava dome.	
3: How can the internal structures in lava domes be attributed to eruption style?	Flow bands are produced from movement-induced shear, and will reflect the shape of the conduit during ascent. During extrusion, the flow bands will become modified by the direction of flow of the lava. Analysis of flow band orientations has been used to identify the shape and locations of vents at Ngongotaha and Ruawahia, which controls the style of eruption. Internal breccia zones are attributed to the movement of vertical intrusions. At Ngongotaha, crystal-poor obsidian sheets have formed breccia zones during intrusion past other crystal-poor lavas, while at Ruawahia, breccias zones mark the margins of successive, confined spiny lobes as they intrude past each other.	4
4: What links can be drawn between internal structures of lava domes and their structural setting?	The morphology and vent locations of both domes are linked to the NE-SW trending regional structure across Rotorua caldera and the OCC. At Ngongotaha, the northernmost flow lobe shows a N-S trending elongation which is connected to the edge of a similarly orientated gravity low, attributed to caldera ring faults.	5
5: What can lava domes tell us about the structure and history of calderas?	The interactions between lava domes and structures at Rotorua caldera shows that lava dome effusion occurred over three time periods – pre-caldera collapse lava domes (one dated at 451 ka), post-caldera collapse domes (~200 ka) and a final period not associated with caldera activity (likely between 60 and 36 ka). The time differences between the eruptions, as well as geochemical trends, suggests that multiple, small magma batches were located beneath Rotorua caldera, or were sourced from Okataina caldera complex.	5
6: What implications to volcanic hazards does this research show?	The eruption models of Ruawahia and Ngongotaha help explain the differences in block and ash flow deposits. Ruawahia has extensive block and ash flow deposits, sourced from stalling front of the unconfined flow lobes, while Ngongotaha has very few linked block and ash flow deposits due to the transition to the extrusion of the confined sheets.	6

Table 6.1 Conclusions of thesis

6.3 Future research

This thesis has shown the links between internal structures and eruption styles. The eruption timeline of Ngongotaha and Ruawahia was suggested from differences in facies and structures, but is unable to be confirmed due to the age of the eruptions. The recent eruptions of lava domes such as Unzen (Nakada et al. 1999), Santiaguito (Scott et al. 2013), Soufrière Hills (Watts et al. 2002a) and Showa-Shinzan (Masao 1995) all have detailed chronologies and records of eruption styles. Mapping of the surface structures of these domes will link these to extrusion styles and processes temporally as well as spatially, which will improve our knowledge of dome forming processes and hazards. Prediction of the behaviour of lava domes is at the forefront of current volcanological research.

Collapse scars at Ruawahia were identified from spherical bubble textures (within an otherwise elongated bubble-textured carapace) as well as bread-crusting and 'ropey' skin textures. These features indicate in situ vesiculation without shear or movement, following collapse of part of the lava dome. The temperature and internal pressure conditions at which this occurred on Ruawahia is unknown; it likely happened during final emplacement of the flow, but when the interior of the flow was still hot and pressurised. A series of vesiculation experiments on cores of dense, internal facies Ruawahia samples in a high temperature, high pressure autoclave ('The Magma Brewery') aims to investigate the pressure and temperature window this process occurs at, and may explain why the Ruawahia flows did not explosively fragment upon collapse.

I have explored the role of dykes in dome-forming eruptions, and show eruption styles and morphologies at Ngongotaha and Ruawahia were controlled by dykes, which were themselves controlled by the regional rifting or caldera collapse structures. This link suggests that analysis of dyke orientations in older rocks may indicate the orientation of the stress regime during the time of emplacement. Well constrained dykes are located in many other places in New Zealand, associated with extinct volcanic edifices (Shelley 1988; Hampton & Cole 2009) and intruding

through deformed basement rocks (Pirajno 1982; Grapes et al. 1992). Analysis of these dykes may lead to a better understanding of the structural history of the area at the time of intrusion, a method that could easily be employed in other structural settings.

Chapter 7

References

Acocella, V., Korme, T., Salvini, F., & Funiciello, R. 2002. Elliptic calderas in the Ethiopian Rift: control of pre-existing structures. *Journal of Volcanology and Geothermal Research*, 119, p.189-203.

Acocella, V., Spinks, K.D., Cole, J.W. & Nicol, A. 2003. Oblique back arc rifting of Taupo Volcanic Zone, New Zealand. *Tectonics*, 22 (4), p.1-18.

Acocella, V. 2006. Caldera types: How end-members relate to evolutionary stages of collapse. *Geophysical Research Letters*, 33 (18), p.2-6.

Acocella, V. 2007. Understanding caldera structure and development: An overview of analogue models compared to natural calderas. *Earth-Science Reviews*, 85 (3-4), p.125-160.

Acocella, V. 2010. Evaluating fracture patterns within a resurgent caldera: Campi Flegrei, Italy. *Bulletin of Volcanology*, 72, p. 623–638.

Adams, N.K., Houghton, B.F., Fagents, S.A. & Hildreth, W. 2006. The transition from explosive to effusive eruptive regime: The example of the 1912 Novarupta eruption, Alaska. *Geological Society of America Bulletin*, 118 (5-6), p.620–634.

Aguirre-Díaz, G.J. & Labarthe-Hernandez, G. 2003. Fissure ignimbrites: Fissure-source origin for voluminous ignimbrites of the Sierra Madre Occidental and its relationship with Basin and Range faulting. *Geology*, 31 (9), p.773–776.

Anderson, S.W. & Fink, J.H. 1992. Crease structures: Indicators of emplacement rates and surface stress regimes of lava flows. *Geological Society of America Bulletin*, 104, p.615–625.

- Avard, G. & Whittington, A.G. 2012. Rheology of arc dacite lavas: experimental determination at low strain rates. *Bulletin of Volcanology*, 74 (5), p.1039–1056.
- Bai, L., Baker, D.R. & Rivers, M. 2008. Experimental study of bubble growth in Stromboli basalt melts at 1 atm. *Earth and Planetary Science Letters*, 267, p.533–547.
- Bailey, R.A., Dalrymple, G.B. & Lanphere, M.A. 1976. Volcanism, Structure, and Geochronology of Long Valley Caldera, Mono County, California. *Journal of Geophysical Research*, 81 (5), p.725-744.
- Bailey, R.A. & Carr, R.G. 1994. Physical geology and eruptive history of the Matahina ignimbrite, Taupo volcanic zone, North Island, New Zealand. *New Zealand Journal of Geology and Geophysics*, 37 (3), p.319–344.
- Bagdassarov, N.S. & Pinkerton, H. 2004. Transient phenomena in vesicular lava flows based on laboratory experiments with analogue materials. *Journal of Volcanology and Geothermal Research*, 132 (2-3), p.115–136.
- Bercovici, D. & Michaut, C. 2010. Two-phase dynamics of volcanins eruptions: compaction, compression and the conditions for choking. *Geophysical Journal International*, 182, p.843–864.
- Beresford, S.W. & Cole, J.W. 2000. Kaingaroa Ignimbrite, Taupo Volcanic Zone, New Zealand: Evidence for asymmetric caldera subsidence of the Reporoa Caldera. *New Zealand Journal of Geology and Geophysics*, 43, p.471–481.
- Bernstein, M., Pavez, A., Varley, N., Whelley, P. & Calder, E.S. 2013. Rhyolite lava dome growth styles at Chaitén Volcano, Chile (2008-2009): Interpretation of thermal imagery. *Andean Geology*, 40 (2), p.295–309.

- Bibby, H.M., Caldwell, T.G., Davey, F. & Webb, T. 1995. Geophysical evidence on the structure of the Taupo Volcanic Zone and its hydrothermal circulation. *Journal of Volcanology and Geothermal Research*, 68 (1-3), p.29-58.
- Bouvet de Maisonneuve, C., Bachmann, O. & Burgisser, A. 2009. Characterization of juvenile pyroclasts from the Kos Plateau Tuff (Aegean Arc): insights into the eruptive dynamics of a large rhyolitic eruption. *Bulletin of Volcanology*, 71 (6), p.643–658.
- Branney, M. J., & Kokelaar, P. 1994. Volcanotectonic faulting, soft-state deformation and rheomorphism of tuffs during development of a piecemeal caldera, English Lake District. *Geological Society of America Bulletin*, 106, p.507-530.
- Briggs, R.M., Gifford, M.G., Moyle, A.R., Taylor, S.R., Norman, M.D., Houghton, B.F. Wilson, C.J.N. 1993. Geochemical zoning and eruptive mixing in ignimbrites from Mangakino volcano, Taupo Volcanic Zone, New Zealand. *Journal of Volcanology and Geothermal Research*, 56, p.175 – 203.
- Brown, S.J.A. 1994. *Geology and geochemistry of the Whakamaru Group ignimbrites, and associated rhyolite domes, Taupo Volcanic Zone, New Zealand*. PhD Thesis, University of Canterbury, New Zealand.
- Brown, S.J.A., Wilson, C.J.N., Cole, J.W. & Wooden, J. 1998. The Whakamaru group ignimbrites, Taupo Volcanic Zone, New Zealand: evidence for reverse tapping of a zoned silicic magmatic system. *Journal of Volcanology and Geothermal Research*, 84, p.1–37.
- Bull, K.F. et al., 2012. Emplacement of the final lava dome of the 2009 eruption of Redoubt Volcano, Alaska. *Journal of Volcanology and Geothermal Research*, 259, p. 334-348.
- Burgisser, A. & Gardner, J.E . 2004. Experimental constraints on degassing and permeability in volcanic conduit flow. *Bulletin of Volcanology*, 67 (1), p.42–56.

- Burgisser, A., Poussineau, S., Arbaret, L., Druitt, T.H., Giachetti, T. & Bourdier, J. 2010. Pre-explosive conduit conditions of the 1997 Vulcanian explosions at Soufrière Hills Volcano, Montserrat: I. Pressure and vesicularity distributions. *Journal of Volcanology and Geothermal Research*, 194 (1-3), p.27–41.
- Bursik, M. 2009. A general model for tectonic control of magmatism : Examples from Long Valley Caldera (USA) and El Chichón (México). *Geofísica Internacional*, 48 (1), p.171-183.
- Cabrera, A., Weinberg, R.F., Wright, H.M.N., Zlotnik, S. & Cas, R.A.F. 2011. Melt fracturing and healing: A mechanism for degassing and origin of silicic obsidian. *Geology*, 39 (1), p.67–70.
- Calder, E.S., Lockett, R., Sparks, R.S.J. & Voight, B. 2002. Mechanisms of lava dome instability and generation of rockfalls and pyroclastic flows at Soufriere Hills Volcano, Montserrat. *Memoirs of the Geological Society of London*, 21, p.173–190.
- Carey, R.J., Houghton, B.F., Sable, J.E. & Wilson, C.J.N. 2007. Contrasting grain size and componentry in complex proximal deposits of the 1886 Tarawera basaltic Plinian eruption. *Bulletin of Volcanology*, 69 (8), p.903–926.
- Caricchi, L., Burlini, L., Ulmer, P., Gerya, T., Vassalli, M. & Papale, P. 2007. Non-Newtonian rheology of crystal-bearing magmas and implications for magma ascent dynamics. *Earth and Planetary Science Letters*, 264 (3-4), p.402–419.
- Caricchi, L., Pommier, A., Pistone, M., Castro, J.M., Burgisser, A. & Pergugini, D. 2011. Strain-induced magma degassing: insights from simple-shear experiments on bubble bearing melts. *Bulletin of Volcanology*, 73 (9), p.1245–1257.
- Carn, S.A., Watts, R.B., Thompson, G. & Norton, G.E. 2004. Anatomy of a lava dome collapse: the 20 March 2000 event at Soufrière Hills Volcano, Montserrat. *Journal of Volcanology and Geothermal Research*, 131 (3-4), p.241–264.

Cas, R.A.F. & Wright, J.V. 1988. *Volcanic Successions, Modern and Ancient*, London: Unwin Hyman Ltd.

Cas, R.A.F., Allen, R.L., Bull, S.W., Clifford, B.A. & Wright, J.V. 1990. Subaqueous, rhyolitic dome-top tuff cones: a model based on the Devonian Bunga Beds, southeastern Australia and a modern analogue. *Bulletin of Volcanology*, 52, p. 159–174.

Cashman, K.V., Sturtevant, B., Papale, P., Navon, O. & Ballard, R.D. 2000. Magmatic fragmentation. *In: H. Sigurdsson et al., eds. Encyclopedia of Volcanoes*. San Diego, CA, USA: Academic Press, p. 421–431.

Cashman, K.V., Thornber, C.R. & Pallister, J.S. 2008. From Dome to Dust: Shallow Crystallization and Fragmentation of Conduit Magma During the 2004 – 2006 Dome Extrusion of Mount St. Helens, Washington. *In: D. R. Sherrod, W. E. Scott, & P. H. Stauffer, eds. A Volcano Rekindled: The Renewed Eruption of Mt St Helens, 2004-2006*. USGS, p. 387–413.

Cashman, K.V. & Sparks, R.S.J. 2013 . How volcanoes work: A 25 year perspective. *Geological Society of America Bulletin*, 125(5-6), p.664–690.

Castro, J.M. & Cashman, K.V. 1999. Constraints on rheology of obsidian lavas based on mesoscopic folds. *Journal of Structural Geology*, 21, p.807–819.

Castro, J.M., Burgisser, A., Schipper, C.I. & Mancini, S. 2012. Mechanisms of bubble coalescence in silicic magmas. *Bulletin of Volcanology*, 74 (10), p.2339–2352.

Castro, J.M., Cordonnier, B., Tuffen, H., Tobin, M.J., Puskar, L., Martin, M.C. & Bechtel, H.A. 2012. The role of melt-fracture degassing in defusing explosive rhyolite eruptions at volcán Chaitén. *Earth and Planetary Science Letters*, 333-334, p.63–69.

Castro, J.M., Schipper, C.I., Tuffen, H., James, M. & Militzer, A. 2013. Reassembling a volcanic conduit using bombs at Cordon Caulle, Chile. *IAVCEI Scientific Assembly*. Kagoshima, p. 649.

- Christiansen, R.L. & Lipman, P.W. 1966. Emplacement and Thermal History of a Rhyolite Lava Flow near Fortymile Canyon, Southern Nevada. *Geological Society of America Bulletin*, 77, p.671–684.
- Cole, J.W. & Hunt, T.M. 1968. Basalt Dikes in the Tarawera Volcanic Complex, New Zealand. *New Zealand Journal of Geology and Geophysics*, 11 (5), p.1203–1206.
- Cole, J.W. 1970a. Petrography of the rhyolite lavas of Tarawera Volcanic Complex. *New Zealand Journal of Geology and Geophysics*, 13 (4), p.903-924.
- Cole, J.W. 1970b. Structure and eruptive history of the Tarawera Volcanic Complex. *New Zealand Journal of Geology And Geophysics*, 13 (4), p.881–902.
- Cole, J.W. & Lewis, K.B. 1981. Evolution of the Taupo-Hikurangi subduction system. *Tectonophysics*, 72, p.1-21.
- Cole, J.W. 1990. Structural control and origin of volcanism in the Taupo volcanic zone, New Zealand. *Bulletin of volcanology*, p.445-459.
- Cole, J.W., Brown, S.J.A., Burt, R.M., Beresford, S.W. & Wilson, C.J.N. 1998. Lithic types in ignimbrites as a guide to the evolution of a caldera complex, Taupo volcanic centre, New Zealand. *Journal of Volcanology and Geothermal Research*, 80, p.217–237.
- Cole, J.W. & Spinks, K.D. 2009. Caldera volcanism and rift structure in the Taupo Volcanic Zone, New Zealand. *Geological Society, London, Special Publications*, 327 (1), p.9-29.
- Cole, J.W., Spinks, K.D., Deering, C.D., Nairn, I.A. & Leonard, G.S. 2010. Volcanic and structural evolution of the Okataina Volcanic Centre; dominantly silicic volcanism associated with the Taupo Rift, New Zealand. *Journal of Volcanology and Geothermal Research*, 190 (1-2), p.123-135.
- Collinson, A.S.D. & Neuberg, J.W. 2012. Gas storage, transport and pressure changes in an evolving permeable volcanic edifice. *Journal of Volcanology and Geothermal Research*, 243-244, p.1–13.

Cordonnier, B., Hess, K.- U., Lavallée, Y. & Dingwell, D.B. 2009. Rheological properties of dome lavas: Case study of Unzen volcano. *Earth and Planetary Science Letters*, 279 (3-4), p.263–272.

Cortese, M., Frazzetta, G. & La Volpe, L. 1986. Volcanic history of Lipari (Aeolian Islands, Italy) during the last 10,000 years. *Journal of Volcanology and Geothermal Research*, 27, p.117–133.

Dadd, K.A. 1992. Structures within large volume rhyolite lava flows of the Devonian Comerong Volcanics, southeastern Australia, and the Pleistocene Ngongotaha lava dome, New Zealand. *Journal of Volcanology and Geothermal Research*, 54, p.33-51.

Danišík, M., Shane, P., Schmitt, A.K., Hogg, A., Santos, G.M., Storm, S., Evans, N.J., Fifield, L.K. & Lindsay, J.M. 2012. Re-anchoring the late Pleistocene tephrochronology of New Zealand based on concordant radiocarbon ages and combined $^{238}\text{U}/^{230}\text{Th}$ disequilibrium and (U–Th)/He zircon ages. *Earth and Planetary Science Letters*, 349-350, p.240–250.

Davy, B.W. & Caldwell, T.G. 1998. Gravity, magnetic and seismic surveys of the caldera complex, Lake Taupo, North Island, New Zealand. *Journal of Volcanology and Geothermal Research*, 81 (1-2), p.69–89.

Deering, C.D. 2009. *Spatial and Temporal Distribution of Rhyolite Compositional Continuum from Wet-oxidizing to Dry-reducing Types Governed by Lower-Middle Crustal P-T-fO₂–fH₂O Conditions in the Taupo Volcanic Zone, New Zealand*. PhD Thesis, University of Canterbury, New Zealand.

Deering, C.D., Gravley, D.M., Vogel, T.A., Cole, J.W. & Leonard, G.S. 2010. Origins of cold-wet-oxidizing to hot-dry-reducing rhyolite magma cycles and distribution in the Taupo Volcanic Zone, New Zealand. *Contributions to Mineralogy and Petrology*, 160 (4), p.609-629.

Deering, C.D., Bachmann, O., Dufek, J. & Gravley, D.M. 2011. Rift-related transition from andesite to rhyolite volcanism in the Taupo Volcanic Zone (New Zealand) controlled by crystal-melt dynamics in mush zones with variable mineral assemblages. *Journal of Petrology*, 52 (11), p.2243–2263.

- Degruyter, W., Burgisser, A., Bachmann, O. & Malaspinas, O. 2010. Synchrotron X-ray microtomography and lattice Boltzmann simulations of gas flow through volcanic pumices. *Geosphere*, 6, p.470–481.
- Degruyter, W., Bachmann, O. & Burgisser, A. 2010. Controls on magma permeability in the volcanic conduit during the climactic phase of the Kos Plateau Tuff eruption (Aegean Arc). *Bulletin of Volcanology*, 72, p.63–74.
- de Silva, S.L., Self, S., Francis, P.W., Drake, R.E. & Carlos Ramirez, R. 1994. Effusive silicic volcanism in the Central Andes: The Chao dacite and other young lavas of the Altiplano-Puna Volcanic Complex. *Journal of Geophysical Research*, 99 (B9), p.17805–17825.
- Deubelbeiss, Y., Kaus, B.J.P., Connolly, J.A.D. & Caricchi, L. 2011. Potential causes for the non-Newtonian rheology of crystal-bearing magmas. *Geochemistry Geophysics Geosystems*, 12 (5), p.1–22.
- Dingwell, D.B. 1996. Volcanic Dilemma: Flow or Blow? *Science*, 273(5278), p.1054–1055.
- Dravitzki, D.N.R. 1999. *The Volcanic History and Lake Sediment Characteristics of Paradise Valley, Rotorua*. MSc Thesis, University of Waikato, New Zealand.
- Drenth, B.J. & Finn, C.A. 2007. Aeromagnetic mapping of the structure of Pine Canyon caldera and Chisos Mountains intrusion, Big Bend National Park, Texas. *Geological Society of America Bulletin*, 119 (11-12), p.1521–1534.
- Eichelberger, J.C. & Westrich, H.R. 1981. Magmatic Volatiles in explosive rhyolitic eruptions. *Geophysical Research Letters*, 8, p.757–760.
- Eichelberger, J.C., Lysne, P.C. & Younker, L.W. 1984. Research Drilling at Inyo Domes, Long Valley Caldera, California. *Eos*, 65 (39), p.1–5.

- Eichelberger, J.C., Lysne, P.C., Miller, C.D. & Younker, L.W. 1985. Research Drilling at Inyo domes, California: 1984 results. *Eos*, 66 (17), p.186–187.
- Eichelberger, J.C., Carrigan, C.R., Westrich, H.R. & Price, R.H. 1986. Non-explosive silicic volcanism. *Nature*, 323, p.598–602.
- Eichelberger, J.C. 1989. Are extrusive rhyolites produced from permeable foam eruptions? A reply. *Bulletin of Volcanology*, 51, p.72–75.
- Fink, J.H. 1980. Surface folding and viscosity of rhyolite flows. *Geology*, 8, p.250–254.
- Fink, J.H. 1983. Structure and emplacement of a rhyolitic obsidian flow: Little Glass Mountain, Medicine Lake Highland, northern California. *Geological Society Of America Bulletin*, 94, p.362–380.
- Fink, J.H. & Pollard, D.D. 1983. Structural evidence for dikes beneath silicic domes, Medicine Lake Highland Volcano, California. *Geology*, 11, p.458–461.
- Fink, J.H. & Manley, C.R. 1987. Origin of pumiceous and glassy textures in rhyolite flows and domes. *Special Paper - Geological Society of America*, 212, p.77–88.
- Fink, J.H., Anderson, S.W. & Manley, C.R. 1992. Textural constraints on effusive silicic volcanism: Beyond the permeable foam model. *Journal of Geophysical Research*, 97 (B6), p.9073–9083.
- Fink, J.H. & Griffiths, R.W. 1998. Morphology, eruption rates, and rheology of lava domes: Insights from laboratory models. *Journal of Geophysical Research*, 103 (B1), p.527–545.
- Fink, J.H. & Anderson, S.W. 2000. Lava Domes and Coulees. In H. Sigurdsson et al., eds. *Encyclopedia of Volcanoes*. San Diego, CA, USA: Academic Press, p. 307 - 319.
- Fortin, J., Stanchits, S., Vinciguerra, S. & Guéguen, Y. 2011. Influence of thermal and mechanical cracks on permeability and elastic wave velocities in a basalt from Mt. Etna volcano subjected to elevated pressure. *Tectonophysics*, 503 (1-2), p.60–74.

Gardner, J.E., Thomas, R.M.E., Jaupart, C. & Tait, S. 1996. Fragmentation of magma during Plinian volcanic eruptions. *Bulletin of Volcanology*, 58, p.144–162.

Gardner, J.E., Hilton, M. & Carroll, M.R. 1999. Experimental constraints on degassing of magma: isothermal bubble growth during continuous decompression from high pressure. *Earth and Planetary Science Letters*, 168, p.201–218.

Gent, A.N. 1960. Theory of the parallel plate viscometer. *British Journal of Applied Physics*, 11 (2), p.85.

Giordano, D., Russell, J.K. & Dingwell, D.B. 2008. Viscosity of magmatic liquids: A model. *Earth and Planetary Science Letters*, 271 (1-4), p.123–134.

Goff, F., Rowley, J., Gardner, J.N., Hawkins, W., Goff, S., Charles, R., Wachs, D., Maassen, L. & Heiken, G. 1986. Initial Results From VC-1, First Continental Scientific Drilling Program Core Hole in Valles Caldera, New Mexico. *Journal of Geophysical Research*, 91 (B2), p.1742–1752.

Goldberg, A.S. 2010. Dike swarms as indicators of major extensional events in the 1.9–1.2Ga Columbia supercontinent. *Journal of Geodynamics*, 50 (3-4), p.176–190.

Gonnermann, H.M. & Manga, M. 2005a. Flow banding in obsidian: A record of evolving textural heterogeneity during magma deformation. *Earth and Planetary Science Letters*, 236, p.135–147.

Gonnermann, H.M. & Manga, M. 2005b. Nonequilibrium magma degassing: Results from modeling of the ca. 1340 A.D. eruption of Mono Craters, California. *Earth and Planetary Science Letters*, 238 (1-2), p.1–16.

Gonnermann, H.M. & Manga, M. 2007. The Fluid Mechanics Inside a Volcano. *Annual Review of Fluid Mechanics*, 39 (1), p.321–356.

Gottsmann, J. & Dingwell, D.B. 2001. The cooling of frontal flow ramps: a calorimetric study on the Rocche Rosse rhyolite flow, Lipari, Aeolian Islands, Italy. *Terra Nova*, 13, p.157–164.

Gottsmann, J., Lavallée, Y., Martí, J. & Aguirre-Díaz, G. 2009. Magma–tectonic interaction and the eruption of silicic batholiths. *Earth and Planetary Science Letters*, 284 (3-4), p.426–434.

Grapes, R.H., Lamb, S.H. & Adams, C.J. 1992. K-Ar ages of basanitic dikes, Awatere Valley, Marlborough, New Zealand. *New Zealand Journal of Geology and Geophysics*, 35 (4), p.415–419.

Gravley, D.M. 2004. *The Ohakuri pyroclastic deposits and the evolution of the Rotorua- Ohakuri volcanotectonic depression*. PhD Thesis, University of Canterbury, New Zealand.

Gravley, D.M., Wilson, C.J.N., Leonard, G.S. & Cole, J.W. 2007. Double trouble: paired ignimbrite eruptions and collateral subsidence in the Taupo Volcanic Zone, New Zealand. *Geological Society of America Bulletin*, 119 (1-2), p.18-30.

Gravley, D.M., Leonard, G.S., Wilson, C.J.N., Rowland, J.V. & Hikuroa, D.C.H. 2009. Build-up to an ignimbrite flare-up; geologic evidence for magmatic-tectonic-volcanic interplay in the central Taupo volcanic zone, New Zealand. *Abstracts with Programs - Geological Society of America*, 41 (7), p.57.

Gudmundsson, A. 1983. Form and dimensions of dikes in eastern Iceland. *Tectonophysics*, 95, pp.295–307.

Hale, A.J. 2008. Lava dome growth and evolution with an independently deformable talus. *Geophysical Journal International*, 174 (1), p.391–417.

Hale, A.J., Calder, E.S., Wadge, G., Loughlin, S.C. & Ryan, G.A. 2009. Modelling the lava dome extruded at Soufrière Hills Volcano, Montserrat, August 2005–May 2006. Part I: Dome shape and internal structure. *Journal of Volcanology and Geothermal Research*, 187 (1-2), p.69–84.

- Hale, A.J. & Wadge, G. 2008. The transition from endogenous to exogenous growth of lava domes with the development of shear bands. *Journal of Volcanology and Geothermal Research*, 171 (3-4), p.237–257.
- Hampton, S.J. & Cole, J.W. 2009. Lyttelton Volcano, Banks Peninsula, New Zealand: Primary volcanic landforms and eruptive centre identification. *Geomorphology*, 104 (3-4), p.284–298.
- Hanenkamp, E. 2011. *Decoupling processes in block-and-ash flows: field evidence and analogue modelling*. PhD Thesis, University of Canterbury, New Zealand.
- Harris, A.J.L., Rose, W.I. & Flynn, L.P. 2003. Temporal trends in lava dome extrusion at Santiaguito 1922-2000. *Bulletin of Volcanology*, 65, p.77–89.
- Harris, A.J.L., Flynn, L.P., Matias, O., Rose, W.I. & Cornejo, J. 2004. The evolution of an active silicic lava flow field: an ETM+ perspective. *Journal of Volcanology and Geothermal Research*, 135 (1-2), p.147–168.
- Harrison, A.J. & White, R.S. 2004. Crustal structure of the Taupo Volcanic Zone, New Zealand: Stretching and igneous intrusion. *Geophysical Research Letters*, 31, p.2–5.
- Heiken, G. 1978. Plinian-type eruptions in the Medicine Lake Highland, California, and the nature of the underlying magma. *Journal of Volcanology and Geothermal Research*, 4, p.375–402.
- Heiken, G., Goff, F., Gardner, J.N., Baldrige, W.S., Hulen, J.B., Nielson, D.L. & Vaniman, D. 1990. The Valles/Toledo Caldera Complex, Jemez Volcanic Field, New Mexico. *Annual Review of Earth Planetary Science*, 18, p.27-53.
- Heise, W., Caldwell, T.G., Hill, G.J., Palmer, N.G. & Bertrand, T.A. 2013. Imaging the deep heat source of the Rotorua Geothermal Field. *GSNZ Conference 2013, Christchurch*.

- Herd, R.A., Edmonds, M. & Bass, V.A. 2005. Catastrophic lava dome failure at Soufrière Hills Volcano, Montserrat, 12–13 July 2003. *Journal of Volcanology and Geothermal Research*, 148 (3-4), p.234–252.
- Hess, K.-U., Cordonnier, B., Lavallée, Y. Dingwell, D.B. 2007. High-load, high-temperature deformation apparatus for synthetic and natural silicate melts. *The Review of scientific instruments*, 78 (7), p.075102.
- Hildreth, W. 2004. Volcanological perspectives on Long Valley, Mammoth Mountain, and Mono Craters: several contiguous but discrete systems. *Journal of Volcanology and Geothermal Research*, 136 (3-4), p.169-198.
- Holland, A.S.P., Watson, I.M., Phillips, J.C., Caricchi, L. & Dalton, M.P. 2011. Degassing processes during lava dome growth: Insights from Santiaguito lava dome, Guatemala. *Journal of Volcanology and Geothermal Research*, 202 (1-2), p.153–166.
- Holohan, E. P., Troll, V. R., Walter, T. R., Münn, S., McDonnell, S., & Shipton, Z. K. 2005. Elliptical calderas in active tectonic settings: an experimental approach. *Journal of Volcanology and Geothermal Research*, 144 (1-4), p.119-136.
- Holohan, E.P., Troll, V.R., van Wyk de Vries, B., Walsh, J.J. & Walter, T.R. 2008. Unzipping Long Valley: An explanation for vent migration patterns during an elliptical ring fracture eruption. *Geology*, 36 (4), p.323.
- Holohan, E. P., Wyk de Vries, B., & Troll, V. R. 2008. Analogue models of caldera collapse in strike-slip tectonic regimes. *Bulletin of Volcanology*, 70, p.773-796.
- Houghton, B.F., Lloyd, E.F., Wilson, C.J.N. & Lanphere, M.A. 1991. K-Ar ages from the Western Dome Belt and associated rhyolitic lavas in the Maroa-Taupo area, Taupo Volcanic Zone, New Zealand. *New Zealand Journal of Geology And Geophysics*, 34, p.99–101.

- Houghton, B.F., Wilson, C.J.N., McWilliams, M.O., Lanphere, M.A., Weaver, S.D., Briggs, R.M. & Pringle, M.S. 1995. Chronology and dynamics of a large silicic magmatic system: central Taupo Volcanic Zone, New Zealand. *Geology*, 23 (1), p.13-16.
- Houghton, B.F., Wilson, C.J.N., del Carlo, P., Coltelli, M., Sable, J.E. & Carey, R.J. 2004. The influence of conduit processes on changes in style of basaltic Plinian eruptions: Tarawera 1886 and Etna 122 BC. *Journal of Volcanology and Geothermal Research*, 137 (1-3), p.1–14.
- Hunt, T.M. 1992. Gravity anomalies, caldera structure and subsurface geology in the Rotorua area, New Zealand. *Geothermics*, 21 (1-2), p.65-74.
- Innocentini, M.D.M., Salvini, V.R., Pandolfelli, V.C. & Coury, J.R. 1999. Assessment of Forchheimer's Equation to Predict the Permeability of Ceramic Foams. *Journal of the American Ceramic Society*, 82 (7), p.1945–1948.
- Irving, A.J., Rhodes, J.M. & Sparks, J.W. 1980. Mt St Helens lava dome, pyroclastic flow and ash samples; major and trace element chemistry. *Eos*, 61 (46), p.1138.
- Jaupart, C. & Allegre, C.J. 1991. Gas content, eruption rate and instabilities of eruption regime in silicic volcanoes. *Earth and Planetary Science Letters*, 102, p.413–429.
- Johnson, J.B., Lees, J.M., Gerst, A., Sahagian, D.L. & Varley, N. 2008. Long-period earthquakes and co-eruptive dome inflation seen with particle image velocimetry. *Nature*, 456 (7220), p.377–81.
- Kaneko, T., Wooster, M.J. & Nakada, S. 2002. Exogenous and endogenous growth of the Unzen lava dome examined by satellite infrared image analysis. *Journal of Volcanology and Geothermal Research*, 116 (1-2), p.151–160.
- Keam, R.F. 1988. *Tarawera: The volcanic eruption of 10th June 1886*, Auckland, New Zealand: R.F. Keam.

- Kendrick, J.E., Lavallée, Y., Ferk, A., Perugini, D., Leonhardt, R. & Dingwell, D.B. 2012. Extreme frictional processes in the volcanic conduit of Mount St. Helens (USA) during the 2004–2008 eruption. *Journal of Structural Geology*, 38, p.61–76.
- Kendrick, J.E., Lavallée, Y., Hess, K.- U., Heap, M.J., Gaunt, H.E., Meredith, P. & Dingwell, D.B. 2013. Tracking the permeable porous network during strain-dependent magmatic flow. *Journal of Volcanology and Geothermal Research*, In press.
- Kennedy, B.M., Stix, J., Vallance, J.W., Lavallée, Y. & Longpré, M. 2004. Controls on caldera structure: Results from analogue sandbox modeling. *Geological Society of America Bulletin*, 116 (5), p.515-524.
- Kennedy, B.M., Spieler, O., Scheu, B., Kueppers, U., Taddeucci, J. & Dingwell, D.B. 2005. Conduit implosion during Vulcanian eruptions. *Geology*, 33 (7), p.581.
- Kennedy, B.M., Jellinek, A.M., Russell, J.K., Nichols, A.R.L. & Vigouroux, N. 2010. Time-and temperature-dependent conduit wall porosity: A key control on degassing and explosivity at Tarawera volcano, New Zealand. *Earth and Planetary Science Letters*, 299 (1-2), p.126–137.
- Kennedy, B.M., Wilcock, J. & Stix, J. 2012. Caldera resurgence during magma replenishment and rejuvenation at Valles and Lake City calderas. *Bulletin of Volcanology*, 74 (8), p.1833-1847.
- Kennedy, N., Pullar, W. & Pain, C. 1978. Late Quaternary land surfaces and geomorphic changes in the Rotorua Basin, North Island, New Zealand. *New Zealand Journal of Science*, 21 (2), p.249-261.
- Kilburn, C.R.J. 2000. Lava flows and flow fields. In H. Sigurdsson et al., eds. *Encyclopedia of Volcanoes*. Academic Press, pp. 291–305.
- Klug, C. & Cashman, K.V. 1996. Permeability development in vesiculating magmas: implications for fragmentation. *Bulletin of Volcanology*, 58, p.87–100.

- Kokelaar, P. 1992. Ordovician marine volcanic and sedimentary record of rifting and volcanotectonism; Snowdon, Wales, United Kingdom. *Geological Society of America Bulletin*, 104 (11), p.1433-1455.
- Kolzenburg, S., Heap, M.J., Lavallée, Y., Russell, J.K., Meredith, P.G. & Dingwell, D.B. 2012. Strength and permeability recovery of tuffisite-bearing andesite. *Solid Earth*, 3 (2), p.191–198.
- Kozono, T., Ueda, H., Ozawa, T., Koyaguchi, T., Fujita, E., Tomiya, A. & Suzuki, Y.J. 2013. Magma discharge variations during the 2011 eruptions of Shinmoe-dake volcano, Japan, revealed by geodetic and satellite observations. *Bulletin of Volcanology*, 75 (3), p.695.
- Kueppers, U., Scheu, B., Spieler, O. & Dingwell, D.B. 2005. Field-based density measurements as tool to identify preeruption dome structure: set-up and first results from Unzen volcano, Japan. *Journal of Volcanology and Geothermal Research*, 141 (1-2), p.65–75.
- Lara, L.E., Naranjo, J.A. & Moreno, H. 2004. Rhyodacitic fissure eruption in Southern Andes (Cordón Caulle; 40.5°S) after the 1960 (Mw:9.5) Chilean earthquake: a structural interpretation. *Journal of Volcanology and Geothermal Research*, 138 (1-2), p.127–138.
- Lara, L.E. 2009. The 2008 eruption of the Chaitén Volcano, Chile: a preliminary report. *Andean Geology*, 36 (1), p.125–129.
- Laumonier, M., Arbaret, L., Burgisser, A. & Champallier, R. 2011. Porosity redistribution enhanced by strain localization in crystal-rich magmas. *Geology*, (8), p.715–718.
- Lavallée, Y., Hess, K.- U., Cordonnier, B. & Dingwell, D.B. 2007. Non-Newtonian rheological law for highly crystalline dome lavas. *Geology*, 35 (9), p.843.
- Lavallée, Y., Meredith, P.G., Dingwell, D.B., Hess, K.- U., Wassermann, J., Cordonnier, B., Gerik, A. & Kruhl, J.H. 2008. Seismogenic lavas and explosive eruption forecasting. *Nature*, 453 (7194), p.507–10.

Lavallée, Y., de Silva, S.L., Salas, G. & Byrnes, J.M. 2009. Structural control on volcanism at the Ubinas, Huaynaputina, and Ticsani Volcanic Group (UHTVG), southern Peru. *Journal of Volcanology and Geothermal Research*, 186 (3-4), p.253-264.

Lavallée, Y., Benson, P.M., Heap, M.J., Hess, K.- U., Flaws, A., Schillinger, B., Meredith, P.G. & Dingwell, D.B. 2013. Reconstructing magma failure and the degassing network of dome-building eruptions. *Geology*, 41 (4), p.515–518.

Lavallée, Y., Mitchell, T.M., Heap, M.J., Kennedy, B.M., Ashwell, P.A., Hirose, T. & Dingwell, D.B. In prep. Lava dome or spine? It's a matter of comminution. Target journal: *Geology*.

Leonard, G.S., Cole, J.W., Nairn, I.A. & Self, S. 2002. Basalt triggering of the c. AD 1305 Kaharoa rhyolite eruption, Tarawera Volcanic Complex, New Zealand. *Journal of Volcanology and Geothermal Research*, 115 (3-4), p.461–486.

Leonard, G.S. 2003. *The Evolution of Maroa Volcanic Centre, Taupo Volcanic Zone, New Zealand*. PhD Thesis, University of Canterbury, New Zealand.

Leonard, G.S., Begg, J.G. & Wilson, C.J.N. 2010. Geology of the Rotorua Area. *Institute of Geological and Nuclear Sciences 1:250000 geological map 5*, Lower Hutt, New Zealand: GNS Science.

Liu, Y., Anderson, A.T., Wilson, C.J.N., Davis, A.M. & Steele, I.M. 2005. Mixing and differentiation in the Oruanui rhyolitic magma, Taupo, New Zealand: evidence from volatiles and trace elements in melt inclusions. *Contributions to Mineralogy and Petrology*, 151 (1), p.71–87.

Loughlin, S.C., Lockett, R., Ryan, G., Christopher, T., Hards, V., De Angelis, S., Jones, L. & Strutt, M.H. 2010. An overview of lava dome evolution, dome collapse and cyclicity at Soufrière Hills Volcano, Montserrat, 2005–2007. *Geophysical Research Letters*, 37, p.4–9.

Lovejoy, S., Gaonac'h, H. & Schertzer, D. 2004. Bubble distributions and dynamics: The expansion-coalescence equation. *Journal of Geophysical Research*, 109 (B11), p.1–16.

Lowe, D.J., Newnham, R.M., McFadgen, B.G. & Higham, T.F.G. 2000. Tephra and New Zealand Archaeology. *Journal of Archaeological Science*, 27, p.859–870.

Mader, H.M., Llewellyn, E.W. & Mueller, S.P. 2013. The rheology of two-phase magmas: A review and analysis. *Journal of Volcanology and Geothermal Research*, 257, p.135–158.

Maeno, F. & Taniguchi, H. 2006. Silicic lava dome growth in the 1934–1935 Showa Iwo-jima eruption, Kikai caldera, south of Kyushu, Japan. *Bulletin of Volcanology*, 68 (7-8), p.673–688.

Manga, M., Castro, J.M., Cashman, K.V. & Loewenberg, M. 1998. Rheology of bubble-bearing magmas. *Journal of Volcanology and Geothermal Research*, 87 (1-4), p.15–28.

Manga, M. & Loewenberg, M. 2001. Viscosity of magmas containing highly deformable bubbles. *Journal of Volcanology and Geothermal Research*, 105 (1-2), p.19–24.

Mangan, M. & Sisson, T.W. 2005. Evolution of melt-vapor surface tension in silicic volcanic systems: Experiments with hydrous melts. *Journal of Geophysical Research*, 110, p.1–9.

Manley, C.R. & Fink, J.H. 1987. Internal textures of rhyolite flows as revealed by research drilling. *Geology*, 15, p.549–552.

Martí, J., Ablay, G.J., Redshaw, L.T. & Sparks, R.S.J. 1994. Experimental studies of collapse calderas. *Journal of the Geological Society, London*, 151, p.919–929.

Marx, R., White, J.D.L. & Manville, V. 2009. Sedimentology and allostratigraphy of post-240 ka to pre-26.5 ka lacustrine terraces at intracaldera Lake Rotorua, Taupo Volcanic Zone, New Zealand. *Sedimentary Geology*, 220 (3-4), p.349–362.

Masao, M., 1995. *Showa-Shinzan Diary*, Sapporo, Japan: Suda Seihan Co., Ltd.

Matthews, N.E., Pyle, D.M., Smith, V.C., Wilson, C.J.N., Huber, C. & van Hinsberg, V. 2012. Quartz zoning and the pre-eruptive evolution of the ~340-ka Whakamaru magma systems, New Zealand. *Contributions to Mineralogy and Petrology*, 163, p.87–107.

Matthews, S.J., Gardeweg, M.C. & Sparks, R.S.J. 1997. The 1984 to 1996 cyclic activity of Lascar Volcano, northern Chile: cycles of dome growth, dome subsidence, degassing and explosive eruptions. *Bulletin of Volcanology*, 59 (1), p.72–82.

Michaut, C., Bercovici, D. & Sparks, R.S.J. 2009. Ascent and compaction of gas rich magma and the effects of hysteretic permeability. *Earth and Planetary Science Letters*, 282 (1-4), p.258–267.

Milner, D.M. 2001. *The Structure and Eruptive History of Rotorua Caldera, Taupo Volcanic Zone, New Zealand*. PhD Thesis, University of Canterbury, New Zealand.

Milner, D.M., Cole, J.W. & Wood, C.P. 2002. Asymmetric, multiple-block collapse at Rotorua Caldera, Taupo Volcanic Zone, New Zealand. *Bulletin of Volcanology*, 64 (2), p.134-149.

Milner, D.M., Cole, J.W. & Wood, C.P. 2003. Mamaku Ignimbrite: a caldera-forming ignimbrite erupted from a compositionally zoned magma chamber in Taupo Volcanic Zone, New Zealand. *Journal of Volcanology and Geothermal Research*, 122 (3-4), p.243-264.

Miyabuchi, Y., Hanada, D., Niimi, H. & Kobayashi, T. 2013. Stratigraphy, grain-size and component characteristics of the 2011 Shinmoedake eruption deposits, Kirishima Volcano, Japan. *Journal of Volcanology and Geothermal Research*, 258, p.31–46.

Mongrain, J., Larsen, J.F. & King, P.L. 2008. Rapid water exsolution, degassing, and bubble collapse observed experimentally in K-phonolite melts. *Journal of Volcanology and Geothermal Research*, 173, p.178–184.

Moore, I., & Kokelaar, P. 1998. Tectonically controlled piecemeal caldera collapse: A case study of Glencoe volcano, Scotland. *Geological Society of America Bulletin*, 110 (11), p.1448-1466.

- Mortimer, N. 2004. New Zealand's Geological Foundations. *Gondwana Research*, 7 (1), p.261–272.
- Mourtada-Bonnefoi, C.C. & Laporte, D. 1999. Experimental study of homogeneous bubble nucleation in rhyolitic magmas. *Geophysical research letters*, 26 (23), p.3505–3508.
- Mueller, S., Melnik, O., Spieler, O., Scheu, B. & Dingwell, D.B. 2005. Permeability and degassing of dome lavas undergoing rapid decompression: An experimental determination. *Bulletin of Volcanology*, 67 (6), p.526–538.
- Mueller, S., Scheu, B., Spieler, O. & Dingwell, D.B. 2008. Permeability control on magma fragmentation. *Geology*, 36 (5), p.399.
- Mueller, S., Scheu, B., Kueppers, U., Spieler, O., Richard, D. & Dingwell, D.B. 2011. The porosity of pyroclasts as an indicator of volcanic explosivity. *Journal of Volcanology and Geothermal Research*, 203 (3-4), p.168–174.
- Mungall, J., Bagdassarov, N.S., Romano, C. & Dingwell, D.B. 1996. Numerical modelling of stress generation and microfracturing of vesicle walls in glassy rocks. *Journal of Volcanology and Geothermal Research*, 73, p.33–46.
- Nairn, I.A. 1979. Rotomahana—Waimangu eruption, 1886: base surge and basalt magma. *New Zealand Journal of Geology and Geophysics*, 22 (3), p.363–378.
- Nairn, I.A. & Cole, J.W. 1981. Basalt dikes in the 1886 Tarawera Rift. *New Zealand Journal of Geology and Geophysics*, 24 (5-6), p.585–592.
- Nairn, I.A., Wood, C.P. & Bailey, R.A. 1994. The Reporoa caldera, Taupo volcanic zone: source of the Kaingaroa ignimbrites. *Bulletin of Volcanology*, 56, p.529–537.

- Nairn, I.A., Kobayashi, T. & Nakagawa, M. 1998. The ~10 ka multiple vent pyroclastic eruption sequence at Tongariro Volcanic Centre, Taupo Volcanic Zone, New Zealand: Part 1. Eruptive processes during regional extension. *Journal of Volcanology and Geothermal Research*, 86, p.19–44.
- Nairn, I.A., Self, S., Cole, J.W., Leonard, G.S. & Scutter, C. 2001. Distribution, stratigraphy and history of proximal deposits from the c. AD 1305 Kaharoa eruption of Tarawera volcano, New Zealand. *New Zealand Journal of Geology and Geophysics*, 44 (3), p.467–484.
- Nairn, I.A., 2002. Geology of the Okataina Volcanic Centre. *Institute of Geological and Nuclear Sciences 1:50000 geological map 25*, Lower Hutt, New Zealand: GNS Science.
- Nairn, I.A., Shane, P., Cole, J.W., Leonard, G.S., Self, S. & Pearson, N. 2004. Rhyolite magma processes of the ~ AD 1315 Kaharoa eruption episode, Tarawera volcano, New Zealand. *Journal of Volcanology and Geothermal Research*, 131, p.265–294.
- Nairn, I.A., Hedenquist, J.W., Villamor, P., Berryman, K.R. Shane, P. 2005. The ~AD1315 Tarawera and Waiotapu eruptions, New Zealand: contemporaneous rhyolite and hydrothermal eruptions driven by an arrested basalt dike system? *Bulletin of Volcanology*, 67, p.186–193.
- Nakada, S., Miyake, Y., Sato, H., Oshima, O. & Fujinawa, A. 1995. Endogenous growth of dacite dome at Unzen volcano (Japan), 1993 – 1994. *Geology*, 23, p.157-160.
- Nakada, S. & Motomura, Y. 1999. Petrology of the 1991 – 1995 eruption at Unzen: effusion pulsation and groundmass crystallization. *Journal of Volcanology and Geothermal Research*, 89, p.173–196.
- Nakada, S., Shimizu, H. & Ohta, K. 1999. Overview of the 1990–1995 eruption at Unzen Volcano. *Journal of Volcanology and Geothermal Research*, 89, p.1–22.

- Nakamura, M., Otaki, K. & Takeuchi, S., 2008. Permeability and pore-connectivity variation of pumices from a single pyroclastic flow eruption: Implications for partial fragmentation. *Journal of Volcanology and Geothermal Research*, 176 (2), pp.302–314.
- Nara, Y., Meredith, P.G., Yoneda, T. & Kaneko, K. 2011. Influence of macro-fractures and micro-fractures on permeability and elastic wave velocities in basalt at elevated pressure. *Tectonophysics*, 503 (1-2), p.52–59.
- Navon, O., Chekhmir, A. & Lyakhovsky, V. 1998. Bubble growth in highly viscous melts: theory, experiments and autoexplosivity of dome lavas. *Earth and Planetary Science Letters*, 160, p.763–776.
- Neuberg, J.W., Tuffen, H., Collier, L., Green, D., Powell, T. & Dingwell, D.B. 2006. The trigger mechanism of low-frequency earthquakes on Montserrat. *Journal of Volcanology and Geothermal Research*, 153 (1-2), p.37–50.
- Nguyen, C.T., Gonnermann, H.M., Chen, Y., Huber, C., Maiorano, A.A., Gouldstone, A. & Dufek, J. 2013. Film drainage and the lifetime of bubbles. *Geochemistry, Geophysics, Geosystems*, in press.
- Norrish, K. & Hutton, J., 1969. An accurate X-ray spectrographic method for the analysis of a wide range of geological samples. *Geochemica et Cosmochimica Acta*, 33, p.431–453.
- Okumura, S., Nakamura, M., Takeuchi, S., Tsuchiyama, A., Nakano, T. & Uesugi, K. 2009. Magma deformation may induce non-explosive volcanism via degassing through bubble networks. *Earth and Planetary Science Letters*, 281 (3-4), p.267–274.
- Orsi, G., De Vita, S. & di Vito, M. 1996. The restless, resurgent Campi Flegrei nested caldera (Italy): constraints on its evolution and configuration. *Journal of Volcanology and Geothermal Research*, 74 (3-4), p.179–214.

- Pardo, N. 2012. *Andesitic Plinian eruptions at Mt. Ruapehu (New Zealand): From lithofacies to eruption dynamics*. PhD Thesis, Massey University, New Zealand.
- Pallister, J.S., Diefenbach, A.K., Griswold, J., Muñoz, J., Lara, L.E., Valenzuela, C., Burton, W.C. & Keeler, R. 2010. Volumes and eruption rates for the 2008-2009 Chaiten rhyolite lava dome. In *Abstract V21D-2350 presented at 2010 Fall Meeting, American Geophysical Union*.
- Pallister, J.S., Diefenbach, A.K., Burton, W.C., Muñoz, J., Griswold, J.P., Lara, L.E., Lowenstern, J.B. & Valenzuela, C.E. 2013. The Chaitén rhyolite lava dome: Eruption sequence, lava dome volumes, rapid effusion rates and source of the rhyolite magma. *Andean Geology*, 40 (2), p.277–294.
- Petrinovic, I. A., Martí, J., Aguirre-Díaz, G. J., Guzmán, S., Geyer, A., & Salado Paz, N. 2010. The Cerro Aguas Calientes caldera, NW Argentina: An example of a tectonically controlled, polygenetic collapse caldera, and its regional significance. *Journal of Volcanology and Geothermal Research*, 194 (1-3), p.15-26.
- Pirajno, F. 1982. Lamprophyre dikes in the Victoria Range sector of the Karamea Batholith, New Zealand. *New Zealand Journal of Geology and Geophysics*, 25 (4), p.499–502.
- Pistone, M., Caricchi, L., Ulmer, P., Burlini, L., Ardia, P., Reusser, E., Marone, F. & Arbaret, L. 2012. Deformation experiments of bubble- and crystal-bearing magmas: Rheological and microstructural analysis. *Journal of Geophysical Research*, 117 (B5), p.1-39.
- Platz, T. 2007. *Understanding Aspects of Andesitic Dome-forming Eruptions Through the Last 1000 yrs of Volcanism at Mt. Taranaki, New Zealand*. PhD Thesis, Massey University, New Zealand.
- Platz, T., Cronin, S.J., Cashman, K.V., Stewart, R.B. & Smith, I.E.M. 2007. Transition from effusive to explosive phases in andesite eruptions — A case-study from the AD1655 eruption of Mt. Taranaki, New Zealand. *Journal of Volcanology and Geothermal Research*, 161 (1-2), p.15–34.

Platz, T., Cronin, S.J., Procter, J.N., Neall, V.E. & Foley, S.F. 2012. Non-explosive, dome-forming eruptions at Mt. Taranaki, New Zealand. *Geomorphology*, 136 (1), p.15-30.

Polacci, M., Baker, D.R., Mancini, L., Tromba, G. & Zanini, F. 2006. Three-dimensional investigation of volcanic textures by X-ray microtomography and implications for conduit processes. *Geophysical Research Letters*, 33 (13), p. 1-5.

Polacci, M., Baker, D.R., Bai, L. & Mancini, L. 2008. Large vesicles record pathways of degassing at basaltic volcanoes. *Bulletin of Volcanology*, 70, p.1023–1029.

Polacci, M., Baker, D.R., Mancini, L., Favretto, S. & Hill, R.J. 2009. Vesiculation in magmas from Stromboli and implications for normal Strombolian activity and paroxysmal explosions in basaltic systems. *Journal of Geophysical Research*, 114 (B1), p. 1-14.

Proussevitch, A.A. & Sahagian, D.L. 1996. Dynamics of coupled diffusive and decompressive bubble growth in magmatic systems. *Journal of Geophysical Research*, 101 (B8), p.17447–17445.

Proussevitch, A.A. & Sahagian, D.L. 1998. Dynamics and energetics of bubble growth in magmas: Analytical formulation and numerical modeling. *Journal of Geophysical Research*, 103 (B8), p.18223 – 18251.

Quane, S.L. & Russell, J.K. 2005. Welding: insights from high-temperature analogue experiments. *Journal of Volcanology and Geothermal Research*, 142 (1-2), p.67–87.

Quane, S.L., Russell, J.K. & Friedlander, E.A. 2009. Time scales of compaction in volcanic systems. *Geology*, 37 (5), p.471–474.

Ramsey, M.S., Wessels, R.L. & Anderson, S.W. 2012. Surface textures and dynamics of the 2005 lava dome at Shiveluch volcano, Kamchatka. *Geological Society of America Bulletin*, 124 (5-6), p.678–689.

Reyners, M., Eberhart-Phillips, D., Stuart, G. & Nishimura, Y. 2006. Imaging subduction from the trench to 300 km depth beneath the central North Island, New Zealand, with Vp and Vp/Vs. *Geophysical Journal International*, 165 (2), p.565–583.

Reynolds, M.A., Best, J.G. & Johnson, R.W. 1980. 1953-57 eruption of Tulumán Volcano; rhyolitic volcanic activity in the northern Bismark Sea. *Memoir - Geological Survey of Papua New Guinea*, 7, p.44.

Richnow, J. 1999. *Eruptional and Post-eruptional Processes in Rhyolite Domes*. PhD Thesis, University of Canterbury, New Zealand.

Rissmann, C., Nicol, A., Cole, J.W., Kennedy, B.M., Fairley, J., Christenson, B., Leybourne, M., Milicich, S., Ring, U. & Gravley, D.M. 2011. Fluid flow associated with silicic lava domes and faults, Ohaaki hydrothermal field, New Zealand. *Journal of Volcanology and Geothermal Research*, 204, p.12-26.

Rogan, A.M. 1982. A geophysical study of the Taupo Volcanic Zone, New Zealand. *Journal of Geophysical Research*, 87 (B5), p.4073-4088.

Rose, W.I. 1972. Santiaguito volcanic dome, Guatemala. *Geological Society of America Bulletin*, 83, p.1413–1434.

Rotella, M.D., Wilson, C.J.N., Barker, S.J. & Wright, I.C. 2013. Highly vesicular pumice generated by buoyant detachment of magma in subaqueous volcanism. *Nature Geoscience*, 6 (2), p.129–132.

Rowland, J.V. & Sibson, R.H. 2001. Extensional fault kinematics within the Taupo Volcanic Zone, New Zealand: soft-linked segmentation of a continental rift system. *New Zealand Journal of Geology and Geophysics*, 44 (2), p.271-283.

Rowland, J.V. & Sibson, R.H. 2004. Structural controls on hydrothermal flow in a segmented rift system, Taupo Volcanic Zone, New Zealand. *Geofluids*, 4 (4), p.259–283.

- Rowland, J.V., Wilson, C.J.N. & Gravley, D.M. 2010. Spatial and temporal variations in magma-assisted rifting, Taupo Volcanic Zone, New Zealand. *Journal of Volcanology and Geothermal Research*, 190 (1-2), p.89–108.
- Rust, A.C. & Manga, M. 2002. Effects of bubble deformation on the viscosity of dilute suspensions. *Journal of Non-Newtonian Fluid Mechanics*, 104 (1), p.53–63.
- Rust, A.C., Manga, M. & Cashman, K.V. 2003. Determining flow type, shear rate and shear stress in magmas from bubble shapes and orientations. *Journal of Volcanology and Geothermal Research*, 122, p.111–132.
- Rust, A.C. & Cashman, K.V. 2004. Permeability of vesicular silicic magma: inertial and hysteresis effects. *Earth and Planetary Science Letters*, 228 (1-2), p.93–107.
- Rust, A.C. & Cashman, K.V. 2011. Permeability controls on expansion and size distributions of pyroclasts. *Journal of Geophysical Research*, 116 (B11), p.1–17.
- Saar, M.O. & Manga, M. 1999. Permeability-porosity relationship in vesicular basalts. *Geophysical Research Letters*, 26 (1), p.111–114.
- Sable, J.E., Houghton, B.F., Wilson, C.J.N. & Carey, R.J. 2006. Complex proximal sedimentation from Plinian plumes: the example of Tarawera 1886. *Bulletin of Volcanology*, 69 (1), p.89–103.
- Sahetapy-Engel, S.T. & Harris, A.J.L. 2008. Thermal structure and heat loss at the summit crater of an active lava dome. *Bulletin of Volcanology*, 71 (1), p.15–28.
- Sahetapy-Engel, S.T., Harris, A.J.L. & Marchetti, E. 2008. Thermal, seismic and infrasound observations of persistent explosive activity and conduit dynamics at Santiaguito lava dome, Guatemala. *Journal of Volcanology and Geothermal Research*, 173 (1-2), p.1–14.

Scheu, B., Spieler, O. & Dingwell, D.B. 2006. Dynamics of explosive volcanism at Unzen volcano: an experimental contribution. *Bulletin of Volcanology*, 69 (2), p.175–187.

Scheu, B., Kueppers, U., Mueller, S., Spieler, O. & Dingwell, D.B. 2008. Experimental volcanology on eruptive products of Unzen volcano. *Journal of Volcanology and Geothermal Research*, 175 (1-2), p.110–119.

Schipper, C.I., Castro, J.M., Tuffen, H., James, M.R. & How, P. 2013. Shallow vent architecture during hybrid explosive–effusive activity at Cordón Caulle (Chile, 2011–12): Evidence from direct observations and pyroclast textures. *Journal of Volcanology and Geothermal Research*, 262, p.25–37.

Scott, J.A.J., Pyle, D.M., Mather, T.A. & Rose, W.I. 2013. Geochemistry and evolution of the Santiaguito volcanic dome complex, Guatemala. *Journal of Volcanology and Geothermal Research*, 252, p.92–107.

Scott, W.E., Sherrod, D.R. & Gardner, C.A. 2008. Overview of the 2004 to 2006, and Continuing, Eruption of Mount St. Helens, Washington. In: D. R. Sherrod, W. E. Scott, & P. H. Stauffer, eds. *A Volcano Rekindled: The Renewed Eruption of Mt St Helens, 2004-2006*. USGS Professional Paper 1750, p. 3–26.

Seaman, S.J., Scherer, E.E. & Standish, J.J. 1995. Multistage magma mingling and the origin of flow banding in the Aliso lava dome, Tumacacori Mountains, southern Arizona. *Journal of Geophysical Research - Solid Earth*, 100, p.8381–8398.

Seaman, S.J., Dyar, M.D. & Marinkovic, N. 2009. The effects of heterogeneity in magma water concentration on the development of flow banding and spherulites in rhyolitic lava. *Journal of Volcanology and Geothermal Research*, 183 (3-4), p.157–169.

Seaman, S.J. 2013. Microtexture development during rapid cooling in three rhyolitic lava flows. *American Mineralogist*, 98 (2-3), p.304–318.

Seebeck, H. & Nicol, A. 2009. Dike intrusion and displacement accumulation at the intersection of the Okataina Volcanic Centre and Paeroa Fault zone, Taupo Rift, New Zealand. *Tectonophysics*, 475 (3-4), p.575–585.

Seebeck, H., Nicol, A., Stern, T.A., Bibby, H.M. & Stagpoole, V. 2010. Fault controls on the geometry and location of the Okataina Caldera, Taupo Volcanic Zone, New Zealand. *Journal of Volcanology and Geothermal Research*, 190 (1-2), p.136-151.

Shane, P., Martin, S.B., Smith, V.C., Beggs, K.F., Darragh, M.B., Cole, J.W. & Nairn, I.A. 2007. Multiple rhyolite magmas and basalt injection in the 17.7 ka Rerewhakaaitu eruption episode from Tarawera volcanic complex, New Zealand. *Journal of Volcanology and Geothermal Research*, 164 (1-2), p.1–26.

Shane, P., Nairn, I.A., Smith, V.C., Darragh, M.B., Beggs, K.F. & Cole, J.W. 2008. Silicic recharge of multiple rhyolite magmas by basaltic intrusion during the 22.6 ka Okareka Eruption Episode, New Zealand. *Lithos*, 103, p.527–549.

Shelley, D. 1988. Radial dikes of Lyttelton Volcano — their structure, form, and petrography. *New Zealand Journal of Geology and Geophysics*, 31 (1), p.65–75.

Shepherd, A.D. 1991. *Volcanology and petrology of the post-caldera rhyolite domes, Rotorua Volcanic Centre, New Zealand*. MSc Thesis, Victoria University of Wellington, New Zealand.

Smith, J.V., Yamauchi, S. & Miyake, Y. 1994. Coaxial progressive deformation textures in extrusive and shallow intrusive rocks, southwest Japan. *Journal of Structural Geology*, 16 (3), p.315–322.

Smith, J.V., Miyake, Y. & Oikawa, T. 2001. Interpretation of porosity in dacite lava domes as ductile - brittle failure textures. *Journal of Volcanology and Geothermal Research*, 112, p.25–35.

Smith, R., Sammonds, P.R. & Kilburn, C.R.J. 2009. Fracturing of volcanic systems: Experimental insights into pre-eruptive conditions. *Earth and Planetary Science Letters*, 280 (1-4), p.211–219.

Smith, R., Sammonds, P.R., Tuffen, H. & Meredith, P.G. 2011. Evolution of the mechanics of the 2004–2008 Mt. St. Helens lava dome with time and temperature. *Earth and Planetary Science Letters*, 307 (1-2), p.191–200.

Smith, R.L. & Bailey, R.A. 1968. Stratigraphy, Structure and Volcanic Evolution of the Jemez Mountains, New Mexico. *Geological Society of America Special Publication*, p.447-448.

Smith, V.C., Shane, P. & Nairn, I.A. 2005. Trends in rhyolite geochemistry, mineralogy, and magma storage during the last 50 kyr at Okataina and Taupo volcanic centres, Taupo Volcanic Zone, New Zealand. *Journal of Volcanology and Geothermal Research*, 148, p.372–406.

Smith, V.C., Shane, P., Nairn, I.A. & Williams, C.M. 2006. Geochemistry and magmatic properties of eruption episodes from Haroharo linear vent zone, Okataina Volcanic Centre, New Zealand during the last 10 kyr. *Bulletin of Volcanology*, 69 (1), p.57–88.

Song, S., Jones, K., Lindquist, B., Dowd, B. & Sahagian, D.L. 2001. Synchrotron X-ray computed microtomography: studies on vesiculated basaltic rocks. *Bulletin of Volcanology*, 63(4), p.252–263.

Spieler, O., Kennedy, B.M., Kueppers, U., Dingwell, D.B., Scheu, B. & Taddeucci, J. 2004. The fragmentation threshold of pyroclastic rocks. *Earth and Planetary Science Letters*, 226 (1-2), p.139–148.

Sparks, R.S.J. 1978. The Dynamics of Bubble Formation and Growth in Magmas: A Review and Analysis. *Journal of Volcanology and Geothermal Research*, 3, p.1–37.

- Sparks, R.S.J., Murphy, M.D., Lejeune, A.M., Watts, R.B., Barclay, J. & Young, S.R. 2000. Control on the emplacement of the andesite lava dome of the Soufriere Hills volcano, Montserrat by degassing-induced crystallization. *Terra Nova*, 12 (1), p.14–20.
- Speed, J., Shane, P. & Nairn, I.A. 2002. Volcanic stratigraphy and phase chemistry of the 11 900 yr BP Waiohau eruptive episode, Tarawera Volcanic Complex, New Zealand. *New Zealand Journal of Geology and Geophysics*, 45 (3), p.395–410.
- Spieler, O., Kennedy, B.M., Kueppers, U., Dingwell, D.B., Scheu, B. & Taddeucci, J. 2004. The fragmentation threshold of pyroclastic rocks. *Earth and Planetary Science Letters*, 226 (1-2), p.139–148.
- Spinks, K.D., Acocella, V., Cole, J.W. & Bassett, K. 2005. Structural control of volcanism and caldera development in the transtensional Taupo Volcanic Zone, New Zealand. *Journal of Volcanology and Geothermal Research*, 144 (1-4), p.7-22.
- Stasiuk, M.V., Barclay, J., Carroll, M.R. & Jaupart, C. 1996. Degassing during magma ascent in the Mule Creek vent (USA). *Bulletin of Volcanology*, 58, p.117-130.
- Stevenson, R.J., Briggs, R.M. & Hodder, A.P.W. 1994. Physical volcanology and emplacement history of the Ben Lomond rhyolite lava flow, Taupo Volcanic Centre, New Zealand. *New Zealand Journal of Geology and Geophysics*, 37 (3), p.345–358.
- Storti, F., Billi, A. & Salvini, F. 2003. Particle size distributions in natural carbonate fault rocks: insights for non-self-similar cataclasis. *Earth and Planetary Science Letters*, 206, p.173–186.
- Suzuki, Y. & Fujii, T. 2010. Effect of syneruptive decompression path on shifting intensity in basaltic sub-Plinian eruption: Implication of microlites in Yufune-2 scoria from Fuji volcano, Japan. *Journal of Volcanology and Geothermal Research*, 198 (1-2), p.158–176.

Swanson, S.E., Naney, M.T., Westrich, H.R. & Eichelberger, J.C. 1989. Crystallisation history of Obsidian Dome, Inyo Domes, California. *Bulletin of Volcanology*, 51, p.161–176.

Takeuchi, S., Nakashima, S., Tomiya, A. & Shinohara, H. 2005. Experimental constraints on the low gas permeability of vesicular magma during decompression. *Geophysical Research Letters*, 32 (10), p.1–5.

Takeuchi, S., Nakashima, S. & Tomiya, A. 2008. Permeability measurements of natural and experimental volcanic materials with a simple permeameter: Toward an understanding of magmatic degassing processes. *Journal of Volcanology and Geothermal Research*, 177, p.329–339.

Takeuchi, S., Tomiya, A. & Shinohara, H. 2009. Degassing conditions for permeable silicic magmas: Implications from decompression experiments with constant rates. *Earth and Planetary Science Letters*, 283 (1-4), p.101–110.

Tanguy, J.-C. 2004. Rapid dome growth at Montagne Pelee during the early stages of the 1902 - 1905 eruption: a reconstruction from Lacroix's data. *Bulletin of Volcanology*, 66 (7), p.615–621.

Taylor, B.E., Eichelberger, J.C. & Westrich, H.R. 1983. Hydrogen isotopic evidence of rhyolitic magma degassing during shallow intrusion and eruption. *Nature*, 306, p.541–545.

Taylor, G.A. 1958. The 1951 eruption of Mount Lamington, Papua. *Bulletin of Australian Bureau of Mineral Resources*, 38, p.1–129.

Tian, Y. & Shan, Y. 2011. The diversity of flow structures in felsic dikes. *Journal of the Geological Society, London*, 168, p.1001–1011.

Tuffen, H., Dingwell, D.B. & Pinkerton, H. 2003. Repeated fracture and healing of silicic magma generate flow banding and earthquakes? *Geology*, 31 (12), p.1089.

Tuffen, H. & Dingwell, D.B. 2004. Fault textures in volcanic conduits: evidence for seismic trigger mechanisms during silicic eruptions. *Bulletin of Volcanology*, 67 (4), p.370–387.

Tuffen, H., Smith, R. & Sammonds, P.R. 2008. Evidence for seismogenic fracture of silicic magma. *Nature*, 453, p.511–4.

Tuffen, H. & Castro, J.M. 2009. The emplacement of an obsidian dike through thin ice: Hrafninnuhryggur, Krafla Iceland. *Journal of Volcanology and Geothermal Research*, 185 (4), p.352–366.

Tuffen, H., James, M.R., Castro, J.M., Schipper, C.I., Davies, A.G., Dabrowska, M. & Farquharson, J. 2013. Dynamics of rhyolitic obsidian flow evolution at Cordon Caulle, Chile. In *IAVCEI Scientific Assembly*. Kagoshima, p. 996.

Tuffen, H., James, M.R., Castro, J.M. & Schipper, C.I. 2013. Exceptional mobility of an advancing rhyolitic obsidian flow at Cordón Caulle volcano in Chile. *Nature communications*, 4, p.2709.

Vallance, J.W., Schneider, D.J. & Schilling, S.P. 2008. Growth of the 2004 – 2006 Lava-Dome Complex at Mount St. Helens, Washington. In: D. R. Sherrod, W. E. Scott, & P. H. Stauffer, eds. *A Volcano Rekindled: The Renewed Eruption of Mt St Helens, 2004-2006*. USGS Professional Paper 1750, pp. 169–208.

Villamor, P., Berryman, K. R., Nairn, I. A., Wilson, K., Litchfield, N., & Ries, W. 2011. Associations between volcanic eruptions from Okataina volcanic center and surface rupture of nearby active faults, Taupo rift, New Zealand: Insights into the nature of volcano-tectonic interactions. *Geological Society of America Bulletin*, 123 (7-8), p.1383-1405.

Vinciguerra, S., Trovato, C., Meredith, P.G. & Benson, P.M. 2005. Relating seismic velocities, thermal cracking and permeability in Mt. Etna and Iceland basalts. *International Journal of Rock Mechanics and Mining Sciences*, 42 (7-8), p.900–910.

Vogel, T.A., Eichelberger, J.C., Younker, L.W., Schuraytz, B.C., Horkowitz, J.P., Stockman, H.W. & Westrich, H.R. 1989. Petrology and emplacement dynamics of intrusive and extrusive rhyolites of Obsidian Dome, Inyo Craters Volcanic Chain, Eastern California. *Journal of Geophysical Research*, 94 (B12), p.17937-17956.

Voight, B. 2000. Structural stability of andesite volcanoes and lava domes. *Philosophical Transactions of the Royal Society of London*, 358 (1770), p.1663–1703.

von Aulock, F.W., Nichols, A.R.L., Kennedy, B.M. & Oze, C. 2013. Timescales of texture development in a cooling lava dome. *Geochimica et Cosmochimica Acta*, 114, p.72–80.

von Aulock, F.W. 2013. *Bubbles, Crystals and Cracks in Cooling Magma*. PhD Thesis, University of Canterbury, New Zealand.

von Aulock, F.W., Kennedy, B.M., Oze, C. & Ashwell, P.A. In review. Water diffusion during bubble growth in magma. *Earth and Planetary Science Letters*.

Walcott, R.I. 1987. Geodetic strain and the deformational history of the North Island of New Zealand during the late Cainozoic. *Philosophical Transactions of the Royal Society of London*, 321, p.163–181.

Walker, G.P.L. 1984. Downsag Caldera, Ring Faults, Caldera Sizes, and incremental caldera growth. *Journal of Geophysical Research*, 89 (B10), p.8407–8416.

Walker, G.P.L. 1999. Volcanic rift zones and their intrusion swarms. *Journal of Volcanology and Geothermal Research*, 94 (1-4), p.21–34.

Watkins, J.M., Manga, M. & DePaolo, D.J. 2012. Bubble geobarometry: A record of pressure changes, degassing, and regassing at Mono Craters, California. *Geology*, 40 (8), p.699–702.

Watts, R.B., Herd, R.A., Sparks, R.S.J. & Young, S.R. 2002a. Growth patterns and emplacement of the andesitic lava dome at Soufriere Hills Volcano, Montserrat. *Geological Society, London, Memoirs*, 21 (1), p.115–152.

Watts, R.B., Herd, R.A., Sparks, R.S.J. & Young, S.R. 2002b. The Eruption of Soufriere Hills Volcano, Montserrat (1995 to 1999). In T. H. Druitt & B. P. Kokelaar, eds. *Memoirs of the Geological Society of London*. Geological Society of London, London, UK, p.115 - 152.

Webb, S.L. & Dingwell, D.B. 1990. Non-Newtonian rheology of igneous melts at high stresses and strain rates: Experimental results for rhyolite, andesite, basalt, and nephelinite. *Journal of Geophysical Research*, 95, p.15695–15701.

Westrich, H.R., Stockman, H.W. & Eichelberger, J.C. 1988. Degassing of rhyolitic magma during ascent and emplacement. *Journal of Geophysical Research*, 93 (B6), p.6503–6511.

Westrich, H.R. & Eichelberger, J.C. 1994. Gas transport and bubble collapse in rhyolitic magma: an experimental approach. *Bulletin of Volcanology*, 56, p.447–458.

Wicks, C., de la Llera, J.C., Lara, L.E. & Lowenstern, J. 2011. The role of dyking and fault control in the rapid onset of eruption at Chaitén volcano, Chile. *Nature*, 478, p.374–7.

Williamson, B.J., Di Muro, A., Horwell, C.J., Spieler, O. & Llewellyn, E.W. 2010. Injection of vesicular magma into an andesitic dome at the effusive–explosive transition. *Earth and Planetary Science Letters*, 295 (1-2), p.83–90.

Wilson, C.J.N., Rogan, A.M., Smith, I.E.M., Northey, D.J., Nairn, I.A. & Houghton, B.F. 1984. Caldera Volcanoes of the Taupo Volcanic Zone, New Zealand. *Journal of Geophysical Research*, 89 (B10), p.8463-8484.

- Wilson, C.J.N., Houghton, B.F., McWilliams, M.O., Lanphere, M.A., Weaver, S.D. & Briggs, R.M. 1995. Volcanic and structural evolution of Taupo Volcanic Zone, New Zealand: a review. *Journal of Volcanology and Geothermal Research*, 68, p.1-28.
- Wilson, C.J.N., Blake, S., Charlier, B.L.A. & Sutton, A.N. 2005. The 26.5 ka Oruanui Eruption, Taupo Volcano, New Zealand: Development, characteristics and evacuation of a large rhyolitic magma body. *Journal of Petrology*, 47 (1), p.35–69.
- Wilson, C.J.N., Gravley, D.M., Leonard, G.S. & Rowland, J.V. 2009. Volcanism in the central Taupo Volcanic Zone, New Zealand: tempo styles and controls. *Studies in Volcanology: The Legacy of George Walker. Special Publications of IAVCEI*, 2, p.225-247.
- Wolff, J.A. & Gardner, J.N. 1995. Is the Valles caldera entering a new cycle of activity? *Geology*, 23 (5), p.411-414.
- Wood, C.P. 1992. Geology of the Rotorua geothermal system. *Geothermics*, 21 (1-2), p.25-41.
- Wright, H.M.N., Roberts, J.J. & Cashman, K.V. 2006. Permeability of anisotropic tube pumice: Model calculations and measurements. *Geophysical Research Letters*, 33 (17), p.1–6.
- Wright, H.M.N., Cashman, K.V., Rosi, M. & Cioni, R. 2007. Breadcrust bombs as indicators of Vulcanian eruption dynamics at Guagua Pichincha volcano, Ecuador. *Bulletin of Volcanology*, 69 (3), p.281–300.
- Wright, H.M.N., Cashman, K.V., Gottesfeld, E.H. & Roberts, J.J. 2009. Pore structure of volcanic clasts: Measurements of permeability and electrical conductivity. *Earth and Planetary Science Letters*, 280 (1-4), p.93–104.
- Wright, H.M.N. & Weinberg, R.F. 2009. Strain localization in vesicular magma: Implications for rheology and fragmentation. *Geology*, 37 (11), p.1023–1026.

Yokoyama, T. & Takeuchi, S. 2009. Porosimetry of vesicular volcanic products by a water-expulsion method and the relationship of pore characteristics to permeability. *Journal of Geophysical Research*, 114 (B2), p. 1-10.

Yoshimura, S. & Nakamura, M. 2008. Diffusive dehydration and bubble resorption during open-system degassing of rhyolitic melts. *Journal of Volcanology and Geothermal Research*, 178 (1), p.72–80.

Yoshimura, S. & Nakamura, M. 2010. Chemically driven growth and resorption of bubbles in a multivolatile magmatic system. *Chemical Geology*, 276, p.18–28.

Zhang, X. & Sanderson, D.J. 1998. Numerical study of critical behaviour of deformation and permeability of fractured rock masses. *Marine and Petroleum Geology*, 15, p.535-548.

Ziv, A. & Rubin, A.M. 2000. Stability of dike intrusion along preexisting fractures. *Journal of Geophysical Research*, 105 (B3), p.5947–5961.

Appendices

Appendix: A

Geochemical Data Table

These tables include all geochemical data used in Chapter 5, and was taken from Richnow (1999), Milner (2001) and Deering (2009). Major oxides are measured in weight %, trace elements in ppm.

Ngongotaha dome samples from Richnow (1999):

Sample	NQ-1	NQ-34 a	NQ-36	NQ-39	NQ-50	NQ-10	NQ-11	NQ-23
SiO ₂	73.61	75.35	74.86	75.45	74.45	74.46	74.87	74.85
TiO ₂	0.18	0.24	0.21	0.19	0.23	0.19	0.17	0.18
Al ₂ O ₃	12.92	13.22	13	13.15	13	12.98	13.13	13.14
Fe ₂ O ₃ (t)	1.74	1.78	1.78	1.78	1.77	1.79	1.8	1.78
MnO	0.06	0.07	0.06	0.06	0.06	0.06	0.06	0.05
MgO	0.19	0.23	0.19	0.22	0.22	0.23	0.2	0.21
CaO	1.12	1.13	1.12	1.13	1.12	1.11	1.11	1.14
Na ₂ O	4.4	4.69	4.9	4.59	4.45	4.66	4.4	4.55
K ₂ O	3.29	3.24	2.8	3.35	3.54	3.23	3.64	3.43
P ₂ O ₅	0.03	0.02	0.03	0.03	0.03	0.02	0.04	0.03
H ₂ O	1.14	0.33	0.36	0.46	1.02	0.87	0.07	0.97
Total	98.68	100.31	99.31	100.42	99.98	99.61	99.48	100.33
V	10	12	10	11	10	10	10	8
Cr	3	3	3	3	3	3	3	3
Ni	3	3	3	4	3	3	3	3
Zn	50	52	40	49	58	42	49	46
Zr	210	210	217	212	211	214	219	218
Nb	7	8	10	9	7	9	9	9
Ba	784	783	775	771	798	776	788	783
La	28	29	31	27	28	30	32	30
Ce	58	67	59	59	54	68	65	63
Nd	33	27	33	30	32	32	31	32
Ga	14	14	14	17	15	15	17	14
Pb	19	17	17	27	41	16	28	22
Rb	105	105	102	110	106	107	125	106
Sr	83	82	83	84	82	83	86	83
Th	13	12	14	13	13	13	13	14
Y	35	35	33	33	34	32	35	32

Sample	NQ-48	NQ-56	NQ-57	NQ-58	NQ-59	NQ-12	NQ-14 a	NQ-26
SiO ₂	75.22	74.59	73.94	73.42	73.98	75.49	75.68	74.68
TiO ₂	0.19	0.19	0.2	0.21	0.22	0.21	0.2	0.21
Al ₂ O ₃	13.13	13.14	13.39	13	12.85	13.25	13.21	13.16
Fe ₂ O ₃ (t)	1.76	1.75	1.82	1.75	1.74	1.81	1.78	1.77
MnO	0.05	0.06	0.06	0.06	0.06	0.05	0.06	0.06
MgO	0.21	0.21	0.2	0.22	0.21	0.19	0.22	0.18
CaO	1.13	1.14	1.09	1.11	1.12	1.08	1.14	1.13
Na ₂ O	4.54	4.55	4.36	4.41	4.42	4.62	4.6	5.08
K ₂ O	3.45	3.24	3.32	3.29	3.32	3.38	3.31	3.49
P ₂ O ₅	0.03	0.03	0.03	0.03	0.04	0.02	0.03	0.03
H ₂ O	0.71	0.44	0.57	2.47	1.86	0.07	0.27	0.06
Total	100.42	99.34	98.98	99.96	99.81	100.17	100.5	99.85
V	10	10	11	9	10	11	11	10
Cr	3	3	3	3	3	3	3	3
Ni	3	3	3	3	3	3	3	3
Zn	43	47	51	68	45	43	48	41
Zr	208	216	212	211	215	213	213	216
Nb	8	11	9	9	9	8	9	10
Ba	808	801	791	781	766	818	809	799
La	29	31	27	31	31	29	29	33
Ce	58	58	53	63	65	69	63	63
Nd	30	34	31	38	32	33	37	32
Ga	14	15	15	15	15	14	16	15
Pb	18	21	18	52	17	14	19	16
Rb	118	106	104	106	106	124	100	118
Sr	83	84	84	82	82	83	83	83
Th	13	13	14	11	12	12	13	13
Y	32	33	32	33	32	34	34	33

Sample	NQ-28	NQ-29	NQ-37	NQ-38	NQ-40	NQ-41	NQ-60	NQ-9
SiO ₂	75.39	74.95	75.52	74.25	75.35	74.51	75.15	74.19
TiO ₂	0.21	0.22	0.2	0.18	0.22	0.2	0.21	0.22
Al ₂ O ₃	13.1	12.98	13.15	12.96	13.15	13.12	13.19	13.7
Fe ₂ O ₃ (t)	1.78	1.78	1.75	1.75	1.78	1.75	1.77	1.75
MnO	0.06	0.06	0.05	0.06	0.06	0.06	0.06	0.22
MgO	0.2	0.23	0.21	0.19	0.21	0.22	0.22	0.18
CaO	1.13	1.12	1.13	1.15	1.14	1.11	1.12	1.08
Na ₂ O	4.53	4.54	4.62	4.6	4.6	4.56	4.62	4.48
K ₂ O	3.36	3.37	3.27	3.24	3.37	3.26	3.28	3.47
P ₂ O ₅	0.04	0.03	0.02	0.03	0.04	0.02	0.02	0.3
H ₂ O	0.17	0.5	0.32	0.37	0.03	0.2	0.2	0.1
Total	99.98	99.78	100.25	98.78	99.93	99.02	99.84	99.41
V	10	9	9	10	10	10	9	8
Cr	3	3	3	3	3	3	3	3
Ni	3	3	3	3	3	3	3	3
Zn	40	40	42	36	37	40	43	140
Zr	215	217	216	214	221	210	218	215
Nb	9	10	9	10	9	9	10	10
Ba	769	810	794	782	804	808	782	833
La	30	32	32	32	31	28	32	44
Ce	59	66	63	63	62	54	62	95
Nd	29	29	32	33	34	32	33	60
Ga	15	15	15	15	15	15	15	16
Pb	21	19	16	17	16	20	17	27
Rb	110	112	100	114	102	102	106	97
Sr	84	83	85	85	84	85	81	87
Th	12	12	13	11	13	12	14	12
Y	34	33	33	33	33	33	33	62

Sample	NQ-14 b	NQ-22	NQ-25	NQ-30	NQ-34 b	NQ-42	NQ-45	NQ-49
SiO ₂	75.66	74.27	74.77	75.48	75.01	74.31	74.3	75.3
TiO ₂	0.22	0.22	0.2	0.22	0.21	0.22	0.2	0.22
Al ₂ O ₃	13.18	13.06	13.2	13.1	13.01	13.24	12.9	13.08
Fe ₂ O ₃ (t)	1.75	1.74	1.75	1.77	1.78	1.79	1.73	1.77
MnO	0.06	0.06	0.06	0.05	0.06	0.06	0.06	0.06
MgO	0.22	0.21	0.2	0.22	0.19	0.24	0.18	0.22
CaO	1.14	1.13	1.14	1.13	1.14	1.12	1.12	1.12
Na ₂ O	4.68	4.57	4.55	4.66	4.64	4.53	4.62	4.62
K ₂ O	3.3	3.21	3.29	3.29	3.28	3.3	3.15	3.38
P ₂ O ₅	0.03	0.03	0.03	0.03	0.03	0.03	0.03	0.04
H ₂ O	0	1.37	0.48	0.07	0.46	0.02	1.15	0.69
Total	100.23	99.87	99.68	100.04	99.81	98.88	99.45	100.5
V	10	10	9	10	9	9	10	10
Cr	3	3	3	3	3	3	3	3
Ni	3	3	3	3	3	3	3	3
Zn	46	45	44	38	38	33	47	41
Zr	213	215	220	214	218	215	209	217
Nb	8	10	10	11	9	9	8	10
Ba	805	793	790	768	776	792	773	786
La	28	34	28	30	30	32	28	33
Ce	62	67	60	70	56	66	65	68
Nd	36	38	36	31	28	28	24	28
Ga	16	14	14	16	16	15	15	13
Pb	19	21	18	16	20	16	19	18
Rb	102	107	107	93	100	104	103	118
Sr	84	86	85	84	84	85	83	83
Th	13	13	12	13	13	14	13	13
Y	35	33	33	34	33	35	32	33

Sample	NQ-6	NQ-15	NQ-16	NQ-18	NQ-44	NQ-8	NQ-19	NQ-21
SiO ₂	75.43	74.97	75.08	73.67	75.41	74.97	75.21	74.81
TiO ₂	0.19	0.2	0.22	0.22	0.22	0.21	0.2	0.22
Al ₂ O ₃	13.11	13.26	13.29	13.29	13.18	13.08	13.2	13.13
Fe ₂ O ₃ (t)	1.8	1.79	1.76	1.83	1.74	1.77	1.75	1.7
MnO	0.07	0.06	0.06	0.04	0.06	0.06	0.06	0.05
MgO	0.19	0.2	0.22	0.2	0.19	0.21	0.2	0.16
CaO	1.15	1.1	1.11	1.03	1.13	1.13	1.05	1.1
Na ₂ O	4.57	4.62	4.65	4.61	4.71	4.7	4.54	4.66
K ₂ O	3.42	3.31	3.19	3.28	3.3	3.24	3.28	3.17
P ₂ O ₅	0.03	0.03	0.02	0.02	0.02	0.04	0.03	0.04
H ₂ O	0.49	0.41	0.56	0.47	0.16	0.2	0.11	0.23
Total	100.43	99.95	100.17	98.66	100.13	99.59	99.64	99.27
V	10	10	10	11	10	11	8	10
Cr	3	3	3	3	3	3	3	3
Ni	4	3	3	3	3	3	3	3
Zn	46	37	41	37	26	53	36	40
Zr	211	216	212	216	206	215	217	211
Nb	9	10	10	10	9	10	10	8
Ba	784	809	771	805	797	787	820	766
La	29	31	28	25	28	31	32	31
Ce	61	63	51	51	56	66	67	68
Nd	29	31	28	18	37	29	29	30
Ga	15	15	15	16	14	15	15	16
Pb	18	16	22	17	16	14	11	22
Rb	105	113	97	121	120	101	106	93
Sr	84	84	84	85	85	85	84	84
Th	13	12	12	14	11	12	12	12
Y	34	33	29	46	34	33	29	32

Sample	NQ-21*	NQ-31 a	NQ-31 b	NQ-43	NQ-2	NQ-27	NQ-3	NQ-51
SiO ₂	74.22	75.37	74.97	72.85	75.08	75.05	74.48	74.63
TiO ₂	0.22	0.23	0.19	0.19	0.21	0.21	0.2	0.2
Al ₂ O ₃	12.94	13.28	13	13.05	13.15	13.05	13.02	12.99
Fe ₂ O ₃ (t)	1.74	1.78	1.79	5.1	1.76	1.77	1.76	1.75
MnO	0.05	0.06	0.06	0.05	0.06	0.06	0.05	0.07
MgO	0.21	0.26	0.24	0.16	0.22	0.21	0.2	0.22
CaO	1.1	1.17	1.14	1	1.13	1.12	1.13	1.12
Na ₂ O	4.33	4.65	4.58	4.48	4.59	4.35	4.61	4.53
K ₂ O	3.42	3.32	3.28	3.17	3.31	3.71	3.18	3.27
P ₂ O ₅	0.03	0.04	0.04	0.05	0.03	0.03	0.03	0.02
H ₂ O	1.37	0.19	0.13	0.36	-0.13	0.93	0.17	0.86
Total	99.64	100.34	99.42	100.46	99.41	100.49	98.83	99.66
V	8	11	9	9	11	11	11	10
Cr	3	3	3	3	3	3	3	3
Ni	3	3	3	4	4	3	4	3
Zn	46	19	34	40	55	48	62	44
Zr	220	214	219	198	210	210	206	210
Nb	10	9	9	8	7	8	8	8
Ba	784	746	758	889	810	771	792	796
La	32	24	29	80	28	28	29	28
Ce	68	60	60	96	58	64	62	60
Nd	32	29	28	67	26	29	22	26
Ga	16	16	16	17	14	16	14	15
Pb	20	10	14	23	22	18	25	19
Rb	106	107	108	91	107	116	106	105
Sr	83	82	83	101	83	82	85	84
Th	12	13	12	15	13	13	13	11
Y	33	32	32	61	31	33	34	33

Sample	NQ-52	NQ-53	NQ-54	NQ-55	NQ-20	NQ-24	NQ-32	NQ-33	NQ-7
SiO ₂	74.87	75.18	74.8	74.39	74.35	75.39	75.31	74.56	74.58
TiO ₂	0.19	0.22	0.22	0.21	0.18	0.21	0.23	0.22	0.22
Al ₂ O ₃	13.03	13.23	13.17	13.04	12.97	13.22	13.35	13.03	13.03
Fe ₂ O ₃ (t)	1.76	1.78	1.73	1.76	1.81	1.83	1.69	1.76	1.81
MnO	0.06	0.06	0.06	0.06	0.05	0.05	0.06	0.06	0.05
MgO	0.2	0.22	0.21	0.21	0.14	0.18	0.2	0.18	0.2
CaO	1.14	1.14	1.12	1.12	1.06	1.1	1.12	1.08	1.16
Na ₂ O	4.56	4.62	4.54	4.52	4.56	4.57	4.67	4.54	4.57
K ₂ O	3.32	3.32	3.27	3.29	3.24	3.39	3.31	3.31	3.39
P ₂ O ₅	0.03	0.03	0.03	0.03	0.02	0.03	0.02	0.02	0.03
H ₂ O	0.83	0.36	0.83	1.64	0.44	0.42	0.33	0.3	0.04
Total	99.99	100.16	99.99	100.27	98.83	100.39	100.3	99.07	99.08
V	11	11	11	11	10	11	11	9	10
Cr	3	3	3	3	3	3	3	3	3
Ni	3	3	4	3	3	3	3	3	3
Zn	50	51	52	50	32	31	24	39	42
Zr	210	213	218	211	217	223	208	214	220
Nb	8	7	8	7	9	9	8	10	10
Ba	800	803	827	833	826	799	817	773	778
La	30	31	31	30	33	28	28	31	32
Ce	64	66	62	72	72	52	47	61	60
Nd	32	28	29	32	51	26	21	31	33
Ga	15	16	16	16	15	15	16	15	15
Pb	19	21	20	24	19	17	12	16	18
Rb	106	108	102	106	105	101	98	105	110
Sr	83	81	83	83	86	86	85	84	88
Th	12	12	13	12	13	12	12	12	13
Y	34	33	35	33	36	24	29	36	34

Ngongotaha and other dome samples from Milner (2001):

Sample	RR1	RR5	RR8	RR9	RR11	RR15
Dome source	Endean Dome Rhyolite	Ngongotaha	Ngongotaha	Ngongotaha	Ngongotaha	Ngongotaha
SiO ₂	72.97	75.05	75.59	74.91	75.42	74.25
TiO ₂	0.29	0.19	0.19	0.19	0.2	0.2
Al ₂ O ₃	14.55	13.52	13.53	13.61	13.6	13.74
Fe ₂ O ₃ (t)	2.41	1.81	1.79	1.77	1.84	1.84
MnO	0.06	0.06	0.06	0.06	0.06	0.06
MgO	0.42	0.17	0.11	0.17	0.11	0.18
CaO	1.96	1.01	0.99	1.05	0.9	1.07
Na ₂ O	3.84	4.29	4.52	4.78	4.31	4.49
K ₂ O	3.04	3.49	3.18	3.17	3.35	3.18
P ₂ O ₅	0.06	0.02	0.02	0.03	0.03	0.03
H ₂ O	0.67	0.64	0.5	0.53	0.65	1.35
Total	100.26	100.26	100.48	100.26	100.45	100.41
V	29	14	14	13	12	13
Cr	7	4	3	3	5	5
Ni	4	4	3	3	3	3
Zn	40	50	37	48	49	55
Zr	154	228	228	223	221	230
Nb	7	11	11	11	10	10
Ba	832	841	931	823	842	851
La	27	32	34	26	24	32
Ce	54	76	73	74	63	62
Nd	13	18	20	21	17	24
Ga	14	15	15	15	15	15
Pb	11	20	15	18	18	20
Rb	72	106	81	94	110	104
Sr	160	75	81	83	75	82
Th	12	12	11	11	11	10
Y	18	37	36	32	27	36

Sample	RR16	RR17	RR19	RR20	RR21	RR22
Dome source	Mokoia Island Rhyolite	Mokoia Island Rhyolite	Hamurana Dome Rhyolite	Pukehangi Dome Rhyolite	Hinemoa Point Rhyolite	Hinemoa Point Rhyolite
SiO₂	73.89	73.69	73.48	75.42	71.14	71.63
TiO₂	0.25	0.24	0.35	0.19	0.3	0.29
Al₂O₃	13.91	13.02	14.39	13.19	14.94	14.6
Fe₂O₃ (t)	1.44	2.15	2.09	1.74	2.19	2.23
MnO	0.04	0.05	0.03	0.06	0.06	0.06
MgO	0.25	0.28	0.3	0.17	0.46	0.44
CaO	1.47	1.39	1.84	1.07	2.03	1.86
Na₂O	4.32	4.21	3.84	4.6	4.22	4.07
K₂O	2.9	3.21	3.15	3.37	2.79	2.81
P₂O₅	0.06	0.08	0.03	0.03	0.03	0.02
H₂O	1.7	1.99	0.72	0.47	2.16	2.26
Total	100.22	100.32	100.2	100.31	100.31	100.28
V	16	23	27	12	26	24
Cr	5	3	3	3	4	4
Ni	3	3	3	3	3	3
Zn	35	43	31	51	39	48
Zr	186	179	219	220	181	168
Nb	9	8	7	10	8	8
Ba	758	716	722	779	770	748
La	23	23	22	28	15	14
Ce	60	79	69	83	60	61
Nd	17	23	37	45	10	10
Ga	16	14	14	14	15	15
Pb	17	15	13	18	12	14
Rb	96	107	105	107	94	100
Sr	125	107	154	80	163	149
Th	10	10	11	12	11	9
Y	26	31	23	36	25	22

Sample	RR28	RR29	RR32	RR33	RR34
Dome source	Endean Dome Rhyolite	Endean Dome Rhyolite	Kawaha Point Rhyolite	Kawaha Point Rhyolite	Buried Domes
SiO₂	74.23	73.6	75.52	75.36	77.13
TiO₂	0.31	0.28	0.21	0.2	0.13
Al₂O₃	13.77	14.28	13.39	13.14	12.95
Fe₂O₃ (t)	2.4	2.22	1.66	1.73	0.91
MnO	0.03	0.04	0.03	0.06	0.03
MgO	0.26	0.33	0.06	0.2	0.05
CaO	1.52	1.73	0.99	1.17	0.88
Na₂O	3.47	3.68	4.38	4.62	4.08
K₂O	3.37	3.18	3.32	3.27	3.53
P₂O₅	0.03	0.03	0.03	0.03	0.02
H₂O	0.83	0.89	0.7	0.46	0.55
Total	100.23	100.25	100.27	100.23	100.25
V	30	27	17	13	6
Cr	8	5	3	3	5
Ni	3	4	4	5	4
Zn	29	32	32	47	30
Zr	153	151	228	223	143
Nb	6	7	11	10	9
Ba	732	759	767	804	795
La	13	16	23	25	26
Ce	47	47	55	65	62
Nd	10	10	10	27	35
Ga	14	13	15	14	13
Pb	12	12	14	18	18
Rb	120	115	106	105	108
Sr	128	145	85	90	77
Th	11	12	12	10	13
Y	14	13	20	33	27

Ngongotaha and other dome samples from Deering (2009):

Sample	UC1229	UC1232	UC1233
Dome source	Hamurana Dome	Ngongotaha Dome	Endean Dome
SiO ₂	74.02	76.17	73.79
TiO ₂	0.35	0.18	0.31
Al ₂ O ₃	13.46	12.7	13.82
Fe ₂ O ₃ (t)	2.58	1.76	2.42
MnO	0.05	0.06	0.05
MgO	0.49	0.21	0.44
CaO	1.92	0.96	1.79
Na ₂ O	4	4.6	3.93
K ₂ O	3.07	3.32	3.4
P ₂ O ₅	0.06	0.02	0.05
H ₂ O	1.64	2.09	1.63
Total	98.23	97.78	98.26
V	31.75	7.71	32.03
Cr	5	4	6
Ni	-	-	-
Zn	38	40	35
Zr	243	227	180
Nb	10	15	9
Ba	813	926	894
La	25	30	23
Ce	49	69	46
Nd	19	25	16
Ga	-	-	-
Pb	20	33	22
Rb	105	108	125
Sr	154	76	143
Th	11	12	13
Y	25	37	16

Appendix: B

Digital appendix of video files from ImageJ of tomography samples from Chapter 3, as listed below. The following videos are from CT scans of cores performed at LMU (see Chapter 2 and 3, and Figure 3.5):

B1 – NP undeformed CT.avi

B2 – NP 20% strain CT.avi

B3 – NP 60% strain CT.avi

B4 – TP undeformed CT.avi

B5 – TP 20% strain CT.avi

B6 – TP 60% strain CT.avi [NOTE: This CT was performed on the Australian Synchrotron, and therefore the size of the core, and quality of the video is different to others]

B7 – TD undeformed CT.avi

B8 – TD 20% strain CT.avi

B9 TD 60% strain CT.avi

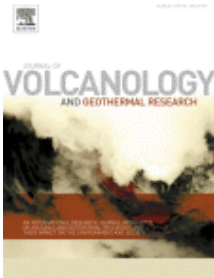
The following videos are 3D reconstructions of bubble shapes (see Chapter 3, Figure 3.6)

B10 – NP undeformed bubble shape.avi

B11 – NP 60% strain bubble shape.avi

Appendix: C

Copy of journal article from Journal of Volcanology and Geothermal Research of Chapter 5.



<http://ars.els-cdn.com/content/image/1-s2.0-S0377027313X00083-cov150h.gif> class="toprightlogo"/>

Insights into caldera and regional structures and magma body distribution from lava domes at Rotorua Caldera, New Zealand

- [P.A. Ashwell](#)  <http://origin-cdn.els-cdn.com/sd/entities/REcor.gif>  <http://origin-cdn.els-cdn.com/sd/entities/REemail.gif> alt="E-mail the corresponding author",
- [B.M. Kennedy](#),
- [D.M. Gravley](#),
- [F.W. von Aulock](#),
- [J.W. Cole](#)

Show more

Show less

<http://dx.doi.org/10.1016/j.jvolgeores.2013.04.014>